MODELLING CO- AND POST-SEISMIC DISPLACEMENTS REVEALED BY INSAR, AND THEIR IMPLICATIONS FOR FAULT BEHAVIOUR

WANPENG FENG (MSc)

THESIS SUBMITTED TO THE UNIVERSITY OF GLASGOW FOR THE DEGREE OF DOCTOR OF PHILOSOPHY

February 2015

SCHOOL OF GEOGRAPHICAL AND EARTH SCIENCES
COLLEGE OF SCIENCE AND ENGINEERING
UNIVERSITY OF GLASGOW

SUPERVISED BY

PROFESSORS ZHENHONG LI AND TREVOR HOEY

Declaration

The contents of this thesis are the result of my own work, except where material from other sources has been properly and fully acknowledged. The thesis has not been submitted for any degree at the University of Glasgow or any other institution. The views and opinions expressed herein are mine and not necessarily those of any other person or organization, unless so attributed.

Selected figures used within Chapter 2 are, in part, a reformatted version of material appearing in Feng, W., Li, Z., Elliott, J.R., et al., 2013. The 2011 M_W 6.8 Burma earthquake: fault constraints provided by multiple SAR techniques. Geophysical Journal International 195, 650-660. doi:10.1093/gji/ggt254. The thesis author was the principal researcher who processed SAR data, carried out geodetic modelling, plotted most figures and wrote the first draft, whilst all other co-authors listed in this publication reviewed the manuscript and contributed to data interpretation.

Main text and selected figures used within Chapter 4 are material appearing in Feng, W., Li, Z., Hoey, T., et al., 2014. Patterns and Mechanisms of Coseismic and Postseismic Slips of the 2011 $\mathrm{M_W}$ 7.1 Van (Turkey) Earthquake Revealed by Multi-platform Synthetic Aperture Radar Interferometry. Tectonophysics. doi:10.1016/j.tecto.2014.06.011. The thesis author processed most SAR data, carried out co- and post-seismic displacements modelling, plotted all figures and wrote the first draft, whilst all other co-authors listed in this publication carefully reviewed the manuscript and contributed to data interpretation. The co-author, Sergey Samsonov processed RADARSAT-2 data for postseismic analysis.

Main text and selected figures used within Chapter 5 are reformatted versions of material appearing in Feng, W., Li, Z., Li, Q., 2014. Coseismic slip model of 2011 Tohoku Japan $\mathrm{M_W}$ 9.0 Earthquake by a joint inversion from terrestrial GPS and GRACE gravity changes. Geophysical Journal International (*in revision*). The thesis author was the principal researcher who conducted the joint inversion strategy, developed the codes, carried out geodetic modelling, plotted most figures and wrote the first draft, whilst all other co-authors listed in this publication commented the manuscript and contributed to data interpretation. The co-author, Dr. Qiong Li implemented GRACE data processing, plotted gravity time series used in Figure 5.2, provided part of codes on data processing that was involved in theoretical GRACE gravity changes simulation, and prepared for the explanation for GRACE data processing. This work was initiated by a College Prize International Internship.

Wanpeng Feng

October 2014, Glasgow

Acknowledgements

It is in September again. Since I landed in Glasgow on 26th September 2011, a three-year long PhD study has nearly been finished. I left this section until now to leave me an opportunity to recall people whom I owe thanks to, and invaluable life-experiences in Glasgow that will influence my whole life.

First of all, I would like to express a big thank you to my supervisors Prof. Zhenhong Li and Prof. Trevor Hoey. I truly appreciate the opportunity of pursuing a doctoral degree in the University of Glasgow. Before that, I had worked with Zhenhong for nearly 5 years. I cannot commence this study without his encouragement and great help. To my second supervisor Prof. Trevor Hoey, I owe a big thank to him. His patience and encouragement always made me feel easy when he answers my puzzles. Without their advice and patient guidance through the last three years, I cannot reach to a PhD degree.

Staff and postgraduate students in our school should also be given lots of thanks. Thank Jane and John's invitation for a traditional Scottish dinner at their home. It is unforgettable for my family to have a nice evening with this couple. I remember "The pain shared, the pain halved!" that was learnt during a talk with Paul. I really appreciated for Susan's well-intentioned criticisms in my annual interviews. She even offered me a cup of coffee during a personal talk on how to undertake a PhD in the UK. I am also grateful to Dr. Cristina and Dr. Daniel for their taking time in my seminars. The friendship should be recorded from other peers within the UoG: Julius, Andy, Haval, Hannah, Paul, James, Alessa, Flavia, Zairis, Robin, Peng, Zhiwei and Julia. I am really lucky to share the office with Julius and Andy. Lots of great help and warm moments will never be forgotten.

I need to express great thanks to those who gave me countless help from outside Glasgow. Thank Prof. Zhonghuai Xu from IGP for always answering my questions on seismology. Thank Dr. Rongjiang Wang (GFZ) for his patient explanation on use of his deformation simulation package, PSGRN/PSCMP. Thank Dr. Barbot Sylvain from NTU for his quick response to my questions on AZISAR. Thank Miss Ling Chang (DELFT) for her uninterrupted help on how to use DORIS. Thank Dr. Qiong Li (WHU) for her great support on GRACE gravity data processing. Thank Dr. Dominique from Centre Spatial de Liège (CSL) for his patient lecture on the SAR range splitting theory. I am still missing the period when I studied in IGPP of SIO, California. Without help from Prof. Yuri Fialko and Mrs. Michell Parks, I could not implement such invaluable trip in UCSD. Prof. Yuri Fialko deserves a big thank for his guidance on earthquake mechanics that just enlightened me to work on the friction law in this thesis. Without Mr Kang Wang's kind help, I could not master RELEX in such a short period. Thank Dr. Xiaopeng Tong for his answering my queries on GMTSAR. My landlord in San Diego will also never be forgotten. Wish this nice family always being well and happy.

Part of material used in this thesis is based on some publications during my study. My co-authors, Dr. John Elliott (from Oxford), Dr. Qiong Li (again), Dr. Yo Fukushima (from the University of Kyoto), Dr. Andrew Singleton (Andy again), Mr. Robert Cook (UoG), Dr. Rongjiang Wang (again, GFZ), Dr. Yong Zhang (Peking University), Dr. Sergey Samsonov (Canada), Dr. Yadong Wang (CAS), should be given many thanks for their great contributions in our papers.

Many thanks for my Chinese friends in Glasgow. Because of them, including Lei Wang, Jia Zhao, Min Hou, Robin (again), Di Xu, Beibei Li, Lei Zhang, Jie Ding, Guowen Huang, Ying Zheng, Qi Nan, Baoqing Sun, Chao Qiu and some others, many badminton and ping-pong games brought me lots of fun. Lei Wang should be acknowledged again for giving me many introductions on mathematics and FEM.

It is your turn, my adorable little daughter Coco and my lovely wife Dr. Yuzhen Shi. Without them staying with me in Glasgow, two more journal papers might have been published. However, nothing matters than to stay together for a family. To witness Coco's growth is one of my greatest happiness. Thank Coco for bringing endless joy into my life. I must give great thanks to Yuzhen for her caring and patience. Yuzhen gave up her own research position in China to be a full-time mother looking after our family. Her sacrifice to our family will never be forgotten.

Thank my mum Yuling Bai and dad Yongqing Feng for their selfless care and support throughout my life. I am lucky to be their son.

I am really grateful to the joint scholarship from Chinese Scholar Council (CSC) and the University of Glasgow, the mobility scholarship from the college of Science and Engineering of the University of Glasgow for providing me a financial support to work in SIO, the young scientist grants sponsored by European Geosciences Union (EGU) 2013, and enjoyable meetings organized by the Observations and Modelling of Earthquakes and Tectonics (COMET).

Wanpeng Feng

26 October 2014, Glasgow

Abstract

The ultimate goal of seismology is to estimate the timing, magnitude and potential spatial extent of future seismic events along pre-existing faults. Based on the rate-state friction law, several theoretical physical earthquake models have been proposed towards this goal. Tectonic loading rate and frictional properties of faults are required in these models. Modern geodetic observations, e.g. GPS and InSAR, have provided unprecedented near-field observations following large earthquakes. In theory, according to the frictional rate and state asperity earthquake model, velocity-weakening regions holding seismic motions on faults should be separated with velocity-strengthening regions within which faults slip only aseismically. However, early afterslip following the 2011 M_W 9.1 Tohoku-Oki earthquake revealed from GPS measurements was largely overlaid on the historical rupture zones, which challenged the velocity weakening asperity model. Therefore, the performance of the laboratory based friction law in the natural events needs further investigation, and the factors that may affect the estimates of slip models through geodetic modelling should also be discussed systematically. In this thesis, several moderate-strong events were investigated in order to address this important issue.

The best-fit co- and post-seismic slip models following the 2009 M_W 6.3 Haixi, Qinghai thrust-slip earthquake determined by InSAR deformation time-series suggest that the maximum afterslip is concentrated in the same area as the coseismic slip model, which is similar to the patterns observed in the 2011 Japan earthquake. In this case, complex geometric asperity may play a vital role in the coseismic nucleation and postseismic faulting. The major early afterslip after the 2011 M_W 7.1 Van mainshock, which was revealed by one COSMO-SkyMed postseismic interferogram, is found just above the coseismic slip pattern. In this event, a postseismic modelling that did not allow slip across the coseismic asperity was also tested, suggesting that the slip model without slip in the asperities can explain the postseismic observations as well as the afterslip model without constraints on slip in the asperities. In the 2011 M_W 9.1 Tohoku-Oki earthquake, a joint inversion with the GRACE coseismic gravity changes and inland coseismic GPS observations was conducted to re-investigate the coseismic slip model of the mainshock. A comparison of slip models from these different datasets suggests that significant variations of slip models can be observed, particularly the locations of the maximum slips. The joint slip model shows that the maximum slip of ~42 m appears near the seafloor surface close to the Japan Trench. Meanwhile, the accumulative afterslip patterns (slip >2 m) determined in previous studies appear in spatial correlation with the Coulomb stress changes generated using the joint slip model. As a strike-slip faulting event, the 2011 M_W 6.8 Yushu earthquake was also investigated through co- and post-seismic modelling with more SAR data than was used in previous study. Best slip models suggest that the major afterslip is concentrated in shallow parts of the faults and between the two major coseismic slip patterns, suggesting that the performance of the rate and state frictional asperity model is appropriate in this

event. Other postseismic physical mechanisms, pore-elastic rebound and viscoelastic relaxation have also been examined, which cannot significantly affect the estimate of the shallow afterslip model in this study. It is believed that the shallow afterslip predominantly controlled the postseismic behaviour after the mainshock in this case. In comparison to another 21 earthquakes investigated using geodetic data from other studies, complementary spatial extents between co- and post-seismic slip models can be identified. The 2009 M_W 6.3 Qinghai earthquake is an exceptional case, in which the faulting behaviours might be dominated by the fault structure (e.g. fault bending).

In conclusion, the major contributions from this thesis include: 1) the friction law gives a first order fit in most of natural events examined in this thesis; 2) geometric asperities may play an important role in faulting during earthquake cycles; 3) significant uncertainties in co- and post-seismic slip models can appreciably bias the estimation of fault frictional properties; 4) new insights derived from each earthquake regarding their fault structures and complex faulting behaviours have been observed in this thesis; and (5) a novel package for geodetic earthquake modelling has been developed, which can handle multiple datasets including InSAR, GPS and land/space based gravity changes.

List of figures

List of tables

Contents

CHAPTER 4 INSAR MEASUREMENTS FOR THE 2011 M_W 7.1 VAN (TURKEY) EARTHQUAKE 74

CHAPTER 5 LARGE COSEISMIC SLIP VARIATION OF THE 2011 M_W 9.0 TOHOKU-OKI, JAPAN EARTHQUAKE 98

Chapter 1

Introduction

Every year, nearly 60,000 people die worldwide on average in natural disasters (Kenny, 2009), the majority of which are caused by secondary disasters triggered by earthquakes, e.g. building collapses, fires and tsunamis. For example, the 2008 M_W 7.9 Wenchuan earthquake killed over 70,000 people (Zhang et al., 2010a). During the 2010 M_W 6.8 Yushu earthquake, at least 2,600 people were confirmed dead (http://en.wikipedia.org/wiki/2010_Yushu_earthquake). The 2011 M_W 9.1 Tohoku-Oki earthquake triggered a devastating tsunami and over 15,000 people were killed by following secondary disasters (Daneill et al., 2011). It is widely believed that tectonic earthquakes resulting from sudden slip on faults (Isacks et al., 1968; Kanamori and Brodsky, 2004) are the major sources that pose dangers to people. Whether the time, location and magnitude of a forthcoming earthquake on a specific fault can be predicted is still being debated (Geller, 1991; Geller et al., 1997; Kagan and Jackson, 2011, 2014), but efforts from those in a wide range of disciplines, e.g. seismology, geophysics engineering and geodesy, are continuously being made to improve the understanding of the nature of earthquakes, identify active faults and construct earthquake-resistant buildings. This thesis addresses one aspect of this hazard, the physics of faulting evolution on pre-existing faults using modern geodetic measurements.

The classic elastic rebound theory (Reid, 1910) gives the first satisfactory explanation of earthquakes. According to its principles (Reid, 1910; Thatcher, 1975; Scholz, 2002), if immediate geodetic measurements across the fault were made after a large earthquake, there would be the potential to evaluate when the next similar-size earthquake could occur. However, a number of observations indicate that the slip released during earthquakes might be only a fraction of the energy accumulated by tectonic loading between two successive earthquakes (Solomon et al., 1988; Pacheco et al., 1993; DeMets, 1997). Thus, how to quantitatively assess detailed faulting behaviours has been beyond the scope of this theory.

About 50 years ago, stick-slip was proposed to be the mechanism of earthquakes (Brace and Byerlee, 1966). According to observations in laboratory-based experiments (Dieterich, 1978; Dieterich, 1979a, b), the rate and state dependent friction law was used to explain faulting processes during an earthquake cycle (e.g. Marone, 1998a; Scholz, 1998; Scholz, 2002). Under the frictional stability regime, several theoretical physical earthquake models have recently been proposed to evaluate faulting processes, so that the timings of next earthquakes may be simulated numerically (Kaneko et al., 2010; Barbot et al., 2012; Rubinstein et al., 2012). Fault frictional properties that are required for this estimation can be identified through co- and post-seismic displacement modelling, which is a key aspect of this thesis.

Seismic and aseismic slips on faults have been revealed by fault-rock textures (e.g. Sibson, 1977, 1980; Knipe, 1989; Fagereng and Toy, 2011). However, it may be impossible to image the slip patterns in detail at kilometre scales using geological survey. Geodetic modelling with an elastic dislocation theory (Okada, 1985) offers a unique opportunity to obtain information at this scale mapping spatial extents of both seismic and aseismic slip. In this study, I utilize Synthetic Aperture Radar Interferometry (InSAR) techniques to map co- and post-seismic surface movements of several large earthquakes, including both intraplate and interplate events. Co- and post-seismic slip models are imaged using a new numerical inversion package. Performance of the frictional law on the natural faults is then systematically addressed through analyzing these results.

1.1 The earthquake cycle

In terms of crustal deformation, a seismic cycle is generally divided into four different phases: interseismic, preseismic, coseismic and postseismic (Scholz, 2002). Corresponding fault slip history during an earthquake cycle is depicted in Figure 1.1 (Tse and Rice, 1986; Scholz, 1998) . Plausible foreshocks have been frequently identified prior to large earthquakes (e.g. Nettles et al., 2011; Bouchon et al., 2013; Brodsky and Lay, 2014), but the surface response corresponding to earthquake nucleation (Figure 1.1) has not yet been convincingly observed by geodetic observations.

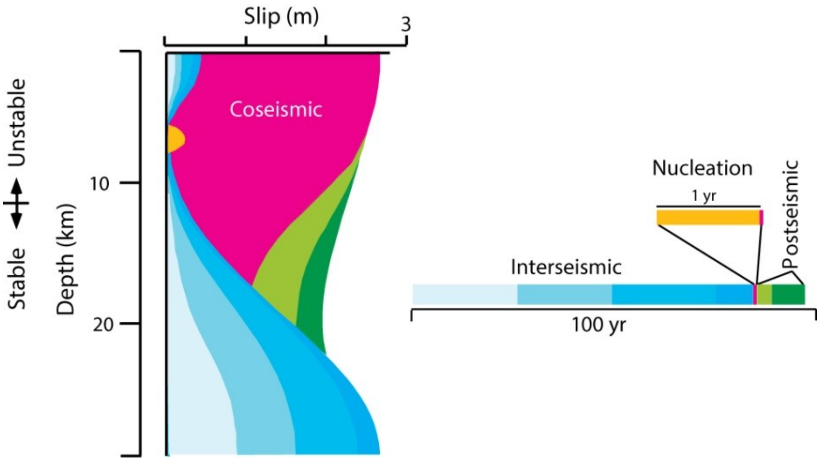

Figure 1.1 Slip as a function of depth during a seismic cycle of a strike-slip fault (Scholz, 1998). Different colours indicate different periods in the earthquake cycle. For example, stable creep usually occurs in the blue zone at the deep part of a fault.

1.2 Interseismic strain accumulation

During the interseismic period, a fault is loaded from the blue zones in Figure 1.1. Using InSAR and GPS measurements, present crustal deformation across large active fault systems has been widely observed, e.g. Northern Anatolian fault in Turkey (e.g. Wright et al., 2001b; Kaneko et al., 2013), San Andreas fault in North America (e.g. Fialko, 2006; Smith-Konter et al., 2011; Tong et al., 2013) and the Altyn Tagh fault in China (e.g. Elliott et al., 2008; Jolivet et al., 2008; Cowgill et al., 2009; Hetzel, 2013). From a simple screw dislocation (Weertman and Weertman, 1964; Savage and Burford, 1973), the creep rate on an infinite strike-slip fault in the elastic half-space crust with depth can be estimated by

$$v(x) = \frac{V}{\pi} tan^{-1}({}^{x}/_{D}) \qquad \textbf{(1.1)}$$

where x is the distance away from the fault in km, D is the locked depth [km] above which the fault is locked without creep and $v(x)$ is the observed slip rate [m.yr^{-1}] across the fault. In some active fault systems, interseismic creep tends to be complicated due to nearby large earthquakes (Wei et al., 2013). However, over relatively long-time scales elastic strain energy accumulation across faults is usually treated as a constant rate (e.g. Elliott et al., 2008; Walters et al., 2013; Tong et al., 2014; 2014).

Shallow creep has also been reported in several fault zones including the central San Andreas fault with a surface creep rate of 25-34 mm.yr^{-1} (Titus et al., 2005; Ryder and Burgmann, 2008), northern Anatolia fault with a shallow creep of ~13 mm/yr (Walters et al., 2014) and the northeast segment of Altyn Tagh fault with a surface creep rate of 5 mm.yr^{-1} (Jolivet et al., 2012). The mechanisms of shallow creep may differ between faults. Shallow frictional heterogeneity, past earthquakes or microseismic activities may contribute in part to the shallow creep which can be episodic (Jolivet et al., 2013; Wei et al., 2013).

1.2.1 Coseismic fault rupture and complex slip patterns

When accumulated strain exceeds the shear strength of a fault, an earthquake will occur with a sudden slip on the fault surface. Depending on the magnitude (Scholz et al., 1986; Kanamori, 1994), destructive earthquakes ruptures can be a few kilometres or even hundreds of kilometres long, like the 2011 M_W 8.1 Kokoxili earthquake with a 400-km rupture belt and the 2008 M_W 7.9 Wenchuan earthquake with a 350-km surface rupture (Klinger et al., 2006; Zhang et al., 2010a). The 2004 M_W 9.2 Sumatra-Andaman earthquake even unusually produced a 1100-km surface rupture along the Sunda trench subduction zone (Kruger and Ohrnberger, 2005).

Coseismic slips along finite faults usually appear inhomogeneous, and have been widely imaged using geodetic and seismic observations. For instance, more than four separate slip concentrations have been observed in the 2001 M_W 8.1 Kokoxili strike-slip earthquake using InSAR observations (Lasserre et al., 2005). During the 2008 M_W 7.9 Wenchuan earthquake, at least three slip centres were observed by both geodetic and seismic observations and significant variation of slip vectors from south to north have also been retrieved (Zhang et al., 2009a). Three separate slip centres associated with the 2010 M_W 6.8 Yushu strike-slip earthquake were determined from InSAR observations (Li et al., 2011). Using seismic inversion, coseismic rupture through different asperities can also be directly identified by the source time function (STF) that can show multiple peaks corresponding to sub-events (Haeussler et al., 2004; Zhang et al., 2010b, c).

Complex geometry (e.g. fault bends) has long been recognized as an important cause of complex slip history during mainshocks (King and Nabelek, 1985; Barka and Kadinsky-Cade, 1988; Dunham et al., 2011). Following significant strike changes, slip vectors can vary dramatically as observed in the 2008 M_W 7.9 Wenchuan earthquake (Shen et al., 2009) and the 2010 M_W7.1 New

Zealand strike-slip event (Elliott et al., 2012). However, uneven slip patterns observed on relatively straight and continuous fault surfaces may be attributed to other physical mechanisms, such as heterogeneity of the frictional properties.

1.2.2 Postseismic processes and afterslip

Following large earthquakes, the ubiquitous postseismic motions that can last for months or years, have been well observed with modern geodetic means (Wang et al., 2012b). Significant postseismic surface motion was first noticed a half century ago, just after the 1966 M_W 6.4 Parkfield earthquake (Smith and Wyss, 1968). The postseismic displacements following this earthquake accumulated logarithmically with time (Figure 1.2). Similar postseismic surface motion has been documented following other large earthquakes, e.g. the 2001 M_W 8.1 Kokoxili earthquake (Ryder et al., 2011; Wen et al., 2012a), the 2002 M_W 7.5 Izmit earthquake (Burgmann et al., 2002b), the 2004 M_W 6.4 Parkfield earthquake (Barbot et al., 2009a), and the 2005 M_W 8.5 Nias earthquake (Hsu et al., 2006). Among these studies, afterslip was commonly seen following large earthquakes and InSAR played an important role in mapping postseismic movements.

In addition to afterslip, poroelastic rebound and viscoelastic relaxation can also contribute to postseismic surface changes. Significant postseismic deformation following the 1992 Landers earthquake may partly be attributed to poroelastic rebound (Peltzer et al., 1998; Fialko, 2004a). A similar phenomenon was also observed in the 2000 Iceland earthquakes (Jonsson et al., 2003). In comparison to afterslip, fluid flow driven by changing pore-pressure can form different surface displacement patterns that may be able to be used to infer the principal physical mechanism.

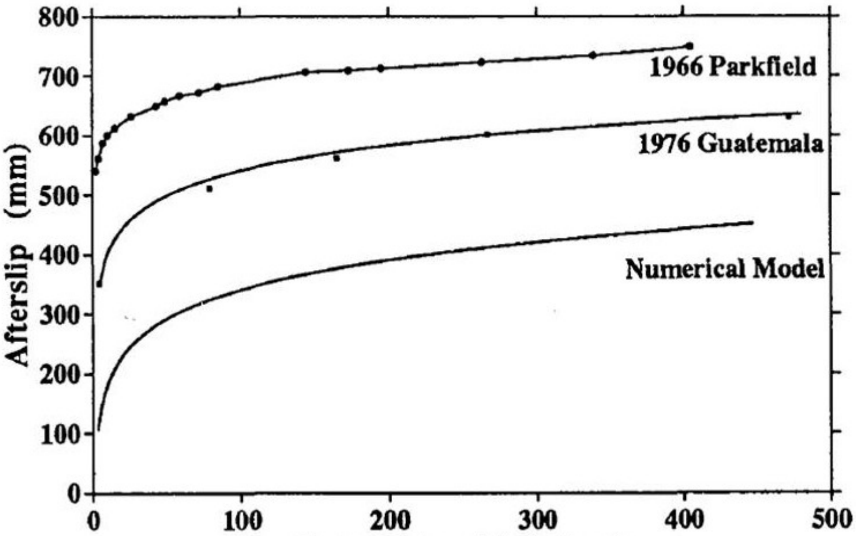

Figure 1.2 Measured and numerical modelled measurements of afterslip following two earthquakes (Marone et al., 1991). The model is calculated using typical earthquake parameters and laboratory-derived values for the constitutive parameter (a-b). Parkfield data are from Smith et al. (1968). Guatemala data are from Bucknam et al. (1978).

In the traditional view of tectonics, a weak ductile layer exists beneath the brittle seismogenic zone

(Scholz, 1998).Viscous flow following large earthquakes should commonly be seen under the coseismic stress perturbation. With ERS-1/2 SAR images spanning two years after the 1997 M_W 7.5 earthquake, Ryder *et al.* (2007a) suggested that viscoelastic relaxation could be the major source for the postseismic observations. Significant postseismic observations a few years after the 2011 Kokoxili earthquake were also explained by the viscous flow in the lower crust and upper mantle (Ryder et al., 2011; Wen et al., 2012a). As mentioned previously (Ryder et al., 2007a), postseismic surface deformation patterns produced by viscous flow in the lower crust and/or upper mantle can be comparable to those due to afterslip at depth, which is difficult to be distinguished .

1.3 Rate-state friction law

Based on observations across different fault systems, faulting behaviour through the earthquake cycle appears variable in space and time. The rate and state friction law based on rock mechanics experiments (Dieterich, 1978; 1994) is believed to be able to explain what happens during an earthquake cycle. Under this theoretical frictional framework, earthquakes have been recognised as resulting from a stick-slip frictional instability (Scholz et al., 1969; Scholz et al., 1972; Kanamori, 1977; Ruina, 1983; Marone et al., 1991; Scholz, 1998). The basic mathematical expression is given through rock frictional experiments (Scholz, 1998) as

$$\boldsymbol{\tau} = \left[\boldsymbol{\mu_0} + \boldsymbol{a}\, \boldsymbol{ln}\left({}^{\boldsymbol{V}}\!/_{\boldsymbol{V_0}}\right) + \boldsymbol{b}\, \boldsymbol{ln}\left({}^{\boldsymbol{V_0\theta}}\!/_{\boldsymbol{L}}\right)\right] \overline{\boldsymbol{\sigma}} \qquad \textbf{(1.2)}$$

where τ is shear stress, $\boldsymbol{\mu_0}$ is the reference frictional coefficient at slip rate (V_0), $\overline{\sigma}$ is effective normal stress ($\overline{\sigma} = \sigma - p$, p is fluid pore pressure.), V is slip velocity, θ is the state variable and a, b and L are empirically-derived friction constitutive parameters. Slip critical distance (L) has the following relationship with the state variable (θ)

$$\begin{cases} \dfrac{\boldsymbol{d\theta}}{\boldsymbol{dt}} = \mathbf{1} - \dfrac{\boldsymbol{\theta V}}{\boldsymbol{L}} & \text{(Dieterich}'\text{slaw)} \\ \dot{\boldsymbol{\theta}} = \left(-\frac{\boldsymbol{V}}{\boldsymbol{d_c}}\right)\left[\boldsymbol{\theta} + \boldsymbol{Bln}\left(\frac{\boldsymbol{\theta V}}{\boldsymbol{L}}\right)\right] & \text{(Runia}'\text{slaw)} \end{cases} \qquad \textbf{(1.3)}$$

At steady state (Dieterich, 1978; Ruina, 1980), the friction is

$$\boldsymbol{\tau} = \left[\boldsymbol{\mu_0} + (\boldsymbol{a} - \boldsymbol{b})\, \boldsymbol{ln}\left({}^{\boldsymbol{V}}\!/_{\boldsymbol{V_0}}\right)\right] \overline{\boldsymbol{\sigma}} \qquad \textbf{(1.4).}$$

Following Equation (1.4), the friction at steady state does not depend on material properties, and this can be modelled by a simple spring-slider system. The transition from a stable state to dynamic processes occurs when the effective normal stress reaches a critical value $\overline{\sigma_c}$ that is defined as

$$\overline{\boldsymbol{\sigma_c}} = \frac{\boldsymbol{kL}}{-(\boldsymbol{a}-\boldsymbol{b})} \qquad \textbf{(1.5)}$$

where k is the stiffness of the spring. The combined parameter (a-b) in Equation 1.5 is consistent with that in Equation (1.4), which characterizes the frictional properties of fault zones (Boatwright and Cocco, 1996; Lapusta and Barbot, 2012). If $(a-b)<0$, the regions tend to be velocity-weakening (VW), and stay unstable or conditionally stable. Velocity-strengthening (VS) regions with $(a-b)\geq 0$ tend to be stable. In an earthquake cycle, velocity weakening regions (VW, also termed asperities) arrest stain energy constantly from tectonic loading. Theoretically, the spatial extent of VS and VW regions can be directly identified by co- and post-seismic geodetic modelling. As shown in Figure 1.1, the coseismic rupture zone (red) can be recognized as the VW asperity, whilst the blue and green regions are velocity-strengthening. A shallow VS layer may also exist on the top, which may account for the phenomenon of shallow coseismic slip deficit observed in several large strike-slip earthquakes (Fialko et al., 2005; Kaneko and Fialko, 2011).

1.4 Lessons from past earthquakes and outstanding issues

Spatial extents of the frictional properties on faults are vital for the estimation of faulting behaviours during earthquake cycles (Barbot et al., 2009a; Lapusta and Barbot, 2012). Theoretically, there should be a distinct boundary between VW and VS regions. However, previous geodetic applications to earthquake slip models do not always show the friction properties partitioned as expected. Following the 2005 M_W 8.7 Nias-Simeulue earthquake, complementary distribution of coseismic slip and afterslip was imaged using observations from 10 GPS sites, whilst GPS-based early afterslip models suggested that significant afterslip following the 2011 M_W 9.1 Tohoku-Oki earthquake occurred in historic coseismic slip zones (Figure 1.3) (Ozawa et al., 2011; Johnson et al., 2012a). The latter findings challenged the rate-state asperities law (Johnson et al., 2012a). Note that the GPS data used for the 2005 event were from the islands above the rupture interface (i.e. in the near field), but the most of observations for the 2011 Tohoku-Oki event were observed in the far field only. Large uncertainties in coseismic slip models have also been pointed out in many cases, even for the best-observed events, such as the 1999 M_W7.6 Izmit earthquake (Utkucu and Durmus, 2012), the 2004 M_W9.2 Sumatra earthquake (Shearer and Bürgmann, 2010) and the 2011 M_W 9.1 Tohoku-Oki earthquake (MacInnes et al., 2013). The uncertainties in co- and/or post-seismic slip models may significantly bias our estimates of the spatial distribution of the frictional properties on faults. Overall, considerable uncertainties in geodetic slip models were commonly found in previous studies and limited near-field data may be the key reason for this (Diao et al., 2013).

As mentioned in Section 1.1.2, afterslip is only one of the possibilities responsible for postseismic surface motions. Various physical mechanisms, e.g. viscoelastic relaxation and afterslip, may act together following large earthquakes, e.g. the 1992 Landers earthquake and the 2000 Iceland earthquake (Peltzer et al., 1998; Masterlark and Wang, 2002; Jonsson et al., 2003; Fialko, 2004a). Whether poroelastic rebound and viscoelastic relaxation could severely bias estimates of shallow afterslip still needs further investigation.

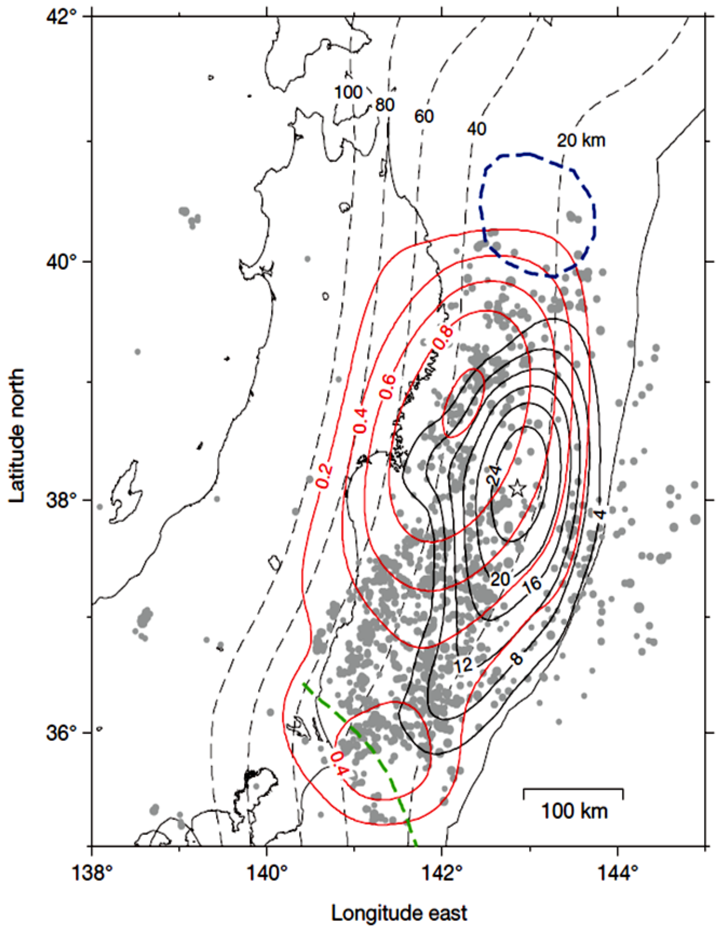

Figure 1.3 Co- and post-seismic models of the 2011 M_W 9.1 Japan earthquake derived from GPS observations from Ozawa *et al.* (2011). Black solid contours show the coseismic slip model, whilst red ones are recorded afterslip for 12-25 March 2011.

1.5 Space based geodetic data: a powerful tool for earthquake monitoring

Many published slip models of previous earthquakes result from the application of modern geodetic techniques, e.g. GPS and InSAR (e.g. Segall and Matthews, 1997; Bie et al., 2013). GPS has successfully provided high-frequency and high-accuracy measurements (Bilich et al., 2008; Larson, 2009), but it is criticized for its sparse spatial coverage and expensive operating cost. InSAR can efficiently compensate for the spatial coverage limitation. For a typical space-based SAR image (Table 1.1), pixel spacing can be 1-100 m within a 100-km-wide swath (Burgmann et al., 2000).

Table 1.1 Basic information of spaceborne SAR sensors.

Sensor	Operator	Operating period	Band	Pixel Spacing(m)	Revisit time(days)	Imaging Mode[a]
ERS-1	ESA	1992-1998	C	20 x 4	35	Stripmap
ERS-2	ESA	1995-2011	C	20 x 4	35	Stripmap
Envisat	ESA	2002-2011	C	20 x 4	35	Mul
Sentinel-1A	ESA	2014-?	C	4 x 4	12[b]	Mul
RadarSAT-1	CSA	1995-2013	C	8 x 8	24	Mul
RadarSAT-2	CSA	2007-?	C	1 x 3	24	Mul
JERS-1	JAXA	1992-1998	L	18 x 18	44	Stripmap
ALOS-1	JAXA	2006-2011	L	7 x 7	45	Mul
ALOS-2	JAXA	2014-?	L	7 x 7	14	Mul
KOMPSat-5	Korean	2014-?	X	3 x 3	28	Mul
TerraSAR-X (TSX)	DLR	2007-?	X	2 x 2	11[b]	Mul
COSMO-Skymed (CSK)	ASI	2007-?	X	2 x 2	16[b]	Mul

Note: a) 'Mul' stands for multiple imaging modes including Stripmap, ScanSAR and Spotlight. b) The revisit time is only for a single satellite. For a constellation, the revisit time can be reduced.

Previous and current SAR sensors in Table 1.1, particularly those deployed by the European Space Agency (ESA), have generated a wealth of observations (Salvi et al., 2012). Their use to resolve earthquake parameters have been well demonstrated (e.g. Massonnet et al., 1993). Together with other SAR sensors (e.g. ALOS-1, TSX and COSM-SkyMED (CSK), multiple tracks of SAR data can be available for previous events, and make the estimation of co- and post-seismic slip distributions possible. Although inherent limitations of InSAR techniques may restrict their applications to earthquake studies, e.g. atmospheric effects and line of sight (LOS) ambiguity, a combination of data from multiple tracks and/or with other types of observations, e.g. space gravity changes and GPS, can improve our understanding of surface deformation response to faulting behaviours (Wei et al., 2010a).

For megathrust earthquakes in subduction zones, near-field displacements have rarely been observed due to most displacements taking place under the ocean. Since the mass distribution within the Earth can be permanently changed by these largest subduction events, an alternative approach is to use coseismic gravity changes sensed from the ranging instrument onboard the Gravity Recovery and Climate Experiment (GRACE) satellite. So far, coseismic gravity changes caused by several largest earthquakes, such as the 2004 M_W 9.4 Sumatra-Andaman earthquake, the 2010 M_W 8.8 Maule and the 2011 M_W 9.1 Tohoku-Oki, Japan earthquake, have been successfully revealed by GRACE (Han et al., 2006; 2010; Cambiotti and Sabadini, 2012; Wang et al., 2012e).

Without being limited to mapping displacements on land, GRACE coseismic measurements can cover surface changes on the two sides of seismic faults. These relatively complete observations for megathrust earthquakes may provide a new important source of information that cannot be seen from distant seismometers and GPS stations. In this thesis, GRACE derived coseismic gravity changes will be used to re-investigate the coseismic slip model of the 2011 M_W 9.1 Tohoku-Oki earthquake in combination with inland GPS data.

1.6 Aims of this study

In order to better understand the spatial variation of fault frictional properties during earthquake cycles, four past earthquakes are revisited in this thesis using geodetic data to determine their source parameters, coseismic and afterslip slip distributions. The earthquakes are: the 2003-2009 M_W 6.3 Qinghai (China) earthquake sequence, the 2011 M_W 7.1 Van (Turkey) earthquake, the 2011 M_W 9.1 Tohoku-Oki (Japan) earthquake and the 2010 M_W 6.8 Yushu (China) earthquake (Figure 1.4).

The questions to be addressed in this thesis are as follows:

1) Is the fault friction law applicable for these natural events?
2) Is there any impact of early afterslip on the determination of coseismic slip models?
3) Do the uncertainties in the geodetic models bias our understanding of fault frictional properties since geophysical modelling is always non-unique?
4) Do other postseismic mechanisms following large earthquakes affect the estimates of shallow afterslip?

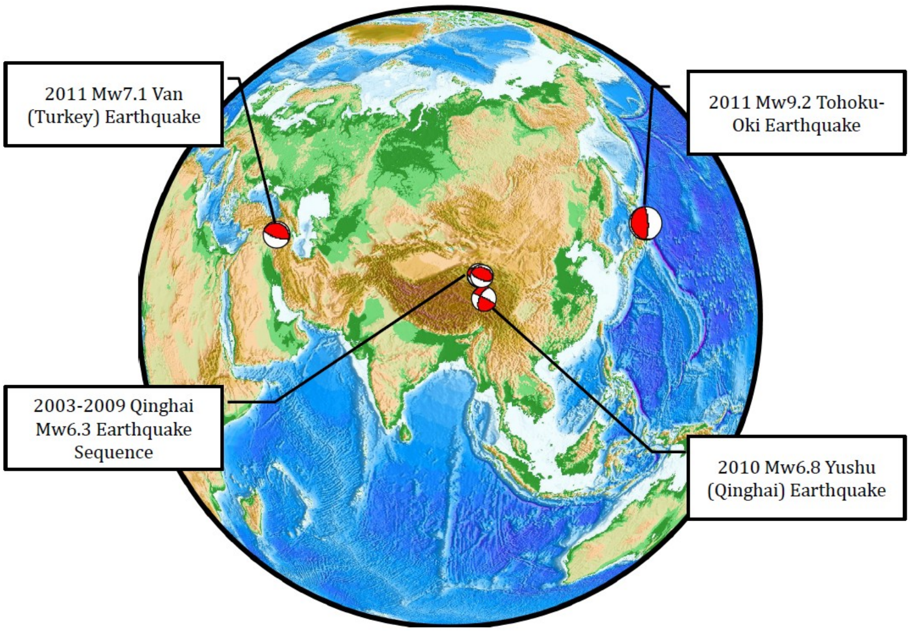

Figure 1.4 Locations of earthquakes to be revisited in this thesis.

1.7 Roadmap of the thesis

The thesis is structured as follows:

Chapter 2: a concise introduction to InSAR principles and geodetic inversion.

Chapter 3: InSAR deformation time series are used to map surface deformation history accompanying the 2003-2009 Qinghai earthquake sequence. The source parameters of slip models of three M_W 6.3 mainshocks are determined by InSAR inversion. A time-dependent inversion based on postseismic deformation associated with afterslip after the 2009 mainshock is carried out. The spatial variation of fault frictional properties of across a whole sequence is evaluated.

Chapter 4: the slip model of the 2011 M_W 7.1 Van Earthquake is refined using carefully selected SAR data. Along-track InSAR and across-track InSAR are both used for determination of fault parameters. Rapid afterslip is revealed by both CSK and Radarsat-2 interferograms. The spatial extent of VS and VW regions is compared through modelling coseismic and postseismic InSAR measurements.

Chapter 5: space-based gravity changes (GRACE) are employed to determine the slip distribution of the 2011 M_W 9.1 Japan earthquake. The afterslip models determined in previous studies are employed to assess if the large uncertainties in coseismic slip models can significantly influence estimation of fault frictional properties.

Chapter 6: six tracks of SAR data are collected to revisit coseismic slip model of 2010 M_W 6.8 Yushu earthquake. The biggest aftershock whose surface response was encapsulated into coseismic interferograms is isolated based on post-analysis of the residuals. The afterslip is also modelled by C-band ScanSAR and L-band Stripmap interferograms. The effects of other physical mechanisms on the estimates of shallow afterslip are analyzed.

Chapter 7: summarize outputs from the case studies in Chapters 3-6. The similarities and differences of VS and VW spatial extensions in these four earthquakes and other large earthquakes investigated previously are compared. Limitations in this thesis are also pointed out, and suggestions for future work following this thesis are given at the end.

Chapter 2

Synthetic Aperture Radar Interferometry: Deformation Mapping and Earthquake Modelling

In the past two decades, Interferometric Synthetic Aperture Radar (InSAR) (Rosen et al., 1996) has become a widely used deformation mapping technique in Earth science. Since the first coseismic interferogram, associated with the 1992 M_W 7.4 Landers earthquake, was published (Massonnet et al., 1993), InSAR has made contributions to seismology by determining earthquake locations, fault geometries and dynamic processes from its measured deformation fields, and has increasingly been used in a wide range of other Earth science fields due to its high quality and vast quantity of observations (e.g. Bamler and Hartl, 1998; Fielding et al., 1998; Burgmann et al., 2000; Hanssen, 2001; Lu et al., 2007). In this study, InSAR observations are the major source of data for the determination of fault parameters and slip distributions.

In this chapter, SAR and InSAR principles are firstly introduced with emphasis on InSAR processing techniques using open-source software rather than repeating detailed mathematical background that can be found in a number of previous publications (e.g. Zebker et al., 1994; Rosen et al., 1996; Burgmann et al., 2000; Rosen et al., 2000; Simons and Rosen, 2007). Secondly, geodetic inversion for earthquake source parameters and slip distributions with InSAR is described by a concise introduction to an inversion package, PSOKINV, which is developed by the author.

2.1 InSAR observations

2.1.1 Overview of InSAR

2.1.1.1 Synthetic Aperture Radar (SAR)

Synthetic Aperture Radar (SAR) is an active microwave ranging system to produce high resolution images of ground targets. It is an extension of classic radar for improving spatial resolution of imaging by synthesizing an efficient long antenna through signal processing. The special image geometry shown in Figure 1 is determined by the physics of the radar: cross-track resolution results from ordering the echoes from each emitted pulse by their round trip travel time, whilst the forward motion of the plane or satellite repeats the observations (Massonnet and Feigl, 1998). More details on SAR imaging geometry can be found in Massonnet *et al*'s review paper (Massonnet and Feigl, 1998).

Focused SAR data are similar to optical images in providing two-dimensional surface textures (Cutrona, 1990; Curlander and McDonough, 1991). However, some features of SAR data are very different from images in the visible spectrum. For example, the coherent phase information in SAR images can be used to measure surface topography and motion through SAR interferometric processing. From early imaging SAR sensors that were not designed for interferometry, e.g. SeaSAT (1978), ERS-1/2 (1992,1995) and JERS-1 (1992), to later InSAR-aimed ones, e.g. Envisat (2002), ALOS-1/2 (2006, 2014) and Sentinel-1A (2014), interferometric capabilities differ from one to another due to different carrier frequencies and viewing geometries.

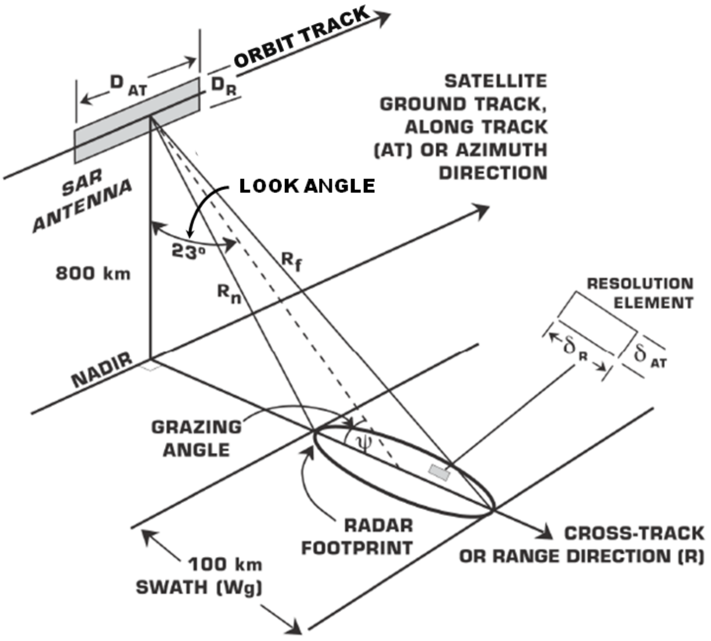

Figure 2.1 Illustration of SAR imaging geometry (modified from (Jackson et al., 2004)). The range resolution ($\boldsymbol{\delta_r}$) of the footprint, defined as $\frac{c\tau_p}{2sin\theta}$ is governed only by look angle and pulse duration ($\boldsymbol{\tau_p}$), whilst the resolution in azimuth ($\boldsymbol{\delta_{AT}}$) relies on the aperture length $\frac{R\lambda}{l}$, where $\boldsymbol{R}$ is the range distance and $\boldsymbol{l}$ is the synthetic aperture length.

Modern SAR sensors can be operated in different modes, e.g. Stripmap, Spotlight, ScanSAR and TOPS, for different imaging aims. To image a moderate spatial coverage (100 km) at an intermediate resolution (12.5 m), the traditional Stripmap mode assumes a fixed radar pointing direction to illuminate the surface with a moving radar transmitting a stream of pulses perpendicular to the orbit track as shown in Figure 2.1. The area illuminated by each pulse is called a radar footprint. The inclination of the antenna with respect to the nadir is the look angle (θ) that can vary between 20° and 50°. In the case of Envisat, the footprint swath of a Stripmap SAR is ~100 km, which varies slightly with different operating look angles corresponding to the different beam modes (IS1-7) (Schättler, 2002). The grazing angle in Figure 2.1 is the complementary angle of θ, which governs the range resolution (δ_r). In this thesis, Stripmap mode data is the major data source for most of the case studies.

A focused SAR image is also referred to as single look complex (SLC) data consisting of two parts of information, amplitude and phase. The amplitude of SAR data reflects the strength of the backscattered signal in terms of surface geometry and relies more on the roughness than on the chemical composition of the scatterers on the surface. The phase component, due to the periodic nature of the signals, is just a measure of the last fraction of the two-way travel distance between the radar and ground targets (Ferretti et al., 2007). Because the radar wavelength is much smaller than the resolution cell, the phase image presents essentially random, which is of no practical utility (Rocca et al., 1997; Ferretti et al., 2007).

2.1.1.2 InSAR principle

Although the phase part in a single SLC image is rarely interpreted, the phase difference between two coherent SLC images can provide useful information, e.g. topography and/or surface motion. The technique to calculate the phase difference is named Radar Interferometry, InSAR. SAR images from different operating modes have different spatial coverage and resolution, but there are no significant differences in interferometric processing after SAR data are focused. In this section, the principles of cross-track interferometry are introduced based on the data in the Stripmap mode.

With two coherent SLC images (also termed master and slave), an interferogram $\vartheta(u_{t1}, u_{t2})$ is formed by the conjugate multiplication of the master and slave images as

$$\begin{cases} \boldsymbol{u}_{t1} = s(t1, \tau)\exp\left(j2\pi\left(\frac{\Delta f}{2}\right)t1\right) \\ \boldsymbol{u}_{t2} = s(t2, \tau)\exp\left(j2\pi\left(\frac{\Delta f}{2}\right)t2\right) \\ \quad \boldsymbol{\vartheta}(\boldsymbol{u}_{t1}, \boldsymbol{u}_{t2}) = \boldsymbol{u}_{t1}(.)\boldsymbol{u}_{t2}^{*}(.) \end{cases} \tag{2.1}$$

The interferometric phase (φ_{int}) of an interferogram can be calculated from the arctangent between **I** and **Q** parts of $\boldsymbol{\vartheta}(u_{t1}, u_{t2})$. The resulting interferogram provides only ambiguous information on the 2 π cyclic nature of the interferometric phase (φ_{int}). To simplify the expression, φ_{int} can be re-written as

$$\boldsymbol{\varphi}_{int} = \boldsymbol{\varphi}_{t1} - \boldsymbol{\varphi}_{t2} \tag{2.2}$$

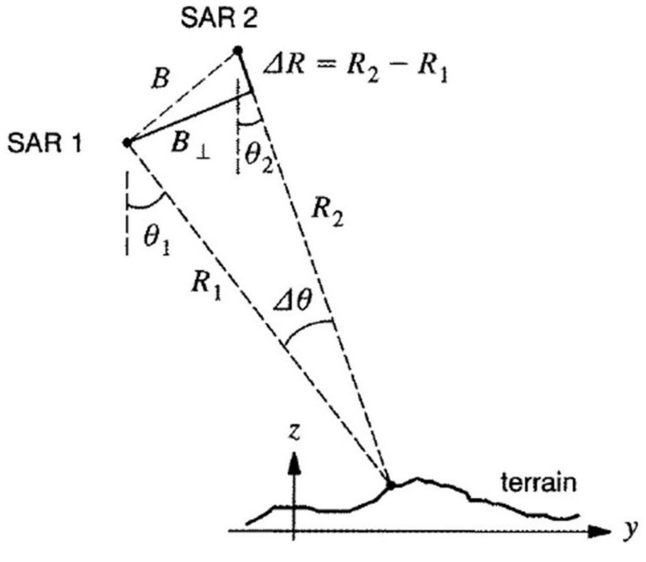

Figure 2.2 Geometry of two-pass interferometry (Bamler and Hartl, 1998).

Based on the geometry of two-pass interferometry (Figure 2.2) the physical properties of φ_{int} are composed of contributions from topography φ_{topo}, deformation φ_{def}, effects of flat earth projection φ_{flat} and a sum of various errors φ_{err} as

$$\boldsymbol{\varphi_{int} = \varphi_{flat} + \varphi_{topo} + \varphi_{def} + \varphi_{err}} \qquad \textbf{(2.3).}$$

In Equation (2.3) the flat earth phase component φ_{flat} is due to the look angle changing from near to far range (Figure 2.1), which can be estimated using precise orbit information (Rosen et al., 1996; Hanssen, 2001).

Topography component (φ_{topo}) is one of the essential elements in the interferometric phase, which is proportional to the baseline between master and slave images. As shown in Figure 2.2, for an interferometric pair with a perpendicular baseline ($B_\perp$) of 500 m, a look angle of 21° and a platform altitude of 780 km, the look angle difference ($\Delta\theta$) between θ_1 and θ_2 is less than 0.007° based on the cosines law. Therefore, the rays from SAR1 and SAR2 (Figure 2.2) are approximately parallel (Zebker and Goldstein, 1986) so that the topography contribution (φ_{topo}) can be simplified as

$$\boldsymbol{\varphi_{topo} \approx \frac{4\pi}{\lambda}\frac{hB_\perp}{R_1 sin\theta_1}} \qquad \textbf{(2.4).}$$

Following Equation (2.4), using an external DEM the effects of surface topography can be estimated and then removed from Equation (2.3). After that, only the contribution from surface deformation remains in the interferometric phase. Note that random errors (φ_{err}) are temporarily ignored here. Figure 2.3 shows interferograms formed from an ASAR interferometric pair of 23 April 2008 vs 15 Oct 2008, which has a perpendicular baseline of ~70 m. Intensive and nearly parallel interferometric fringes can be observed across the original interferogram (Figure 2.3 (a)). After flattening, the interferogram (Figure 2.3 (b)) still includes dense topography-related fringes and no clear deformation pattern can be identified at this stage. Following Equation (2.4), the topographic phase contribution is removed using external DEM data from the Shuttle Radar Topography Mission (SRTM) and deformation fringes caused by a M_W 6.3 earthquake in 2008 near Damxung, Tibet then become evident in Figure 2.3(c). It should be pointed out that some long wavelength signals in the far-field in Figure 2.3(c) might be mainly due to atmospheric delay (Feng et al., 2010a; Liu et al., 2012).

After removing topographic phase, filtering, masking, phase unwrapping and SAR geocoding are still required to produce continuous deformation maps. Goldstein filter (Goldstein and Werner, 1998) is one of most widely used filtering algorithms to be able to effectively suppress noise prior to unwrapping.

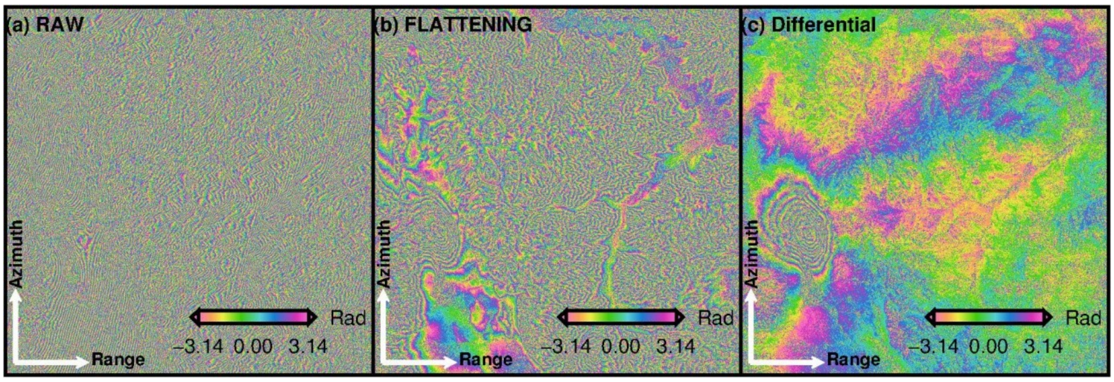

Figure 2.3 Original, flattened and differential interferograms. Interferograms (a,b and c) were all made from an ASAR ascending interferometric pair (23 April 2008 vs 15 Oct 2008) using DORIS.

It is notable that InSAR only provides relative measurements. Based on the seed selection in phase unwrapping, a constant phase shift remains in an unwrapped interferogram, which needs to be considered in further analysis. Meanwhile, cross-track interferogram can provide only measurements in one dimension, which is projected from surface three-dimensional displacements onto the satellite line of sight (LOS). Otherwise stated, positive values in radian mean that the ground has moved away from the satellite, whilst negative ones imply that the ground has moved towards the satellite.

2.1.1.3 Look vector of LOS changes

As described in last section, interferometric phase is surface changes along LOS direction. In order to determine geophysical parameters using LOS changes, it is necessary to exactly know the relationship between surface E/N/U and the LOS direction. Previous studies have derived this mathematic expressions in their own coordinate systems (e.g. Fialko et al., 2001; Wright et al., 2004b; Samieie-Esfahany et al., 2009). Here, one general expression given by Fialko et al. (2001) is

$$\boldsymbol{d_{los}} = \begin{bmatrix} -\boldsymbol{cos\phi\ sin\delta} \\ \boldsymbol{sin\phi\ sin\delta} \\ \boldsymbol{cos\delta} \end{bmatrix} [\boldsymbol{d_e}, \boldsymbol{d_n}, \boldsymbol{d_u}] + \boldsymbol{\epsilon} \tag{2.5}$$

where (d_e, d_n, d_u) are the surface E/N/U deformation components, d_{los} is the InSAR measurement, ϕ is the satellite flight direction measured clockwise from the north, δ is the incidence angle, and ϵ is the observation error. As shown in a simulated result (Figure 2.4), LOS deformation patterns (Figure 2.4 (d)) are different from each of the E/N/U components. Meanwhile, the projection expression for changes along the satellite flight direction (azimuth) measured using an along-track interferometry (Bechor and Zebker, 2006) or offset tracking (Michel et al., 1999a), which will be introduced later, is defined as

$$\boldsymbol{d_{azi}} = \begin{bmatrix} \boldsymbol{sin\delta} \\ \boldsymbol{cos\delta} \\ \boldsymbol{0} \end{bmatrix} [\boldsymbol{d_e}, \boldsymbol{d_n}, \boldsymbol{d_u}] + \boldsymbol{\epsilon} \qquad \textbf{(2.6).}$$

Ideally, two interferometric pairs with different viewing geometries covering the same area can be used to retrieve displacement fields in E/N/U based on Equations (2.5) and (2.6) since each pair can provide two different measurements such as range and azimuth observations, respectively. However, InSAR sensitivities in components of E/N/U are different, decreasing from Up to E to N components (e.g. Massonnet and Feigl, 1998), which makes surface 3D deformation restoration from InSAR difficult. Only in a limited number of cases have three deformation fields been obtained with InSAR techniques (Hu et al., 2014) because multiple SAR images from different viewing geometries are rarely available for the same area and it is also usually difficult to obtain effective azimuth measurements due to low coherence.

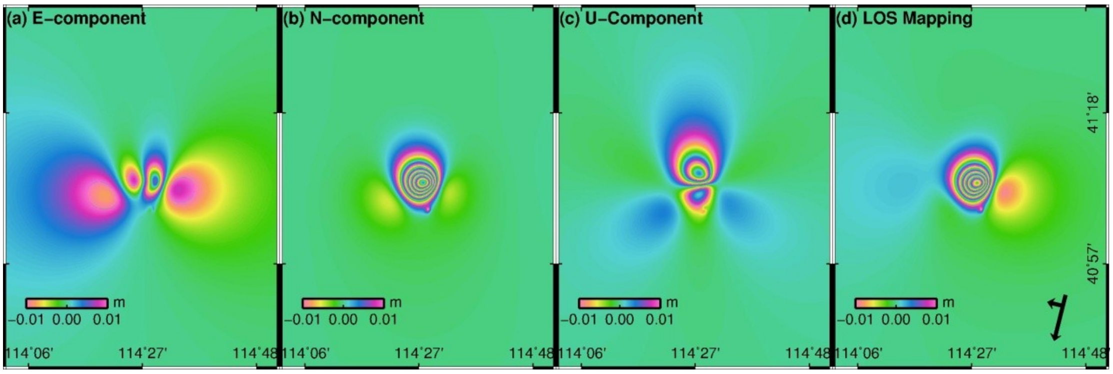

Figure 2.4 An example of synthetic LOS displacements from E/N/U surface displacement components. (a,b,c) are simulated by the normal faulting source using classic elastic dislocation theory (Okada, 1985). (d) is synthesized from (a,b,c) using azimuth and incidence angles of -166° and 23° respectively. All figures have been rewrapped with the range of [-0.01,0.01].

Additionally, two range LOS changes with different viewing geometries may be able to obtain E/N components due to interseismic creep on a strike-slip fault under the assumption that the vertical displacement component is zero (Lindsey et al., 2014; Walters et al., 2014). Similarly, in applications to land subsidence (e.g. Dehghani et al., 2009; Plattner et al., 2010; Ebmeier et al., 2012; Wang et al., 2012a; Chaussard et al., 2014; Tao and Liu, 2014), the vertical movement can be derived from Equation (2.5) when horizontal surface deformation components are fixed to zero.

2.1.1.4 Interferometric coherence and effective factors

The correlation coefficient of interferograms (also termed coherence, γ) is a quantitative measure of the similarity of two radar epochs (Zebker and Chen, 2005) as

$$\gamma = \frac{|\langle S_1 S_2^* \rangle|}{\sqrt{\langle S_1 S_2^* \rangle \langle S_1 S_2^* \rangle}} \tag{2.7}$$

where S_1 and S_2 are complex signals received at the two radar antennas and $\langle . \rangle$ represents an ensemble average. In practice, there is no way to directly obtain ensemble averages, so the estimate of this correlation is approximated by a local spatial average. In general, the correlation comprises contributions from a number of effects (Simons and Rosen, 2007) as

$$\gamma = \gamma_N \gamma_G \gamma_Z \gamma_T \tag{2.8}$$

where γ_N is the term from the radar system and processing approach, γ_G stands for the influence from the different viewing geometries, γ_Z represents the correlation of vertical extent of scatters (e.g. vegetation), and γ_T describes the temporal changes within a resolution cell (Bamler and Hartl, 1998; Rosen et al., 2000).

Both γ_Z and γ_T are based on the inherent characters of local scatterers. Interferometric coherence is usually worse in densely vegetated areas than those without much vegetation. γ_G is also termed baseline decorrelation. Phases from two antennas with a spatial separation greater than a critical distance (critical baseline, $B_\perp^C$), cannot be used to generate an efficient interferogram. $B_\perp^C$ is defined as (Zebker and Villasenor, 1992)

$$B_\perp^C \sim \frac{\lambda R}{n\rho_g sin\theta} \tag{2.9}$$

where R is the slant range (Figure 2.1), and n depends on the radar system. In a system that transmits and receives separately on each aperture, n is 2. θ is the incidence angle and ρ_g is the range resolution. For instance, the critical baseline of Envisat Stripmap SAR data is ~1100 m, whilst one of an ASAR ScanSAR pair with pixel spacing of 150 m is ~200 m.

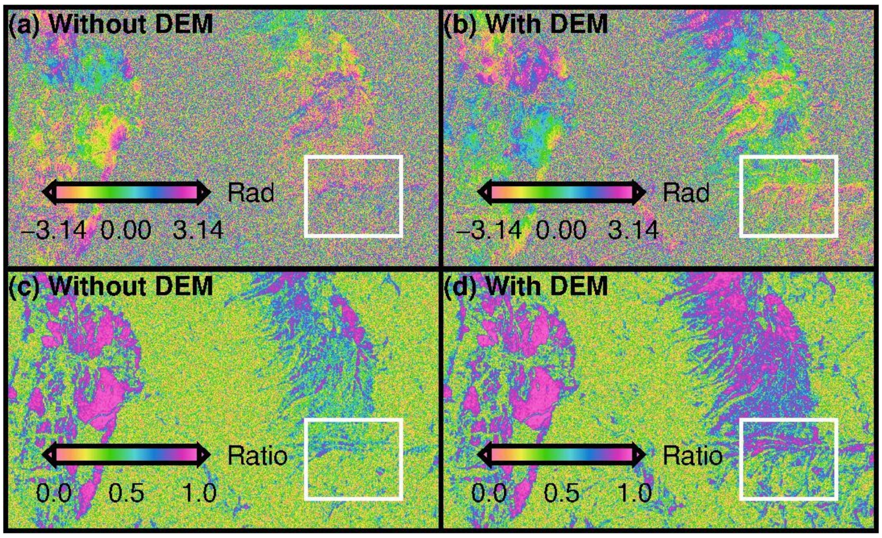

Figure 2.5 Comparison of interferograms without and with the DEM-assisted algorithm. (a) ASAR interferogram (28 Feb 2010 vs 09 May 2010) with a perpendicular baseline of ~480 m; (b) As (a), but the DEM-assisted algorithm applied. (c) and (d) are the corresponding correlation maps, respectively.

For those InSAR pairs with a large spatial baseline, spectrum filtering in range can be useful to partly reduce the effects of baseline decorrelation (Gatelli et al., 1994). The difference of viewing angles between antenna and ground target as shown in Figure 2.2, is proportional to the baseline.

Once the baseline is big, for example a 500-m-long baseline for a C-band interferometric pair, image alignment using a traditional low-degree polynomial method may lead to serious loss of interferometric coherence (Yun et al., 2007; Nitti et al., 2011). With the assist of a DEM (Nitti et al., 2011), the coherence can be improved significantly, particularly in the areas with rugged terrain. Using the DEM-based algorithm, the offset at each pixel is estimated from the reference DEM and orbital information of master and slave images. As seen in Figure 2.5, the C-band ASAR pair has a perpendicular baseline of ~480 m, which was processed using the traditional coregistration and DEM-assisted method, respectively. In the small highlighted region (Figure 2.5), the mean correlation coefficient of resultant interferogram using the DEM-assisted method increases to 0.52 from 0.37 corresponding to the traditional method.

2.1.1.5 Open InSAR processing packages: DORIS, GMTSAR, ISCE and ROI_PAC

Several non-commercial InSAR software packages are freely available to produce interferograms as listed in Table 2.1, e.g. DORIS, GMTSAR, ISCE and ROI_PAC. Although the processing flow of interferometry is similar for all InSAR packages, some specific features in each software make them unique and attractive for different applications.

DORIS (Kampes et al., 2003) is one of the earliest open InSAR packages, which has been widely used. Because of some advanced algorithms such as oversampling, range filtering and azimuth filtering, DORIS has been selected as the basic InSAR tool by several popular InSAR time-series analysis packages (Hooper et al., 2007; Agram et al., 2013), e.g. StaMPS, GIAnT.

GMTSAR is a newly developed and easy-to-use package (Sandwell et al., 2011). Because this software utilizes accurate satellite orbit information in image registration, GMTSAR can robustly generate an interferogram without human interference. GMTSAR employs the genetic mapping tool (GMT) to manage all data in processing, which makes it easy to plot results with utilities in GMT (Wessel and Smith, 1998). Many internal scripts that can help users to easily conduct a SBAS-InSAR or stacking InSAR processing make it attractive.

ROI_PAC is the most popular package in the geophysical community (Rosen et al., 2004b) and it has had a wide range of elements contributed by the InSAR community, in which one Perl script can help to finish a repeat pass InSAR processing. In this thesis, ROI_PAC is used to process most interferograms for modelling, but in some cases other packages are also employed to generate interferograms.

ISCE is the latest package which is motivated by the geophysical community's requirements (Rosen et al., 2011b). It combines two current InSAR processors, ROI_PAC (Rosen et al., 2004b) and STD_PRO from the Stanford group (Zebker et al., 2010), and uses a uniform open computer language, Python, in an object-oriented way, thus this package should meet most geophysical users' needs in future. However, currently it is not ideal due to many unknown bugs.

To compare their abilities for repeat-pass InSAR processing, a C-band InSAR pair of 4 May 2008 vs 18 July 2010 for the 2008 M_W 6.3 Damxung earthquake in Tibet from descending track 176 was employed to generate interferograms and coherence images. As shown in Figure 2.6, the coherence slightly varies from one InSAR processing package to another, although the fringe patterns appear similar. Therein, the interferogram from GMTSAR looks much smoother than others, which is due to a Gaussian filter used in multilooking by default. Comparatively, the interferogram generated using DORIS (Kampes et al., 2003) (Figure 2.6 (d)) has significantly different fringe patterns from the rest, which may be induced by the different flattening algorithm and/or the use of different baseline calculation methods.

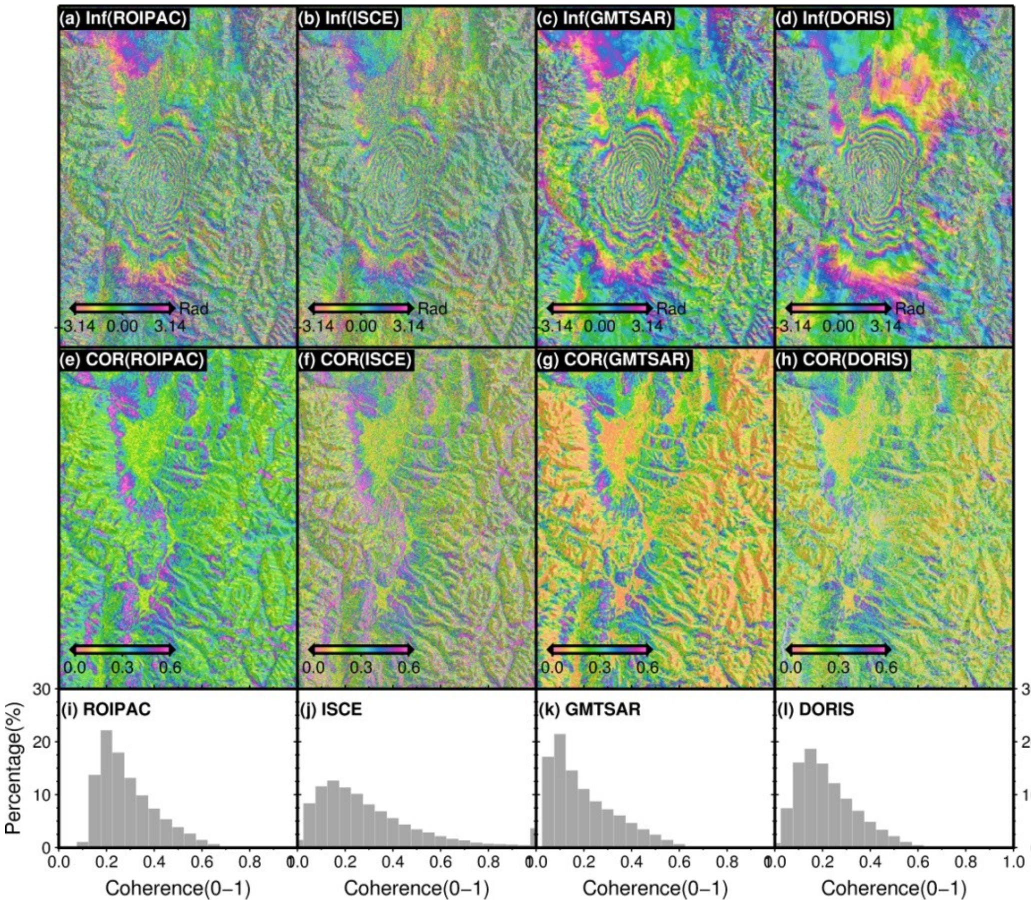

Figure 2.6 Comparisons of ASAR interferograms produced using different InSAR packages. (a-d) are the interferograms generated by ROI_PAC, ISCE, GMTSAR and DORIS respectively; (d-g) are the corresponding coherences and (h-k) are histograms of coherence. The ASAR pair (4 May 2008 vs 18 July 2010) was used for the comparison.

Table 2.1 Open-source InSAR Processing Toolboxes.

Name	Platform	Languages	Strength	Weakness	Source
DORIS	Linux/Mac/Win	C++/C-shell	1) RNG/AZI filtering available 2) DEM-assisted registration 3) a GUI interface available, NEST (ESA)	1) interferometry from SLC only 2) processing is slower than ROI_PAC 3) Estimation of the timing errors between DEM and the master is slow and not robust.	(Kampes et al., 2003)
GMTSAR	Linux/Mac	C/c-shell	1) highly automated processing 2) SAR focusing 3) supports most current/past SAR data 4) works under the standard general format, e.g. netCDF grid file (GRD)	1) Hard to debug in C-shell. 2) Precise orbits required. 3) RadarSAT-1/2 data not supported.	(Sandwell et al., 2011)
ISCE	Linux/Mac/Win	Python	1) fully developed in Python 2) highly automated package including preparing DEM data 3) combines the STD_PROC in Stanford with some new features.	1) an early version with plenty of known/unknown bugs. 2) lack of instant supports.	(Rosen et al., 2011a)
ROI_PAC	Linux/Mac	Fortran/C/Perl	1) a widely used free InSAR package 2) wide contributions from whole InSAR Community 3) provide full solution on two-pass interferometry including SAR focusing 4) numerous packages available based on it, e.g. StaMPS, ScanSAR-InSAR, Pi-Rate…	1) SAR simulation by external DEM is not ideal, particularly for high-resolution SAR 2) Focusing may not be accurate, in particular with very long track data.	(Rosen et al., 2004b)

2.1.2 InSAR measurement errors

2.1.2.1 InSAR error sources

The error term (φ_{err}) of Equation (2.3) is composed of contributions from variable error sources (Berardino et al., 2002) that are usually present in most InSAR applications. It can be extended as

$$\boldsymbol{\varphi_{err} = \varphi_{err}^{orb} + \varphi_{err}^{aps} + \varphi_{err}^{iono} + \varphi_{err}^{dem} + \varphi_{err}^{sys} + \varepsilon} \tag{2.10}$$

where φ_{err}^{orb} represents orbital errors, φ_{err}^{aps} the contribution from atmosphere path delays, and φ_{err}^{iono} describes the source from ionopheric anomaly (Meyer et al., 2006; Meyer, 2010; Rosen et al., 2010; Heki, 2011). The inaccuracy of an external DEM used in the repeat-pass InSAR processing also results in phase errors (φ_{err}^{dem}). φ_{err}^{sys} is partly due to non-efficient data processing, which is not easy to quantify and can be grouped into the random noise term (ε).

Atmospheric phase screen (APS) φ_{err}^{aps} is one of the major error sources in the conventional InSAR measurements (e.g. Hanssen et al., 1999; Hanssen, 2001; Li et al., 2006), which can lead to an order of ~0.1 m in deformation products (Zebker et al., 1997). In small deformation analysis, the magnitude of APS can be even greater than targeted signals. Utilizing external atmospheric water vapour datasets (e.g. Li, 2004; Li et al., 2006; Li et al., 2009c; Walters et al., 2013; Jolivet et al., 2014), e.g. GPS, MERIS, MODIS and meteorological data, its effects on SAR interferograms can be partly reduced. In cases without external datasets, time-series analysis can provide an alternative way to separate deformation signals from APS (e.g. Lanari et al., 2007; Li et al., 2009d; Reeves et al., 2011; Cetin et al., 2012).

Regular and long-wavelength fringes in unwrapped interferograms are usually induced by orbit-related errors. Recent studies have also pointed out that timing errors and oscillator clock drifts over time may also contribute to orbit-like fringes (Bekaert et al., 2013; Marinkovic and Larsen, 2013; Teng et al., 2014). A best-fitting polynomial of order one or higher can be sufficient to reduce its effects in an individual interferogram. A spectrum domain method (Shirzaei and Walter, 2011) is also feasible to estimate its distribution. For the applications in interseismic creep rate estimations, a network approach (Biggs et al., 2007) with multiple interferograms is proposed to split orbital errors into master and slave components. This method can avoid effects of long-wavelength tectonic signals and APS on the orbital errors estimates to an extent. In this method, the rank of the designed matrix is insufficient. SVD is suggested to solve such an underdetermined linear problem (Biggs et al., 2007). An improved network approach with a two-step strategy is developed in this thesis. Details can be found in Chapter 3.

2.1.2.2 Spatial characterization of APS

APS is a common issue when applying InSAR techniques since radar signals travel through the troposphere. All methods for correcting for APS in an individual interferogram remains challenging

(Knospe and Jonsson, 2010). The confidence intervals and uncertainties in model parameters induced by InSAR errors must be provided in geodetic applications (e.g. Menke, 1989; Lohman and Simons, 2005). The geostatistic method is an effective way to characterize the dispersion of the observations using the structure function (or variogram), variance and covariance (Hanssen, 2001).

Without loss of generality, the anisotropic covariance $C_n(r,\theta)$ can be expanded from the Hanssen's (2001) isotropic model by combining a scalar distance r and azimuth θ between any two points as

$$\boldsymbol{C_n(r,\theta) = cov(f(x;0), f(x+r;\theta)) = E([f(x;0)f(x+r;\theta)])} \quad \textbf{(2.11)}$$

where r is always non-negative, $f(x;0)$ is the observation at position x in an interferogram. The variogram originates from geostatistics, whilst the structure function $S(r,\theta)$ is widely used in the turbulence literature (e.g. Antonia and Smalley, 2001; Emardson et al., 2003). Both can be defined as a variance of the difference of two points separated by a distance r and azimuth angle θ,

$$\boldsymbol{S(r,\theta) = E[f(x;0) - f(x+r;\theta)]} \quad \textbf{(2.12)}$$

and

$$\boldsymbol{C_n(r,\theta) = \sigma^2 - s(r,\theta)} \quad \textbf{(2.13)}$$

where σ^2 is the variance of the interferogram. Since elements in covariance are always positive, the variances from the azimuths of θ and $\theta + 180$ with the same distance should be equivalent. $S(r,\theta)$ and $C_n(r,\theta)$ can be computed by either a full variogram where all point pairs between any two points are computed, or a sample variogram where only a certain number of random pixel pairs are chosen for computation. A full variogram should always be given priority to unless the computational burden in spatial domain is an issue. In this study, a FFT method (Marcotte, 1996) is suggested to compute full interferogram variograms in the frequency domain, which can provide a very fast computation. As shown in Figure 2.7, the original interferogram contains 649 by 663 pixels. All of possible point pairs reach to $1.9*10^{11}$. It took only 3 seconds to produce the full variogram (Figure 2.7 (b)) using the FFT method. Note that null value in the interferograms should be interpolated before the calculation.

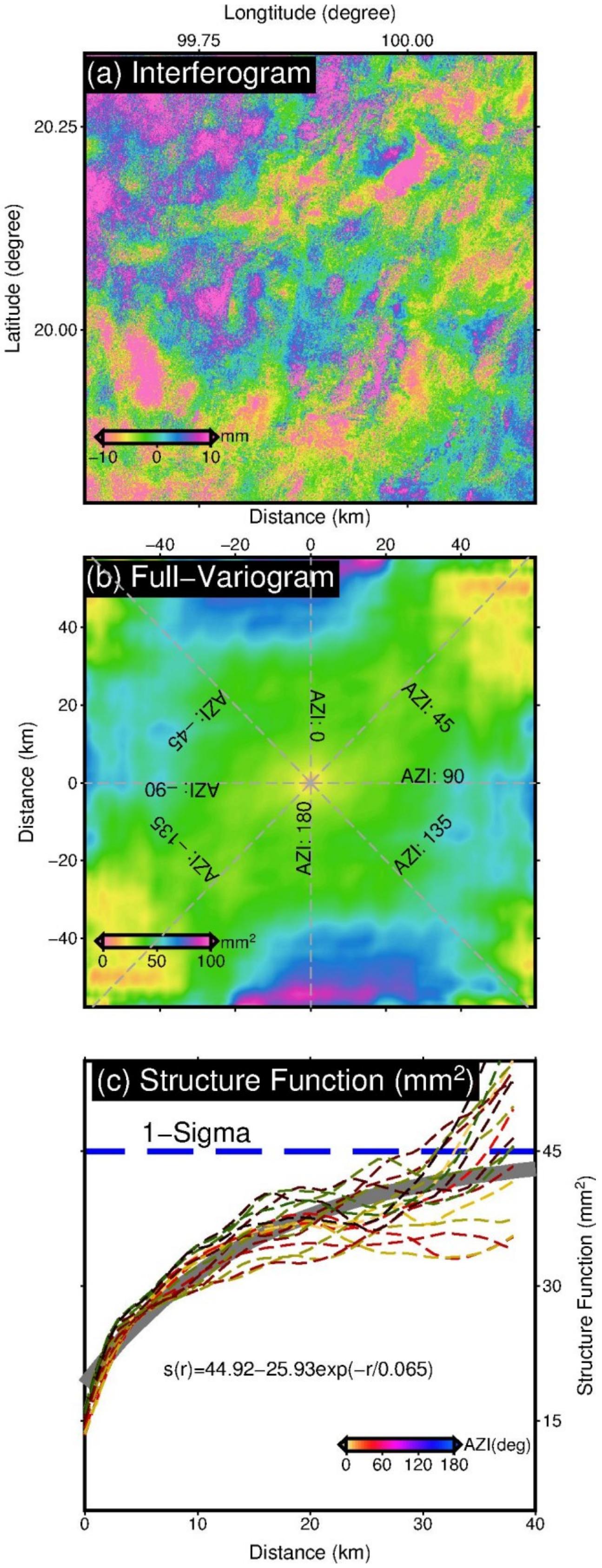

Figure 2.7 Example of an interferogram, a full variogram and structure function with distance $\boldsymbol{r}$ and azimuth $\boldsymbol{\theta}$. The Interferogram used in (a) was generated from ascending ASAR track 026 covering the Damxung area in the southern Tibet.

Figure 2.7 shows the two-dimensional full variogram (Figure 2.7(b)) of the interferogram (Figure 2.7 (a)) and one-dimensional structure function along different azimuth angles (Figure 2.7 (c)). The structure functions over 20 km are relatively variable. In practice, APS spatial distribution is usually simplified to be an isotropic problem as used in most of previous cases (e.g. Hanssen, 2001; Parsons et al., 2006). An isotropic theoretical function $s^{i}(r)$ can be modelled by an exponential function over distance as

$$\boldsymbol{s^{i}(r) = \sigma^{2} - a * \exp\left(-\frac{r}{b}\right) = 44.92 - 25.93 \exp\left(-\frac{r}{0.065}\right)} \qquad \textbf{(2.14)}$$

where a is the parameter that is theoretically equal to the standard variation σ^{2} of the data errors, b is another controlling parameter. Because of the presence of white noise, $\boldsymbol{s^{i}(r)}$ is not zero at each pixel, which is usually estimated using a small window. In the case of Figure 2.7, the best-fit model of the structure function shows the variance (σ^{2}) of 44.92 mm^{2}, and model parameters for a of 25.93 and b of 0.065. The data σ^{2} of coseismic interferogram is larger than the parameter b, which is similar with the phenominon in the 2011 Iceland earthquake (Sudhaus and Jonsson, 2009), suggesting that white noise in the InSAR measurements is common.

Note that data in the far-field without no detectable deformation, are used to estimate the variogram. If insufficient far field pixels are available in the case of large shallow earthquakes, the residuals after removing the modelled displacements with a best-fit slip model can be used instead (Elliott et al., 2010).

2.1.3 Advanced InSAR techniques

2.1.3.1 Large deformation mapping

In this thesis, InSAR is used to map co- and post-seismic surface motions. Conventional cross-track interferometry usually suffers from decorrelation due to the large deformation gradients in the near-field for large shallow earthquakes, volcano eruptions and landslides (Yun et al., 2007; Singleton et al., 2014). Theoretically, the maximum detectable deformation gradient (D_x) in LOS direction is defined by a functional model proposed by Baran *et al.* (2005) as

$$\boldsymbol{D_x = \frac{\lambda}{2\rho}} \qquad \textbf{(2.15)}$$

where ρ is the image resolution and λ is the wavelength. D_x is dimensionless. Based on the corresponding SAR parameters, the maximum deformation gradients are ~1.4×10^{-3} and ~7.5×10^{-3} for original resolution interferograms of C-band (Envisat ASAR) and L-band (ALOS PALSAR) data, respectively. The gradient estimate is slightly different between sensor viewing geometries. More detailed analysis of the maximum measurement ability of InSAR can be seen in previous studies (Baran et al., 2005; Jiang et al., 2011; Singleton et al., 2014).

For those cases with large deformation beyond cross-track InSAR ability, another two techniques may be able to provide feasible surface displacement measurements: sub-pixel offsets (SPO)

(Michel et al., 1999a; Michel et al., 1999b) and multiple aperture interferometry (MAI) (Bechor and Zebker, 2006; Barbot et al., 2008). SPO utilizes the amplitude of SAR images to measure offsets within one resolution cell. Due to limited spatial resolution of ERS-1 SAR data, uncertainties in range and azimuth deformation maps associated with the 1992 Landers earthquake are 0.8 m and 0.4 m, respectively (Michel et al., 1999b). With respect to high resolution SAR images, e.g. TerraSAR-X and Cosmo-Skymed, an accuracy of 1/10 to 1/32 of single SLC pixel can be obtained by SPO (Singleton et al., 2014).

MAI specifically senses surface motions along the satellite flight path, which uses the different information in each radar beam due to existence of squint angle. Conventional MAI (Bechor and Zebker, 2006) starts with azimuth sub-banding during SAR data focusing, whilst a post-processing strategy proposed by Barbot *et al* (2008), also termed AZISAR, can achieve the same purpose through splitting an already-focused SLC into forward and backward bands using a spectral analysis method. In comparison to SPO, MAI makes use of phase components. However, the accuracy of MAI is much lower than cross-track InSAR measurements. A correlation-dependent root-mean-square (RMS) of MAI measurements with a correlation coefficient of 0.4 is ~0.08 m (Ben-Dov and Herring, 2011), whilst RMS sharply drops to 0.02 m at pixels with a correlation coefficient of 0.75.

Technically, SPO can provide two dimensional displacement maps in both range and azimuth directions. However, the range offsets of C-band data (e.g. ERS-1/2 and Envisat) are rarely used for geophysical interpretation due to its limited accuracy. The azimuth component of SPO can be much better than range component due to higher azimuth resolution, which can be comparable to corresponding MAI results for both C- and L-band SAR data (Bechor and Zebker, 2006; Feng et al., 2013a). One example is presented in Figure 2.8.

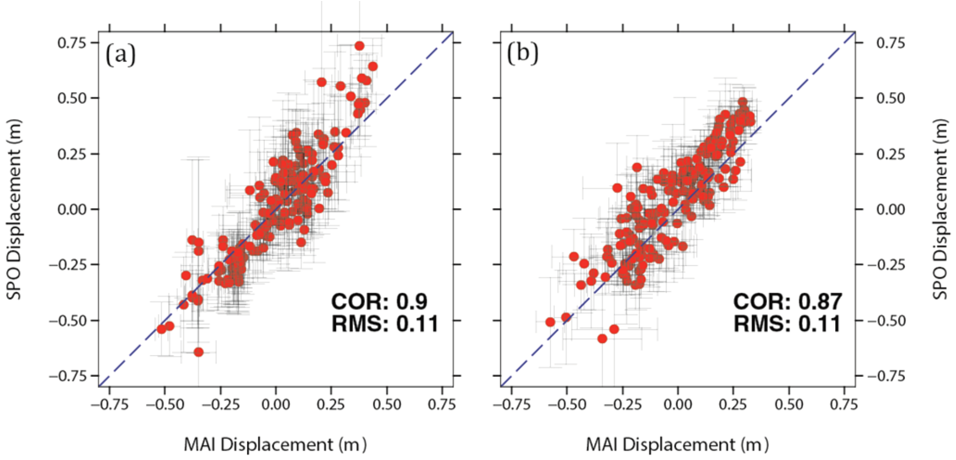

Figure 2.8 Comparison between SPO and MAI along-track measurements (Feng et al., 2013a). The data used in these figures are for the 2011 M_W 6.8 Burma earthquake. (a) Comparison between SPO and MAI for ALOS track 126D; (b) As (a), but for ALOS track 486A. Dashed lines are 1:1 agreement. Error bars are based on the standard deviation within a 3 by 3 pixels window.

2.1.3.2 InSAR time series

Stacking InSAR (e.g. Wright et al., 2001b; Fialko et al., 2002; Fialko, 2004a; Tong et al., 2013; Tong et al., 2014), small-baseline InSAR (SBAS) (Berardino et al., 2002; Lanari et al., 2004) and Permanent Scatterer InSAR (PS-InSAR) (Ferretti et al., 2001; Ferretti et al., 2011) are effective methods to reduce observation errors by using multi-temporal acquisitions. Stacking InSAR is based on the principle that the desired geophysical signal is a systematic pattern, but that atmospheric noise is random. Deformation signals in a stacked interferogram from N interferograms are N time larger than a single interferogram, whilst the noise is only $\sqrt{N}$ times larger (Biggs et al., 2007). This method works for those whose targeted deformation history is linear over time. To address more complicated deformation time series, SBAS (e.g. Berardino et al., 2002; Lanari et al., 2004; Li et al., 2009b) and PSInSAR (e.g. Ferretti et al., 2001; Hooper et al., 2007) methods have been well developed.

As a post-processing tactic, SBAS is more practical than PSInSAR because the former avoids complicated algorithms for identifying persistent pixels in all involved SAR images. However, to obtain reliable results SBAS usually needs a good network of SAR acquisitions. So far there are many applications applying SBAS successfully for city subsidence, postseismic deformation mapping and interseismic creep estimation (e.g. Hooper, 2008; Casu et al., 2009; Dehghani et al., 2009; Fernandez et al., 2009; Li et al., 2009d; Samsonov, 2010; Buckley and Gudipati, 2011; Ducret et al., 2011; Lauknes, 2011). In Chapter 3, the SBAS method is utilized to retrieve postseismic deformation time series following the 2009 M_W6.3 Haixi, Qinghai earthquake.

2.2 Geodetic modelling

2.2.1 General inverse problem

It is an inverse problem to determine fault parameters (m) from geodetic measurements (d), which can be defined as

$$\boldsymbol{d} = \boldsymbol{f}(\boldsymbol{m}) + \boldsymbol{\epsilon} \quad \textbf{(2.16).}$$

In practice, no data are perfectly accurate (Yanovskaya, 2003; Tarantola, 2005; Aster et al., 2013). Therefore, noise (ϵ) as in Equation (2.16) should always be carefully taken into account in the interpretation. For a finite rectangle fault source (Okada, 1985, 1992), three linear slip components, and seven non-linear geometric parameters need to be considered in surface displacement simulation in Equation (2.16). A geodetic inversion for earthquake parameters is generally implemented using a two-step approach (e.g. Fukahata and Wright, 2008). Firstly, to determine the fault geometry by minimizing the square misfit under an assumption of a uniform slip on a rectangular fault; secondly, to estimate the slip distribution on an extended fault plane with linear inversion techniques. So, earthquake modelling with InSAR observations usually includes both nonlinear and linear problems.

2.2.1.1 Nonlinear problem: determination of fault geometry

To determine fault geometric parameters with geodetic measurements, various nonlinear optimization methods have been developed (e.g. Wright et al., 1999; Delouis et al., 2002; Stramondo et al., 2011; Velez et al., 2011), e.g. down-hill simplex, simulated annealing, neural network method and genetic algorithm. Each optimization has their own strengths that make themselves successful in some applications. It is difficult to know if there exists a universal method that is capable of solving all kinds of nonlinear problems. Feasibility and efficiency of nonlinear optimization algorithms largely rely on users' understanding of the nonlinear problem. An improved Particle Swarm Optimization (PSO) has been developed for geodetic modelling by the thesis author since 2006 (Feng et al., 2009; Feng and Li, 2010). All nonlinear problems in this study are solved using this method.

PSO is proposed based on the social behaviour metaphor. More details can be found in previous papers (Kennedy and Eberhart, 1995; Trelea, 2003). It assumes that n particles are involved in a global searching. The velocity v_{j+1}^{i} of the ith particle at the $(j+1)$th iteration depends on both the present global minimum of all particles and the minimum of its own search history, which can be mathematically expressed as

$$\boldsymbol{v_{j+1}^{i} = v_{j}^{i} + c_1 r_1 \left(L_o^{j} - p_j^{i}\right) + c_2 r_2 \left(G_o^{j} - p_j^{i}\right)} \quad \textbf{(2.17)}$$

and

$$\boldsymbol{x_{j+1}^{i} = x_{j}^{i} + v_{j+1}^{i}} \quad \textbf{(2.18)}$$

where c_1 and c_2 are local and global learning (or controlling) factors respectively, which control the space exploration ability. They are also termed inertia weights. r_1 and r_2 are two random factors that are both fixed in a small range of [0,1]. v_{j+1}^{i} and x_{j+1}^{i} are n-dimensional variables depending on the inversion problem itself. Inertia weights and random factors can also be considered over the same dimension as the velocity fields, but the computational burden has to be taken into account. In the searching history, particles tend to temporally converge in local minima. This phenomenon is fully utilized by a 1D histogram analysis in the improved PSO method, (hereafter also termed MPSO). After that, a down-hill simplex method (Nelder and Mead, 1965) is employed to further search the preferable solution determined through a histogram analysis. The global minimum solution should exist in the outputs after a series of searching by the down-hill simplex method. MPSO keeps the strengths of both the simplex and PSO approaches to avoid the convergence at a local minimum.

In practice, the problem of determining fault geometric parameters from geodetic observations is not highly nonlinear. After parameter searching by PSO, limited local minima are usually determined. Meanwhile, the Simplex method is usually speedy. Therefore, MPSO can be a fast and reliable way to solve the inversion problem for earthquake parameters at a relatively high convergence rate. During the inversion, the misfit function (δ) between the fault geometric model ($\boldsymbol{m}$) and observations (d) is defined as

$$\boldsymbol{\delta} = \|\boldsymbol{W}(\boldsymbol{d} - \boldsymbol{g}(\boldsymbol{m})\|_2 \qquad \textbf{(2.19)}$$

where $\boldsymbol{W}$ is the weight matrix produced through Cholesky decomposition of the data covariance matrix inverse (Strang and Borre, 1997; Jonsson, 2002): $\boldsymbol{W}^{\top}\boldsymbol{W} = \boldsymbol{\Sigma}^{-1}$.

To compare the effects of different learning factors in the inversion, two simple examples were carried out. As shown in Figure 2.9, in test-1 (Figure 2.9 (a)), control factors of [1,1.5] were used for the local learning factor and the global one respectively, whilst 1.5 and 1 were used in test-2 (Figure 2.9 (b)). All the strike angles displayed in the histograms represent solutions that MPSO returned. In test-1 (Figure 2.9 (a)), the large global factor tends to drive most particles swarming around B. In contrast, test-2 (Figure 2.9 (b)) shows that particles swarm towards multiple local minima like A, B and C due to the relatively large local learning factor. However, the global minimum of around 205 has been detected in both test-1 and test-2. The simplex algorithm can be applied iteratively with these detected local minima. The global minimum solution can then be determined quickly and robustly.

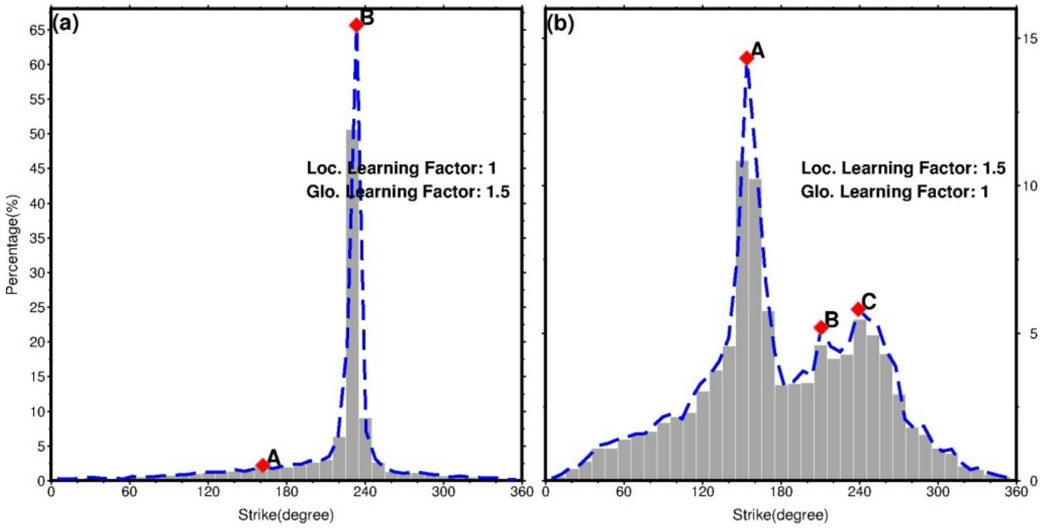

Figure 2.9 Examples of local minima detected by the MPSO method.

2.2.1.2 Linear problem: determination of slip distribution

Once the fault geometric parameters are determined, resolving the slip distribution on the fault plane is a linear problem. In some large shallow earthquake applications (e.g. Simons et al., 2002), the fault locations and dimensions can be observed in the field. In this case, only dip angle remains unknown, which can be solved during the linear inversion step. Therefore, the step of the nonlinear inversion can be neglected. Equation (2.19) here can be re-defined as

$$\boldsymbol{d} = \boldsymbol{GS} + \boldsymbol{\epsilon} \qquad \textbf{(2.20)}$$

where G is the Green's matrix relating surface displacements to the model parameters and S is the slip vector. Following previous linear strategies (Funning et al., 2007; Zhang et al., 2009a), two orthogonal slip vectors are usually considered in generating the Green's matrix (G) as

$$\boldsymbol{G} = \begin{bmatrix} \boldsymbol{G_{r1}} & \boldsymbol{0} \\ \boldsymbol{0} & \boldsymbol{G_{r2}} \end{bmatrix} \tag{2.21}$$

where G_{r1} and G_{r2} are equal-sized matrices corresponding to two slip components orthogonal to each other. Note that r_1 can be the slip component along any rake ($r_1 \in [-180,180]$). r_2 is then usually defined by $r_1 + 90$. Correspondingly, slip vector S includes two components as

$$\boldsymbol{S} = \begin{bmatrix} \boldsymbol{s_{r_1}} \\ \boldsymbol{s_{r_2}} \end{bmatrix} \tag{2.22}$$

The general slip components along the fault orientation and Updip direction can be derived from S based on the given rakes using the simple trigonometric functions by the following equation as

$$\begin{bmatrix} \boldsymbol{s_s} \\ \boldsymbol{s_d} \end{bmatrix} = \begin{bmatrix} \boldsymbol{cos(r_1)} & \boldsymbol{cos(r_2)} \\ \boldsymbol{sin(r_1)} & \boldsymbol{sin(r_2)} \end{bmatrix} \begin{bmatrix} \boldsymbol{s_{r_1}} \\ \boldsymbol{s_{r_2}} \end{bmatrix} \tag{2.23).}$$

To avoid the slip oscillations in the inversion, a two-dimensional two-order Laplacian operator (∇) is proposed to constrain the smoothness of slips in two dimensions (Harris and Segall, 1987). Combining Equations (2.23-25) and ∇, the final equation for the slip solution can be re-written as

$$\begin{bmatrix} \boldsymbol{Wd} \\ \boldsymbol{0} \\ \boldsymbol{0} \\ \boldsymbol{0} \end{bmatrix} = \begin{bmatrix} \boldsymbol{WG_{r_1}} & \boldsymbol{0} \\ \boldsymbol{0} & \boldsymbol{WG_{r_2}} \\ \boldsymbol{\alpha^2\nabla} & \boldsymbol{0} \\ \boldsymbol{0} & \boldsymbol{\alpha^2\nabla} \end{bmatrix} \begin{bmatrix} \boldsymbol{s_{r_1}} \\ \boldsymbol{s_{r_2}} \end{bmatrix} \tag{2.24}$$

where $\boldsymbol{\alpha^2}$ is a hyperparameter that is introduced to help to select a smooth slip model, which can be determined by a trade-off curve plot between slip roughness and data misfit. Meanwhile, some others have also been suggested to be able to select an optimal value of $\boldsymbol{\alpha^2}$ quantitatively, such as an ABIC algorithm (Fukahata and Wright, 2008) and a fully Bayesian approach (Fukuda and Johnson, 2008) and a cross validation (CV) based method (Matthews and Segall, 1993). To solve slip in Equation 2.24, a gradient method (Ward and Barrientos, 1986) is recommended to use in this thesis, which can solve a large least-squares problem fast.

2.2.1.3 Time-dependent geodetic modelling

Along with high-frequency GPS measurements provided from GNSS, InSAR time-series plays a vital role in understanding crustal time-dependent movements and their physical mechanisms (Segall and Matthews, 1997; Segall, 2000; Burgmann et al., 2002b). Although time-dependent observations can be intuitively inverted for the spatial and temporal variations in fault slip, space-time dependent inversion is often hampered by poor signal to noise ratios (SNR) in geodetic measurements. An extended network inversion with a Kalman filtering (ENIF) under the constraints of GPS time series was proposed for solving the spatial-temporal evolution of fault slip or magma transport (Segall and Matthews, 1997; Aoki et al., 1999; Burgmann et al., 2002b). In this method, a constant scaling parameter was employed to control the smoothness of temporal fault slips at each fault patch. A Monte Carlo strategy was also introduced to improve this method regarding temporal smoothness of slip as a statistic variable (Fukuda et al., 2004).

ENIF is computationally intensive. For instance, the inversion for the afterslip model following the 2005 M_W 8.7 Nias earthquake using GPS displacement time series took approximately two hours on a typical 2005 laptop (Hsu et al., 2006; Kositsky and Avouac, 2010). Actually, ENIF was specifically designed for GPS data, which is not capable of inverting InSAR time series. To overcome part of these limitations, a principal component analysis-based inversion method (PCAIM) was proposed for time-dependent inversion that can efficiently handle both GPS and InSAR deformation time-series (Kositsky and Avouac, 2010; Lin et al., 2010). The basic principle of PCAIM is to decompose deformation observations into the sum of multiple principal components, of which each component is individually inverted for a corresponding principal slip model. This method takes advantage of the linearity between surface displacements and fault slip, which makes it possible to retrieve a source model by a linear combination of principal slip models derived from the inversion of each component. PCAIM has been successfully applied in several time-dependent geodetic inversions, e.g. the magmatic inflation beneath the long Valley Caldera and the afterslip following the 2005 Nias earthquake. However, it is very sensitive to high-amplitude noise in the observations (Lin et al., 2010).

A good SAR acquisition network can offer an opportunity to resolve deformation time series with limited effects of data errors such as APS and DEM errors, by SBAS-InSAR and/or PS-InSAR. Then, it is possible to determine the cumulative slip between any two SAR acquisitions individually (Ryder et al., 2007a). To obtain relatively continuous slip history, the gap between the event occurrence and the first SAR acquisition can be interpolated based on deformation time series (Ryder et al., 2007a). A similar strategy has also been applied in the GPS-based afterslip model of the 2011 M_W 9.0 Japan earthquake (Diao et al., 2013). However, rate oscillation in temporal fault slip due to unexpected observations errors cannot be controlled during inverting time series individually.

An integrated equation for space-temporal slip history based on InSAR time-series is proposed in the Qinghai afterslip analysis (Chapter 3), in which an additional hyperparameter is introduced to constrain slip rate oscillation between the afterslip history.

2.2.1.4 Layered Earth model

The classic dislocation theory (Okada, 1985, 1992) in an elastic half space has been successfully applied in the prediction of crustal deformation fields. However, efforts to develop the formulations for a more realistic Earth model have been advanced since the 1950's (e.g. Steketee, 1958; Maruyama, 1964; Singh, 1971; Comninou and Dundurs, 1975; Savage, 1998; Wang, 1999; Zhu and Rivera, 2002; He et al., 2003). The effects of Earth curvature, lateral inhomogeneity, crustal layering and obliquely layered media have separately been considered in numerical implementations. As described previously (Okada, 1985; Wang et al., 2006b), the effect of Earth curvature can be negligible for shallow events at distances of less than 2,000 km, whilst lateral inhomogeneity or crustal layering can sometimes cause considerable effects on the surface deformation simulation.

To examine effects of a layered medium, theoretical surface displacements due to the slip model of the 2011 M_W 9.1 Japan earthquake, determined by a joint inversion (more details in Chapter 5), were calculated using Okada's method and Wang *et al.*'s method, respectively (Okada, 1992; Wang et al., 2006b). Four layers of crust exist in the database of Crust2.0 for this region (Tenzer et al., 2011). As shown in Figure 2.10, vertical displacements determined with the elastic half-space Earth model show good agreement with the layered elastic model with a correlation of 0.996 and a p-value of 0.0001.

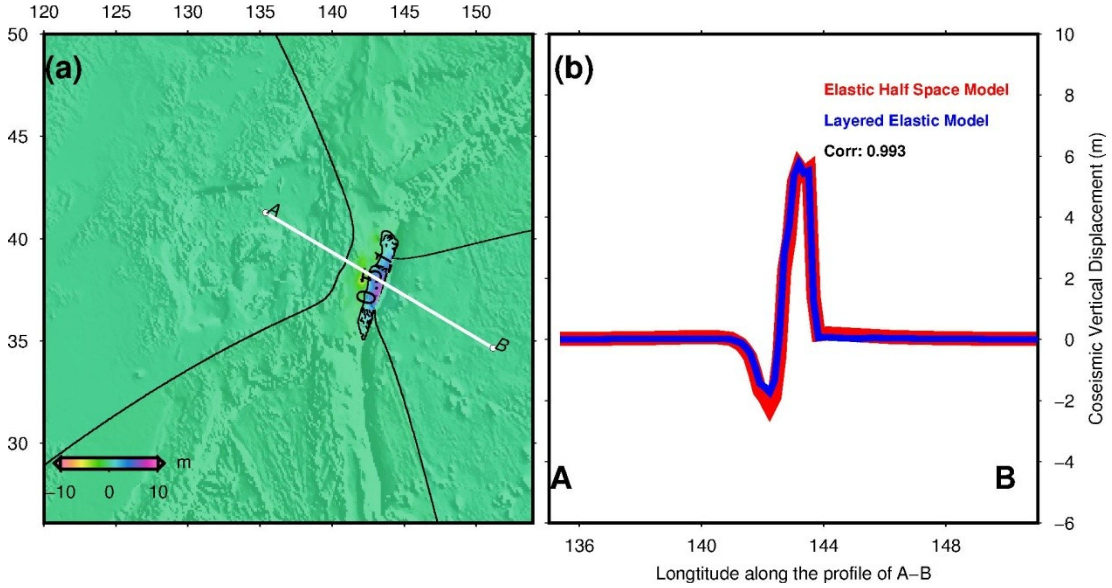

Figure 2.10 Comparison of the predicted vertical displacements from elastic half-space and layered Earth models. (a) The vertical displacement field associated with the M_W 9.1 Tohoku-Oki earthquake. White line is the location of Profile A-B. (b) Comparison of the vertical displacement along Profile A-B derived from the elastic half-space earth model (red line) and the layered elastic one (blue).

2.2.2 InSAR observations downsampling

In comparison to GPS and any other conventional geodetic means, InSAR technique can provide measurements covering epicentral areas at a spatial resolution of a few tens of metres. Millions observations can be usually available for an earthquake source modelling, which significantly increases computational cost. Thousands of forward computations usually need to be performed during the inversion. It is unlikely to involve all InSAR valid pixels in the inversion. Therefore, InSAR observations are often downsampled to few thousands of points prior to modelling (e.g. Jonsson, 2002; Lohman, 2004; Lohman and Simons, 2005). Because of the high degree of spatial correlation in InSAR data, loss of data information for source in this process can be ignored (Hanssen, 2001; Wright et al., 2004a). Three down-sampling algorithms in the spatial domain have been developed, such as regular-grid sampling, Quadtree decomposition (Jónsson et al., 2002;

Simons et al., 2002) and data Resolution based (Rb) method (Lohman and Simons, 2005).

As the simplest algorithm, the regular-grid sampling method can be implemented by sub-sampling unwrapped interferograms to a coarse grid with regular spacing. The value at each new grid pixel can be re-assigned using a mean value of all valid value within the sampling window, e.g. 20 by 20 pixels (Jonsson, 2002). This method has a severe trade-off between the efficiency of reduction and deformation details near to the fault trace, but this limitation can partly be overcome by the Quadtree algorithm. The Quadtree method utilizes the displacement gradients to determine the sub-sampling window size. Ideally, the sampling size of pixels near the fault should be small, whilst the window size in the far-fields is large. However, it is impossible to avoid oversampling in the far fields due to the effects of observation errors (non-deformation signals). The Rb method avoids all of the above limitations to some degrees. The sampled data density depends on both the sensitivity of data to the fault model and displacement gradients (Lohman and Simons, 2005). In this method, the fact that individual pixels far from slip sources contribute approximately identical information to the model, is fully taken into account (Lohman and Simons, 2005). As shown in Figure 2.11, the three methods were employed for downsampling a L-band interferogram from ALOS track 126 that was used for determining the fault parameters of the 2011 M_W 6.8 Burma earthquake (Feng et al., 2013a).

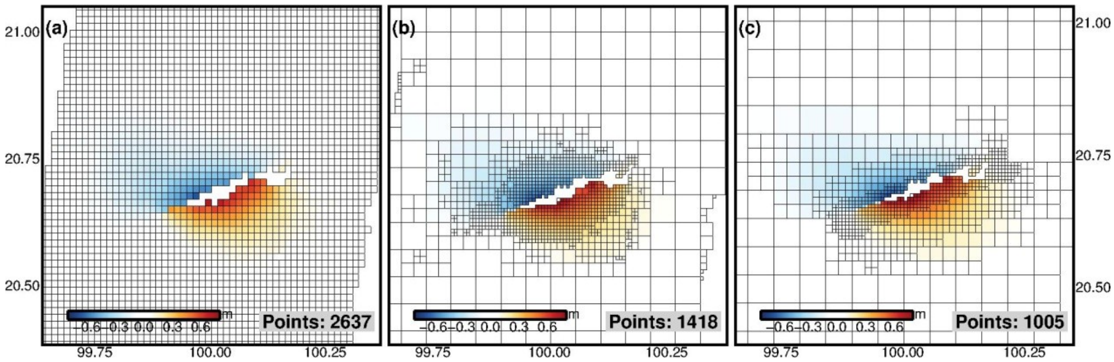

Figure 2.11 Comparison of different downsampling methods. (a) Result by the uniform downsampling method, (b) by quadtree downsampling method and (c) by data resolution based downsampling method.

2.2.3 PSOKINV

Several geodetic inversion packages have been developed, e.g. nonlinear Okinv and Slipinv (Wright et al., 1999; Funning et al., 2005b), GEODMOD in Miami University (Amelung et al., 2011) and SDM (Wang et al., 2013a). Nonlinear Okinv has been widely applied in earthquake modelling, particularly in UK NERC COMET team (e.g. 1999; Wright et al., 2001a; 2003; Parsons et al., 2006; Walters et al., 2009; 2012; Elliott et al., 2013). GEODMOD is designed for earthquake and volcano modelling by the InSAR team in Miami University. SDM is fully released by Dr. Rongjiang Wang in GFZ, which is specifically used for linear slip inversion. Here, a novel self-developed Matlab-based geodetic inversion package, PSOKINV will be introduced, which is employed to solve all linear/nonlinear problems in this thesis.

2.2.3.1 Overview of PSOKINV

PSOKINV is an acronym for the Particle Swarm Optimization and OKada Inversion Package. As its name suggests, the package was originally tailored for InSAR inversion using the MPSO nonlinear algorithm based on the elastic Okada dislocation models (Okada, 1985, 1992). The first version of PSOKINV was completed in the summer of 2009. After a few years' development, particularly during the period of my PhD study, the latest version is able to handle multiple geodetic datasets including InSAR, GPS, land and/or space-based gravity changes and field survey measurements. Combining with PSGRN/PSCMP (Wang et al., 2006b), PSOKINV can also treat a geodetic modelling in a layered Earth medium smoothly. As shown in Figure 2.12, four independent sub-packages are included in the current version of PSOKINV such as data preprocessing, nonlinear inversion, linear slip inversion and forward simulation.

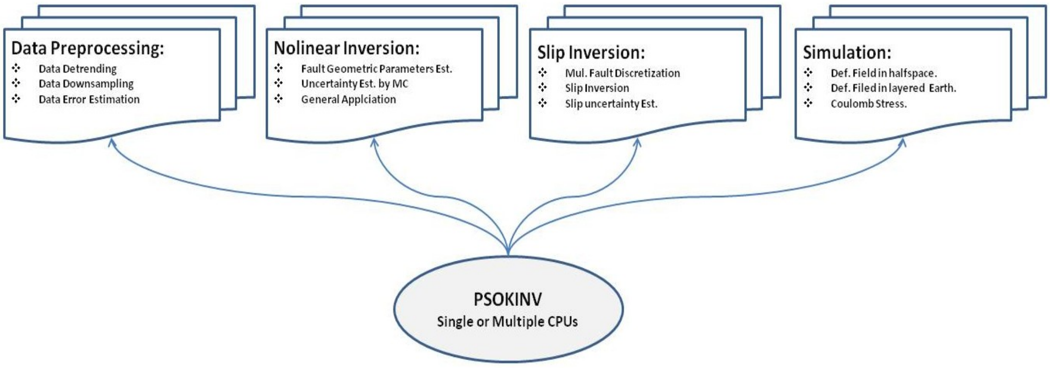

Figure 2.12 Flow chart of PSOKINV.

2.2.3.2 PSOKINV features

PSOKINV has following features which make it efficient and easy-to-use:

1) Flexible definitions of a rectangular fault. PSOKINV provides seven different fault definitions that are useful to control the relative locations between adjacent faults.
2) Optional parallel computing. Utilizing the parallel computing environment in Matlab, PSOKINV can automatically assign a computation task to different CPUs. Using Laptop or personal computer with four CPU cores, an inversion job using full computer resources can be accelerated by at least 3 times than that in a single CPU core computer.
3) Fault discretization. PSOKINV provides three strategies to divide a single fault into discrete subfaults for slip distribution inversion (Figure 2.14 (b,c,d)) including regular size sampling, depth-dependent variable size sampling and slip sensitivity analysis based fault discretization. The regular size method was widely used in previous studies (e.g. Talebian et al., 2004; Funning et al., 2005a; Biggs et al., 2007), in which each fault patch has equal size. The depth-dependent fault discretization method (DDD) was also applied in several previous studies (e.g. Simons et al., 2002; Fialko, 2004b). A damping factor that controls the sub-patch size increasing with depth is introduced to keep a high model resolution in the shallow part of a fault and also split the fault into a limited number of subfaults. The slip sensitivity analysis

based method (SSAM) is a new method first proposed in this thesis. This method is similar with a method proposed in Atzori *et al*'s study (Atzori and Antonioli, 2011), but the method in this study is fully derived from the data and the smallest patch size is not necessary on the top. Its basic principle is to allow a smaller patch size where the faults have greater abilities to explain observations, which is similar to the ideas to sample a fault based on aftershock spatial distribution (Ziv, 2012). Triangular dislocation elements are also already allowed in the current version of PSOKINV. However, forward modelling of the angular dislocation derived by Meade *et al.* (2007) is computationally expensive, thus in practice, rectangular elements are recommended by default.

4) Estimation of parameters uncertainties. Similar to the Monte Carlo method proposed in nonlinear Okinv (e.g. Wright et al., 1999; 2003; Biggs et al., 2006; Parsons et al., 2006), the uncertainties in fault parameters and slip distributions can be estimated in terms of the observation errors.
5) Modular programming. Over 400 m-scripts are developed in PSOKINV, which are also helpful for other independent applications, e.g. Coulomb stress calculation, seismic statistics, regression analysis and geographic applications. For examples, a plane equation in 3D with three control points can be estimated using only one m-script.
6) Being compatible with other public packages. PSOKINV provides independent utilities to implement model format conversion for packages, e.g. Coulomb3.1, PSGRN/PSCMP and OKSAR.

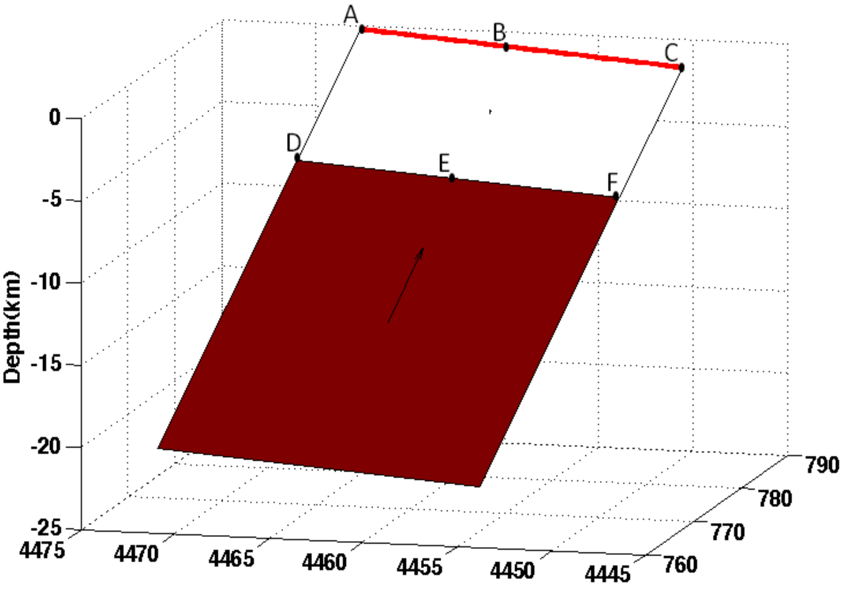

Figure 2.13 An example of a single fault plane with different reference points. Six different definitions for the same fault are given. A, top-left corner on the surface. B, top-middle on the surface. C, top-right corner on the surface. D, E and F are as for A-C, but define the top boundary of real fault plane (red rectangle). Arrow shows the slip vector, and red thick line shows the fault trace, the line of intersection between the fault plane and the Earth's surface. E is used in the inversion by default.

7) Quick maps using the genetic mapping tools (GMT). An additional package was developed during this thesis, which can plot figures using GMT. In the subpackage, Matlab is used to

organize and analyze data, and automatically generate GMT scripts for a high resolution PS. Some scripts are also available to generate KML files to publish slip models in Google Earth.

2.2.3.3 Validation: a checkerboard test

To validate the efficiency of PSOKINV and compare the effects of different fault discretization methods, a checkerboard test was carried out using 1,005 LOS observations with the same SAR viewing geometric parameters as Figure 2.11 (c). The fault geometric parameters for theoretical simulation were inherited from the 2011 M_W 6.8 Burma earthquake by Feng *et al*. (2013). The three fault discretization methods were all applied to retrieve slip models. Their resultant optimal slip models are shown in Figure 2.14, which can explain the observations equally well with the RMSs of 1.02×10^{-4}, 1.1×10^{-4} and 1.02×10^{-4} m, respectively. Due to the roles of slip smoothing and different patch sizes used in the fault discretization, the determined slip models are not completely identical to the input model (Figure 2.14 (a)). However, the two major slip patterns have all been retrieved in the three slip models. Figure 2.15 shows that the stress drop calculated from the SSAM slip model (Figure 2.14 (d)) trends to be uniform, whilst the stress drop resulting from the regular size (Figure 2.14 (b)) and DDD slip models (Figure 2.14 (c)) are highly variable.

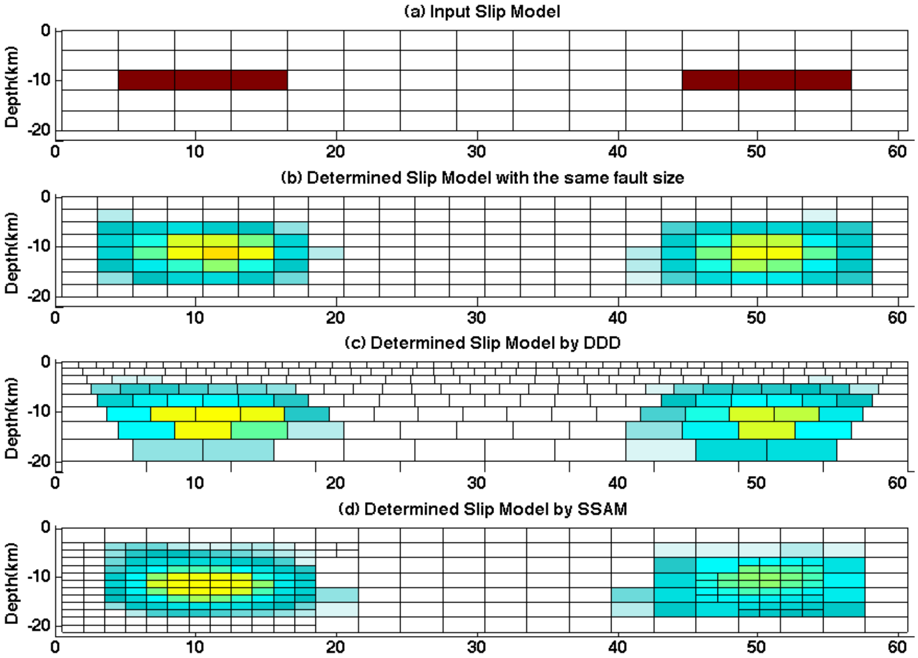

Figure 2.14 Slip inversion validation with three discretized fault models by a checkerboard test.

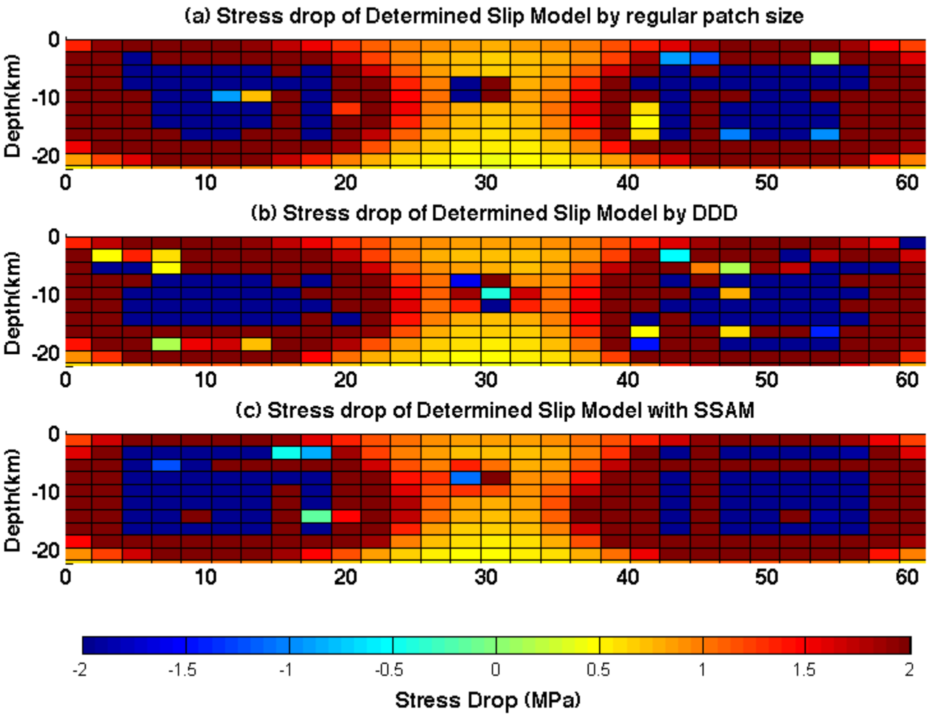

Figure 2.15 Shear stress drop corresponding to the three resolved slip models in Figure 2.14.

2.3 Summary

This chapter provided a concise introduction to SAR and InSAR techniques followed by brief comparisons between four freely InSAR packages, DORIS, GMTSAT, ISCE and ROI_PAC. The mathematical basis of geodetic modelling for fault geometry parameters and slip distributions was also summarized. The principle of a novel hybrid non-linear global optimization method, MPSO that was developed by the thesis author, was outlined briefly. All nonlinear problems in this thesis are solved using this method. A new geodetic inversion package, PSOKINV was also introduced, and will be employed to determine fault parameters and distributed slip models discussed in later chapters.

Chapter 3

InSAR measurements of the 2003-2009 Qinghai earthquake sequence

In this chapter, a number of ASAR SAR images are collected to revisit co- and post-seismic surface responses to the 2003-2009 earthquake sequence that occurred on the northern margin of the Qaidam basin including three M_W 6.3 thrust-slip earthquakes. Fault geometric parameters and coseismic slip models of the three mainshocks are determined through inverting InSAR coseismic observations. The afterslip history following the 2009 mainshock is investigated using InSAR postseismic displacement time series. A time-dependent inversion strategy is conducted for retrieving the afterslip history. The coseismic and cumulative afterslip models associated with the 2009 mainshock are then used to partition frictional properties on its seismic fault. The performance of the rate-state friction law in the 2009 M_W 6.3 earthquake is addressed at the end.

3.1 Introduction

A sequence of earthquakes from 2003 to 2009 occurred on the northern margin of the Qaidam basin, Tibet Plateau including three $M \sim 6.3$ earthquakes (the 2003 Delingha, the 2008 and 2009 two Haixi events) and their aftershocks. As listed in Table 3.1, the sequence started with a M_W 6.3 earthquake on 17th April 2003 with purely thrust slip. On 10th November 2008, another M_W 6.3 earthquake took place, located ~40 km west of the epicentre of the 2003 mainshock, at a depth of 27 km (GCMT). Only 11 months after the 2008 event, the third M_W 6.3 earthquake occurred at nearly the same location as the 2008 event, but at a shallow depth of 12 km (GCMT). Because no serious damage was caused during the events, the sequence did not draw people's much attention. So far, only a few studies have been undertaken, looking at the fault locations and coseismic rupture patterns utilizing seismic, geologic and geodetic means (Elliott et al., 2011; Sun et al., 2012; Wen et al., 2012b; Chen et al., 2013).

Through seismic moment inversion and regional stress analysis, Sun *et al*. (2012) suggested that the 2003 M_W 6.3 Delingha mainshock occurred on a south-dipping thrust fault. Zha *et al.* (2013) reached to a similar conclusion using seismic inversion. Elliott *et al*. (2011) revealed that the 2008 and 2009 M_W 6.3 earthquakes were nearly coplanar on the south-dipping Dachaidan-Zongwulongshan (DCDZWLS) fault using coseismic InSAR measurements, whilst Chen *et al.* (2013) suggested that the 2008 event might occur on the NNE-dipping Xitieshan (XTS) fault with left-lateral thrust slip through the analysis of relocated aftershocks and field data.

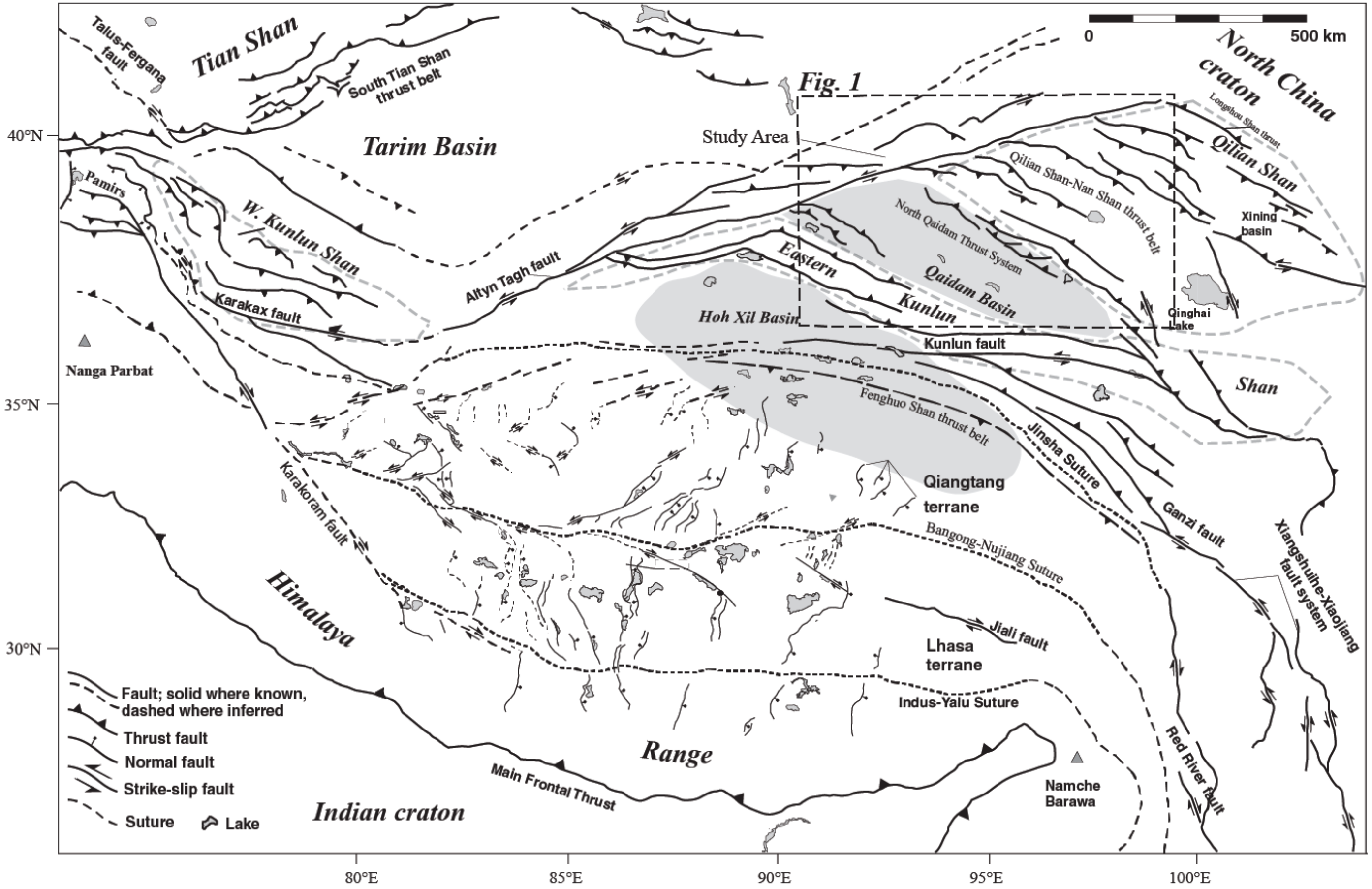

Figure 3.1 Tectonic features around the Qaidam basin, modified from Yin *et al*. (2008b). Dashed rectangle denotes the spatial coverage of Figure 3.2.

From a tectonic point of view, there has long been a debate upon the local thrust fault structure on the northern margin of the Qaidam basin. Some geologists inferred that south-dipping thrust faults should principally control the evolution of the basin (Métivier et al., 1998; Wang et al., 2012f), whilst others argued that the thrust belt should be predominantly north-dipping (Wang et al., 2006a; Yin et al., 2008a). Therefore, to fix the ambiguity of the fault geometric parameters of these three large earthquakes shall improve our understanding of the fault structure in the region. In order to address these issues, this chapter is conducted as follow. Firstly, a number of Envisat SAR images in both Stripmap and ScanSAR modes are processed to map the surface motions following the sequence. Secondly, the fault geometric parameters and slip distributions of the 2009 mainshock are determined from InSAR observations followed by the determination of its afterslip model. Finally, the patterns of the fault frictional properties inferred from the co- and post-seismic slip models of the 2009 mainshock are presented. Although surface changes associated with several aftershocks after the 2003 mainshock (Figure 3.2) have been detected, data analysis for the aftershocks is not implemented in this chapter. These aftershocks are all far away from the 2009 event, without analysis, which is believed to have little impacts on the analysis of the frictional properties of the 2009 mainshock fault.

3.2 Tectonic backgrounds

As the largest topographic depression in the Tibetan Plateau, the Cenozoic Qaidam basin is bounded by the Altyn Tagh fault in the northwest, the Qilianshan-Nanshan thrust belt (see Figure 3.1) in the northeast and the Eastern Kunlun thrust belt in the south (Chen et al., 1999; Xia et al., 2001; Wang et al., 2006a; Zhou et al., 2006; 2008a; Yin et al., 2008b). In plan view, the entire basin presents a triangular geometric shape which may result from northeast-southwest compression driven by continental collision (Molnar and Tapponnier, 1975). The formation and evolution of the Qaidam basin have widely been investigated on the significant implications for the evolution of the Tibetan Plateau, the post-collisional behaviour and oil exploration.

The Qaidam basin sits at the northern margin of the Tibetan Plateau with an average elevation of ~3,000 m above sea level. As one of the major tectonic elements in the Tibetan Plateau, present large scale crustal deformation rates have been detected by GPS measurements across the basin (Wang et al., 2001; Gan et al., 2007). A convergence rate of ~5-7 mm yr^{-1} is revealed across the Qilianshan-Nanshan (Wang et al., 2001; Gan et al., 2007). Their observations and other GPS observations suggest that ~19% Indo-Asia continental collision is accommodated by the horizontal crustal shortening along the fold-thrust belts in the north Tibetan plateau (Dobretsov et al., 1996; Shen et al., 2001; Gan et al., 2007; Yin et al., 2008a). As the north edge of the Tibetan Plateau, the deformation history along the Altyn Tagh fault has important significance for understanding tectonic evolution of the plateau (Yin et al., 2002). A left-lateral creep at a rate of ~9 mm yr^{-1} on the Altyn Tagh fault revealed by GPS (Shen et al., 2001) suggests a predominant mechanism controlling present crustal deformation in the most north of the Tibetan Plateau. Thus, the present clockwise rotation and thrust-slip seismicities observed in the north margin of the Qaidam basin should mainly be under the control of both the Indo-Asia continental collision and large left-lateral creep on the Altyn Tagh fault (e.g. Molnar and Tapponnier, 1975, 1977; Armijo et al., 1989; Shen et al., 2001; Wang et al., 2006a; Liu-Zeng et al., 2008). In contrast to the southern Tibet plateau, rare large destructive earthquakes were recorded in the Qaidam basin, implying that the mechanical strength of Qaidam lithosphere is relatively strong (Braitenberg et al., 2003; Yin et al., 2008b). As shown in Figure 3.2, besides the 2003-2009 Qinghai earthquake sequence, only ~850 earthquakes with magnitudes from 1 to 5.5 have been recorded by China Seismic network (CSN) since 1977. About 90% of these earthquakes were located at depths of >16 km. Since investigations have rarely been carried out in this region, the present slip rates and paleoseismic history along the DCDZWLS fault still remain unclear. The three M_W 6.3 earthquakes can provide an important opportunity to better understand the local fault structure and shear strength of the DCDZWLS fault.

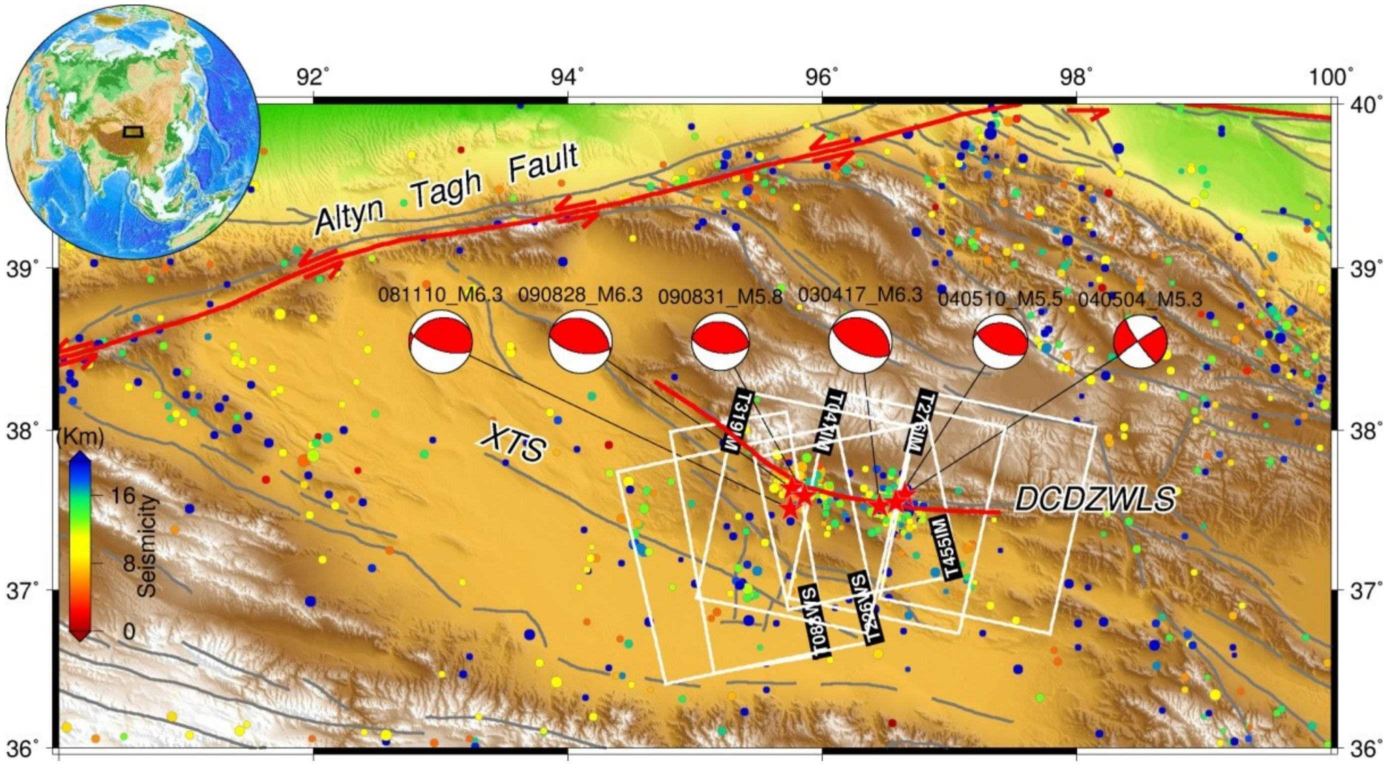

Figure 3.2 Tectonic setting and SAR data spatial coverage overlaid on topographic relief**.** Grey lines indicate the active faults in this region (Deng et al., 2003), whilst colour dots represent seismicities with their depth information during the period from 1970 to 2014 (CSN). White solid rectangles indicate the spatial coverage of Envisat ASAR in Stripmap mode (tracks 047, 276, 319 and 455) and ScanSAR mode (tracks 083 and 226). XTS stands for Xitieshan fault and DCDZWLS for Dachaidan-Zongwulongshan fault. The beachballs are the three M_W 6.3 mainshocks and their large aftershocks from GCMT. The topographic relief was made using the 90-m-spacing DEM data from the shuttle radar topography mission, SRTM (Farr et al., 2007)**.**

3.3 InSAR deformation time series

In this section, multiple tracks of Envisat C-band SAR data are used for measuring the surface responses to the 2003-2009 Qinghai earthquake sequence. An improved network method is proposed to reduce the impacts of orbit ramps on SAR interferograms. The deformation patterns associated with the three mainshocks are explored. The postseismic deformation time series following the 2009 mainshock is revealed by SBAS-InSAR.

3.3.1 SAR data

Figure 3.2 shows six tracks of Envisat ASAR images covering the Qinghai earthquake sequence region including two ScanSAR tracks and four Stripmap tracks. Only one SAR image from track 276 was acquired prior to the 2003 Delingha earthquake, which is necessary for mapping coseismic surface motion caused by the mainshock. Each dashed line in Figure 3.3, represents an interferometric pair with a perpendicular baseline less than 350 m and a temporal interval shorter than three years. Those with large perpendicular baselines (>350 m) can rarely generate valid observations in the epicentral areas due to local rugged terrain, whilst the interferometric coherence of the pairs having over three years temporal intervals in this region is also dramatically degraded due to ground objects changing over time. Therefore, the pairs shown in Figure 3.3 were selected for monitoring surface displacements caused by the earthquake sequence. More detailed information about SAR data is listed in Table 3.2.

Table 3.1 SAR images used in this study.

Orbit	Mode	Sat. Heading	Acquisitions	Interferograms	Events*
319	Stripmap	Descending	24	144	b,c,d,e
276	Stripmap	Descending	24	120	a,b,c
455	Stripmap	Ascending	9	13	d,e
047	Stripmap	Descending	22	69	d,e
083	ScanSAR	Ascending	12	34	d,e
226	ScanSAR	Ascending	8	15	d

Note: * a- 2003 M_W 6.3 Delingha earthquake; b- 2004 aftershock; c- 2005 aftershock; d- 2008 M_W 6.3 Haixi earthquake and e- 2009 M_W 6.3 Haixi earthquake. The spatial locations of these events can be found in Figure 3.2.

3.3.2 Interferogram formation

All interferometric pairs shown in Figure 3.3 were processed using the ROI_PAC(v3.01) software (Rosen et al., 2004b) with the two-pass InSAR processing strategy (Chapter 2). The SRTM 90-m DEM data (Farr et al., 2007) were employed to remove topographic phase in interferograms. To save computational resources, only the fifth sub-swath of ScanSAR track 083 and the first sub-swath of ScanSAR track 226 were processed since they fully covere the epicentral areas of the 2008 and 2009 mainshocks. In total, 395 interferograms from six tracks were generated as listed in Table 3.2. Most of the interferograms do not include detectable deformation signals related to the earthquake sequence. However, they were all kept for orbital ramp corrections based on an improved network strategy that will be introduced later.

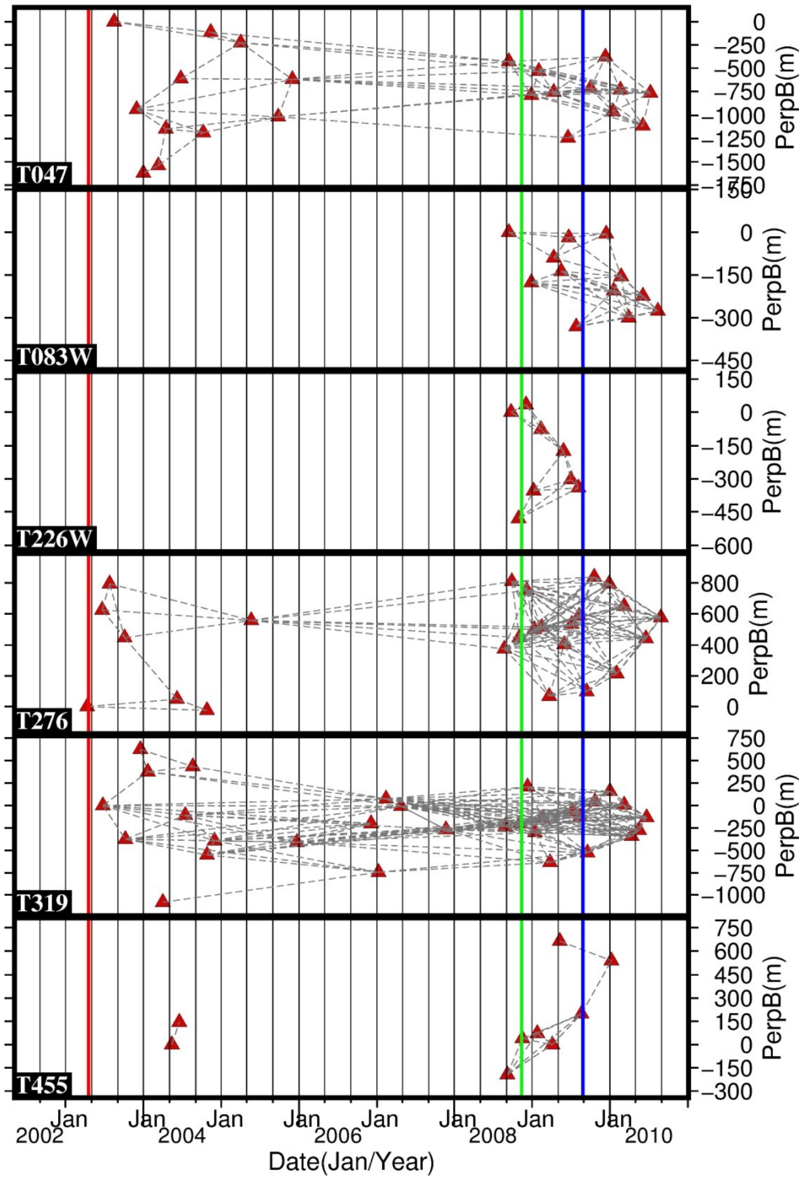

Figure 3.3 Baseline plot for the interferometric pairs of all ASAR tracks**.** Dark red triangles represent SAR acquisitions, and dashed lines between red triangles indicate the interferograms used in this chapter. Three colour lines mark the three M_W 6.3 earthquake occurrences: red for the 2003 Delingha event, green for the 2008 Haixi event and blue for the 2009 Haixi event. PerpB is the perpendicular baseline between master and slave SAR images.

Six interferograms covering coseismic deformation of the three M_W 6.3 mainshocks are shown in Figure 3.4. Interferograms from track 276 provides unique coseismic deformation measurements of the 2003 M_W 6.3 earthquake (Figure 3.4 (c)), but only half of the coseismic deformation area with a maximum LOS displacement of +0.21 m is covered. Interferograms from tracks 319, 455, 047, 083 and 226 fully record coseismic surface changes caused by the 2008 M_W 6.3 event. A maximum LOS range change of +0.08 m is observed in the descending interferogram of track 319, and similar maximum LOS range changes (0.09 m) are observed in both ascending tracks 047 and 455. Since the similar LOS displacement patterns are shown in both the descending and ascending interferograms, vertical movements should be predominant in the coseismic deformation filed of the mainshock. A similar situation is observed for the 2009 mainshock. However, the maximum LOS surface changes for the 2009 mainshock from tracks 047 (ascending) and 319 (descending) reach up to +0.3 and +0.29 m, respectively. Three separate surface deformation centres can also be recognized (Figure 3.4 (d)), suggesting that significant aftershocks following the 2009 event may also mainly contribute to the coseismic motion.

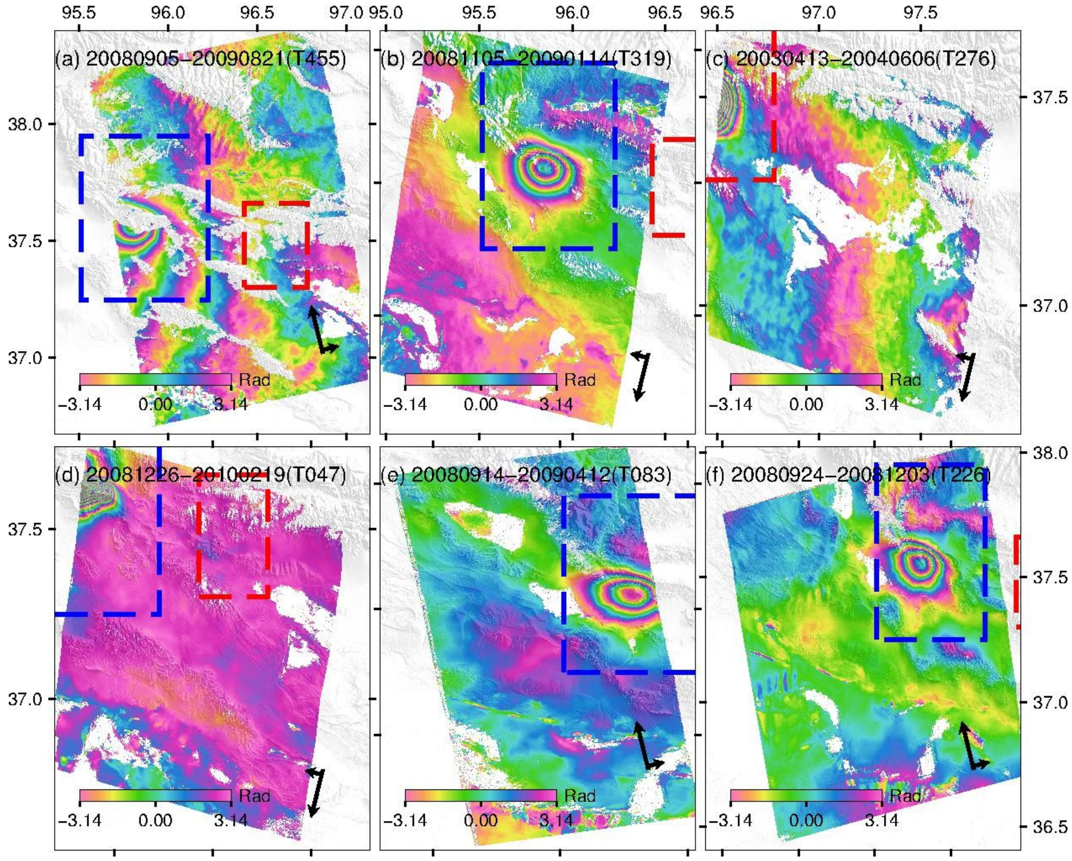

Figure 3.4 Coseismic interferograms from six Envisat tracks associated with the three 2003-2009 M_W 6.3 mainshocks. The temporal information of the interferometric pairs is noted inside the subfigures by "<yyyymmdd>-<yyyymmdd> (<Track Number>)". Interferograms are re-wrapped into [$-\pi$, π]. Blue rectangles denote the epicentral areas of the 2008 and 2009 mainshocks, whilst red ones imply for that of the 2003 event.

Significant postseismic LOS motion following the 2009 event has been identified in several postseismic interferograms of track 319 (Figure 3.6 (g)). The effects of atmospheric perturbation also appear considerable in most of these interferograms. It is difficult to precisely extract small surface motions caused by the postseismic processes of the 2009 event from these interferograms contaminated by atmospheric delays. A small-baseline InSAR strategy will then be applied to separate the postseismic deformation history.

3.3.3 An improved network method for orbit correction

Orbit ramps are common in InSAR measurements, which usually show long-wavelength signals

(Zebker et al., 1994; Hanssen, 2001). Many efforts have been made to reduce the effects of orbital errors in the topography and deformation mapping (Biggs et al., 2007; Bahr and Hanssen, 2012; Fattahi and Amelung, 2014; Wang and Jonsson, 2014). A correction method was recently developed in the frequency domain to isolate long-wavelength signals from a single interferogram (Shirzaei and Walter, 2011). However, the most widely used method is to remove a best-fit plane or a curved surface from an individual interferogram (Pritchard et al., 2002; Wright et al., 2004a). A best-fit plane can be written as

$$\boldsymbol{ax+by+c=d} \tag{3.1}$$

where a, b and c are the parameters that need be estimated, $[x, y]$ are the pixel coordinates and d is the InSAR observation. Generally, millions of pixels in an interferogram are available to estimate the three parameters, which makes Equation (3.1) over-determined. However, as noted by Biggs *et al.* (2007), due to interseismic tectonic signals and atmospheric delays that can contribute to long-wavelength signals in InSAR measurements, this method can easily lead to over- or under-estimation of orbital errors in a single interferogram. Usually, a single image acquisition can be used to generate several interferograms. Therefore, orbital errors in two interferograms sharing one image should be correlated. A network correction strategy based on this correlation was proposed by Biggs *et al.* (2007) to split the orbit errors in an individual interferogram into master and slave components. The relationship between InSAR measurements with orbital errors for each SAR acquisition was written as

$$\boldsymbol{d_{mnp}=a_m x-a_n x+b_m y-b_n y+c_{mn}} \tag{3.2}$$

where m and n stand for indexes of images used in the interferograms, and $\boldsymbol{c_{mn}}$ is the phase shift for each interferogram. In Equation (3.2), five independent parameters need to be solved for one interferogram. For N SAR images, $N(N$-1)/2 interferograms can be formed. Based on Equation (3.2), the rank of the design matrix is 2(N-1)+ N(N-1)/2, which is smaller than the number of unsolved parameters, 2N+N(N-1)/2. Therefore, the problem of Equation (3.2) is underdetermined. A truncated singular value decomposition (SVD) method was suggested to find a minimum norm solution by Biggs *et al.* (2007). In this thesis, a full-rank design matrix is proposed based on Equation (3.2) as

$$\boldsymbol{d_{mnp}-d_f=a_m(x-x_f)-a_n(x-x_f)+b_m(y-y_f)-b_n(y-y_f)+c_{mn}-c_{mn(f)}} \tag{3.3}$$

where f stands for the reference point. Note that reference points for different interferograms can be different. But it is preferential to select those points without atmospheric effects and tectonic motions. The phase shift for any points in an interferogram should be constant. Then Equation (3.3) can directly be simplified as

$$\boldsymbol{d_{mnp}-d_f=a_m(x-x_f)-a_n(x-x_f)+b_m(y-y_f)-b_n(y-y_f)} \tag{3.4}$$

In Equation (3.4) the number of parameters drops to **2*N*** only. However, the rank of the design matrix is 2(*N*-1), in which condition numbers are still insufficient. To further solve this issue, a phase closure (Biggs et al., 2007) is used to provide additional constraints. With three acquisitions (m,n,q), three interferograms $(d_{mnp}, d_{mqp}, d_{qnp})$ can be generated at most. Then, a closure phase at any pixel (p) from these three interferograms can be described as

$$\boldsymbol{d_{mnp} - d_{mqp} + d_{qnp} = \epsilon} \tag{3.5}$$

If a common reference point is selected in all three interferograms for Equation (3.5), the left term of Equation (3.5) should be zero, and Equation (3.5) can be rewritten as

$$\boldsymbol{(d_{mnp} - d_{mqp} + d_{qnp}) - (d^f_{mnp} - d^f_{mqp} + d^f_{qnp}) = 0} \tag{3.6}$$

Based on Equation (3.6), a two-step strategy can be considered to reduce the effects of orbital errors. Firstly, the orbital-error related phase is split from original interferograms. Effects of unwrapping errors or other abrupt surface changes included in specific interferograms can be avoided, which also can be used for repairing unwrapping errors in other InSAR applications. Secondly, retrieved phase can be utilized for estimation of orbital errors based Equations (3.4) and (3.5). SVD is also required. If orbital errors in one acquisition are assumed zero, the design matrix can then be fully determined. In this case, simple most of linear-square algorithms can be efficient to solve this problem. With this strategy, the coseismic fringes are not necessary to be masked out before the estimation.

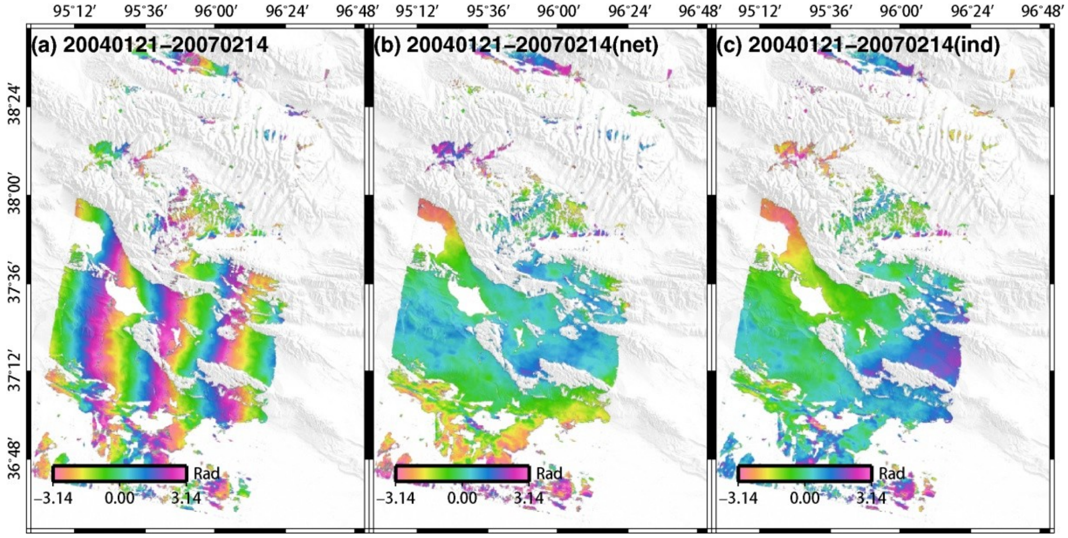

Figure 3.5 Comparison of orbital corrected interferograms. (a) The original interferogram of 20040121-20070214; (b) the corrected interferogram by the improved network method and (c) the corrected one using the traditional method.

To validate the improved network approach, the interferogram of 21 January 2004 vs 14 February 2007 from track 319 was used for comparison (Figure 3.5). A resultant interferogram corrected using an order-two polynomial is shown in Figure 3.5 (c), whilst another resultant interferogram utilizing all interferograms from track 319 based on the improved network method is presented in

Figure 3.5(b). Significant differences between these two corrected interferograms can be identified. The long-wavelength signals observed in the centre of Figure 3.5(c) disappear in Figure 3.5(b).

The phase closure (Biggs et al., 2007) provides an alternative way to validate the improved network method. Figure 3.6 illustrates the resultant interferograms corrected individually using a polynomial of order two. According to the phase closure strategy, the synthetic interferogram generated from three correlated interferograms (Figure 3.6 (a, b and c)) should be constant, but clear phase gradients can be observed in Figure 3.6 (d). A similar situation was also found for another three corrected interferograms (Figure 3.6 (e, f and g). So, a best-fit method to correct orbit errors individually can easily over- or under-estimate orbital ramps due to other long-wavelength signals, e.g. atmospheric delays and/or tectonic motion. For resultant interferograms corrected by the improved network method from the same two phase loops used in Figure 3.6, their synthetic interferograms (Figure 3.7 (d and h)) remain constant only and no significant phase gradient can be observed. To further examine the performance of the new correction method, interferograms from track 455 with (Table 3.2) was also corrected using the improved network approach, in which only 13 interferograms in total are available to estimate orbital errors for each SAR image. No significant phase gradient can be seen in resultant interferograms (Figure 3.8 (d and h)) .

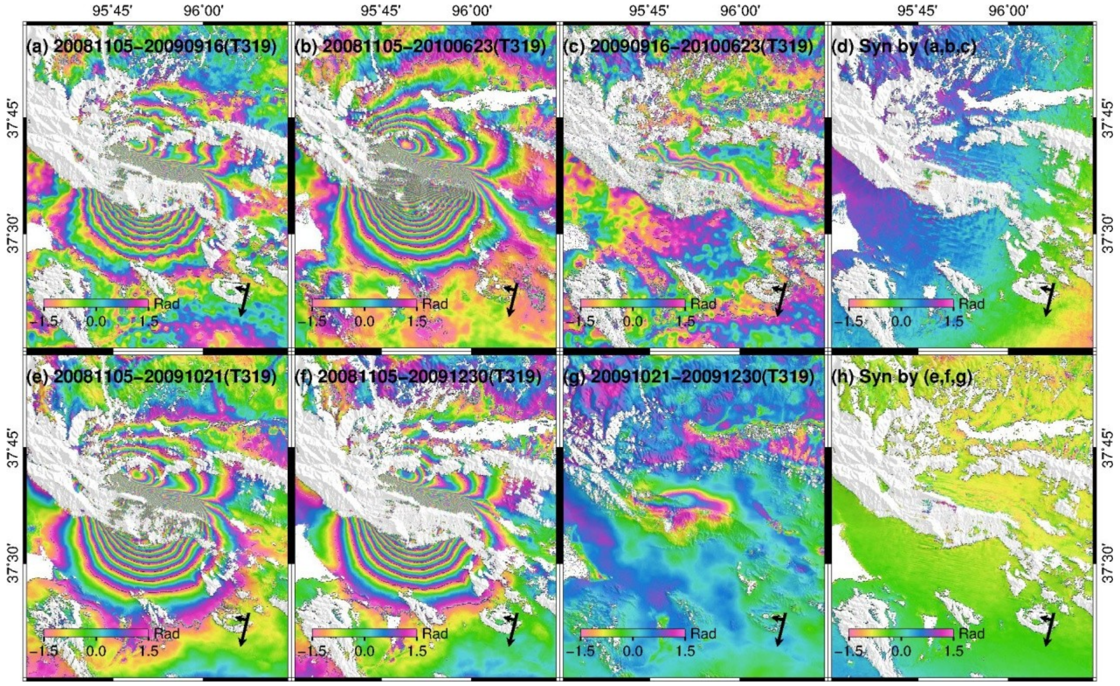

Figure 3.6 Phase closure loops for checking orbit correction**.** The interferograms have been rewrapped by a phase cycle ranging from -1.5 to 1.5 rad. The spatial coverage of the interferograms is the same as shown by the blue rectangles in Figure 3.4. (a-c) are three orbit-corrected interferograms using the traditional best-fit correction method, (d) is the synthetic one that was computed by (a)-(b)+(c). (e-h) are similar to the (a-d), but for another three SAR images.

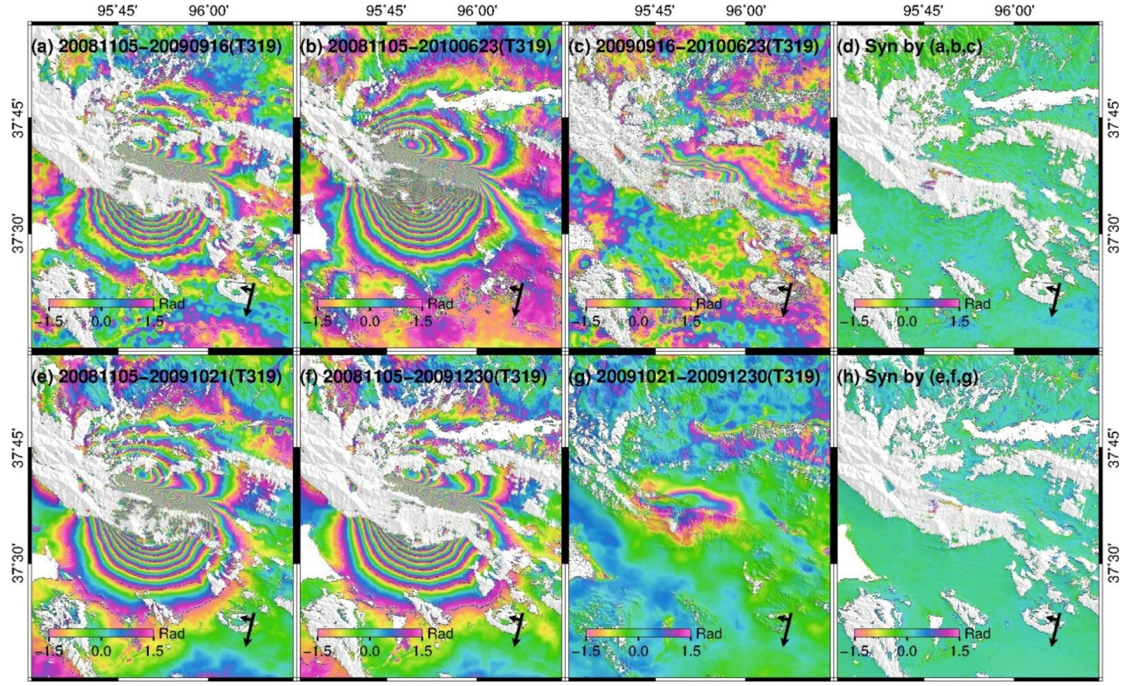

Figure 3.7 Similar to Figure 3.6, but interferograms were corrected using the improved network method. Noting that the synthetic interferograms (d) and (h) are constant only after corrected using the new network orbit correction method.

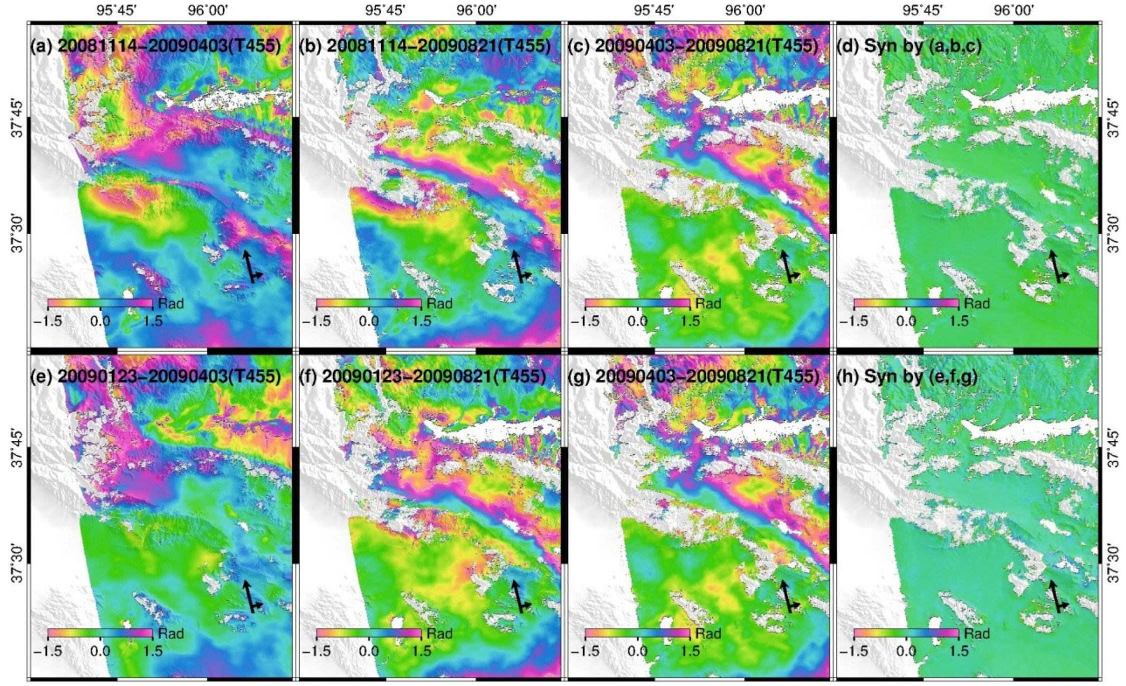

Figure 3.8 Examples of phase closure for track 455 after orbit correction using the new network strategy.

In this chapter, interferograms of tracks 319 and 455 and 047 with enough connections between interferometric pairs were corrected for orbit errors using this improved network approach prior to further time series analysis. The rest tracks used in this chapter were still corrected individually.

3.3.4 Coseismic InSAR displacements associated with the three M_W 6.3 earthquakes

As shown in Figure 3.8, interferograms from track 455 include significant artefacts from topography correlated atmospheric delays. Actually, atmospheric effects seem to be common in this region. This is partly why the traditional orbit correction does not work well in this case as shown for two interferograms from track 319 in Figure 3.6. As mentioned in Chapter 2, stacking InSAR is one of the effective techniques to reduce the atmospheric effects by averaging multiple interferograms. This technique was employed in this chapter to extract surface LOS changes caused by the 2008 and 2009 mainshocks. For the 2003 event, only two coseismic interferograms were generated with a common master image acquired on 13 April 2003. The interferogram of 20030413-20040606 was selected to determine fault parameters and slip distribution of the 2003 mainshock.

26 coseismic interferograms from track 319 associated with the 2008 mainshock are available, which are collected to build a stacked interferogram (Figure 3.9 (c)). All these coseismic interferograms have relatively good coherence, even in the epicentral area. In processing, only coherent pixels from the interferograms were stacked. For the ith pixel, the stacked phase is calculated by

$$\boldsymbol{\varphi_i} = {\sum_{j=1}^{k}(\boldsymbol{\varphi_i^j} - \boldsymbol{\varphi_r^j})}\Big/{\boldsymbol{k}} \tag{3.7}$$

where k is the number of the interferograms, and φ_r^j is the reference phase in the jth interferogram. A reference point (r) was selected in the far-field which is free from the deformation. Ideally, the point r should also be free from atmospheric delays.

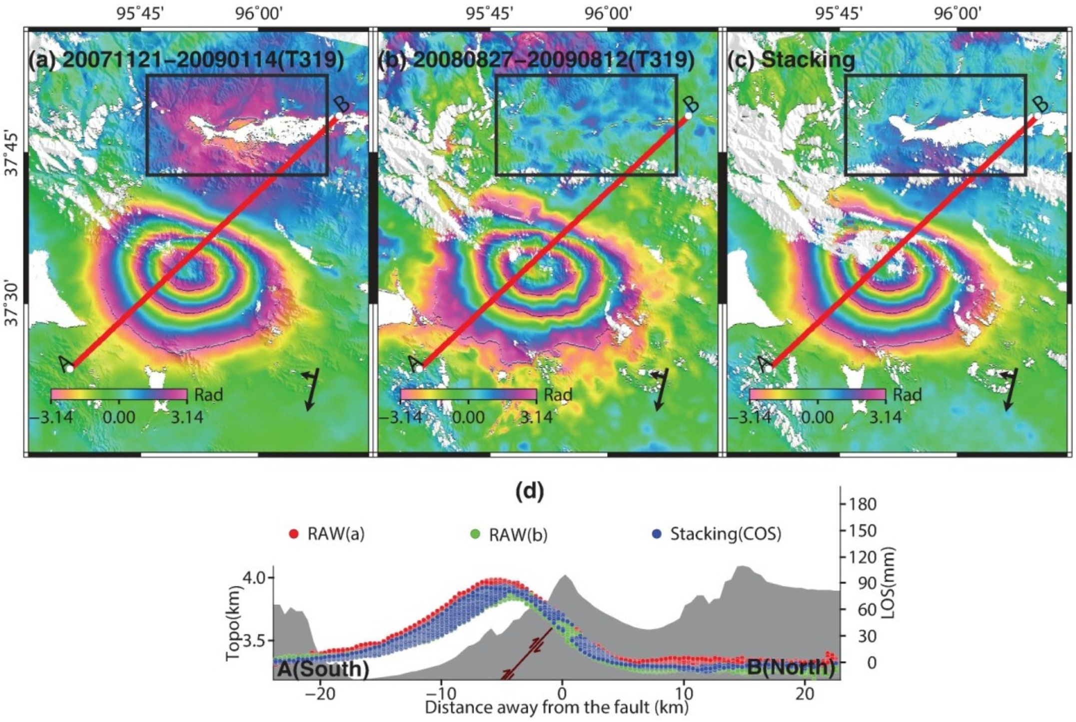

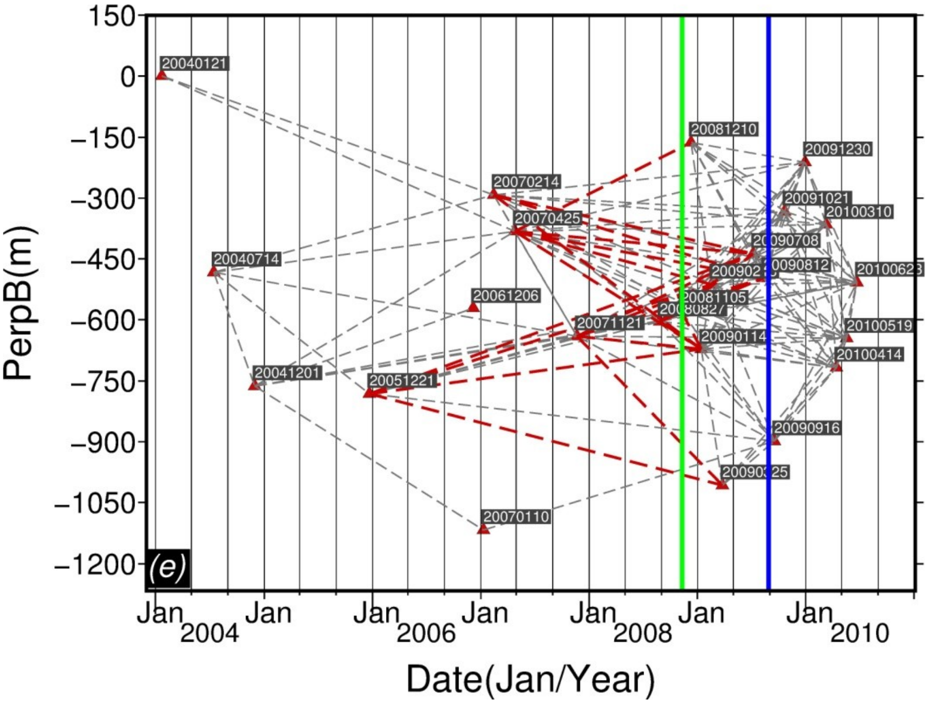

Figure 3.9 Comparison of original coseismic interferograms and the stacked one with profile analysis of coseismic LOS changes associated with the 2008 M_W 6.3 Haixi earthquake. Note that the stacked interferogram (c) is made using 24 original coseismic interferograms. (a) and (b) are two original interferograms both spanning the earthquake occurrence. (d) LOS displacements along Profile A-B are extracted from interferograms within a 1-km-wide narrow swath along line A-B. Brown line shows the location of the fault in depth, which is not scaled. (e) The baseline information of the pairs used in the stacking. Dashed red lines represents the pairs used in (a).

Figure 3.9 shows the comparison between original coseismic interferograms and the stacked interferogram. Both original coseismic interferograms (Figure 3.9 (a and b)) keep good coherence, but large phase variations can be observed between themselves in the denoted region with the solid rectangle (Figure 3.9). The stacked interferogram (Figure 3.9(c)) presents smoother phases than the original two, which has a maximum LOS subsidence of -9 mm in the rectangle region. Using the same method, another 11 interferograms of track 319 from Nov 2008 to July 2009 were stacked to identify postseismic surface motion following the 2008 mainshock (Figure 3.10 (c)). No detectable postseismic signals can be found (Figure 3.10). Therefore, effects of postseismic deformation after the 2008 mainshock in its coseismic stacked interferogram from track 319 can be ignored.

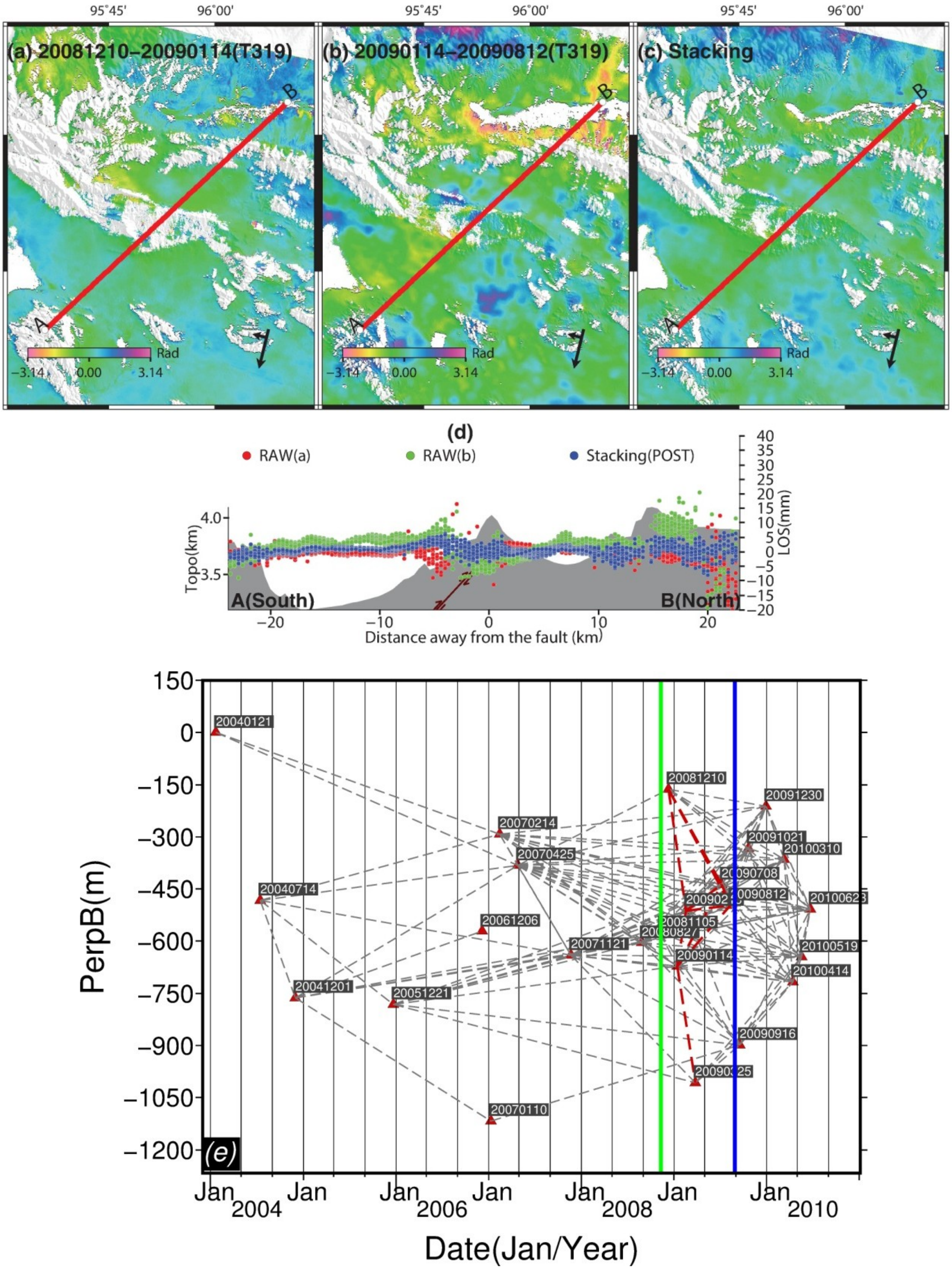

Figure 3.10 As Figure 3.9, but for postseismic observations following the 2008 M_W 6.3 mainshock.

The same approach was employed for mapping coseismic surface changes associated with the 2009 M_W 6.3 mainshock. To reduce the effects of incoherent pixels in some interferograms, seven interferograms from track 319 covering the epicentral area of the 2009 mainshock were selected for generating the stacked interferogram. As shown in Figure 3.11, three separated deformation centres can be found with a maximum LOS change of 0.42 m. LOS changes along Profile A-B from the original coseismic (Figure 3.11 (a and b)) and stacked interferograms (Figure 3.11 (c)) show good agreement (Figure 3.11 (d)), suggesting that the contribution from postseismic deformation after the 2009 mainshock to its coseismic LOS measurements is not significant. Topography-correlated signals have been suppressed in the stacked interferogram (Figure 3.11 (c)), which can be observed in the original interferograms (Figure 3.11 (a and b)). Therefore, the stacked interferogram (Figure 3.11(c)) should be optimal to use for determination of the slip distribution of the 2009 mainshock.

3.3.5 Deformation time series following the 2009 M_W 6.3 mainshock

21 postseismic interferograms from track 319 were generated using ROI_PAC(v3.01) from seven SAR images acquired after the 2009 M_W 6.3 mainshock from 16 September 2009 to 23 June 2010. 17 interferograms were finally selected after rejecting four interferograms due to loss of coherence in the epicentral area (Figure 3.12). The all remained interferograms were checked to exclude phase unwrapping errors using a phase closure analysis (Wang et al., 2012a). Pixels with absolute phases > 2π in synthetic interferograms, were removed. More details on the SBAS-InSAR technique used in this chapter can be found in Appendix 1.1. A comparison of resultant displacement time series derived between different deformation models used in the inversion are presented in Figure A.1.

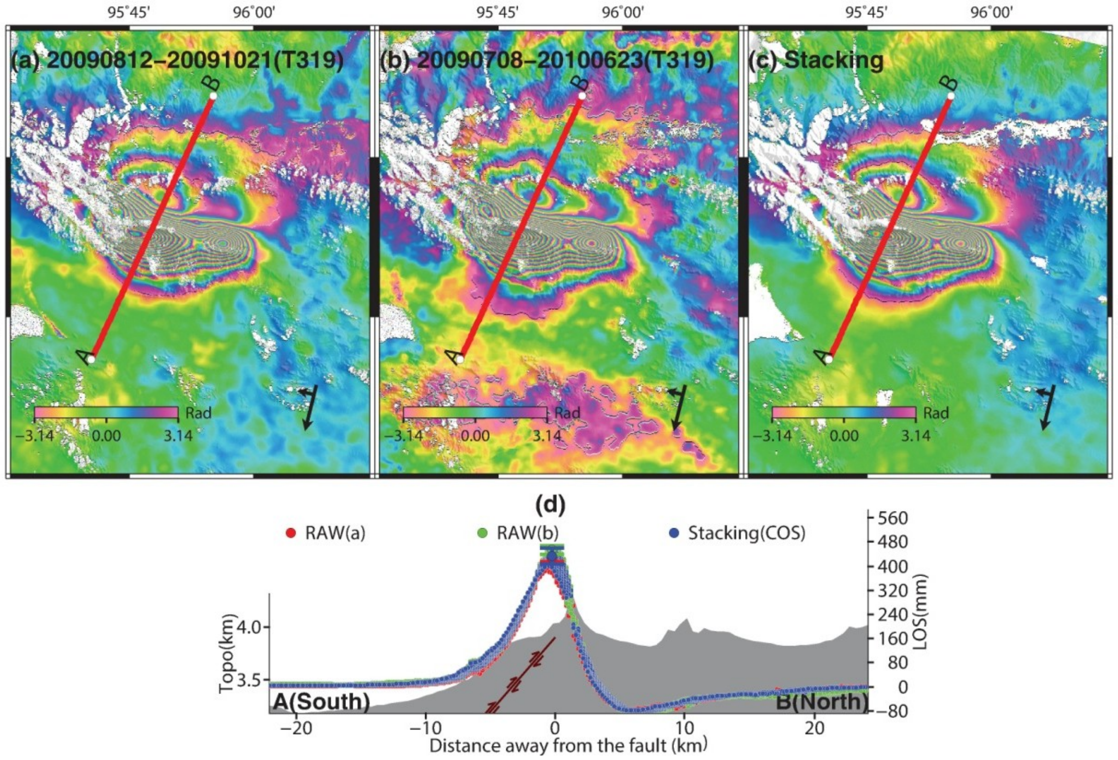

(Figure 3.11)

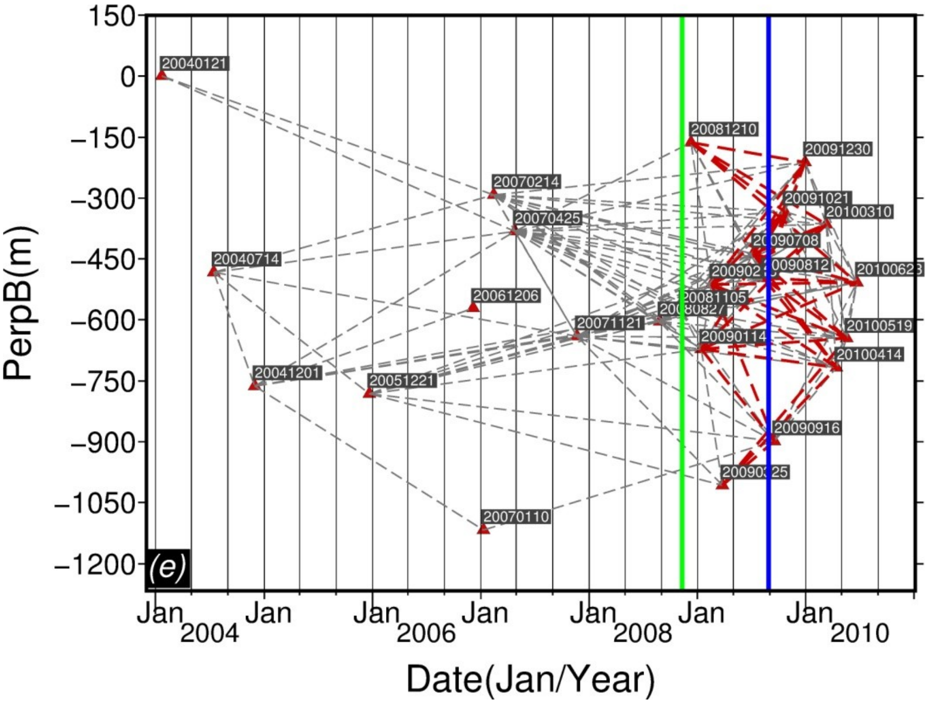

Figure 3.11 As Figure 3.9, but for coseismic LOS surface motions caused by the 2009 M_W 6.3 mainshock.

Postseismic surface deformation following large earthquakes usually decays logarithmically with time (e.g. Marone et al., 1991; Hsu et al., 2006; Freed, 2007; Savage and Svarc, 2009; Gonzalez-Ortega et al., 2014). Thus, a logarithm function between cumulated LOS changes and time (days), $d(t) = c\ ln(1+t/\tau)$ (*c*, a constant parameter), was employed in the SBAS-InSAR analysis to isolate APS and deformation signals from these interferograms. Decay constant τ, was determined by several trials based on far-field LOS observations. A decay time of 1.5 days was selected for retrieving the postseismic displacement time series after the 2009 mainshock.

To validate the postseismic time series results, the cumulative postseismic displacements (Figure 3.12 (a-1~7)) at each epoch relative to the first acquisition on 16 September 2009 was resolved using the SVD algorithm from the selected 17 interferograms (Berardino et al., 2002). The displacement at the first acquisition was set as zero. Three pixels (A, B and C) were chosen for examining the postseismic displacement history. At C, significant 'subsidence' (~20 mm) is observed in the resultant interferogram of 20100623 (Figure 3.13 (a-7)), whilst its cumulative LOS displacement at the acquisition of 20100623, retrieved from the SBAS method is in an order of 4 mm (Figure 3.14(c)). Since Point C is far from the deformation centre, the measured displacement perturbation in Figure 3.13 (a-1~7) should be mainly due to APS that has been fully suppressed in the final time series (Figure 3.13(c-1~7)). Derived APS component for each acquisition is presented in the second row of Figure 3.13. No significant deformation patterns can be visually seen, suggesting that the deformation model of log(time) used in this chapter is effective, and the logarithm of time may directly reflect the characteristics of the postseismic deformation trend after the 2009 mainshock. The cumulative postseismic displacements by 23 June 2010 suggest that the maximum LOS change near the reference A (Figure 3.12) is ~30 mm with respect to 16 September 2009.

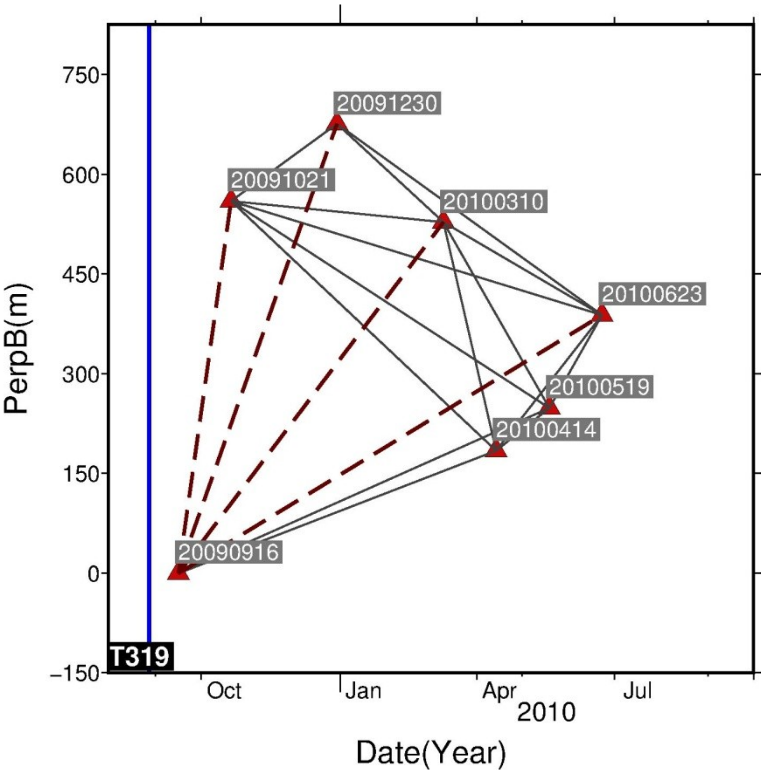

Figure 3.12 Baseline-time plot using seven ASAR images. Solid lines represent interferograms used for postseismic deformation time series analysis after the 2009 mainshock, whilst the dashed lines are the pairs with loss of coherence in the epicentral area.

Variable decay days at different observation sites have been observed in the postseismic measurements after the 2010 M_W7.2 EI-Mayor-Cucapah earthquake (Gonzalez-Ortega et al., 2014), which vary from 0.2 to 20 days to the natural logarithmic deformation model as used in this chapter. Decay days in this research area after the 2009 mainshock may also vary from pixel to pixel, but it has been difficult to assess. Although different decay time can slightly affect final deformation time series, the difference of the maximum accumulative postseismic deformation is only in an order of 5 mm (Figure 3.14). Therefore, even though a decay time of 20 days was used in the InSAR inversion, accumulative postseismic displacements after the mainshock and deformation patterns should not be changed significantly. Therefore, the conclusion on the relative slip extents between co- and post-seismic afterslip following the 2009 mainshock will not be influenced. Figure 3.14 shows the different time series by the different decay time.

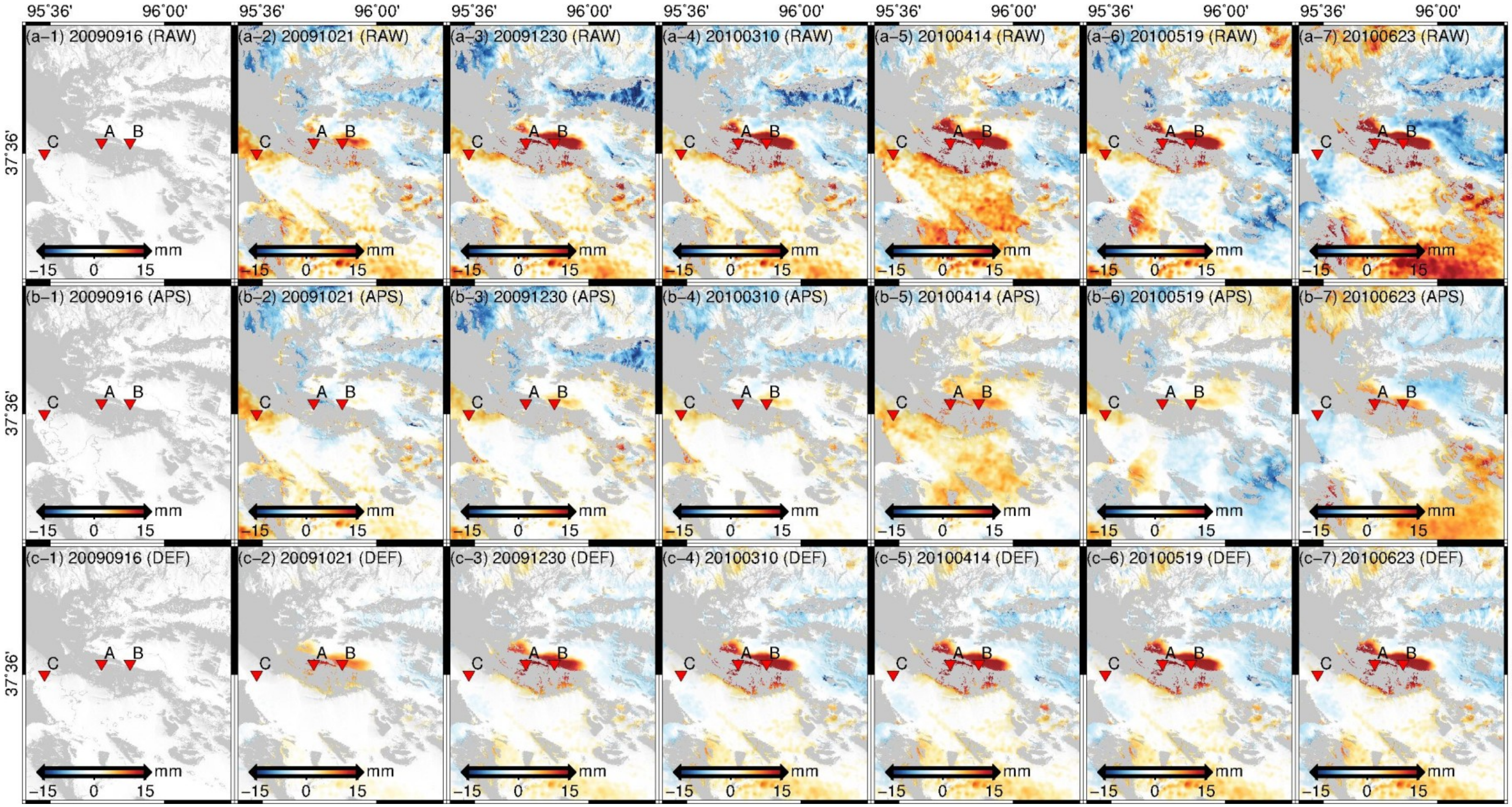

Figure 3.13 Postseismic displacement time series following the 2009 M_W 6.3 earthquake. a(1-7) are resolved displacement time series without applying the SBAS method. b(1-7) are the APS components with SBAS method and c(1-7) are the displacement components after removing isolated errors (APS and DEM errors).

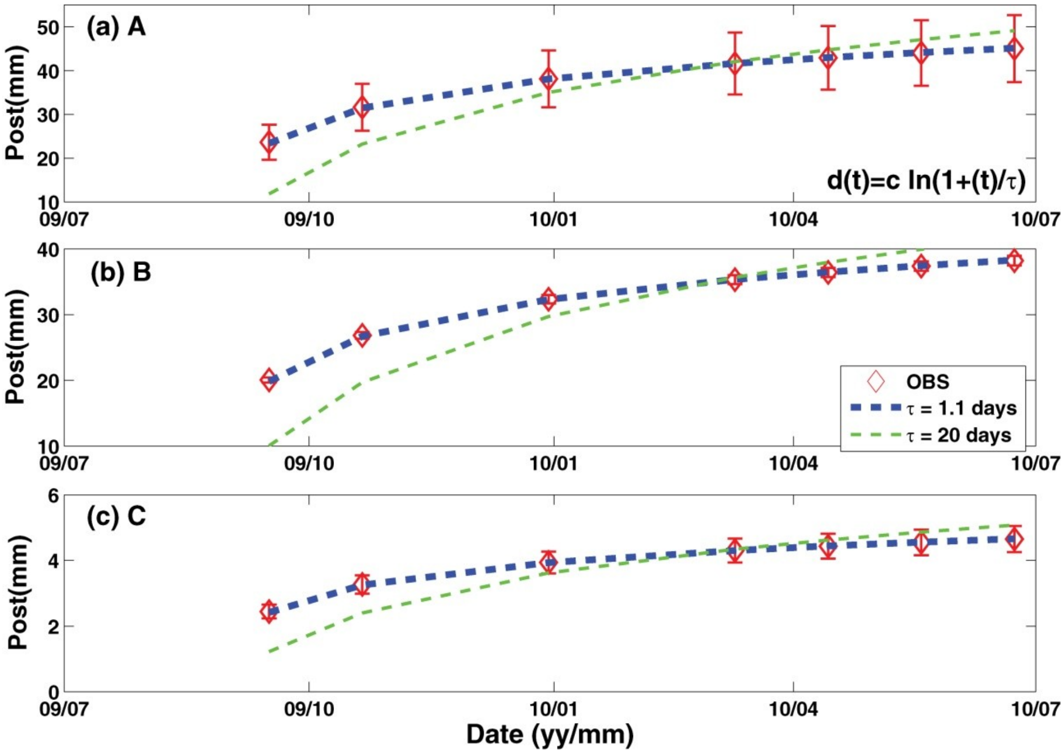

Figure 3.14 Postseismic LOS displacements time series at reference pixels (A~C) relative to the 2009 mainshock. Error bars represent one standard deviation within a window of 3×3 pixels.

3.4 Coseismic modelling

Using PSOKINV, fault geometric parameters and slip distribution of the 2003-2009 three mainshocks were determined based on InSAR LOS coseismic surface changes. First, fault geometric parameters are determined using the improved particle swarm optimization (MPSO) (Kennedy and Eberhart, 1995; Feng and Li, 2010). Second, slip distributions over the fault planes are retrieved using an iterative strategy for assessing optimal dip angle and smoothing factors (Feng et al., 2013a), in which optimal dip angle of fault models can be further refined as well as smoothing factors. More details on the inversion strategy have been described in Chapter 2. For the 2009 event, the first step was avoided since its fault location was determined directly from its coseismic interferograms.

Based on the data resolution based (Rb) method (Lohman and Simons, 2005), original interferograms used for coseismic modelling were down-sampled into limited discrete points (details can be found in Figure 3.15). In this thesis, data weights ($\boldsymbol{W}$) were calculated by $\boldsymbol{W}^{\mathrm{T}}\boldsymbol{W} = \boldsymbol{\Sigma}^{-\mathbf{1}}$, in which $\boldsymbol{\Sigma}$ is the data covariance matrix (as described in Chapter 2). The data error covariance matrixes were estimated based on non deforming areas in the original interferograms. A simple 1-D exponential function was used to quantify InSAR noise spatial characteristics as

$$\boldsymbol{C(r) = \sigma^2 e^{-ar}} \tag{3.8}$$

where σ^2 is the variance of data [m^2], r is the separation of the observations [km] and a

determines the e-folding correlation length scale (Parsons et al., 2006). Using Equation (3.8) empirical errors can be generated to estimate parameter uncertainties induced by spatially correlated observation errors.

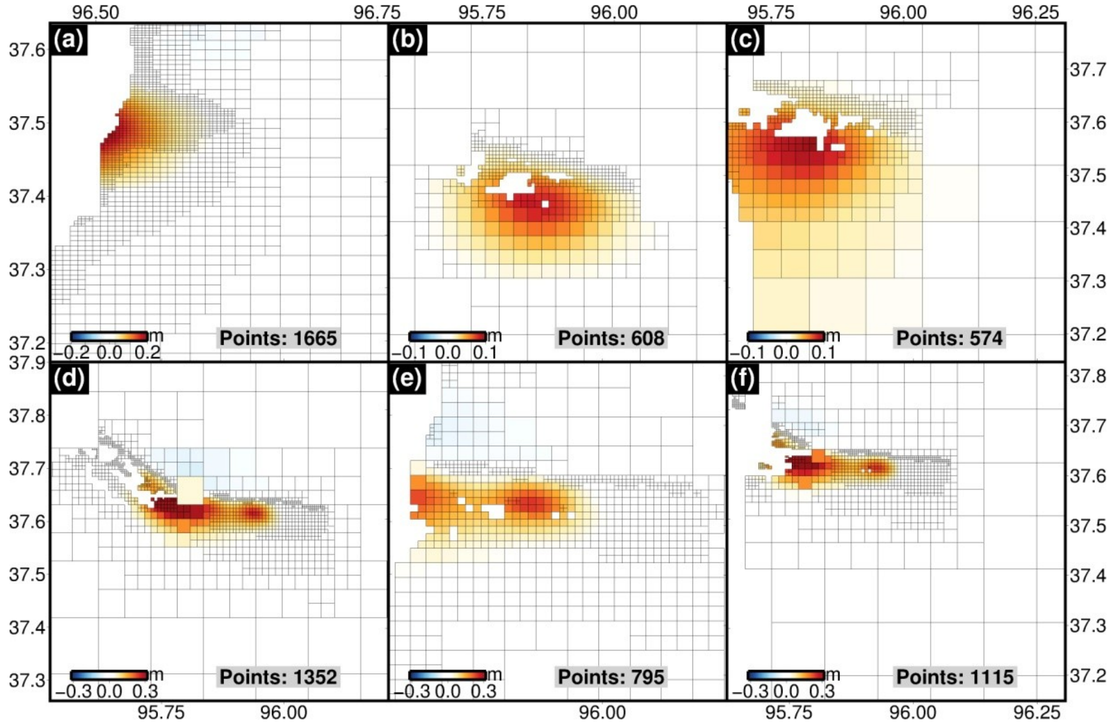

Figure 3.15 Downsampled points from interferograms using the data resolution based method (Lohman and Simons, 2005). (a) From track 276 for the 2003 event; (b) and (c) for the 2008 event from tracks 319 and 455, respectively; (d) - (f) for the 2009 event from tracks 319, 047 and 455.

3.4.1 2003 M_W 6.3 Delingha earthquake

Only half of the deformation area associated with the 2003 M_W 6.3 Delingha earthquake, was observed by the ASAR interferograms of track 276. North- (ND) and south-dipping (SD) fault models were taken into account in the inversion since they were both possibly associated with the mainshock by previous studies (Sun et al., 2012; Zha and Dai, 2013). During the nonlinear inversion, the strike of the fault was strongly constrained in the narrow search spaces of [70°, 110°], and the dip angle can be allowed to vary in [-90°, 90°]. The south-dipping best-fit fault suggests that the mainshock occurred on the fault with a strike of 116.7°, a dip of 46° and a rake of 97°, whilst the best-fit north-dipping fault has a strike of 292.1°, a dip of 42° and a rake of 81°. They are almost conjugate. With these two fault geometric parameters, two slip models were determined under the constraints of the same downsampled datapoints. Optimal dip angles of the slip models were further refined during the slip inversion step using an iteration method (Feng et al., 2013a). In this case, the optimal dip determined in the slip inversion step is identical with that determined in the nonlinear inversion step.

As shown in Figure 3.17 (a), the optimal north- and south-dipping slip models can explain the interferogram equally well. Modelled LOS displacements along Profile A-B in Figure 3.17 (e) show good agreement with observations and their correlation coefficients are 0.993 and 0.990 for the north- and south-dipping models, respectively.

Using the Monte Carlo method proposed by Parsons *et al.* (2006), the uncertainties of fault geometric parameters were estimated. 100 sets of predicted errors were simulated based on the one-dimensional empirical error distribution estimated with Equation (3.8), and 100 sets of observations were then generated by adding the simulated errors into original observations. Finally, 100 sets of fault geometric parameters were determined based on these simulated observations. The trade-offs between each pair of the fault geometric parameters were plotted as well as the distribution of each parameter (Figure 3.16). As shown in Figure 3.16, a significant trade-off can be found between rake and seismic moment release in this case. However, all parameters have small standard deviations, suggesting that either of fault models should be the best model regarding their given dipping directions.

For the north-dipping model, a maximum slip is ~2.3 m at a depth of 10 km, whilst a maximum slip in the south-dipping model is ~1.6 m also at a depth of ~10 km. Similar seismic moments are obtained from the both models. Note that the fault length of 2.0 km was fixed in the uniform fault inversions; otherwise the length tends to converge to an infinitesimal value, implying that the major rupture was concentrated in a narrow zone and the length of the uniform slip model is not sensitive with respect to the current observations. Whether the north- or south-dipping fault plane is associated with the 2003 mainshock still remains unsolved from the InSAR modelling in this thesis, but the three-dimensional (3D) location of the major slip of the earthquake has been determined robustly, at a depth of ~10 km at [37.51° N, 96.47° E].

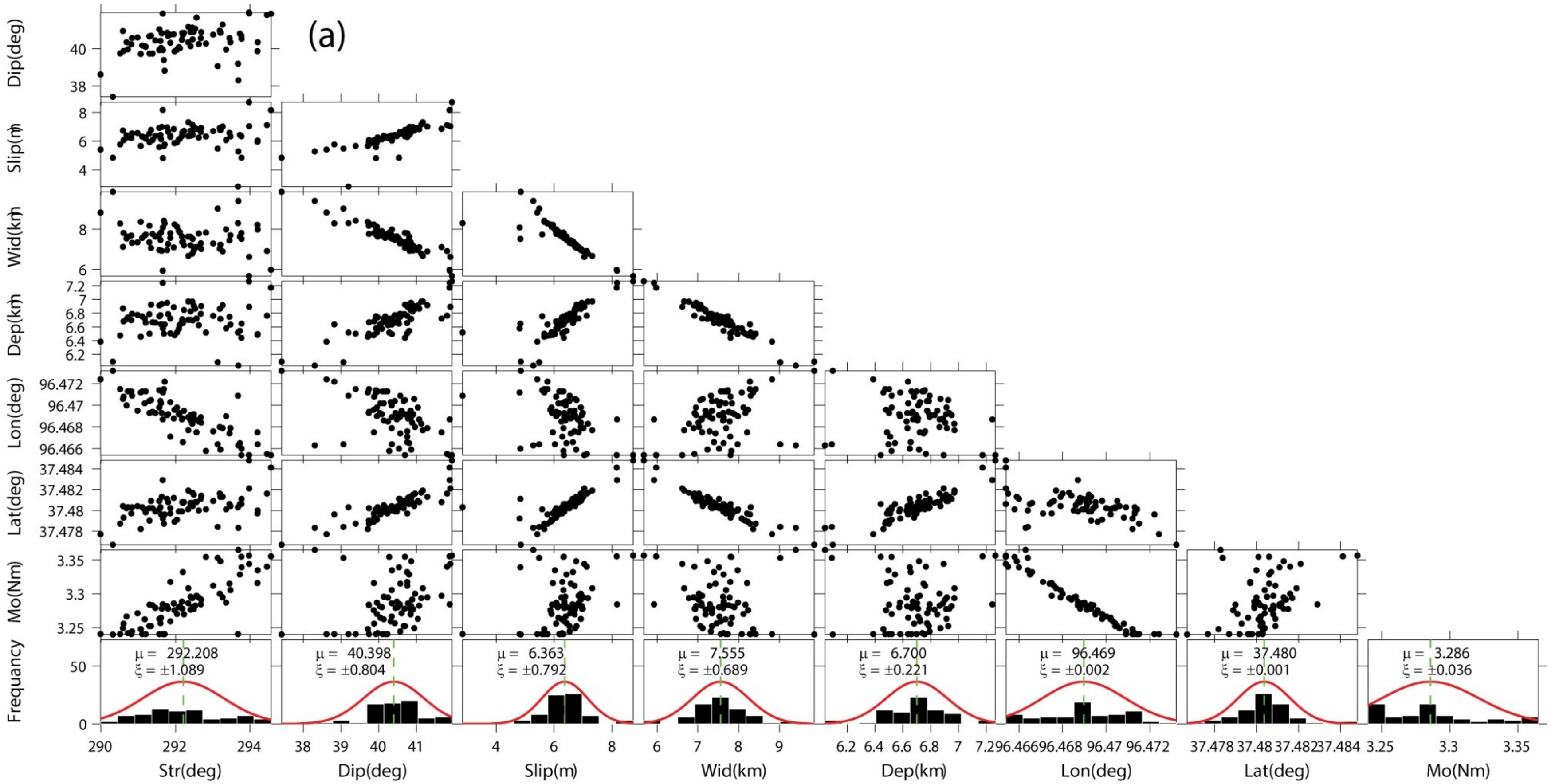
(a)
Dip(deg)
40
38
Slip(m)
8
6
4
Wid(km)
8
6
Dep(km)
7.2
7
6.8
6.6
6.4
6.2
Lon(deg)
96.472
96.47
96.468
96.466
Lat(deg)
37.484
37.482
37.48
37.478
Mo(Nm)
3.35
3.3
3.25
Frequency
50
0
μ = 292.208
ξ = ±1.089
μ = 40.398
ξ = ±0.804
μ = 6.363
ξ = ±0.792
μ = 7.555
ξ = ±0.689
μ = 6.700
ξ = ±0.221
μ = 96.469
ξ = ±0.002
μ = 37.480
ξ = ±0.001
μ = 3.286
ξ = ±0.036
290
292
294
Str(deg)
38
39
40
41
Dip(deg)
4
6
8
Slip(m)
6
7
8
9
Wid(km)
6.2
6.4
6.6
6.8
7
7.2
Dep(km)
96.466
96.468
96.47
96.472
Lon(deg)
37.478
37.48
37.482
37.484
Lat(deg)
3.25
3.3
3.35
Mo(Nm)

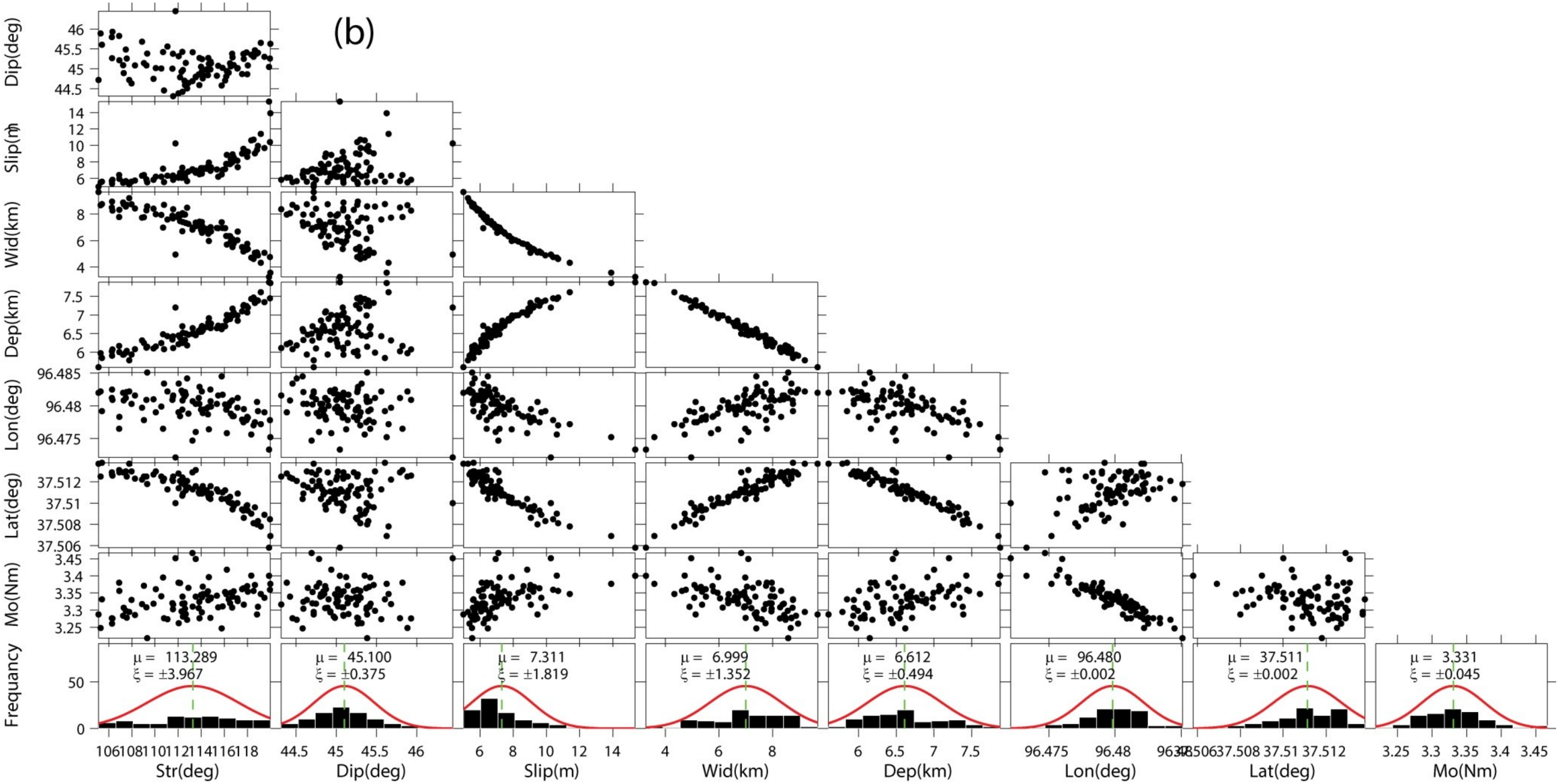

Figure 3.16 Uncertainties and trade-offs of fault geometric parameters computed using Monte Carlo analysis. (a) North-dipping fault model; (b) South-dipping fault model.

3.4.2 2008 M_W 6.3 Haixi earthquake

Due to significant atmospheric effects on interferograms, only the stacked coseismic interferogram from track 319 for the 2008 Haixi mainshock was used for the determination of the fault parameters and slip model. As for the 2003 event, both north- and south-dipping fault geometries were considered in the inversion. The optimal fault parameters of the 2008 mainshock suggest that the fault parameters of the north-dipping fault are strike 288°, dip 29° and rake 95°, whilst the south-dipping fault is conjugate with the north-dipping fault (details listed in Table 3.2). Using these two fault geometric models, two slip distributions of the 2008 mainshock were determined with the same surface constraints.

The coseismic interferograms of tracks 319, 047 and 455 were employed to validate the best-fit slip models. Although the latter two tracks were not used in inversion, the residuals from these two tracks were also expected to provide independent evidence for identifying the optimal model of the mainshock. Figure 3.17 shows agreement between observed and modelled InSAR LOS changes from the both north- and south-dipping models. Similar LOS coseismic deformation patterns were modelled for these three tracks. The difference between residuals of track 455 (Figure 3.17 (b-4~5)) determined with the two slip models cannot be identified due to the considerable topography-correlated long-wavelength signals. Some residual patterns from the north-dipping model can be recognized from tracks 047 and 319 as shown in the denoted regions (white circles in Figure 3.17 (c-4) and (d-4)). For the stacked interferogram of track 319, the residual RMS determined with the north-dipping model is only ~3.4 mm, which is very close to ~2.4 mm inferred from the south-dipping model. A similar trend is also found in the interferograms of track 047. However, the differences are at millimetre levels and have been even lower than observation errors in the corresponding interferograms. Therefore, the InSAR data used in this chapter for the 2008 mainshock are not sufficient to determine the realistic model responsible for the 2008 mainshock from these two conjugate models. However, the 3D location of the maximum slip of the 2008 mainshock has also been determined robustly as for the 2003 event.

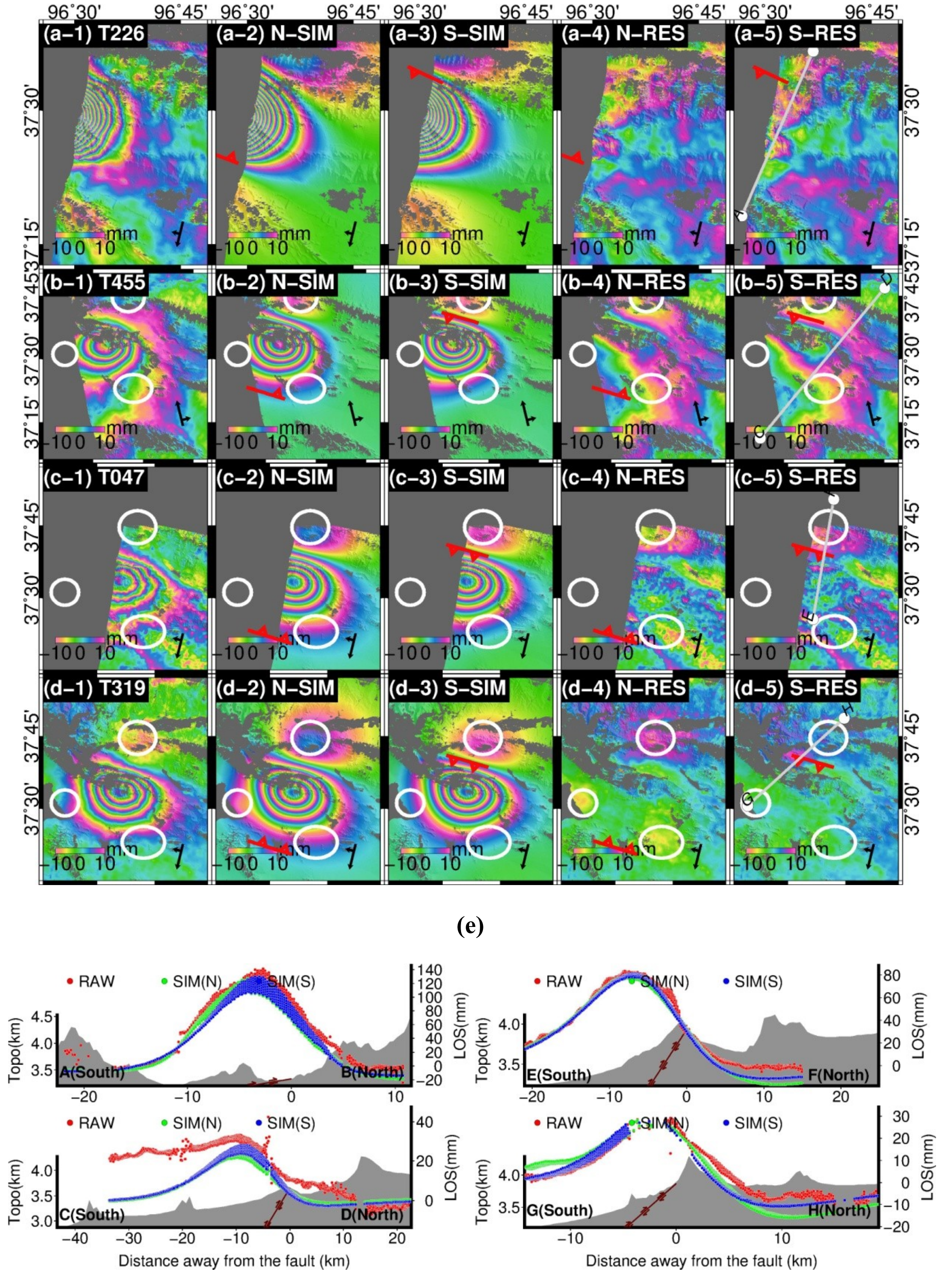

Figure 3.17 Measured and modelled coseismic interferograms with profile analysis. (a-1) The measured cosesimic LOS changes of the 2003 mainshock in track 226. (a-2) and (a-3) are modelled interferograms with the best-fit slip models of the north-dipping and south-dipping slip models respectively. (a-4) and (a-5) are the residuals corresponding to (a-2) and (a-3). (b),(c) and (d) are similar as (a), but they are all for the 2008 mainshock. Red thick lines in (a,b,c,d) denote the surface location of the faults determined by nonlinear geodetic inversion. White lines indicate profiles shown in (d) White ellipses highlight the differences between the north-dipping and south-dipping model. Profiles of line-of-sight (LOS) displacements (red dots), modelled LOS displacements (green and blue dots) by the north-dipping and south-dipping models are plotted in (d). Dark red lines suggest the location of the referred south-fault model in space, which is not scaled.

3.4.3 2009 M_W 6.3 Haixi earthquake

Two distinctive deformation patterns corresponding to the foot and hanging walls of the 2009 earthquake fault can be observed in the coseismic interferograms (Figure 3.18). Therefore, there is no ambiguity on the fault dipping direction in this event. The south-dipping fault should be responsible for the 2009 mainshock. Strike variation along the fault has also been identified in the coseismic interferograms (Figure 3.18), suggesting that the mainshock should occur on a non-planar fault surface. Two straight fault traces were determined manually based on the coseismic interferogram from track 319 (red lines in Figure 3.18). These two fault segments strike at 100° and 130°, respectively. Since the surface locations of the faults were fixed based on the coseismic fringes, only dip angles of the two fault segments remain undetermined in this case, which can be estimated directly using the linear slip inversion step. Thus, the non-linear inversion step as used for the 2003 and 2008 mainshocks is not needed for this event.

In the slip inversion, an assumption was first made that the slip should occur on a continuous fault surface. Based on the fault traces, a quasi-seamless fault plane discretization strategy was proposed to construct a quasi-continuous fault model using rectangular elements, in which two straight fault planes connected together without overlap. A depth-dependent fault discretization method (Simons et al., 2002; Fialko, 2004b) was employed to split the continuous planes into small patches. A dumping factor of 1.2 was selected to increase the patch size over depth. The smallest patch size is 0.5 by 0.5 km at the top, whilst the patches on the bottom of the fault models have a patch size of 5.8 by 5.8 km. Optimal dip angles were estimated using an iterative and grid search method (Feng et al., 2013a), in which the optimal smoothing parameter was also determined. Since two dips for the two sub-planes need be estimated, a series of trials were made to iteratively determine optimal dips for the two fault segments. After several iterations, 51° and 48° were robustly determined for east and west faults, respectively. It is noted that the east fault segment is very close to the south-dipping fault model of the 2008 mainshock.

As shown in Figure 3.21, a maximum slip of ~2 m at a depth of 5 km appears next to the bend of the faults. Another small slip centre 5 km east of the major slip zone corresponds to a small LOS displacement centres on the surface. A M_W 5.8 aftershock three days after the 2009 mainshock was recorded close to the epicentre of the mainshock by seismic data (GCMT). Therefore, residual patterns observed in both descending interferograms (Figure 3.18), likely result from aftershocks rather than atmospheric effects.

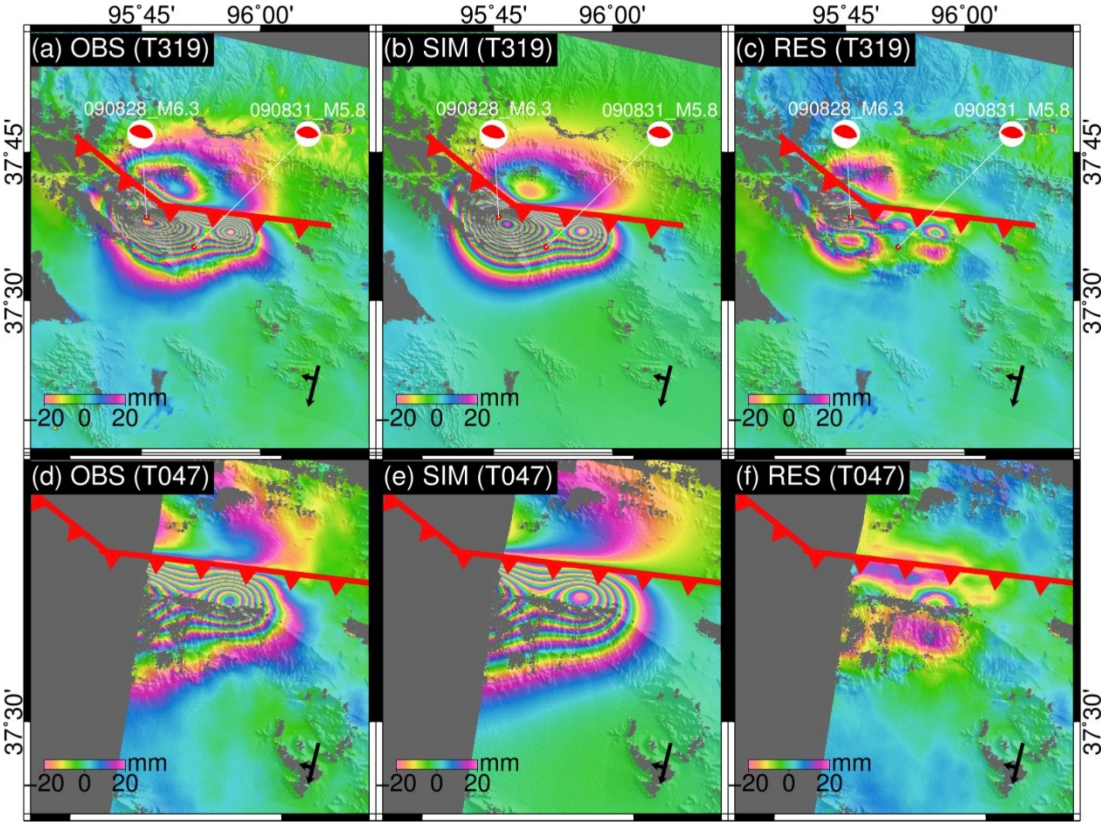

Figure 3.18 Original (OBS), modelled (SIM) interferograms and residuals (RES) of the 2009 M_W 6.3 Haixi Mainshock. (a-c) are for the coseismic interferogram of track 319, whilst (d-f) are for track 047. The beachball in (a)-(c) are for the M_W 5.8 aftershock.

3.4.4 Time-dependent afterslip modelling following the 2009 M_W 6.3 Haixi earthquake

Since the 2009 mainshock was selected as the reference date for the deformation model in the InSAR time series analysis, postseismic displacement history between the mainshock and June 2010 was fully retrieved. Based on InSAR derived postseismic displacement time series (TS), postseismic slip history following the 2009 mainshock is determined in this section.

In postseismic slip inversion, the fault geometric parameters determined from the coseismic inversion of the 2009 mainshock were used. With the given fault geometries, each TS interferogram was downsampled into 735 points based on the Resolution-based method (Lohman and Simons, 2005). As discussed in Chapter 2, postseismic slip history was usually determined by inverting postseismic observations individually (e.g. Ryder et al., 2007a; Ryder et al., 2011; Bie et al., 2013). Using InSAR postseismic LOS observations at each epoch, the slip distribution at each epoch were obtained individually, hereafter afterslip history determined by individual LOS observations will be called Smodel. In the traditional inversion method for Smodel, the temporal variation of slip rate was ignored. To avoid slip rate perturbation, a time-dependent slip inversion strategy for solving the entire afterslip history once was proposed in this study (later also called Tmodel). The integrated expression is defined using a velocity control at each slip epoch as

$$\begin{bmatrix} \boldsymbol{G} & \boldsymbol{0} \\ \boldsymbol{G} & \boldsymbol{log(1+T_i)G} \\ \vdots & \vdots \\ \boldsymbol{G} & \boldsymbol{log(1+T_n)G} \\ \boldsymbol{\alpha^2 L} & \boldsymbol{0} \\ \boldsymbol{0} & \boldsymbol{\beta^2 L_v} \end{bmatrix} \begin{bmatrix} \boldsymbol{s_0} \\ \boldsymbol{a_v} \end{bmatrix} = \begin{bmatrix} \boldsymbol{d_1} \\ \boldsymbol{d_i} \\ \vdots \\ \boldsymbol{d_n} \\ \boldsymbol{0} \\ \boldsymbol{0} \end{bmatrix} \qquad \textbf{(3.9)}$$

where $log(T_i)$ is the logarithm of time interval between ith epoch and the 2009 mainshock occurrence, $\boldsymbol{G}$ is the Green matrix calculated by the elastic dislocation by Okada (1985). The vector a_v is the m-dimension coefficients of slip rates for each subfault. The slip vector (s_i) at the ith acquisition can be computed by $s_0 + a_v log(1 + T_i)$. The design matrix for smoothing velocity $(\boldsymbol{L_v})$ is similar to the Laplacian operator $\boldsymbol{L}$ for estimation of the slip roughness. α^2 and β^2 are hyperparameters that control the slip smoothness for the last epoch and the slip rate smoothness respectively. In practice, the inversion is not sensitive to the slip rate variation. The smoothness of slip models at each epoch is decided by both α^2 and β^2. In this chapter, 3.5 and 100 for α^2 and β^2, respectively, were selected.

Figure 3.19 illustrates the data fit for each epoch using Smodel and Tmodel. An average correlation coefficient between the simulations and InSAR observations for each epoch is >0.91 for both afterslip time series models, suggesting that the time dependent slip inversion strategy proposed in this chapter is reliable. Two points with ~70 mm LOS displacements are not explained well. Several factors may contribute to this discrepancy, e.g. large aftershocks, observation errors or slip uncertainty. Since different smoothness parameters do not improve the fit to these two observations, additional sources of deformation need to be included. A comparison between Smodel and Tmodel for the afterslip history of the 2009 event is shown in Figure 3.20. The major afterslip in both Smodel and Tmodel is concentrated at depths from 5 to 10 km. The maximum accumulative afterslip of these two models is both ~0.25 m upwards with a right-lateral strike-slip component. A slight difference between these two modes can be found in the eastern slip centres. Smodel present a similar afterslip magnitude in the eastern part with the eastern one, whilst Tmodel in the eastern part shows smaller than that in the western centre (Figure 3.20). Based on current data fit, the residuals from the two slip models cannot recognize which model could be more realistic. The cumulative seismic moment of Tmodel until 23 June 2010 reaches up to $2.1\text{x}10^{18}$ N.m, equivalent to a M_{W} 6.18 earthquake. This finding that the energy released during the afterslip processes is close or even larger than the mainshock, has been reported in other cases, such as the 2004 Parkfield earthquake (Bruhat et al., 2011) and the 2011 Van (Turkey) earthquake (Feng et al., 2014). Note that the method for afterslip modelling proposed in this chapter is a specific case of time-dependent slip inversions, in which the slip history was fixed to evolve logarithmically with time. To suit other complex physical time-dependent events, Equation (3.9) needs to be revised based on known physical mechanisms.

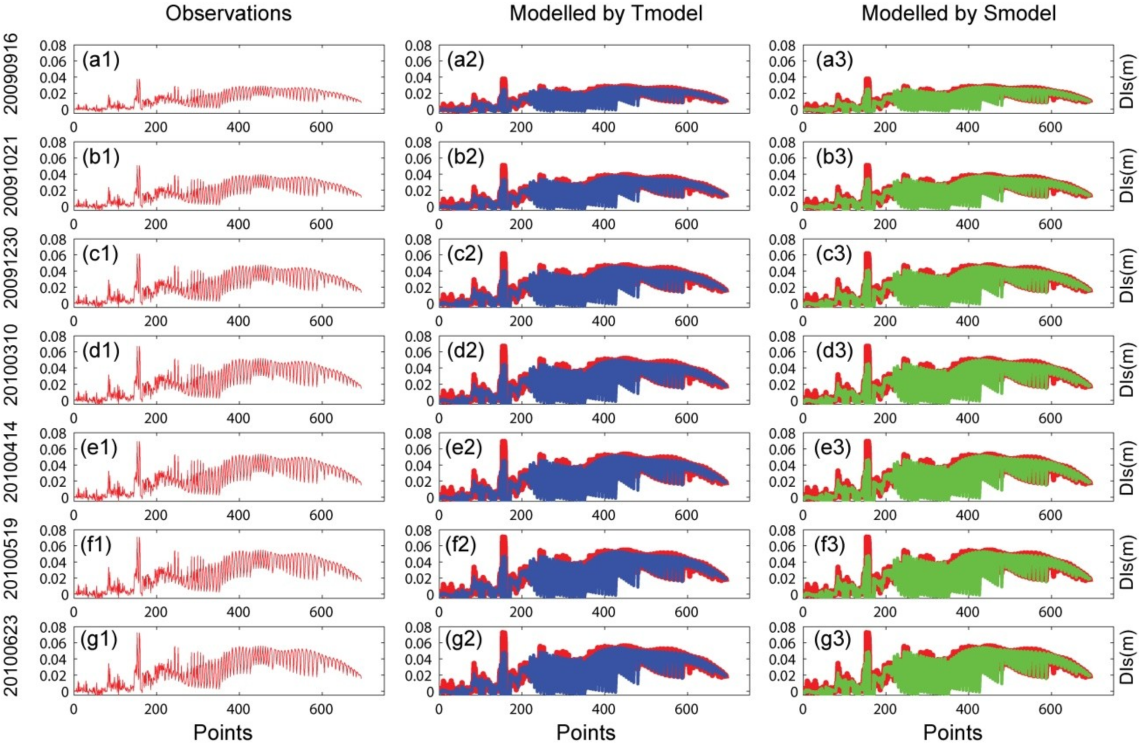

Figure 3.19 Comparison of data-fits to the postseismic deformation time series from different afterslip models. (a-1) is observations at 20090916; (a-2) is modelled using Tmodel and (a-3) is modelled using Smodel. (b-g) are similar to (a), but for observations at 20091021,20100310,20100414,20100519 and 20100623, respectively.

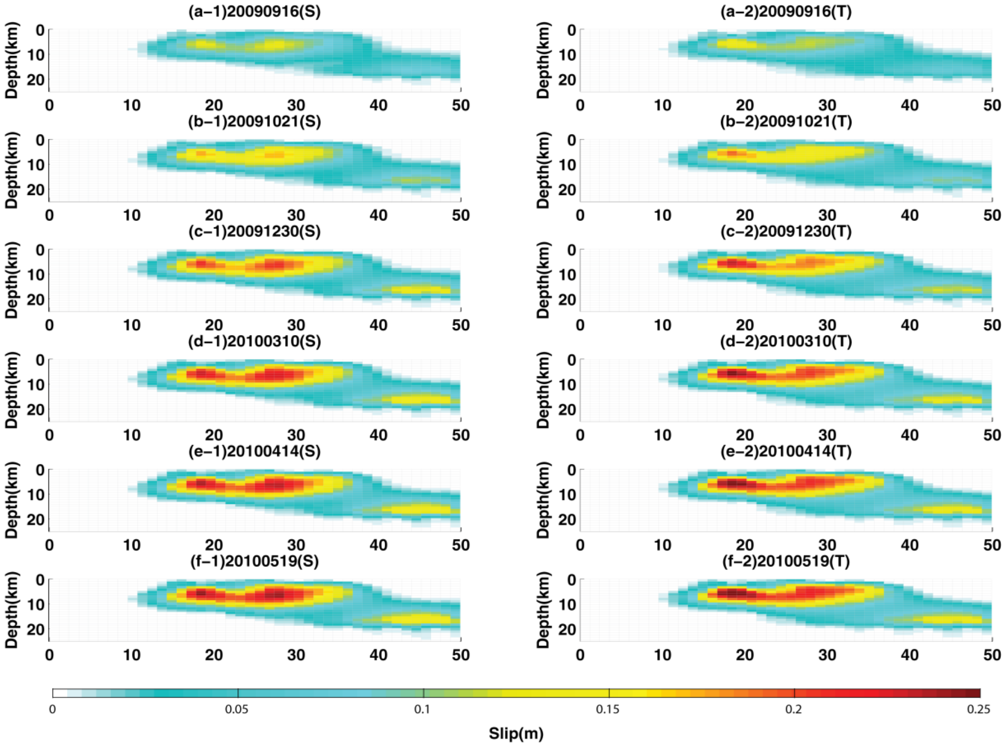

Figure 3.20 Comparison of afterslip time series inferred from individual observations and time-dependent geodetic inversion. The right column that is denoted by (T) is inverted by Tmodel, whilst the left with S is Smodel.

3.5 Discussion

3.5.1 Limitations of InSAR observations for investigating simple deep thrust earthquakes

Due to limited InSAR surface observations and significant atmosphere effects, the fault dipping direction of the 2003 M_W 6.3 mainshock cannot be determined directly from InSAR modelling. Both the north- and south-dipping slip models can explain the available InSAR observations equally well. Figure 3.21 (a) shows that the spatial relationship between aftershocks and the fault planes. The regional aftershocks are randomly distributed around the slip centres. The fault traces of both models also individually correspond to the basin boundaries (Figure 3.17(e)), suggesting that there is no clear geological evidence to rule out one of the two fault planes. However, it is worthwhile pointing out that the maximum slips from both slip models are centred at the same location at a depth of ~10 km.

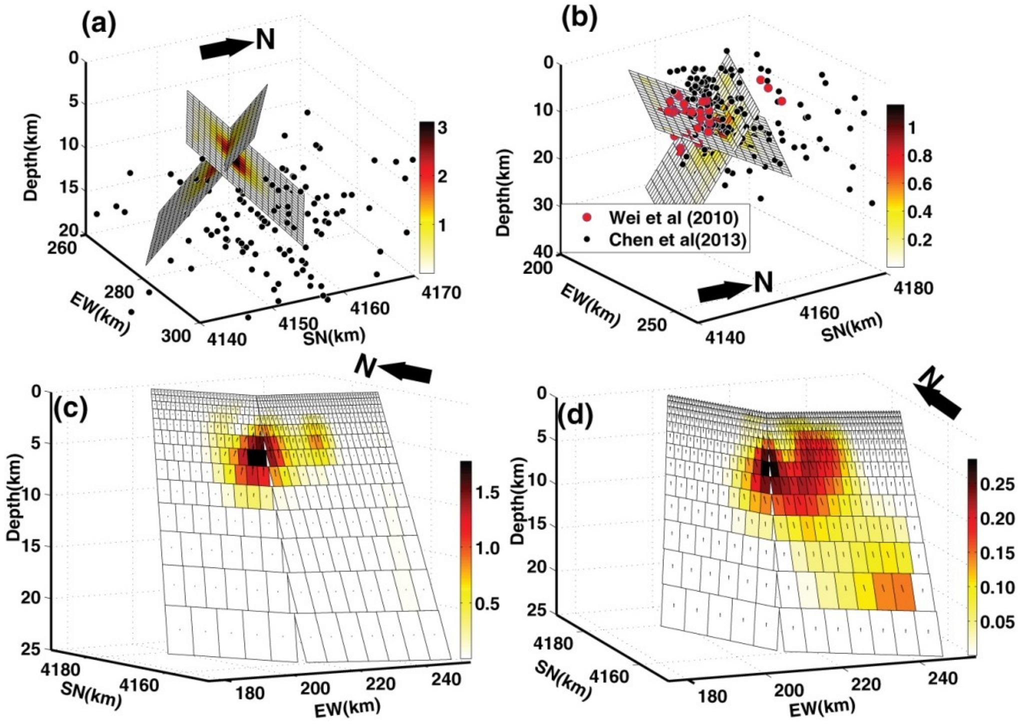

Figure 3.21 Slip models in three dimension and aftershocks. (a) The north-dipping and south dipping slip models of the 2003 mainshock and aftershocks (CSN), (b) as (a), but for the 2008 M_W 6.3 mainshock. Red dots show relocated aftershocks spanning from 10 November 2008 to 13 May 2009 by Wei et al. (2010b), whilst black dots represent the aftershocks provided by Chen et al. (2013). (c) The referred coseismic slip model of the 2009 mainshock and (d) the cumulative afterslip model until June 2010 after the 2009 mainshock. Note that the horizontal coordinates used are in 47(S) zone of the Universal Transverse Mercator Coordinates System.

In comparison to the 2003 event, more interferograms are available for the 2008 M_W 6.3 mainshock. The south-dipping fault model seems to be able to explain InSAR LOS measurements slightly better (Figure 3.17). However, the difference of residual RMS determined from the north-and south-dipping models is only in an order of few mm that is smaller than data observation errors, suggesting that InSAR observations cannot determine an optimal slip model in this case. Figure 3.21 illustrates the locations of 39 relocated earthquakes (denoted by red dots) spanning the period from 10 November 2008 to 13 May 2009 released by Wei *et al.* (2010b). In their analysis, 400 events covering the entire Tibetan plateau from 2007 to 2009 were relocated using the seismic data recorded through the INDEPTH-IV and PKU arrays using hypoDD (Waldhauser and Ellsworth, 2000). The aftershocks following the 2008 event are only part of their results. A clear trend is observed that the aftershocks were mainly located around the north-dipping fault plane at a depth of ~10 km. However, another aftershock dataset (denoted by black dots in Figure 3.21 (b)) do not show a similar trend, which were released by Chen *et al.* (2013) including more events. Therefore, neither of the both models can be ruled out for the 2008 event based on existing observations, and the dipping direction of the fault plane remains unsolved. However, the depth of the major slip at ~15 km has been robustly determined.

3.5.2 Seismogenic depth characteristic in the northern margin of the Qaidam basin

Wright *et al*. (2013) suggested that the seismogenic depth in Tibetan Plateau is 16±6 km from geodetic observations, whilst the locked depth on the faults estimated by interseismic observations is 13±6 km. Their conclusions are further supported by the results of this study. Note that the variation of the source depths in the region of the 2003-2009 earthquake sequence is large. As shown in Figures 3.22 and 3.23, the major slip of the 2003 M_W 6.3 Delingha earthquake is concentrated between depths ranging from 8-12 km, whilst another two M_W 6.3 earthquakes in 2008 and 2009 have their main slip zones at depths of ~15 km and ~5 km, respectively.

Figure 3.23 illustrates the depth characteristics of historical earthquakes (Chinese Seismic Network, CSN), located within a radius of 300 km from the 2008 earthquake epicentre between 1977 and 2014. 95% of events are concentrated at depths between 5 and 15 km. The seismicity rate in the Qaidam basin is low as mentioned in Section 3.2. Nearly 82% of seismicities were recorded after the 2003 Delingha earthquake. They were mainly located around the epicentres of the three M_W 6.3 mainshocks. Therefore, the patterns of historic seismicity recorded by CSN should only reflect the depth characteristics of the aftershocks following the 2003-2009 three mainshocks. Another two seismic datasets provided by Wei *et al.* (2010b) and Chinese earthquake network centre (CENC) mainly focus in the period after the 2003 mainshock. Their depth distributions directly show the features of the aftershocks following the three mainshocks.

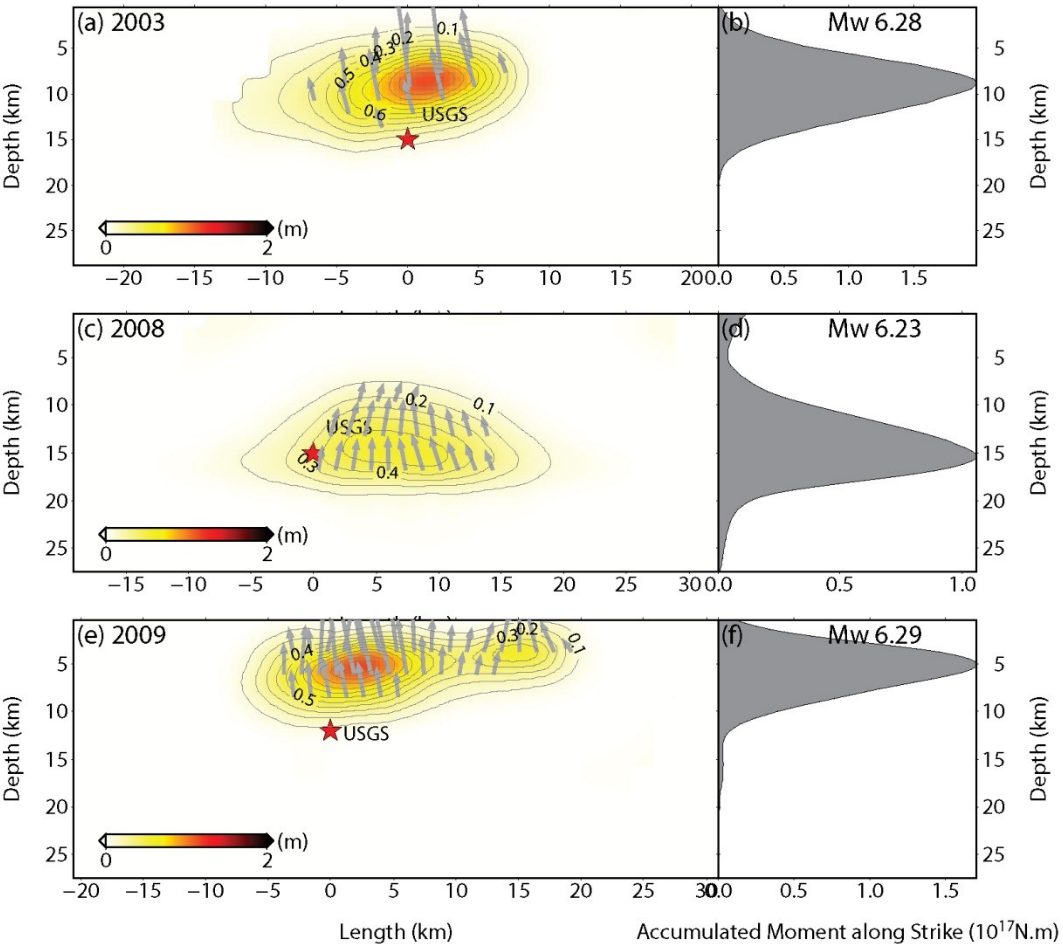

Figure 3.22 Coseismic slip models of three M_W 6.3 mainshocks during 2003-2009 and their seismic moment release over depth. For the 2008 event, only the south dipping slip model is presented here. The north-dipping model is similar in terms of slip distribution patterns.

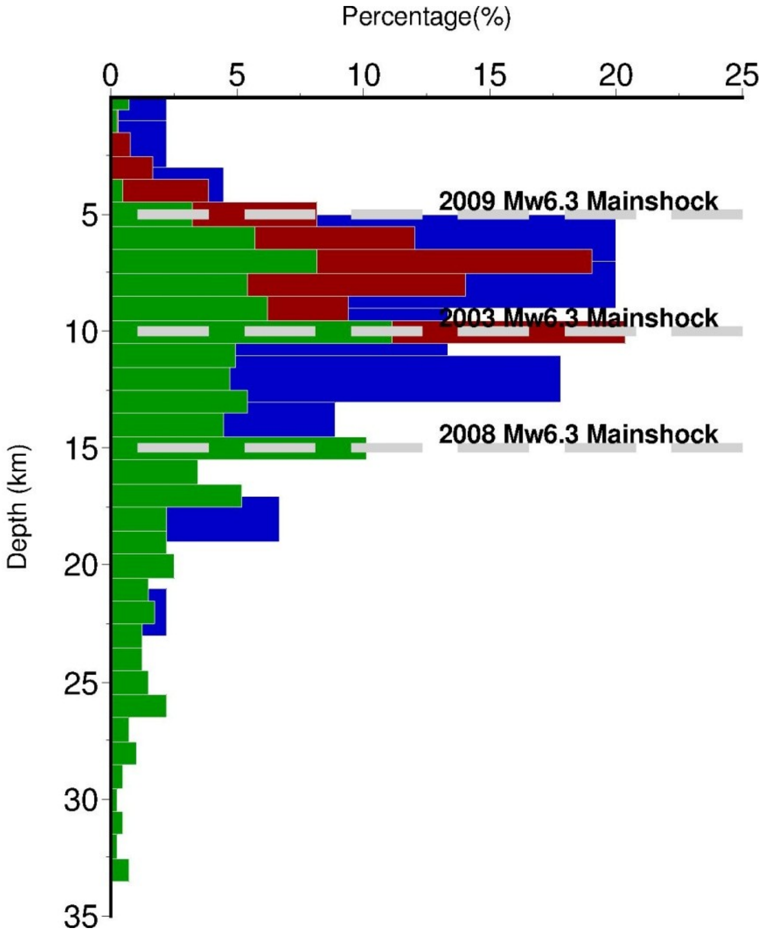

Figure 3.23 Histogram of earthquake depths from different datasets. Relocated earthquakes from 2007-2009 (Wei et al., 2010b) are used for the blue bars. Green bars represent the catalogue including the earthquakes M>3 from 1970 to 2014 recorded by Chinese seismic network (CSN). Red ones are the new datasets from CEA covering from 2008 to 2014.

3.5.3 Challenging the rate-state asperity model: afterslip following the 2009 mainshock

Using a three-dimensional elastic dislocation method by Okada (1992), shear stress drops in the 2008 and 2009 mainshocks were calculated (Figure 3.24). Both north- and south-dipping slip models of the 2008 mainshock were taken into account. The cumulative afterslip after the 2009 event is presented by the blue contours in Figure 3.24 (a and b) and basically covers the coseismic rupture area of the 2009 mainshock near the bend (Figure 3.24(e)). The location of the maximum afterslip nicely corresponds to the maximum coseismic slip of the 2009 mainshock. Afterslip at a depth of 15 km aside the rupture area of the 2008 event was also identified. Since the slip model resolution at depth is low (Elliott et al., 2013), it is hard to know if it is due to remaining observation errors in the deformation time series. Note that the triggering relationship from the north-dipping 2008 slip model to the 2009 mainshock seems more significant than the south-dipping fault plane of the 2008 mainshock.

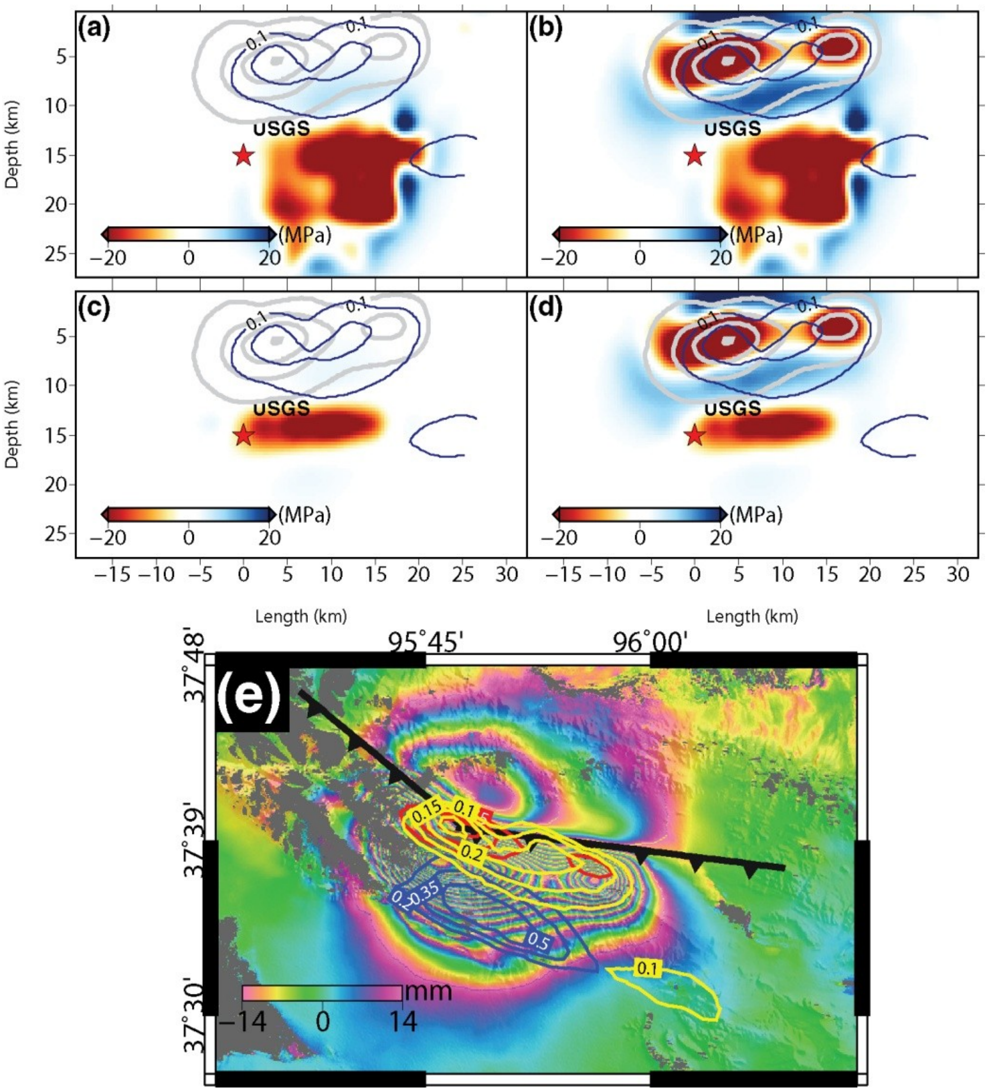

Figure 3.24 Spatial correlation of coseismic stress drop and afterslip following the 2009 mainshock, and slip models overlaid on the coseismic interferogram. (a) The stress drop is calculated by the south-dipping slip model of the 2008 mainshock; (b) is similar to (a), but for the stress drop corresponds to both 2008 and 2009 mainshocks. Blue contours are the afterslip and grey ones for the coseismic slip of the 2009 mainshock. (c) and (d) are similar to (a) and (b), but the north-dipping slip model of the 2008 mainshock is used. (e) The slip models including the coseismic slip of the 2008 mainshock (blue contours), the 2009 mainshock (red ones) and the accumulative afterslip (yellow ones) following the 2009 mainshock overlaid on the coseismic interferogram of the 2009 mainshock.

Following the rate and state stick-slip frictional law (Scholz and Aviles, 1986; Marone, 1998b; Kanda et al., 2012), earthquakes usually terminate within velocity-strengthening regions and propagate in velocity-weakening regions. The afterslip following the 2009 M_W 6.3 mainshock was just basically confined to the zone where the 2009 mainshock ruptured, which significantly challenged the velocity-weakening asperity law. However, the complex fault geometric structure may play a vital role in earthquake evolution in this case. From recent numerical studies (Dolan and Haravitch, 2014; Lindsey et al., 2014), structure maturity of a fault is found in correlation with slip spatial distribution. It may be then inferred that the frictional properties of faults are variable during fault evolution, which should vary during the rupture history of faults. The observations from the 2009 event may suggest that the the 2009 mainshock fault is still in the early stage of the faulting development and the fault structure plays the main role in the development of faulting at this site.

3.6 Conclusions

In this chapter, three M_W 6.3 earthquakes between 2003 and 2009 on the margin of the Qaidam basin were investigated with SAR images from six ASAR tracks. An improved network orbit correction method was proposed to reduce the orbit errors in interferograms, which was validated with the phase closure analysis. Using traditional InSAR, Stacking InSAR and small-baseline InSAR techniques, surface LOS changes covering three mainshocks and postseismic processes following the 2009 mainshock were obtained. The focal mechanism parameters and slip distribution of the mainshocks were determined using the constraints of InSAR observations.

For the 2003 event, near-field coseismic surface observations are obtained for the first time by InSAR in this study. A deep thrust source at a depth of ~10 km associated with the mainshock is determined robustly. However, the dip direction of the seismic fault remains unsolved. The availability of only one interferogram covering half coseismic deformation area makes it difficult (if not impossible) to determine a realistic source model for such a buried event.

A similar phenomenon was found in InSAR modelling for the 2008 mainshock. Although more InSAR coseismic observations are available for this case, the deeper source makes it hard to distinguish the conjugate fault planes. Both north- and south-dipping slip models suggest that the maximum slip of ~1 m appears at the depth of 15 km. Elliott *et al* (2011) suggested only a south-dipping model for the 2008 mainshock based on the characteristics of coseismic InSAR fringes and local topography. The north-dipping model as discussed in this study was not considered in their modelling. The 2009 mainshock was modelled on the nearly same fault plane as the south-dipping slip model of the 2008 event, suggesting that a maximum slip of ~2.0 m at a depth of ~5 km near the fault bend. A subevent centre with a maximum slip of 0.8 m was also found 15 km east of its major slip centre.

The three mainshocks of 2003-2009 earthquake sequence ruptured at completely different source depths: 5 km, 10 km and 15 km. Based on a recent compilation (Wright et al., 2013) of earthquakes investigated by InSAR, the characteristic seismogenic depth for reverse events globally ranges from 4 to 30 km. Therefore, the sequence on the northern margin of the Qaidam basin suggests that the upper crust over a wide range above 20 km depth may be able to nucleate for moderate events. Elliott *et al*. (2011) explained the coplanar events of the 2008 and 2009 mainshocks by a depth segmentation model. Considering the fault structure (Figure 3.24(e)), the fault bend may play an important role in the 2009 mainshock as the rupture on the Xiaoyudong fault segment during the 2008 Wenchuan earthquake (Shen et al., 2009).

Table 3.2 Fault parameters of the three M_W 6.3 earthquakes from 2003 to 2009.

Source	Model	Locations		Depth(km)	Focal Mechanisms			Fault Dimensions		Magnitude	s.d
		Lon(degree)	Lat(degree)		Strike(°)	Dip(°)	Rake(°)	Length(km)	Width(km)		
Mw 6.3 Delingha on 17th April 2003											
Sun *et al.* (2012)	-	96.51^{a}	37.57^{a}	-	115	60	90	-	-	6.7(ML)	-
GCMT		96.45^{b}	37.53^{b}	16	116	61	91	-	-	6.3	-
This study	N	96.45^{b}	37.50^{b}	9.17	292	40	81	7.1	2.1(fixed)	6.35	0.00598
	S	96.47^{b}	37.49^{b}	9.13	116	45	97	6.2	2.1(fixed)	6.35	0.00612
Mw 6.3 Haixi Earthquake on 10th Nov 2008											
GCMT	-	95.75^{b}	37.51^{b}	27.2	108	67	106	-	-	6.3	-
Elliott *et al.* (2011)	-	95.859	37.657	16.4	99	58	95	15	12	6.3	-
This study	N	95.8329	37.5799	15	288	31	90	17	8	6.35(fixed)	0.00616
	S	95.8244	37.5712	16	108	53	117	17	5	6.35(fixed)	0.00635
Mw 6.3 Haixi Earthquake on 28th Aug 2009											
GCMT	-	95.76^{b}	37.64^{b}	12	101	60	83	-	-	6.3	-
Elliott *et al.* (2011)	-	95.811^{c}	37.563^{c}	4.7	100	53	106	12.2	5.4	6.3	-
This study	-	-	-	5	108	53	90	-	-	6.3	-

Note: a, the locations were determined by seismic first motion data, suggesting the first motion location on the fault. b, the locations are determined using ideal rectangle fault models, which stand for the centre of the rectangular fault plane. c, the location for the middle segment.

Chapter 4

InSAR measurements for the 2011 M_W 7.1 Van (Turkey) earthquake

In Chapter 3, postseismic surface displacements in the first 11 months after the 2009 M_W 6.3 Haixi earthquake were retrieved using SBAS-InSAR. However, early postseismic surface displacements after the mainshock were not covered. Based on the postseismic logarithmic decay function estimated using the SBAS InSAR, the cumulative displacement in the first month after the mainshock should be over 50% of the total displacement in the first year. Whether the early postseismic response follows the same trend as observed in the longer term has rarely been assessed.

In this chapter, several COSMO-SkyMED (CSK), Envisat ASAR and RADARSAT-2 interferograms are presented for co- and postseismic slip modelling following the 2011 M_W 7.1 Van, Turkey earthquake. Using SAR images that were acquired only a few days after the mainshock, rapid postseismic surface changes can be seen. The performance of the rate-state friction law in the geodetic based slip models of the event is also discussed. This chapter will: (1) investigate the postseismic motion after the mainshock and assess its potential impacts on coseismic modelling; (2) differentiate coseismic and postseismic slip distributions using carefully selected geodetic data; (3) explore the effects of applying a layered Earth crustal model and discuss the correlation between coseismic slip and topography; and, (4) consider the mechanical implications of the relative spatial distributions of coseismic and postseismic slips.

4.1 Introduction

On 23rd October 2011, a M_W 7.1 thrust fault earthquake occurred 30 km north of Van, western Turkey. This event occurred in the Bardakçı-Saray thrust fault zone (Doğan and Karakaş, 2013), north of the Bitlis-Zagros Suture belt, one of the most tectonically active areas on Earth which has undergone crustal shortening and thickening as a result of the collisions between Arabian and Eurasian plates (Figure 4.1(a)) (Dewey and Pindell, 1985; Aksoy et al., 2005). GPS-derived horizontal velocity fields indicate a general counterclockwise rotation in the region including the Bitlis-Zagros fold belt at the rate of ~20-30 mm a^{-1} near the epicentre (Relinger et al., 2006) (Figure 4.1). A series of large strike-slip historical earthquakes along the boundaries of the Anatolian plateau imply that the major strike-slip faults (both the Northern Anatolian and Eastern Anatolian faults) might accommodate most of the western motion of the Anatolian block as it is compressed during convergence (Jackson and McKenzie, 1984). At a large scale, the Van region sits at the tip of a westward extruding wedge. Relatively complete earthquake records (Utkucu, 2013) for the Van region suggest that several destructive events hit this area since 1500 AD, with at least 40 events (M>5) identified (Utkucu, 2013). For example, the 1670 Mus-Bitlis earthquake extended from

Lake Van in a W-SW direction and a M_S 7.3 strike-slip earthquake in 1976 was 90 km northeast of the 2011 Van event (Stewart and Kanamori, 1982). These events within the triple junction zone of the Anatolian, Eurasian and Arabian plates (Chorowicz et al., 1994) reflect its complex geological background. However, the 1715 earthquake is the only reported destructive event in the Bardakçı-Saray thrust fault zone. For this reason, the fault zone did not appear in existing active fault maps (Utkucu, 2013). Along with several large aftershocks, the 2011 event led to over 600 people being killed and more than 60,000 made homeless.

Several papers have investigated the coseismic deformation, focal mechanisms and aftershocks of this event (Irmak et al., 2012; Altiner et al., 2013; Elliott et al., 2013; Fielding et al., 2013; Utkucu, 2013; Moro et al., 2014; Zahradník and Sokos, 2014). The mechanisms of the mainshock determined from geodetic observations and seismic waveforms are generally consistent. However, both the magnitudes and patterns of slip vary between models. For example, two-equal-sized areas of slip each with a maximum slip of ~9 m were calculated from InSAR observations by Elliott *et al.* (2013), whilst another study that combined InSAR with a SAR pixel offset map and GPS data suggested only one slip patch with a maximum slip of ~ 4 m (Fielding et al., 2013). This discrepancy has not yet been resolved.

4.2 Geodetic observations and modelling

4.2.1 Data sources

Three descending tracks of SAR observations (one track from COSMO-SkyMED (CSK), one track from Envisat ASAR, and one track from RADARSAT-2 (RS2)) were used in this study (Table 4.1). The slave CSK1 image was acquired on 23rd October 2013, just 4 h after the main shock and is considered to exclude any post-seismic motion. The slave ASAR image was acquired 8 days later (31st October 2011) so there should be a postseismic component within its phase measurements. Combining the coseismic CSK1 observations with this ASAR interferogram is ideal for assessing the impacts of postseismic signals on coseismic modelling. In this chapter, two independent interferometric pairs are selected to investigate postseismic motion after the large event: one CSK pair spanning the first 4 days after the main shock, and one RS2 pair covering the subsequent 51 days (Table 4.1).

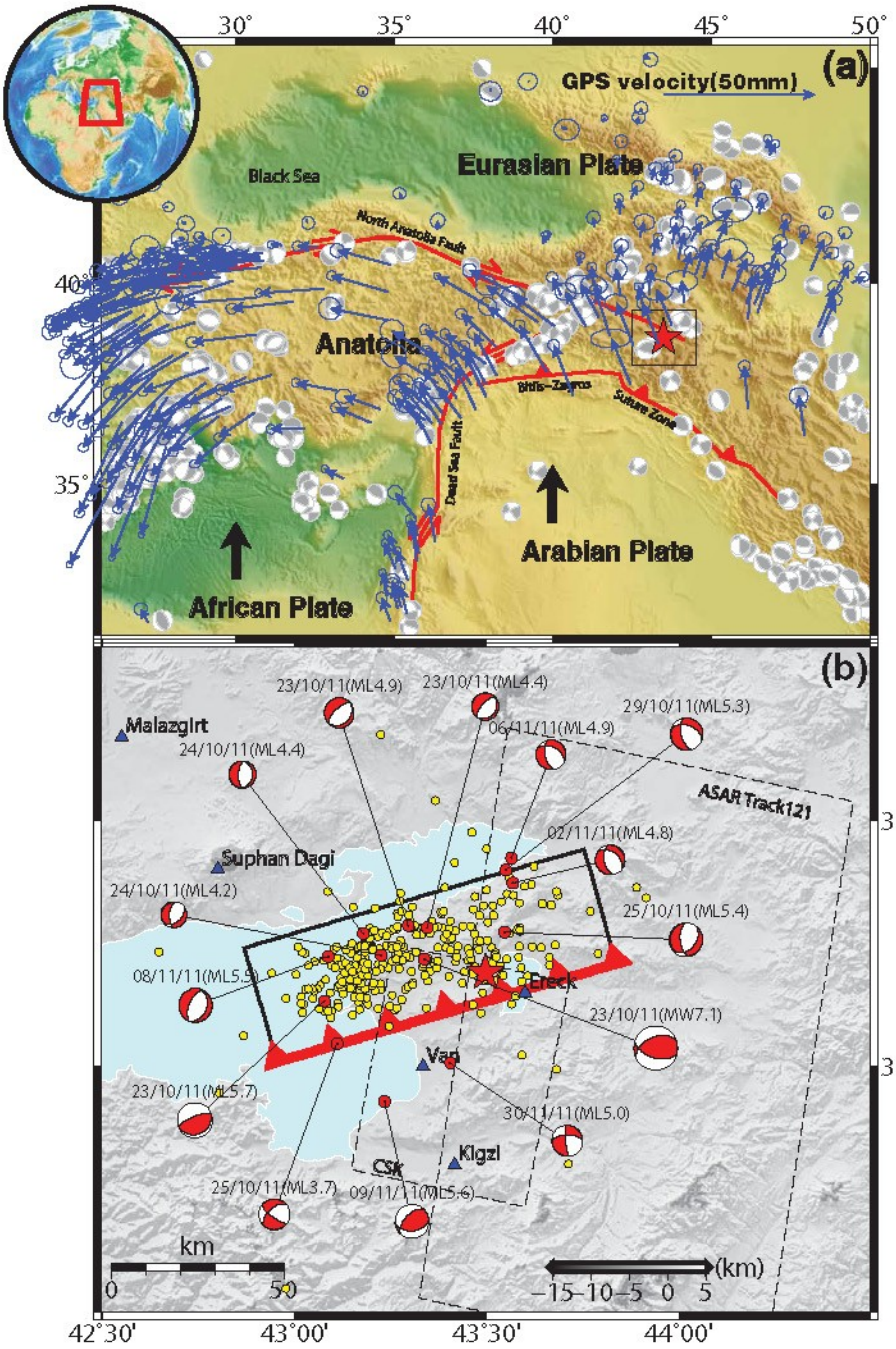

Figure 4.1 Tectonic background and seismic activity in the 2011 Van (Turkey) earthquake area from Feng et al. (2014). (a) Tectonic background of the 2011 M_W 7.1 Van, Turkey earthquake overlaid with GPS velocities (Relinger et al., 2006). Red star is the epicentre of the 2011 earthquake (USGS, 2011). (b) Seismic activity in the Van region, The arrow shows the convergence rate revealed by GPS (Relinger et al., 2006). Dashed rectangles indicate the coverage of SAR images used in this study, yellow circles represent aftershocks (http://www.emsc-csem.org/, last accessed on 28 December 2012) and beach balls show the mechanisms of major aftershocks determined by Irmak et al. (2012). Background is DEM derived from the Shuttle Radar Topography Mission digital elevation model (Farr et al., 2007).

Table 4.1 Details of InSAR pairs used in this study.

Satellite	Index	Master-Slave(Date)	Baseline *	Signals**	Info
CSK	CSK1	20111010-20111023	192.8	COS	Range changes
CSK	CSK1			COS	Azimuth displacements
ASAR	ASAR	20101105-20111031	37.4	COS+POS	Range changes
CSK	CSK2	20111023-20111026	307.1	POS	Range changes
RS2	RS2	20111026-20111213	239.9	POS	Range changes

Note: *: Perpendicular baseline represents the component of the orbital separation perpendicular to the radar line of sight, in meters. **: COS denotes coseismic displacement signals, whilst POS represents postseismic displacement signals.

Eleven GPS coseismic measurements from a previous study (Altiner et al., 2013) are used for model validation. Using 1-second continuous GPS recording from the CORS-TR network, coseismic displacements were determined in the Precise Point Positioning mode with the Bernese GNSS software (Altiner et al., 2013). The maximum horizontal coseismic displacements of -16.95 mm in E-W direction and -34.2 mm in the N-S direction were found at the MURA GPS station, approximately 60 km northeast of the epicentre.

4.2.2 Coseismic interferograms

The CSK and ASAR interferograms were generated using the JPL/Caltech ROI_PAC V3.1Beta (Rosen et al., 2004a) package (Table 4.1), whilst GAMMA software (Wegmüller and Werner, 1997) was employed to produce RS2 interferograms. The topographic phase contribution was removed using a version of the Shuttle Radar Topography Mission (SRTM) 3 arc-second (~90 m) digital elevation model (DEM) (Farr et al., 2007) that has the voids filled from other data sources (Jarvis et al., 2008). The DEM had also been transformed into an ellipsoidal height datum (Li et al., 2013). The interferograms were unwrapped using the SNAPHU algorithm (Chen and Zebker, 2000) to obtain line-of-sight (LOS) displacements with Goldstein filtering (Goldstein and Werner, 1998).

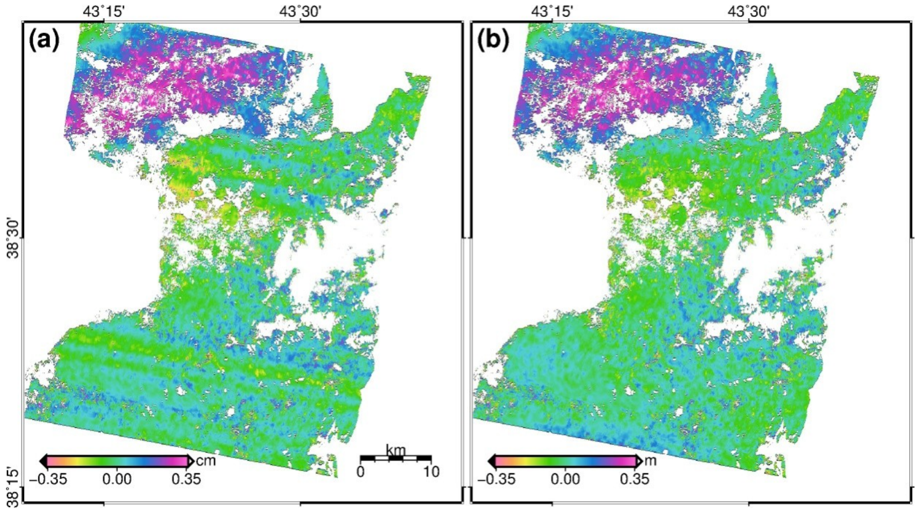

Figure 4.2 CSK azimuth displacement by the along-track interferometry and strips correction. (a) Original

azimuth interferogram with cross-track stripes; (b) corrected azimuth interferogram after applying a band-cut filter.

Along-track interferometry was implemented to generate an along-track (azimuth) interferogram for the CSK pair of 20111010-20111023 using the open-source codes developed by Barbot *et al.* (2008). A precision of 0.1 m can be obtained when a bandpass filter is applied to an already focused SLC image to separate it into forward- and backward-looking scenes (Bechor and Zebker, 2006; Barbot et al., 2008; Hu et al., 2012; Feng et al., 2013b). Note that along-track InSAR phase is not sensitive to SAR orbital errors, in the way that along-track pixel offsets are. Additionally, some across-track stripes can be observed in the original CSK azimuth interferogram (Figure 4.2(a)). These regular signals should not result from the coseismic rupture, which have been largely suppressed by applying a band-cut filter (Kobayashi et al., 2009) (Figure 4.2(b) and Figure 4.3 (b)). A southward movement can be clearly observed in the NW part of Figure 4.3(b), suggesting that the event occurred on a NW-dipping thrust fault which is consistent with the azimuth subpixel offset map in a previous study (Fielding et al., 2013).

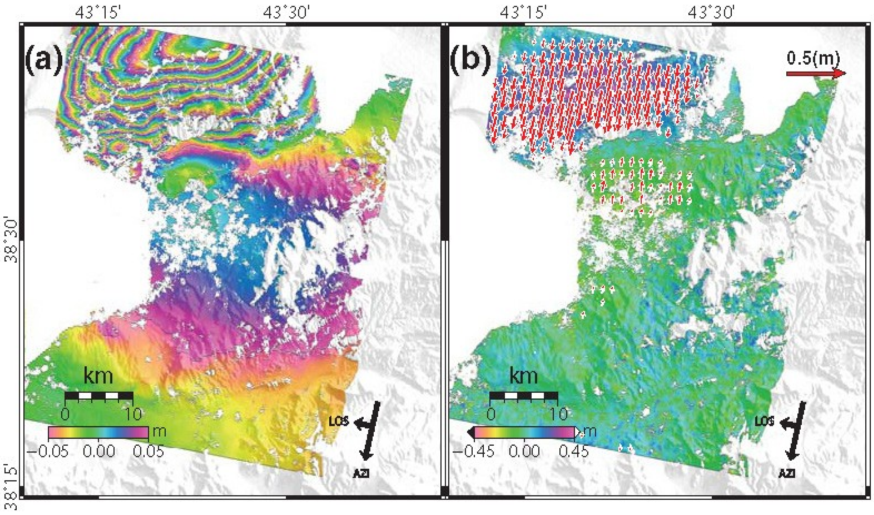

Figure 4.3 Coseismic range and along-track changes associated with the 2011 Van (Turkey) Earthquake from Feng *et al.* (2014). CSK pair spanning the period from 10th October 2011 to 13th October 2011: (a) Coseismic interferogram with LOS range changes being re-wrapped in the range of -0.05 to 0.05 m. (b) Along-track (azimuth) displacement from the spectrum splitting method (Barbot et al. 2008). Arrows represent horizontal surface movements in the along-track direction.

4.2.3 Postseismic motion

Two independent pairs of SAR images collected after the main shock were analysed to investigate postseismic motion: the CSK2 pair from 4 h to three days after the mainshock and the RS2 pair spanning 48 days from the fourth day after the mainshock (Table 4.1). In Profiles A-A', B-B', E-E' and F-F' of Figure 4.4, uplift signals of up to 0.06 m can be observed near the fault trace above 38.65 °N in the CSK2 interferogram, which are thought to be due to aftershocks (Elliott et al., 2013). Subsidence signals can also be seen in all the six CSK2 profiles, and similar signals appear in Profiles B-B', C-C' and D-D' in the RS2 interferogram covering a 48 day interval after the 23 October 2011 mainshock, suggesting that these signals are surface movements and not generated by atmospheric effects. These results also indicate that the ASAR coseismic interferogram using a second image acquired eight days after the main shock will also contain postseismic signals.

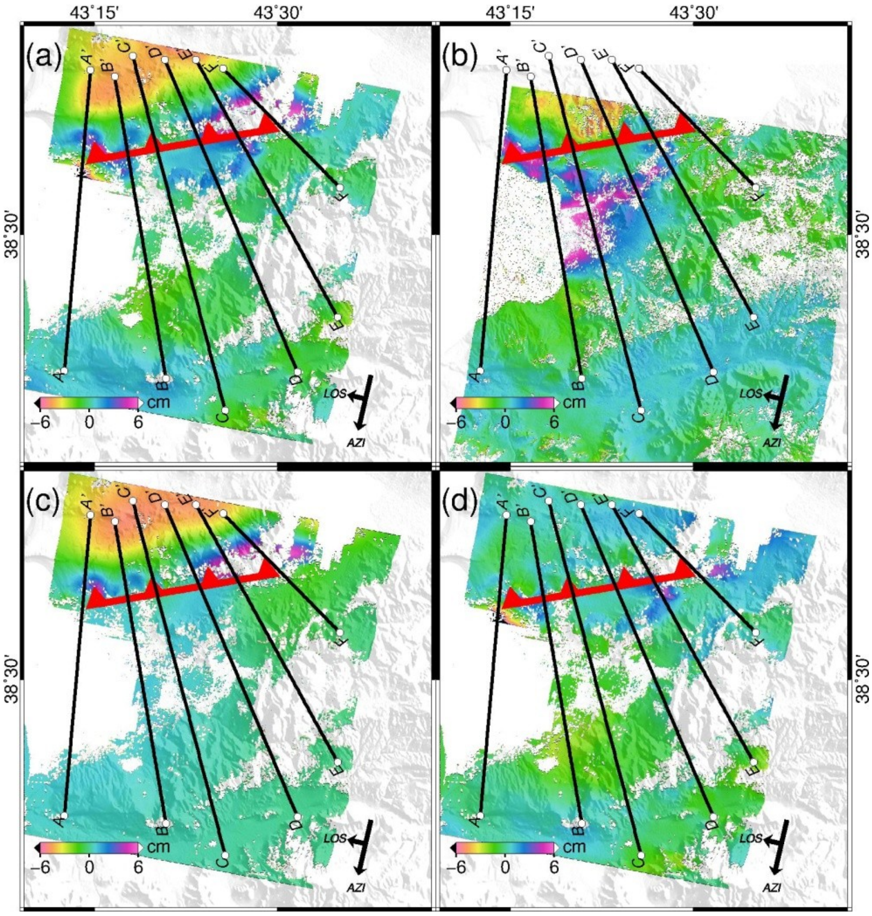

(***Figure 4.4***)

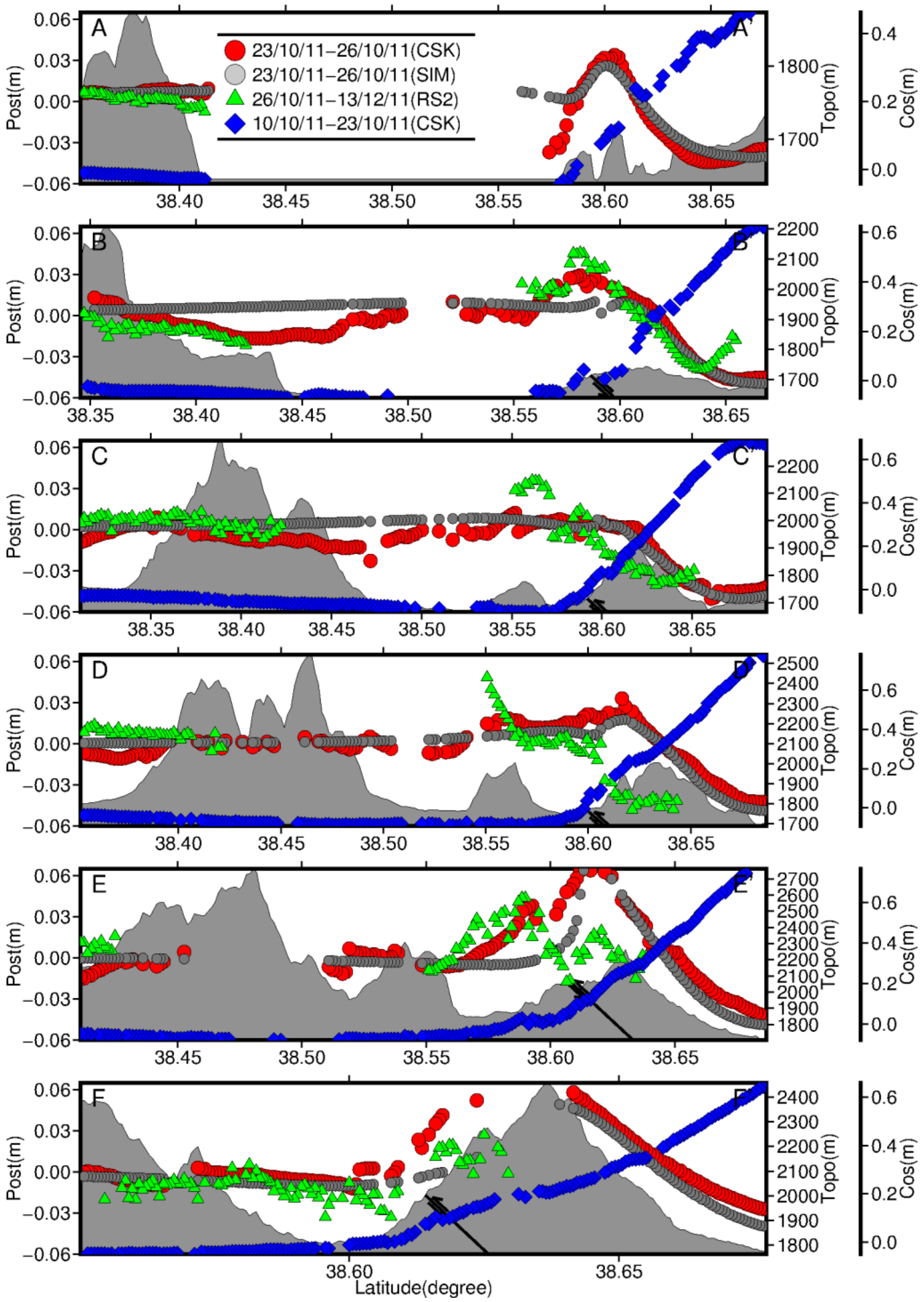

Figure 4.4 Postseismic interferograms from both CSK and RADARSAT SAR images and profiles analysis from Feng *et al.* (2014). (a) CSK2 postseismic interferogram covering the period from 23rd October 2011 to 26th October 2011; (b) RS2 postseismic interferogram covering the period from 26th October 2011 to 13th December 2011. (c) Modelled CSK2 postseismic interferogram from the best-fit afterslip model. (d) the residuals between (a) and (c). Profiles A-A', B-B', C-C', D-D', E-E' and F-F' show postseismic (red dots for CSK2 and green triangles for RS2) and coseismic (blue diamonds) range changes in the LOS direction as well as topography variations (grey shadow). Note that profile locations are shown in (A) and (B), and red lines in (A) and (B) and black lines in all the profiles indicate the fault location.

4.2.4 Coseismic modelling

To avoid possible spatial correlation of pixels and to accelerate modelling, interferograms were downsampled to create more manageable data sets with a data resolution-based (Rb) decomposition algorithm (Lohman and Simons, 2005). 1104 and 1375 points were extracted from the conventional and azimuth CSK interferograms (Figure 4.5 (a,b)), respectively. Azimuth displacements were weighted with a relative factor of 0.15 to LOS range changes based on the residuals after subtracting the best-fitted model with an equal weight, and all data points in each dataset were equally weighted.

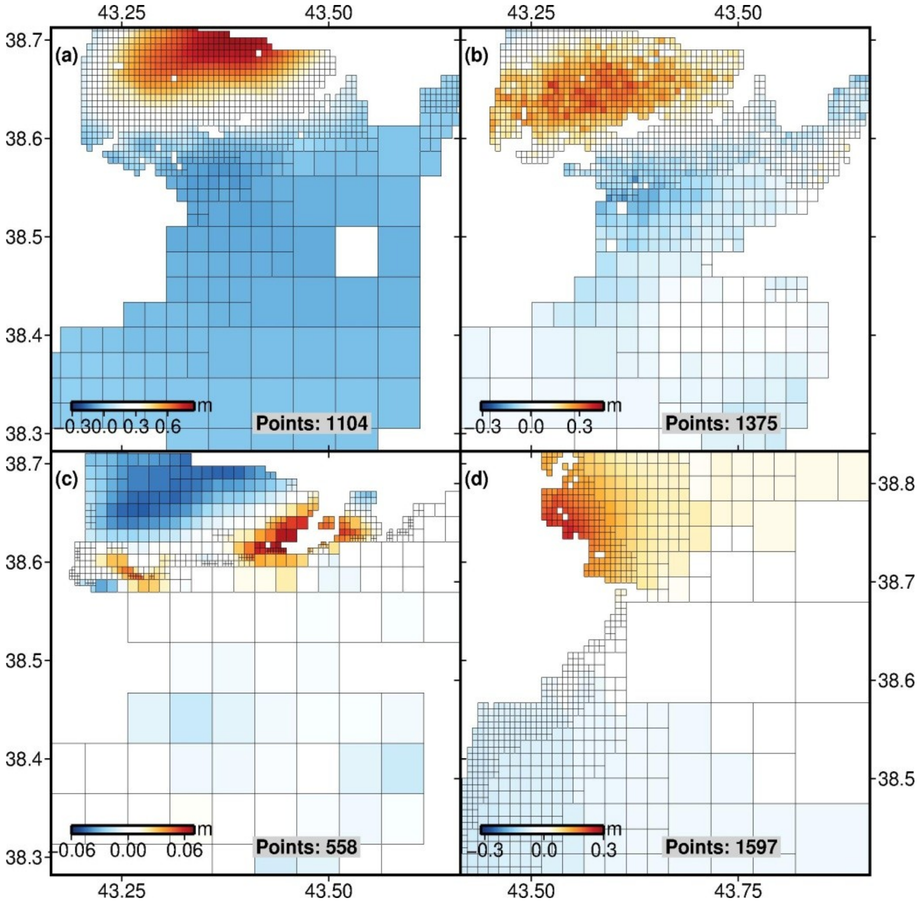

Figure 4.5 Downsampled datapoints from used interferograms. (a) CSK LOS range changes; (b) azimuth displacements; (c) postseismic displacements from CSK2 using the resolution-based method (Lohman and Simons, 2005) and (d) the downsampled datapoints from ASAR LOS range changes by the same method as above.

Based on field survey (Doğan and Karakaş, 2013), the 2011 Van earthquake was recognized as a blind faulting event that did not break the surface. There is insufficient evidence to determine if the rupture occurred over a non-planar surface. Therefore, for simplicity, a single fault plane was used to characterize this earthquake. A two-step inversion strategy was employed to determine its source parameters and variable slip distribution which comprises a nonlinear inversion for determining the fault geometry, and a linear inversion for estimating the slip distribution along the ruptured fault plane. The elastic half-space dislocation model (Okada, 1985) was used for generating a Green's matrix.

In Step 1, the weighted best-fit function ε was designed to determine the optimal geometric parameters using

$$\boldsymbol{\varepsilon} = \sqrt{\frac{(\boldsymbol{W}(\boldsymbol{D}-\boldsymbol{GS}))^2}{N}} \tag{4.1}$$

where G is the design matrix for the surface response of 1 m slip over the uniform rectangular fault in the radar line of sight (LOS) with a unit length and width for both strike and dip components, S is the slip vector, W is the relative weight for each dataset, D are the downsampled coseismic observations and N is the number of observations used in the inversion. The best-fit uniform model suggests that the earthquake occurred on a NNW dipping fault with a strike of 261.3° and a dip of 47.3° (Table 4.2).

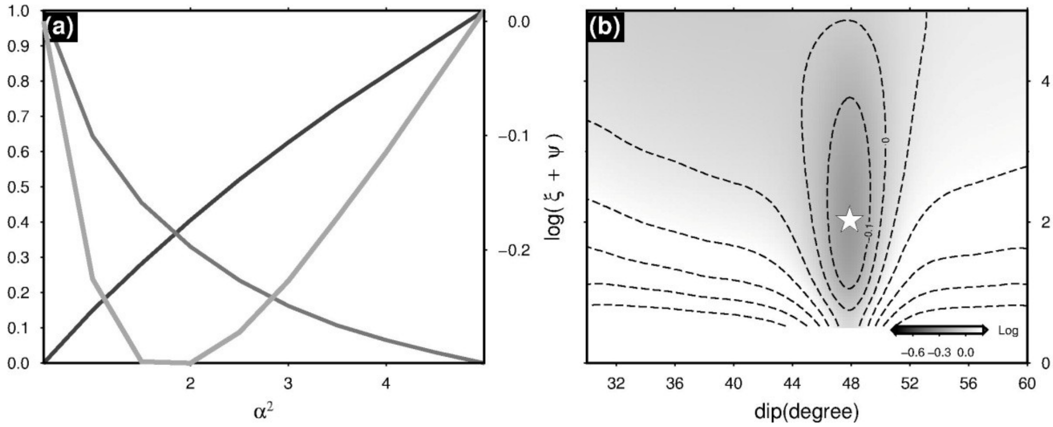

Figure 4.6 Optimal dip angle and smoothing hyperparameter determined by a logarithm analysis. a) Trade-off curve line associated with the model with a dip angle of 49°. Thick black lines show the trends of model roughness and the residuals of modelled simulations after normalizing ($[\boldsymbol{\xi}, \boldsymbol{\psi}]$), respectively, whilst the solid grey line represents $\boldsymbol{log}(\boldsymbol{\xi} + \boldsymbol{\psi})$. (b) Contour map of $\boldsymbol{log}(\boldsymbol{\xi} + \boldsymbol{\psi})$ with variations of dips and the hyperparameter ($\boldsymbol{\alpha}^{\mathbf{2}}$). White star indicates the global minimum.

In Step 2, using the fault geometry determined in Step 1, the fault plane was extended along strike and downdip by increasing its total length to 40 km and downdip width to 40 km, and then divided into 400 sub-faults each measuring 2 km by 2 km. The best fit values of strike-slip and dip-slip motion for each sub-fault were solved using a non-negative least squares algorithm (Ward and Barrientos, 1986). Meanwhile, a Laplacian smoothing constraint was employed to prevent physically impossible oscillatory slip (Harris and Segall, 1987). In the linear inversion step, the basic inverse problem was expressed by

$$\begin{bmatrix} \boldsymbol{G} \\ \boldsymbol{\alpha}^2\boldsymbol{L} \end{bmatrix} \boldsymbol{S} = \begin{bmatrix} \boldsymbol{D} \\ \boldsymbol{0} \end{bmatrix} \tag{4.2}$$

where L is an order-2 differential operator defined by Harris and Segall (1987) for a roughness estimate and α^2 is the controlling parameter. Since the fault dip angle obtained from the uniform inversion (Step 1) may differ slightly from the global optimal parameters for slip distribution (Burgmann et al., 2002a; Fukahata and Wright, 2008), an iterative approach was implemented to estimate the optimal dip angle in the slip inversion (Feng et al., 2013a). As shown in Figure 4.6, the optimal dip angle was determined by minimizing the integrated objective function $log(\xi + \psi)$. ξ

and ψ were RMS and model roughness function of smooth parameter (α^2) corresponding to the given dip angle. Figure 4.6 (a) illustrated that the log function can have only one minimum which can offer us a chance to determine a solution uniquely. More details on this method can be found in our previous paper (Feng et al., 2013a).

Our optimal slip model with CSK LOS range changes and azimuth displacements suggests that the maximum slip of 6.5 m occurred at a depth of 12 km with a purely reverse slip (Figure 4.7(a)). The major slip area is concentrated between 8 and 25 km. Slip of >3 m is found at shallower depths with a secondary maximum at 10 km depth SW of the epicentre, up to ~ 10 km away from the maximum slip location (Figure 4.7(a)). This two-patch slip distribution is supported by a two-point source solution (Zahradník and Sokos, 2014) and the seismic rupture solution in Fielding *et al.* (2013). The released moment from the variable slip model reaches up to $4.19+10^{19}$ N.m, approximately equivalent to a moment magnitude of M_W 7.03. Figure 4.8 shows CSK observations, simulated interferograms from the optimal slip distribution, and their residuals. The best-fit slip distribution agrees well with CSK observed displacements with small root mean square (RMS) misfits: 0.015 m to CSK LOS range changes, 0.070 m to CSK azimuth displacements.

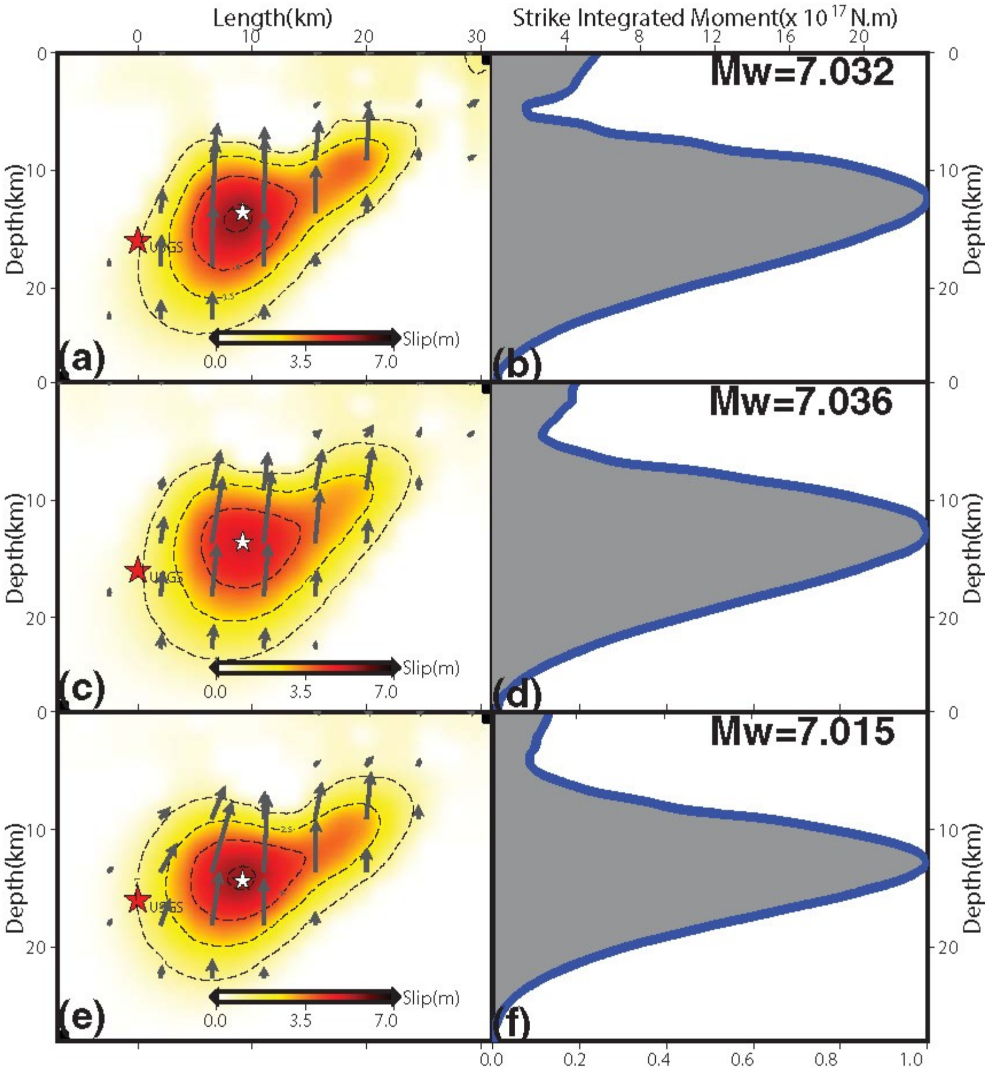

Figure 4.7 Optimal Slip models based on different surface constraints from Feng et al. (2014). (a) Model A: Slip distribution determined with CSK LOS range changes and azimuth offsets; (b) Released moment for Model A; (c) Model C: slip distribution determined with a combination of CSK and ASAR; (d) Released moment for Model C; (e) Model E: slip distribution with a layered earth model using the same constraints as Model A; (f) Released moment for Model E. Noted that an identical dip angle of 49° was used in Models A, B and C.

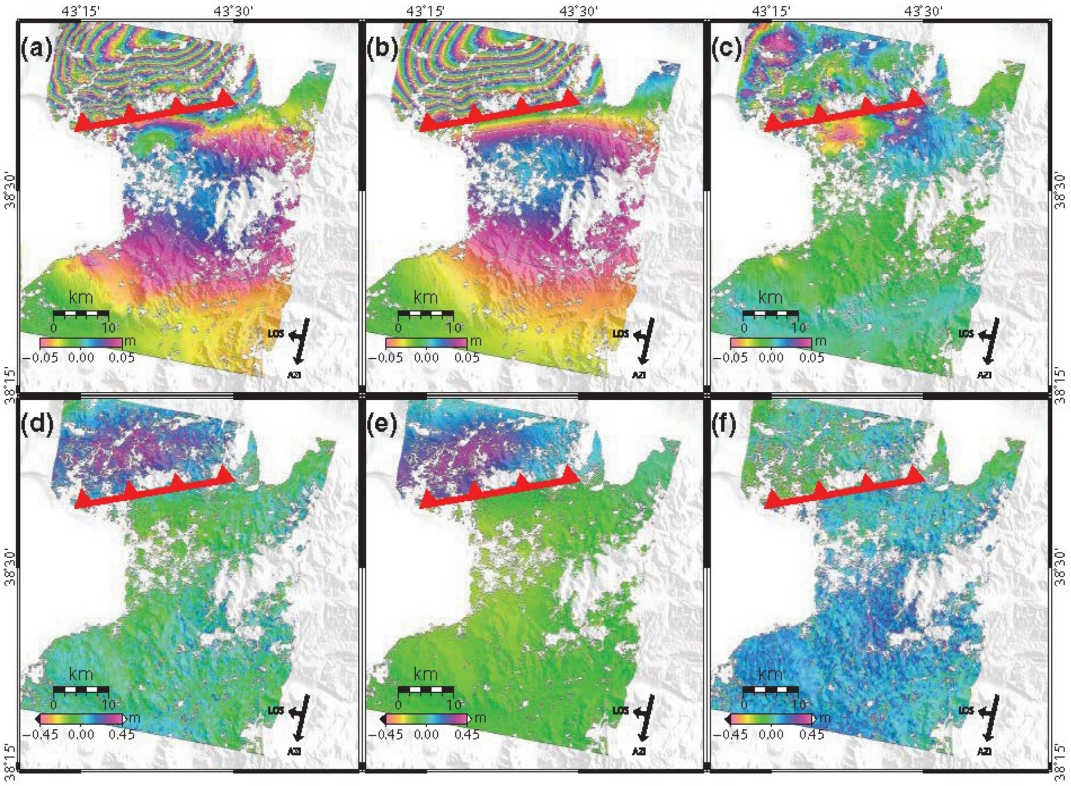

Figure 4.8 InSAR observations, simulations and residuals from the best-fit slip model from Feng *et al.* (2014). (a) Coseismic LOS range changes from CSK1; (b) Simulated interferogram from the best-fitting slip model; (c) Residual interferogram between (a) and (b). (d, e, f) are similar to (a, b, c), but for azimuth displacements from the same pair.

To determine errors for the optimal slip distribution, a Monte Carlo simulation of correlated noise was used (Wright et al., 2003; Funning et al., 2005b; Parsons et al., 2006; Li et al., 2008). A 1-D covariance function was estimated using the residual interferogram. Using a variance-covariance matrix for the sampled data points, 100 sets of correlated noise were simulated to create 100 perturbed data sets. The linear inversion procedure was applied to each of these data sets and the distribution of best fitting solutions provides information on slip errors (Figure 4.9). The largest uncertainties in the dip-slip, < 0.8 m, are at 20 km depth (Figure 4.9(d)), which is an order or magnitude smaller than the optimal slip (Figure 4.9(a)). The uncertainties in the strike slip near the surface (Figure 4.9(c)) might be due to the differences between our simplified fault plane model and the slightly curved and stepped geometry of the real fault trace. The average slip uncertainty is less than 0.25 m, providing confidence about the overall slip distribution.

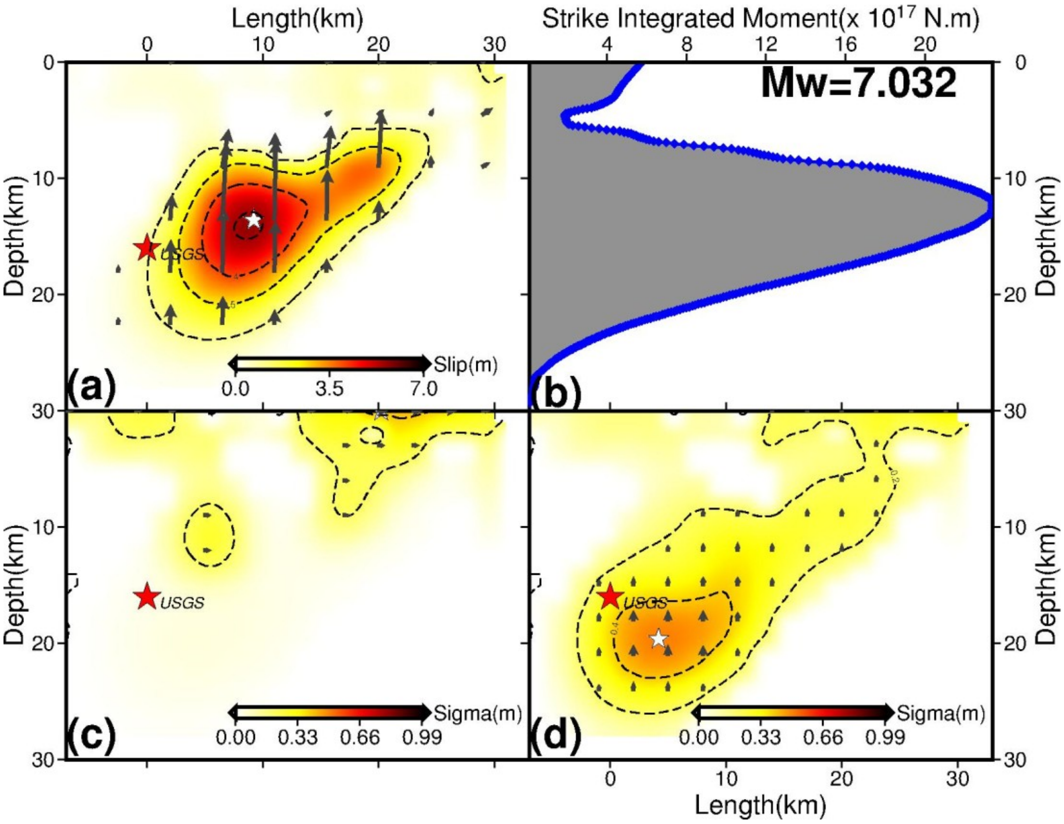

Figure 4.9 Distributed slip model uncertainty analysis from Feng *et al.* (2014). (A) Slip distribution with CSK LOS changes and azimuth displacements; (B) Released moment along depth; (C) and (D) Errors in the distributed slip calculated from the standard deviation of the slip distributions obtained by inverting 100 perturbed interferograms: the former for the strike-slip component, the latter for the dip-slip component. The colour scale is one seventh of the interval used for the slip panel. For all the fault patches the fractional error is small.

The ASAR coseismic interferogram covers the period from 5th November 2010 to 31st October 2011, so it includes postseismic motion within the first 8 days after the mainshock. To examine the impacts of including postseismic signals on coseismic modelling, 1597 datapoints (Figure 4.5(d)) were extracted from the ASAR interferogram using the data resolution-based resampling method as used for CSK data. Equal weights were applied in modelling for both ASAR and CSK1 LOS range changes, as in previous studies (Elliott et al., 2013). Figure 4.7(c) shows the resultant best-fit slip distribution. This overall slip pattern is generally consistent with the model constrained only using CSK data (Figure 4.7(a)), but the maximum slip is more than 1 m lower in the joint inversion. This difference is most likely to be due to postseismic movement affecting the ASAR phase measurements. Therefore, Model A derived from CSK1 LOS range changes and azimuth offsets is the preferred model of the coseismic slip distribution in this study.

4.2.5 Postseismic modelling

The only available CSK2 interferogram covering the period from 4 h to 3 days after the mainshock was used to determine the initial postseismic behaviour following the main shock. Several physical mechanisms can contribute to postseismic deformation (Fialko, 2004a; Ryder et al., 2007b), including afterslip, poroelastic rebound and viscoelastic relaxation. Following Peltzer *et al*'s (1998) approach different Poisson's ratios were used for undrained and drained upper crust conditions to simulate potential surface deformation caused by poroelastic relaxation. This modelling produced a pattern of uplift which is opposite to that observed from the postseismic interferograms in this study. Thus, fluid flow in the porous media can be ruled out as a postseismic deformation mechanism. Viscoelastic relaxation induced deformation in the CSK2 observations should also be limited since this interferogram covers only the first 3 days which is an insufficient time to generate significant surface movements given that the viscosity of lower crust in this region could reach up to 10^{18} Pa.s (Riva and Govers, 2009) that is similar with other estimates from postseismic relaxation (Ryder et al., 2007a; Ryder et al., 2011). Therefore, only afterslip is considered to be a significant contribution to postseismic deformation.

The same optimal fault geometry and fault discretization that were determined in the coseismic modelling were applied in postseismic modelling. 558 points were extracted by the data R-based downsampling method (Figure 4.5(c)) . The same distributed slip inversion strategy as described above was applied to determine a best-fit afterslip model. The best-fit afterslip Model (a) suggests two slip concentrations at the depths of 5 and 20 km respectively (Figure 4.10(a)). It is notable that the deep slip centre is concentrated in the principal coseismic rupture zone (Figure 4.9). The resolution of slip model is usually low at depth (Elliott et al., 2013), therefore the uncertainty of the afterslip model at depth can be relatively high. To rule out the possibility that the deep slip is caused in part by the uncertainty in the inversion, further postseismic slip modelling was carried out as performed in the GPS postseismic displacement modelling by Johnson *et al.* (2012b). In this inversion, afterslip in the coseismic rupture zones with slip >0.5 m was not permitted. Here, the threshold of 0.5 m is based on the coseismic slip uncertainty analysis (Figure 4.9). Then, the new best-fit afterslip, Model (b) was obtained using the same surface constraints as used for Model (a). Model (a) and Model (b) can explain the observation equally well. The standard deviation of residuals for LOS displacements of Profile A-A' (Figure 4.4) are 0.013 m and 0.012 m from Model (a) and Model (b), respectively. Relatively, Model (b) can explain the data slightly better, and so this model is selected for the further analysis.

The postseismic slip is concentrated in the zone directly above the locus of coseismic rupture, has a maximum slip of 1.5 m, and approaches but does not break the surface. The accumulative moment release is up to $1.5+10^{19}$ N.m, which is equivalent to a magnitude 6.7. As shown in Figure 4.4, modelled CSK LOS changes (grey points) are in good agreement with observations (red ones) with an average correlation coefficient of 0.86.

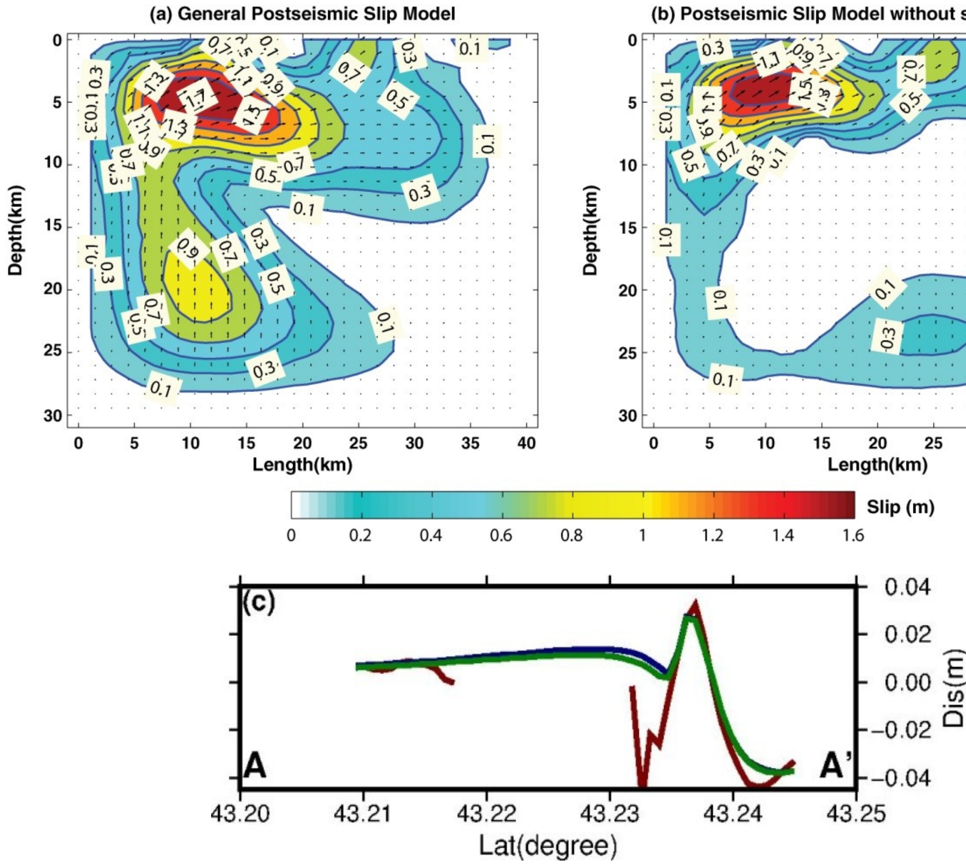

Figure 4.10 Comparison of the postseismic slip models derived by two inversion strategies. (a) The traditional inversion method; (b) the new method without afterslip in the asperity and (c) comparison of observations and modelled values. Red line shows the observations, whilst green and blue ones represent Model (a) and Model (b), respectively. The simulation based on the optimal afterslip model in 2 dimensions can be found in Figure 4.4.

4.3 Discussion

4.3.1 Effects of layered Earth model on the variable slip model

The localized crustal structure in the vicinity of the epicentre from the Crust 2.0 database shows some stratification , particularly in the upper 20 km where the major coseismic rupture occurred. Wang *et al.* (2010) suggested that effects of a layered earth model might be significant in some cases of coseismic modelling, therefore a numerical experiment with a layered model was performed (Figure 4.12). The package PSGRN/PSCMP developed by Wang *et al*. (2006b) was employed to generate the unit slip surface response in the data inversion. As presented in Figure 4.7(e), the best-fit model suggests that the maximum slip and distributed patterns are consistent with those from the elastic half-space Model A, both having RMS of 5 mm for InSAR observations. The average rake angle of the patches with slip > 1.5 m is ~79°, which is closer to the seismic solution (Irmak et al., 2012) relative to an average rake angle of 86° determined from the elastic half-space model.

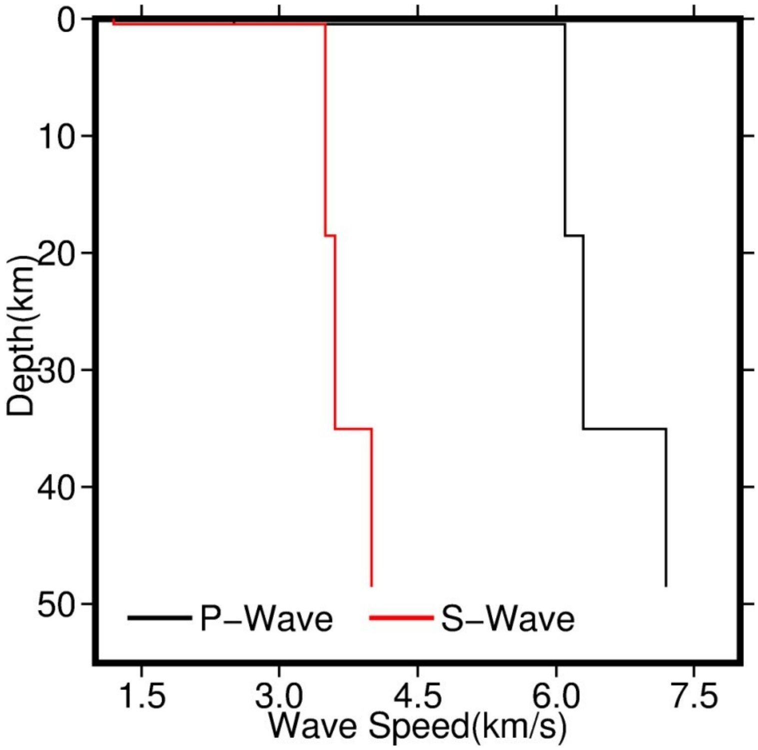

Figure 4.11 Variation in S and P wave speed with depth for the Van region from Feng *et al.* (2014). The data used in the figure is from the Crust2.0. (http://igppweb.ucsd.edu/~gabi/crust2.html).

An independent examination was also performed using regional GPS coseismic measurements (Figure 4.12). The RMS of 3.9 mm for horizontal components from Model A drops to 2.6 mm for those from Model E, whilst the RMS of 5.0 mm for vertical components drops to 4.9 mm for Model E. The correlation between simulated and observed horizontal components exceeds 0.96 for Model E, against 0.86 for Model A. There is a discrepancy between GPS measurements from (Altiner et al., 2013) and those posted on the Geohazard Supersite (http://supersites.earthobservations.org/van.php), possibly due to different strategies used in GPS data processing. For instance, Altiner *et al* (2013) give a south-north displacement at the MURA station of ~34.02 mm (Altiner et al., 2013), whilst the GEO-Supersite provides a value of 54.5±3 mm. The vertical components have large uncertainties (Altiner et al., 2013) and are not suitable for verifying slip models. However, the high consistency between Altiner *et al*'s GPS horizontal components and those simulated by Model E suggests that the layered slip model is preferable in this event. The major differences between Models A and E mainly come from the shallow part (less than 6 km), where there is the largest uncertainty in determining slip (Figure 4.9).

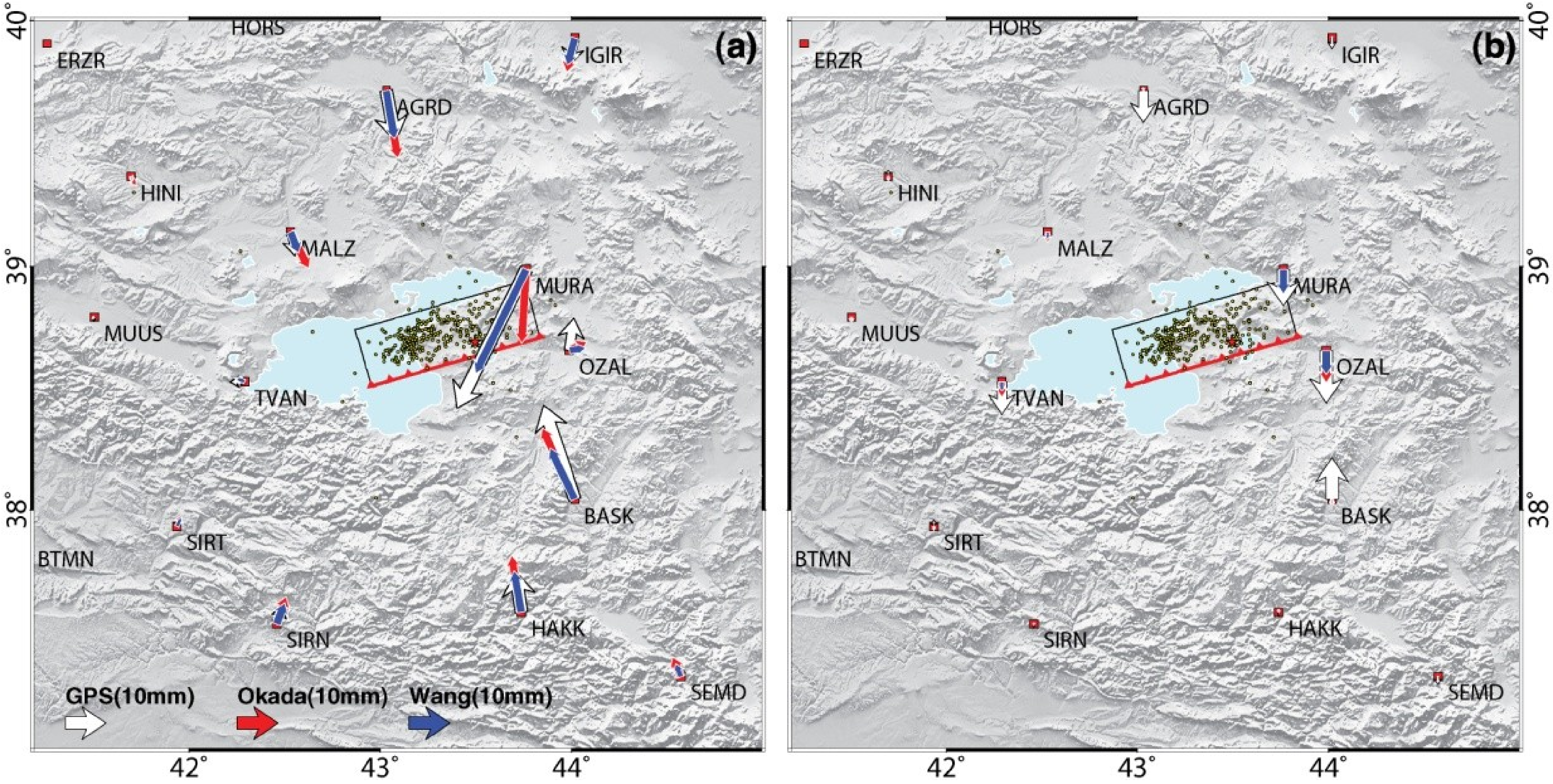

Figure 4.12 Independent validation of the InSAR-based slip model of the 2011 M_W 7.1 Van (Turkey) earthquake from Feng *et al.* (2014). (a) Horizontal GPS coseismic observations (white arrows) provided by Altiner et al. (2013) and simulated displacements using the Elastic half-space Earth model (red arrows), and Elastic layered Earth model (blue arrows). (b) As for A, but for vertical displacements.

4.3.2 Comparisons with published slip distributions

There have been several seismic solutions published for the 2011 Van earthquake (Irmak et al., 2012; Fielding et al., 2013; Utkucu, 2013; Zahradník and Sokos, 2014), most suggesting that the major rupture propagated along the dip direction from its origin to 10 s with a maximum slip of ~4 m near the epicentre, and another small amount of energy was released from 10-18 s (Irmak et al., 2012; Fielding et al., 2013). The entire rupture lasted for less than 20 s. The principal planes with strike ranging from 241° to 281°, dip from 38° to 71° and rake from 59° to 71° were determined through the focal moment inversion. Although the depth of the maximum slip varies in the published slip models, the major slip patch is observed with a maximum magnitude of ~4 m in the deeper part followed by a small shallow event in the seismic waveform inversions (Irmak et al., 2012; Fielding et al., 2013), which is also supported by two-point source modelling (Zahradník and Sokos, 2014).

Two geodetic models have also been published for this large event (Elliott et al., 2013; Fielding et al., 2013), both suggesting that the maximum slip occurred at a depth of 12-14 km, but with different slip magnitudes and patterns as shown in Figure 4.13. A complicated slip model with two-equal-size slip patches with a maximum of ~9 m at a depth of 12-14 km for both patches was determined by Elliott *et al.* (2013), which may relate with the employed geometric model and inversion method. A single-patch slip distribution with a maximum slip of ~ 4 m at a depth of 12 km by Fielding *et al.* (2013) using GPS and a different CSK pair together which includes significant postseismic observations, with identical ASAR pairs. It is notable that: (1) two identical ASAR pairs were used in both studies for coseismic modelling; (2) Elliott *et al.* (2013) used a CSK coseismic pair with the second image acquired just 4 h after the main shock, whilst Fielding *et al.* (2013) used one with a CSK image acquired 3 days later; and, (3) Fielding *et al.* (2013) included CSK azimuth offsets and GPS released by JPL in their modelling.

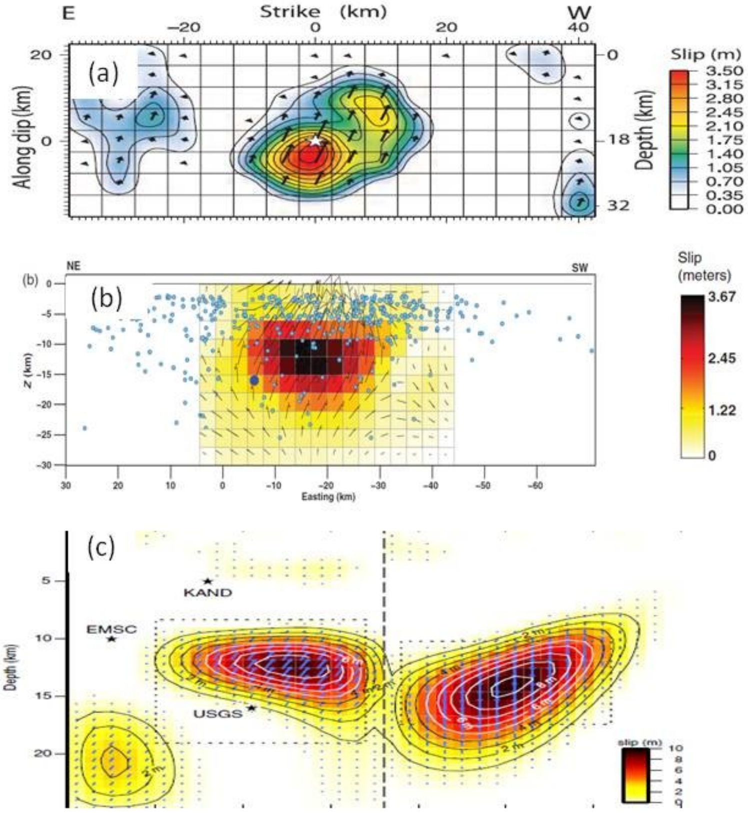

Figure 4.13 Comparison of published slip models determined in other studies. (a) the seismic slip model (Fielding et al., 2013); (b) the InSAR based slip model with subpixel offsets maps and LOS changes from ASAR and CSK SAR observations (Fielding et al., 2013) and (c) the InSAR inferred slip model derived from CSK and Envisat interferograms (Elliott et al., 2013).

To minimize the impacts of postseismic signals, ASAR pairs were excluded and only InSAR observations and along-track (azimuth) displacements from the CSK pair that minimises post-seismic motions were used in our coseismic modelling (Table 4.1; Section 2.4). Note that both the beam splitting technique in this study and the SAR offset technique used by (Fielding et al., 2013) provide horizontal displacements in the satellite azimuth direction (along-track), and the former appears to provide observations with a better precision (~0.08 m for beam splitting, ~0.12 m for azimuth offsets) (Bechor and Zebker, 2006; Jung et al., 2009; Feng et al., 2013b). The maximum slip of 6.5 m at a depth of 12 km is observed in our preferred coseismic model. Additionally, a second shallow slip patch is seen at the southwest of the fault plane, which is similar to another two published seismic models (e.g. Irmak et al., 2012; Fielding et al., 2013) although it does not appear in the two published InSAR models (Elliott et al., 2013; Fielding et al., 2013). As mentioned in Section 2.4, a simplified fault plane was assumed in the coseismic modelling by neglecting the slightly curved and stepped geometry of the fault trace. Figure 4.7 shows that the major slip all occurred at the depth of at least 8 km, implying that the impact of this assumption of a simplified fault plane should be limited. On the basis of independent GPS data, the performance of the single slip model in this study is an improvement on that of the two-fault model determined by Elliott *et al*. (2013). Altiner *et al.* (2013) also gave a simple single-fault slip solution with a maximum slip of 4 m under the constraints of limited far-field GPS measurements. Because GPS observations are too distant from the fault and sparse to accurately determine the fault location and slip pattern, their slip model was not compared here.

4.3.3 Correlation between coseismic slip and topography

Two coseismic slip patches have been revealed through inverting the CSK coseismic observations in section 4.4. One ranges from 0 to 15 km along the strike direction with a maximum slip of 6.5 m at a depth of 12 km, the other ranges from 15 to 22 km along the strike direction with a maximum slip of 2.5 m at a depth of 8 km. The projected slip on the surface (Figure 4.14) is correlated with the surface topography, coseismic rupture extending through the low elevation area.

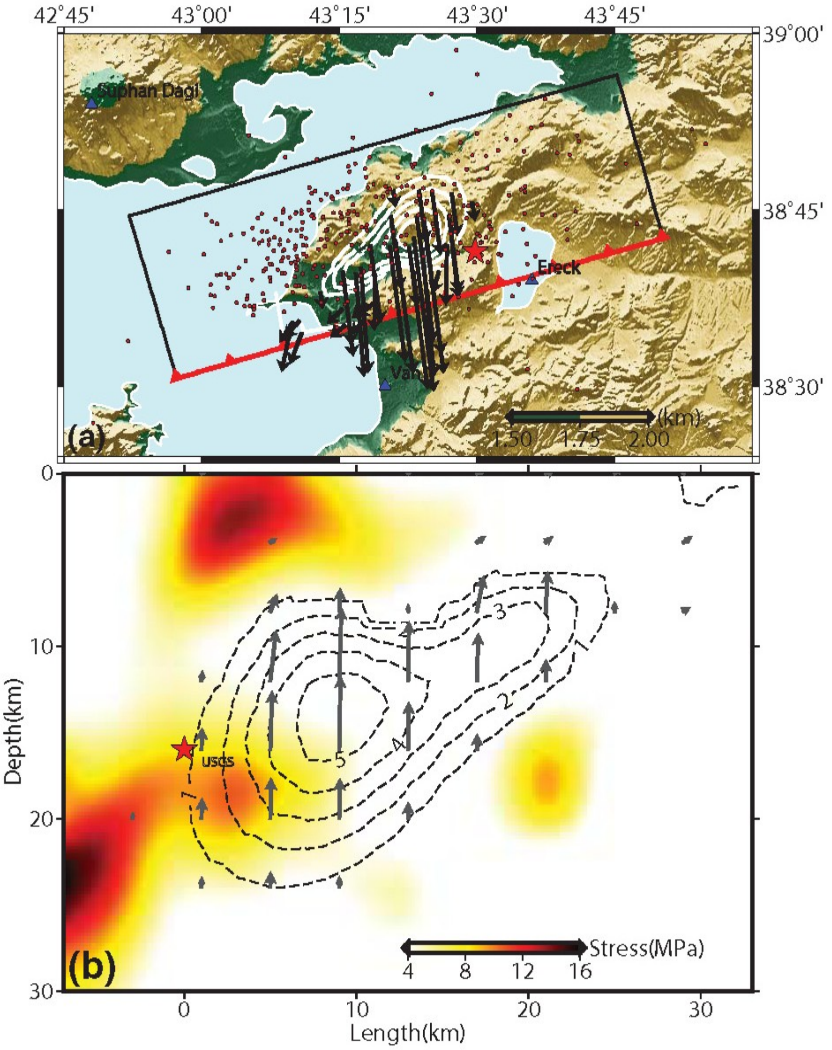

Figure 4.14 Optimal slip model spatial distribution and surface topography from Feng *et al.* (2014). (a) Correlation between the projection of coseismic slip distribution on the surface (white lines) and topography. The arrows imply the projections of slips over the fault surface onto the surface. (b) the down dip force exerted by surface topography onto the fault plane with the effective coefficient of friction of 0.1. The broken lines show slip contours and grey arrows the associated vectors.

The role of subducted seamounts in the nucleation and rupture propagation of large subduction earthquakes have been widely discussed (Bilek et al., 2003; Dixon and Moore, 2007; Das and Watts, 2009; Hicks et al., 2012; Schurr et al., 2012; Yang et al., 2013a). A series of earthquakes between 1983 and 1999 along the Costa Rican subduction zone led to the suggestion that spaced isolated seamounts could act as asperities (Bilek et al., 2003). Recent investigation of the 2010 Mule, Chile earthquake (Hicks et al., 2012) also suggested that the subducted structure can be conductive to the nucleation of earthquakes, and can also hinder coseismic slip and aftershock activities. The latter suggestion is consistent with the conclusions drawn from numerical experiments by Yang *et al.* (2013a).

To examine whether similar features can be found in the 2011 Van event, an intraplate large thrust earthquake, the relative shear stress exerted on the fault plane by the overlying topography was calculated. At a given depth, the relative gravity resistance along the inclined fault can be derived from $\sigma = \tau_t + \theta\sigma_t^n$, here τ_t and σ_t^n are the relative gravity ($\Delta G = \rho g \Delta h$) induced shear stress and normal stress on the plane, which can be determined using a trigonometric function of the fault dip angle. θ is a frictional coefficient (>0) and pore pressure is ignored. These calculations produce relative resistance ranging from 4 to 14 MPa along the fault plane as shown in Figure 4.14(b). Note that the major aim here is to identify the relative locations between mounts and the fault plane qualitatively, rather than quantitative stress analysis from topography. This pattern of stress suggests that the 2011 Van earthquake starts in the zone with relative high resistance and extends towards the area of low resistance, which implies that topography might be one factor influencing nucleation of a large intraplate thrust earthquake as well as the magnitude of rupture.

4.3.4 Mechanical implications of the slip models

Large earthquakes can permanently alter ambient stress level and trigger seismicity over a large area (King et al., 1994). Particularly, slip on blind thrust faults can significantly increase stress above the source fault and in other nearby zones (Lin and Stein, 2004). Driven by the coseismic stress, a fault may creep aseismically (Barbot et al., 2009a). Stress-driven creep has already been observed during postseismic and interseismic phases of earthquake cycles along different active fault systems (Johnson and Segall, 2004; Freed et al., 2006; Barbot et al., 2009a; Hetland and Simons, 2010; Johnson and Fukuda, 2010; Wang et al., 2012c). Therefore, better understanding of the mechanical properties within a fault system will improve seismic risk assessment following a large earthquake.

Stress drop is an important measure of static stress change in earthquakes (Noda et al., 2013), which can provide helpful evidence to estimate relative earthquake repeat time (Kanamori and Allen, 1986). It should also be noted that stress drop in earthquakes is independent with earthquake size based on a previous study (Shaw, 2009). In this study, the shear stress along the fault plane was calculated using a three-dimensional elastic dislocation model (Okada, 1992). The largest shear stress drop located in the earthquake zone reaches up to -12 MPa (decreased) (Figure 4.15(a)), which is compatible with the stress drop of 17 MPa during the 2010 M_W 8.8 earthquake (Luttrell et al., 2011). The upward shear stress increases along the fault plane and reaches a maximum of 5 MPa that is also nearly equivalent in magnitude with the Mule earthquake. Figure 4.15(a) shows that the zone of the greatest shear stress increase overlies the region of maximum afterslip. Since only one M_W 5.6 aftershock was recorded during the period from 4 h to three days after the mainshock, most of the postseismic moments revealed by the CSK2 interferogram are considered to be released by aseismic creep.

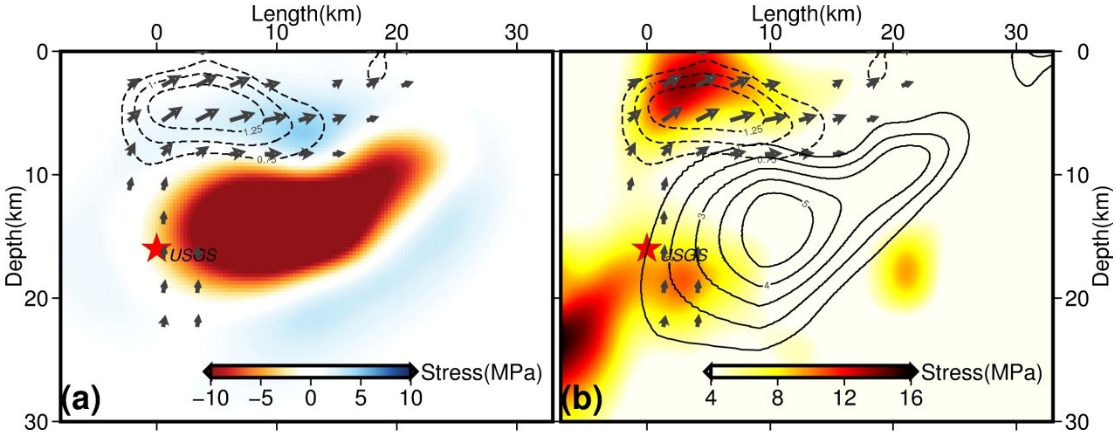

Figure 4.15 Stress triggering analysis on the fault from Feng *et al.* (2014). (a) Postseismic slip (grey arrows and dashed lines) overlaying the coseismic stress drop map. (b) Coseismic (solid lines) and postseismic (broken lines) slip contours overlaying the relative resistance exerted by surface topography.

Significant afterslip is concentrated in a small region that has a relative high resistance exerted by topography (Figure 4.15(b)). This is consistent with the previous suggestion that subducted mounts can be favourable locations for accumulating interseismic strain energy and where the failure threshold can be reached due to the effects of perturbed coseismic stress. Because no further postseismic observations covering the early postseismic period are available, the afterslip model remains uncertain. However, the RS2 postseismic interferogram which covers 4-52 days after the mainshock also shows a similar pattern, implying that the observations used in this study reflect the real postseismic behaviour.

Additionally, postseismic slip has an average rake angle of 30° for those slip patches with >0.5 m slip, which is significantly different from the value of ~80° (nearly pure dipping) determined for coseismic slip. This difference may suggest that large coseismic rupture significantly decreased stress in the vicinity of the earthquake rupture zone. For a thrust earthquake, the three principal stresses should be in the sequence $\sigma_1 > \sigma_2 > \sigma_3$, where the greatest stress σ_1 and intermediate stress σ_2 plunge horizontally, and the minimum principal stress σ_3 is vertical (Zoback et al., 1989). Although region stress cannot be constrained from a single fault (McKenzie, 1969) because the slip patches can be assumed as independent sources in the stress inversion, a qualitative analysis still can offer a chance to explore how coseismic processes affect the variation of the regional stress. The pattern of oblique afterslip with a mean rake angle of 30° implies the P-axes trending NE-SW along 33°, whilst P-axes determined from coseismic slip trend nearly N-S along 354°. Observation errors cannot account for the ~30° difference between these directions. The difference in orientations may indicate that the stress in the earthquake zone was decreased to a low level during the coseismic rupture, which is consistent with one seismicity analysis for this event (Görgün, 2013). If the focal mechanisms of a number of earthquakes before the mainshock can be collected, it would be possible to estimate deviatoric stress in the earthquake zone, as has been done for the 2011 Tohoku-Oki, Japan earthquake (Yang et al., 2013b). However, to determine the actual physical mechanism of the variation of principal stress directions is far beyond the ability of InSAR-only slip models.

4.3.5 Performance of the rate-state frictional law in the InSAR modelling

Afterslip Model (a) was determined without strong constraints on the slip at depth (Figure 4.10). A comparison of the energy along the depth from Model(a) and the coseismic slip model shows that the major afterslip zone with ~65% of the afterslip energy at the depth range from 0 to 10 km produced ~30% of the total seismic moment released during the mainshock (Figure 4.16). Meanwhile, significant afterslip of Model (a) can also be found in the major coseismic slip zone at a depth of ~20 km (Figure 4.16). It is clear that with the traditional geodetic modelling the relative spatial patterns of co- and post-seismic slip models in this case do not fully fit the classic velocity-weakening asperity law.

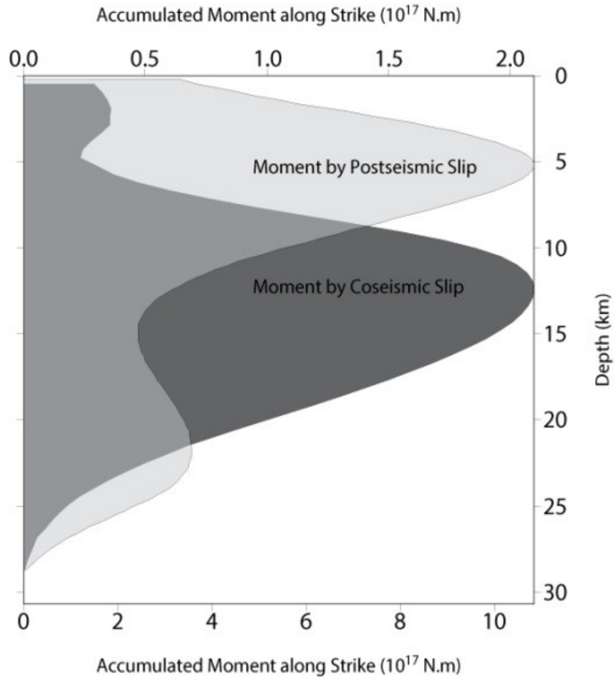

Figure 4.16 Seismic moments of the co- and post-seismic slip models distributed with depth.

However, the afterslip model (Model (b)) was determined using the same observations, but the assumption that no slip is permitted in the coseismic zone was applied. Therefore, the complementary relationship between the coseismic slip distributions and postseismic Model (b) can certainly be found between the coseismic slip model and Model (b) (Figure 4.15). Actually, Model

(a) and Model (b) can explain the data equally well (Figure 4.10). It is difficult to distinguish which model might be closer to the actual model because no additional dataset is available to further validate the afterslip models in this study. Although there is a significant uncertainty in the optimal afterslip model, the major afterslip zone at the shallow part of the fault shows clear complementary relationship with the coseismic slip model.

4.4 Conclusions

In this chapter, multi-source SAR images were used to investigate coseismic displacements of the 2011 Van (Turkey) earthquake, and rapid postseismic signals were observed even in the interferograms covering 3-day and 48-day periods after the main shock. Our modelling suggests that the use of interferograms with obvious postseismic signals can lead to a reduction of about 1 m in the calculated magnitude of the slip distribution, although with a similar slip pattern. Therefore, reliable coseismic slip modelling requires interferograms from data acquired soon after the event. The availability of such data will improve as more SAR missions with smaller repeat cycles are made available in the very near future.

Our preferred coseismic slip model with a careful selection of SAR observations (i.e. CSK1 interferogram and azimuth displacements, Table 4.1 and Figure 4.3) suggests: (1) this large event occurred on a north-west dipping thrust fault with a strike of 261° and dip of 49º; (2) a maximum slip of 6.5 m is observed at a depth of ~12 km; (3) a shallow asperity has been identified in the southwest of the major slip zone; and, (4) the released moment is equivalent to a magnitude of M_W 7.03.

The afterslip is also revealed by the second CSK interferogram which covers the first three days after the main shock. Our optimal afterslip model suggests that a maximum slip of 1.5 m occurred at a depth of 5 km, located directly above the locus of coseismic rupture. The accumulated moment in the first three postseismic days reached up to $1.5+10^{19}$ N.m. The accumulative moment release cannot be accounted for from the recorded aftershocks, suggesting the most of the postseismic moment is released by aseismic creep. An obvious variation in the slip vectors between coseismic and postseismic motions has been identified, which may imply a significant rotation of the axis of the greatest principal stress. As also found in the 1994 Northridge, California earthquake (Donnellan et al., 2002), rapid afterslip may commonly happen after a large earthquake, especially in thrust events.

Table 4.2 Source parameters determined by different techniques.

Def	Dataset	strike(°)	Lon	Lat	dip(°)	rake(°)	Length(km)	Width(km)	M_W[a]	Sources
GCMT	Seismic data	246	43.497[b]	38.691[b]	38	60	-	-	7.2	USGS[c]
Fielding	Seismic data	258	43.497[b]	38.691[b]	46	71	-	-	7.1	(Fielding et al., 2013)
Fielding	CSK & ASAR	259	43.497[b]	38.691[b]	42	-	-	-	7.13	As above
Irmak	Seismic data	246	43.3367	38.7188	46	59	-	-	7.13	(Irmak et al., 2012)
Elliott Model	CSK & ASAR	254	43.499	38.602	40	64	12	16.6	6.8	Elliott *et al.* (2013)
		254	43.329	38.593	55	93	12	8.9	6.8	
CSKU*	CSK Only	261.3	43.403[d]	38.702[d]	47.3	90	20.4	3.1	6.8	this study
CSKM*	CSK Only	261.3	43.403[d]	38.702[d]	49	88	40	40	7.03	this study
JointM	CSK & ASAR	261.3	43.403	38.702	49	90	40	40	6.99	this study

Note: a, M_W was calculated using the formula given by Kanamori *et al*. (1975): $M_W = 0.75\log10(M_o) - 6.033$, where M_o is the seismic moment released during the earthquake. Different values of the shear modulus are used, 44 GPa in Fielding *et al.* (2013) and 32 GPa in this study. b, The location of [lon,lat] represents the first motion determined by seismic wave data. c, http://earthquake.usgs.gov/earthquakes/eqinthenews/2011/usb0006bqc/. d, the location here represents the central point of the top boundary of the fault which has been extended to the Earth surface. *, Model CSKU was determined by the optimal CSK datasets using a uniform rectangular fault plane, whilst CSKM was the variable slip model based on the CSKU.

Chapter 5

Large coseismic slip variation of the 2011 M_W 9.0 Tohoku-Oki, Japan earthquake

In Chapter 4, large variations were found in the afterslip models of the 2011 M_W 7.1 Van, Turkey earthquake, which can directly affect the estimation of the velocity-strengthening (VS) regions on the main seismic fault. A similar situation may also unfold during coseismic slip modelling, thereby identification of velocity-weakening regions or asperities can be significantly influenced. As one of the best-observed subduction zone events, the coseismic slip distribution of the 2011 M_W 9.1 Tohoku-Oki earthquake has been widely investigated using different observations (e.g. Fujiwara et al., 2011; Simons et al., 2011; Minson et al., 2014). Significant differences between the published coseismic slip models have been observed (Huang and Ding, 2012; MacInnes et al., 2013). This chapter will re-estimate the coseismic slip model of this event through a joint inversion with GPS displacements and GRACE-based gravity changes. Meanwhile, two afterslip models derived from GPS observations covering different periods are collected. Combining the new coseismic slip models, the performace of the friction law in this event is discussed.

5.1 Introduction

On 11 March 2011, a M_W 9.0 earthquake struck the Pacific coast of NE Japan and triggered a destructive tsunami with a maximum wave height of up to 40.5 m (Simons et al., 2011). The mainshock occurred on the plate interface near the northeast coast of Houshu where the Pacific Plate is subducting beneath the North American Plate at a convergence rate of ~0.08 m yr^{-1} (DeMets et al., 2010). This was an unexpected event because Houshu region was believed to have a relatively low seismic risk prior to the mainshock (Hashimoto et al., 2009; Sagiya et al., 2011). A number of studies on its slip distribution have already been published using different observations (e.g. Avouac, 2011; Feng and Jonsson, 2012; Kodaira et al., 2012; Hooper et al., 2013; Tajima et al., 2013; Wang et al., 2013b). Using different observations, e.g. GPS, seismic waveform, InSAR and strong ground motions, significant different coseismic slip models have been successively published (e.g. Simons et al., 2011; Minson et al., 2014). Large variations between these models (Bilek et al., 2012; Tajima et al., 2013) imply that the data used in the previous coseismic modelling does not fully reflect the source information of the mainshock. Further efforts on the coseismic slip model of the 2011 mainshock are still needed.

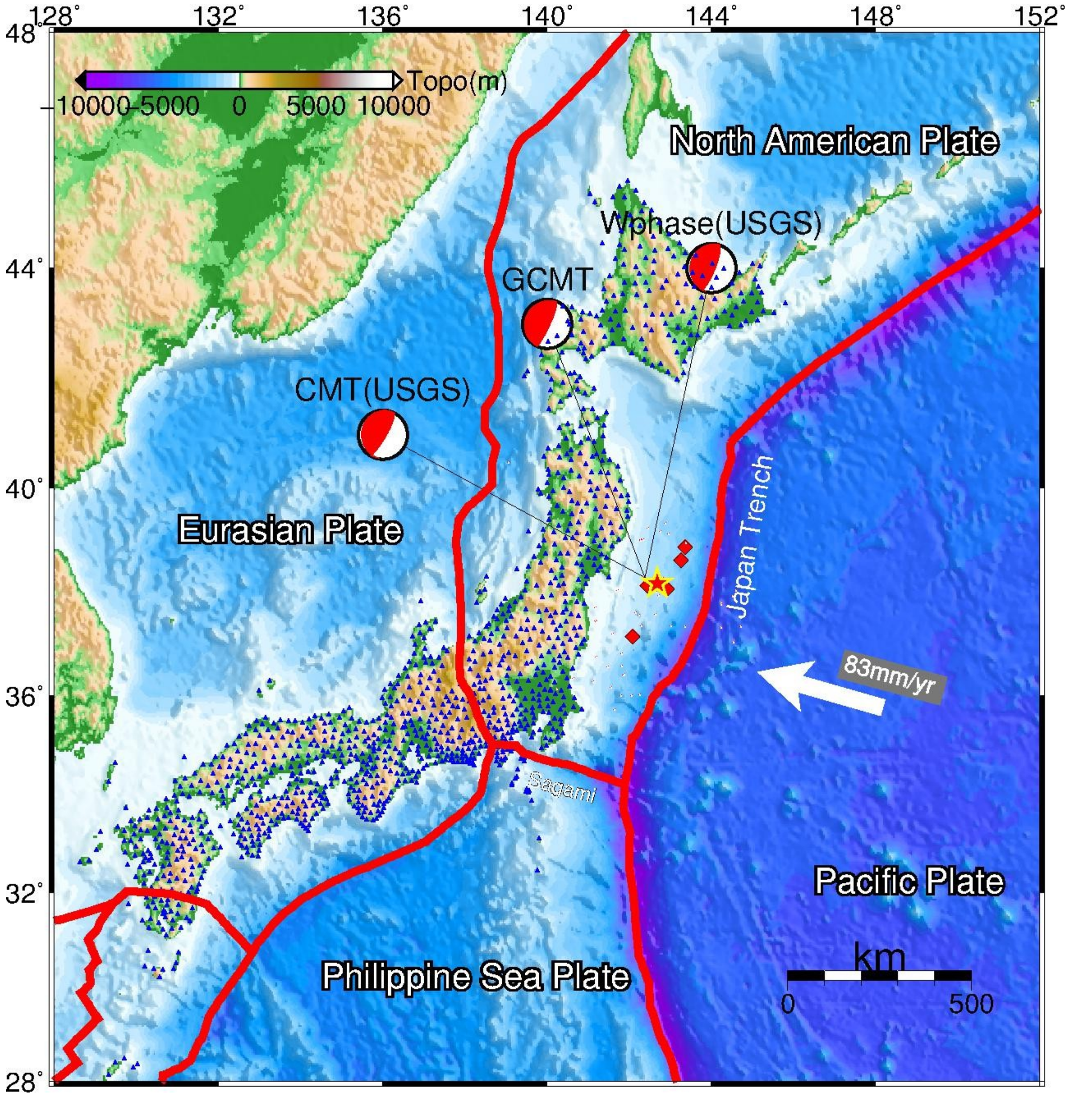

Figure 5.1 Tectonic setting of the 2011 M_W9.1 Tohoku-Oki earthquake. Red lines indicate the plate boundaries around the Japan Islands (Bird, 2003), blue triangles represent inland GPS stations, and red diamonds denote five seafloor GPS sites used by Sato et al (2011b). Red star is the earthquake epicentre provided by USGS.

The GNSS Earth Observation Network (GEONET) operated by the Geospatial Information Authority of Japan (GSI) recorded inland coseismic surface displacements due to the 2011 Tohoku-Oki earthquake with an average station spacing of about 20 km, and these observations have been widely used to determine coseismic slip models for this earthquake (e.g. Ozawa et al., 2011; Simons et al., 2011; Ozawa et al., 2012). Coseismic displacements on the sea floor were also recorded by five GPS/acoustic combination stations that are closer to the epicentre than the GEONET stations (Sato et al., 2011a). These few seafloor measurements have also been employed to constrain slip distributions (Yamazaki et al., 2011; Iinuma et al., 2012; Romano et al., 2012; Yamazaki et al., 2013). As shown in Figure 5.1, the dense onshore GEONET stations are all distant from the source, the nearest station being over 120 km from the epicentre. So far, only coseismic measurements on the hanging wall of the main fault were used for coseismic modelling and no ground geodetic observations have been reported on the footwall side.

The Gravity Recovery and Climate Experiment (GRACE) satellites were launched in 2002, and have been used to successfully recover coseismic gravity changes resulting from large earthquakes including the 2004 M_W 9.1-9.3 Sumatra Andaman earthquake (Han et al., 2006) and the 2010 M_W 8.8 Central Chile (Maule) earthquake (Han et al., 2010; Heki and Matsuo, 2010). Coseismic gravity changes caused by the 2011 Tohoku-Oki earthquake have also been detected by GRACE (Matsuo and Heki, 2011; Zhou et al., 2012; Fuchs et al., 2013; Han et al., 2014). In contrast to the inland GPS observations, GRACE coseismic gravity changes cover the both sides of the fault, providing a complementary dataset to constrain the coseismic slip of the Tohoku-Oki earthquake (Wang et al., 2012e). In this chapter, a joint inversion with GRACE gravity changes and inland GPS observations is conducted to re-estimate the slip distribution of the 2011 Tohoku-Oki earthquake.

5.2 Previous geodetic modelling on the 2011 Tohoku-Oki earthquake

The 2011 M_W 9.1 Tohoku-Oki event caused large-scale movements on the land surface. Coseismic deformation signals were even measured by GPS stations in mainland China thousands of kilometres away from the epicentre (Zhou et al., 2012). The radiated seismic energy was also recorded by global seismic seismometers. Dense seismic and continuous GPS (cGPS) sites on the main islands of Japan, five sea floor cGPS stations and a tsunami detecting network all provided unprecedented observations with respect to the coseismic response to the mainshock. Using these measurements, many investigations on the coseismic slip of this event have been carried out (e.g. Lay et al., 2011; Simons et al., 2011).

Table 5.1 Previous slip models for the 2011 Tohoku-Oki, Japan earthquake.

Source	Dataset*	Patch (km)	Location of Maximum slip			Maximum Slip(m)
			Lon(deg)	Lat(deg)	Dep(km)	
(Ammon et al., 2011)	SW	15×15	142.4870	37.8130	19.7	41
(Ide et al., 2011)	SW	5×5	143.4369	37.4654	7.8	31
(Shao et al., 2011)	SW	25×20	143.3955	37.9631	14.3	60
(Yagi and Fukahata, 2011)	SW	20×20	142.4580	38.2574	9.5	51
(Gusman et al., 2012)	TW and G	50×50	143.3300	37.7999	4.49	42
(Yue and Lay, 2013)	HG and G	30×30	142.5167	37.6527	23	70
(Wang et al., 2013b)	GPS	10×10	143.3182	38.1202	14.4	46
This thesis	GPS	20×20	143.0521	38.3005	10.4	40
This thesis	GRACE	20×20	143.1007	36.9320	0	41
This thesis	Joint	20×20	143.1007	36.9320	0	42

Note: *, SW = seismic wave. TW = tsunami wave, G = ground motions, HG suggests high-rate GPS, GPS indicates static GPS displacements and Joint represents a joint inversion with both GPS and GRACE gravity changes.

Large variations have been found between the derived coseismic slip models using different datasets (MacInnes et al., 2013; Wang et al., 2013b; Jungkyo et al., 2014). From the Inversion Source Validation (ISV) projection (http://equake-rc.info/SIV/), several coseismic slip models of the event were collected. The locations and magnitudes of maximum coseismic slip (MCS) are listed in Table 5.1. Figure 5.2 shows the spatial locations of MCS. The location of MCS determined by Yagi *et al*. (2011) using seismic wave data is near the epicentre (USGS) at a 10 km depth, whilst the MCS location by Ide *et al*. (2011) with static GPS measurements approaches the Japan Trench near the surface. The horizontal distance between these derived MCS is over 120 km. Using tsunami simulation and near-field observations, MacInnes *et al*. (2013) revealed that most of source models that were collected in their study could not explain observations at 39°N, implying that an additional source of tsunamigenic energy was absent from these slip models. Therefore, even for the best observed earthquake (Romano et al., 2014), no universal slip model that can explain all observations has been determined.

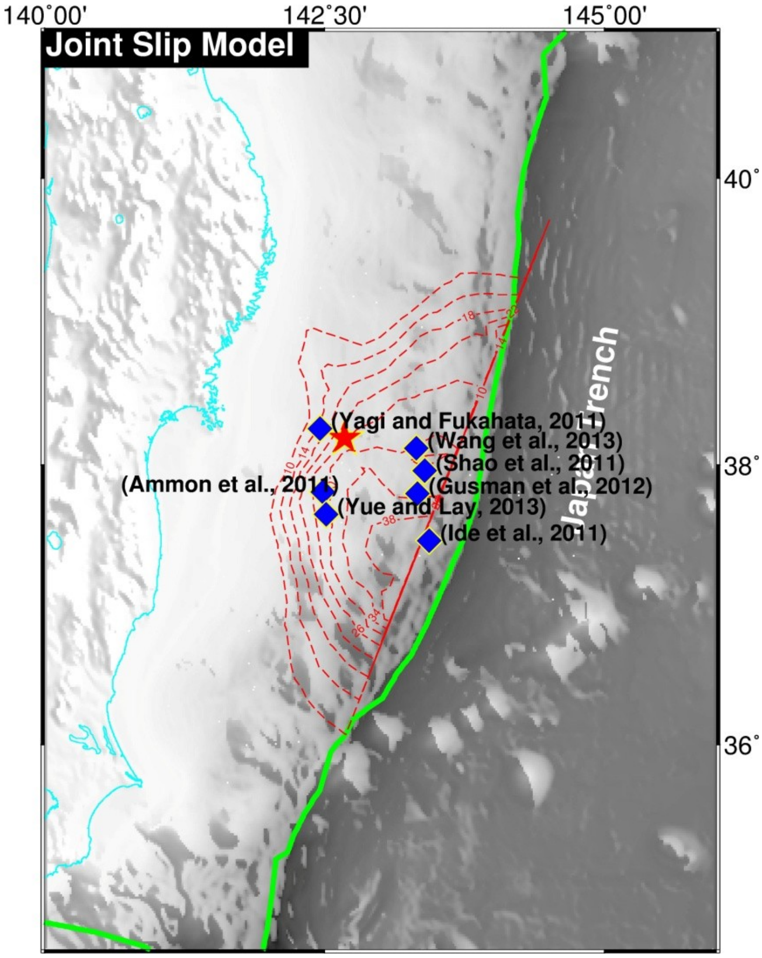

Figure 5.2 Maximum slip locations from published coseismic slip models of the 2011 Tohoku-Oki earthquake. Red star represents the earthquake epicentre from USGS, whilst blue diamonds indicate the locations of maximum slips in previous studies. The red dashed contours are the Joint slip distribution determined in this study.

5.3 Coseismic observations

5.3.1 GPS coseismic displacements

Figure 5.1 shows the locations of the 1231 GEONET cGPS stations in the Japan islands. Coseismic displacements (version 0.3) at these GPS sites were calculated by the ARIA team at JPL/Caltech (ftp://sideshow.jpl.nasa.gov/pub/usrs/ARIA). For each station, 5-minute interval kinematic precise point positioning solutions were obtained with JPL's GIPSY-OASIS software using a single station bias fixing method, and JPL's Rapid orbit and clock products, and then its coseismic displacements were calculated as the difference between the solution at 05:40 UTC and 05:55 UTC (earthquake occurred at 05:46 UTC) to minimize the effects of aftershocks and afterslip following the mainshock. The largest total coseismic displacement of 5.36 m is found at the Oshika station on the Oshika peninsula which is the station with the largest uplift of 1.128 m. The uncertainties of GPS horizontal and vertical displacements are about 6 mm and 20 mm, respectively (Ozawa et al., 2011).

The static displacements released by Sato *et al.* (2011b) at 5 seafloor GPS sites were based on postseismic observations collected during the period from 28 March to 5 April 2011, and likely include some postseismic movements. To further compare the contributions from inland GPS and GRACE gravity changes in the coseismic slip modelling, the sea floor displacements were only used for modelling validation in this study.

5.3.2 GRACE gravity changes

In this chapter, 119 GRACE Level 2 (Release 05) monthly geopotential fields from the Centre for Space Research (CSR) at the University of Texas, from January 2003 to November 2013, were provided by Dr. Qiong Li (Feng *et al*. 2014, in revision). These datasets consist of spherical harmonic coefficients up to degree and order 60, corresponding to a maximum spatial resolution of approximately 333 km (half-wavelength) at the equator. The Earth's oblateness values (C_{20}) were replaced with those from Satellite Laser Ranging due to their poor accuracy (Cheng and Tapley, 2004). A de-correlation filter using order 3 polynomials for coefficients of order 15 (i.e. P3M15) was employed to mitigate longitudinal stripes (Swenson and Wahr, 2006), and an anisotropic Fan filter was used to reduce the remaining N-S stripes around the equator (Zhang et al., 2009b).

The gravity changes derived from monthly GRACE data directly reflect variations in surface mass, including terrestrial water storages, glacier and ice melt, and solid earth deformation. The main cause of temporal gravity variations are thought to be hydrological signals (Tapley et al., 2004). In this study, hydrological effects due to changes in soil moisture, snow and canopy water were removed using the Global Land Data Assimilation System (GLDAS) Hydrological Model (HyM) (Rodell et al., 2004). The GLDAS dataset was truncated to the same degree as GRACE (i.e. a degree of 60), and then an identical spherical harmonic analysis was applied, followed by filtering as used in GRACE data processing, without the de-correlation filter. After subtracting the GLDAS hydrological signals, some seasonal variations remain, which are likely caused by factors inadequately modeled in GLDAS, notably ground water. To separate coseismic signals from the hydrological residuals, the GLDAS corrected time series were modelled with the GPS-like model proposed by Ogawa *et al*. (2011) including linear, seasonal (annual and semiannual) and coseismic terms as

$$\boldsymbol{f(t) = a_0 + a_1(t - t_0) + a_2(t - t_0)^2 + a_3 cos2\pi t + a_4 sin2\pi t + a_5 cos4\pi t + a_6 sin4\pi t + a_7 H(t_{co})} \qquad \textbf{(5.1)}$$

where $H(t_{co}) = \begin{cases} 0 \ (t < t_{co}) \\ 1 (t \geq t_{co}) \end{cases}$, t_{co} is the occurrence time of the earthquake, epoch t_{co} is set as the starting time of the observations, a_1 is a linear term representing the linear trend in gravity variations during the observed period, a_2 is a quadratic term accounting for possible temporal acceleration or deceleration (e.g. precipitation). The following four terms imply seasonal variations (include annual and semi-annual), and the last term is the coseismic offsets. Because the monthly gravity field of March 2011 may include postseismic signals, the coseismic gravity offsets between February and March 2011 might underestimate (or overestimate) the coseismic changes. Therefore, the March 2011 monthly gravity field was excluded in the time series analysis.

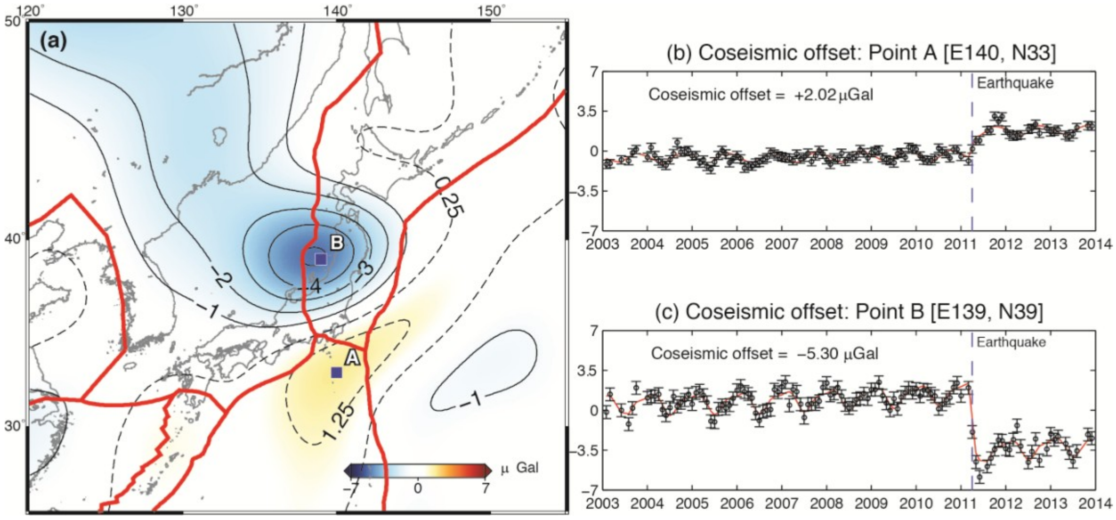

Figure 5.3 Coseismic GRACE gravity changes associated with the 2011 M_W 9.1 Japan earthquake. (a) GRACE derived coseismic gravity changes; (b) Time series of the monthly gravity changes (open circles) at Point A: [E140, N33]; (c) Time series of the monthly gravity changes (open circles) at Point B: [E139, N39]. Note: error bars show one-sigma formal errors inferred a-posteriori by bringing the chi-square of the post-fit residual to unity. Thick red curves indicate the modelled time series using Equation (5.1).

Figure 5.3(b) shows the time series of monthly gravity changes at [38°N, 139°E], and a significant gravity decrease of -5.30 μGal can be observed during the Tohoku-Oki earthquake, which is consistent with previous results (Matsuo and Heki, 2011; Cambiotti and Sabadini, 2012; Wang et al., 2012d). Finally, 400 datapoints covering the region of 31°-45°N and 130°-154°E (Figure 5.3) were produced for coseismic slip modelling.

5.4 Slip distribution models

In this thesis, half-space elastic dislocation models (Okada, 1985; Okubo, 1992) were employed to compute the Green’s functions for coseismic surface displacements and GRACE gravity changes. To build the gravity response component in the inversion, the coseismic high-frequency signals generated by each source, which cannot be detected by GRACE, were truncated using the following procedures as implemented in the GRACE data processing: 1) to convert simulated gravity signals into harmonics Stokes coefficients at order 60; 2) to apply decorrelated filtering with P3M15; 3) to convert coefficients back into gravity changes with the Fan filter (Zhang et al., 2009b). In addition, the seawater effects on coseismic gravity changes were corrected with a density compensation between crust and sea water as implemented in previous studies (Heki and Matsuo, 2010; Wang et al., 2012d). More details on how to simulate GRACE Gravity change based on the Elastic earth model can be found in Appendix A.2.

5.4.1 Fault discretization

A simple fault plane was employed with the fault upper bound fixed at the Japan trench striking at 200°. The epicentre (Figure 5.1) determined by USGS is centred in the finite rectangle fault model. Based on previous studies (Han et al., 2011; Han et al., 2013), GRACE gravity changes are insensitive to fault dip angles. Consequently, the fault dip angle was not estimated in this thesis, and was fixed at 10° in the inversion. This value is consistent with those used in other published slip models (Yue and Lay, 2011; Wang et al., 2012d). The fault plane was then extended along strike and down-dip with a length of 600 km and a width of 200 km. Finally, the fault plane was discretized into 300 subfaults each measuring 20 by 20 km.

5.4.2 GPS and GRACE joint inversion

The discretized observation equation for the GPS and GRACE joint inversion is written as

$$\begin{bmatrix} \boldsymbol{w_{GPS}G_{GPS}} \\ \boldsymbol{\lambda^2 w_{GRACE}G_{GRACE}} \\ \boldsymbol{\alpha^2 L} \end{bmatrix} \boldsymbol{m} = \begin{bmatrix} \boldsymbol{w_{GPS}d_{GPS}} \\ \boldsymbol{\lambda^2 w_{GRACE}d_{GRACE}} \\ \boldsymbol{0} \end{bmatrix} \tag{5.2}$$

where G_{GPS} and G_{GRACE} are the Green's functions for GPS coseismic displacements and GRACE coseismic gravity changes respectively, λ^2 is the relative weight of GRACE Gravity changes. L is a Laplacian operator to smooth the solution to avoid unphysical oscillations in the fault slip, and α^2 is the weight of the smoothing constraint. w_{GPS} and w_{GRACE} are the weight matrixes for GPS coseismic displacements and GRACE gravity changes respectively, of which the latter was estimated using the leave-one-out cross validation (LOOCV) method (Matthews and Segall, 1993).

λ^2 is a nondimensional variable that adjusts relative contributions to the coseismic slip model from both GPS and GRACE measurements. As shown in Figure 5.4, the weighted GPS rms increases with the relative weights. Since no data errors of the GRACE gravity changes have been quantitatively assessed, the central idea in this thesis is to chose a weight based on the RMS of GPS data. As a tradeoff curve approach (Fukuda and Johnson, 2008) to select optimal smoothing parameters in the slip linear inversion, the bend of the tradeoff curve can be chosen as an optimal value. The GPS RMS (μ) of 0. 0318 m from the GPS-only slip model was selected as a reference. Figure 5.4 shows the tradeoff between relative weights and GPS RMS. The red line denotes the selected weight for GRACE gravity changes where the GPS RMS is about 0.035 m, which is close to the GPS RMS of 0.031 m determined from the GPS-only slip model. Relative to the observation error of 0.006 m in the horizontal component of the GPS data, the RMS of 0.035 from the Joint slip model can also be accepted.

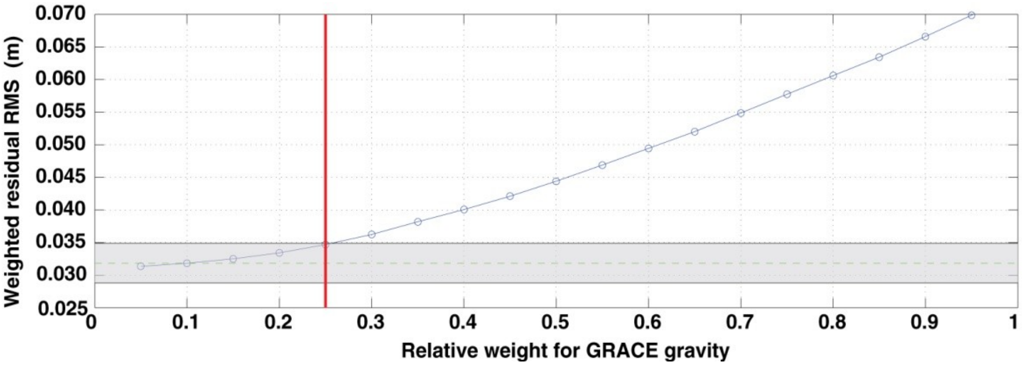

Figure 5.4 Trade-off between relative weights and GPS weighted RMS. Dashed line is the RMS determined using the GPS-only slip model. Red line shows the selected optimal weight for GRACE gravity changes.

Since it is difficult to directly quantify the observation errors in the GRACE gravity change data, the LOOCV approach provides an alternative way for error estimation. The principle of LOOCV is that most information in the dataset is caused by the physical source and that what cannot be explained in the dataset should be regarded as error. The relative weight of each point can be estimated through similarity analysis, in which the data-fit to the point can be estimated using a slip model that is determined by a sub dataset that excludes this point. Theoretically, any individual point with less noise should be explained well by the optimal slip model retrieved from any other data. The estimation can then be implemented using all other points to estimate the residuals at an individual point as follow

$$\boldsymbol{\delta_i = {\sum_k^{n-1}(d_k^i - sim_k^i)^2}/{n-1}} \tag{5.3}$$

and

$$\boldsymbol{w_i = {\bar{\delta}}/{\delta_i}} \tag{5.4}$$

where δ_i represents that the residual of the *i*th point determined by the slip model inferred from all other points without this point and w_i denotes its relative weight. The principle is that those with a poor fit between the observed and modelled values shall be given a relatively low weight, which is consistent with the HVCE method proposed by Xu *et al* (2009).

Figure 5.5 shows the relative weights determined using the LOOCV method. Some signals in the far field greater than 3 μGal seen in Figure 5.3(a) are unlikely to be coseismic signals. Low relative weights are also shown at the datapoints with unexpected measurements (Figure 5.5), implying the feasibility of the LOOCV method for determining the relative weights for GRACE gravity data. A similar strategy was applied to three components of inland GPS data. The resultant weights from all GPS measurements are nearly identical. The possible explanation is that all GPS displacements stations are deployed in the main islands far from the source of the 2011 mainshock, and they are not sensitive to the slip variation on the fault. A unit weight for all GPS data was then applied in the inversion.

The smoothing parameter α^2 of 0.15 was chosen based on the trade-off between data residual RMS and slip model roughness. The bounded-variable least-square algorithm (Stark and Parker, 1992) was employed to solve the slip solution.

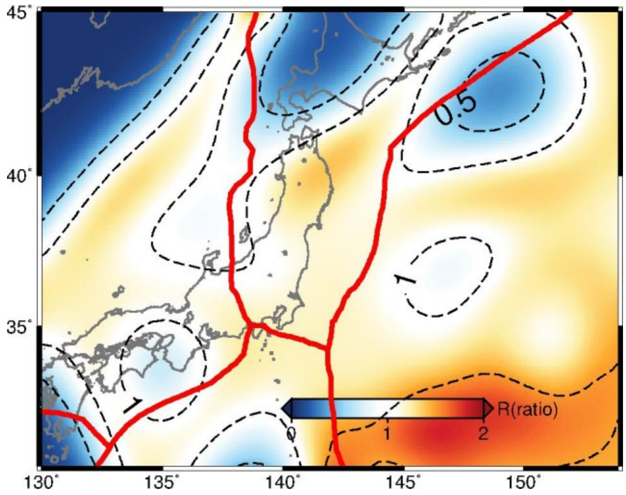

Figure 5.5 Relative weights of GRACE-based coseismic gravity changes ranging from 0 to 2.

5.4.3 Slip distribution of the 2011 Tohoku-Oki earthquake

Figure 5.6 shows that a significant difference exists between the GPS-only slip model and the GRACE-only one, which are reconciled in the joint version (Figure 5.6(e)): (i) a maximum slip of 40 m at a depth of 10 km is revealed in the GPS-only model, whilst both the GRACE-only and the joint models suggest a maximum slip of ~40 m nearly reaching the trench axis, which is consistent with the finding in Fujiwara *et al* (2011). (ii) ~85% of the moment is released in the upper 20 km of the crust in the GPS-only model, but 92.3% in the upper 20 km of the crust in the joint slip model. The difference is likely because the GPS observations are not sensitive to the slip patterns close to the Japan trench, which is examined further below; (iii) the GPS-only model indicates that the maximum moment release is in the segment above the epicentre (i.e. [-50 km, 50 km] along strike), whilst both the GRACE-only and the joint models show the maximum moment release is in the segment of about 100 km south-east of the epicentre (i.e. [50 km, 150 km] along strike).

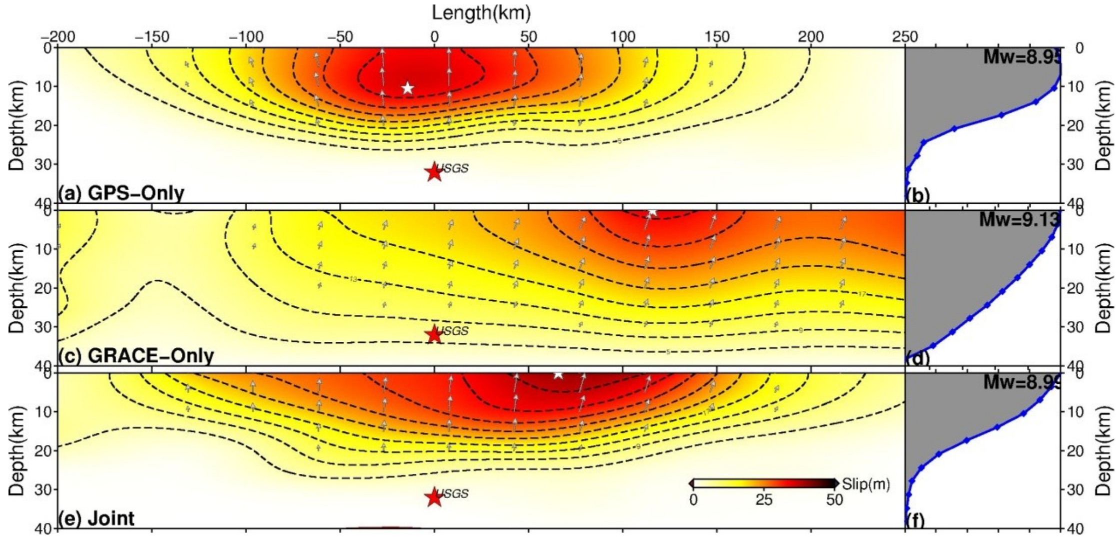

Figure 5.6 Comparison of the 2011 Japan earthquake slip models determined using different datasets. (a) Slip distribution determined by GPS data only, (b) the moment release with depth. (c,d) are as (a,b), but determined by GRACE data only. (e,f) are also as (a,b), but using both GPS and GRACE data.

To clearly compare observed and modelled GPS horizontal displacements, 377 GPS sites used in Ozawa *et al.* (2011) were selected for validation of the three slip models determined in this thesis (Figure 5.7). It appears that the GRACE-only slip model cannot explain GPS horizontal displacements (Figure 5.7 (a)). The GPS displacements modelled by the GRACE-only model have much greater magnitude than the observations, and different deformation vectors. The correlation coefficients between modelled and observed GPS data from the GPS-only slip model are 0.996, 0.996, 0.97 for E/N/U components respectively, whilst the optimal Joint slip can also reach good agreement with correlation coefficients of 0.992, 0.991 and 0.88 respectively. It is clear that the data fit to the GPS data from the joint model is not significantly worse than that from the GPS only model (Figure 5.7 (b)). Conversely, the GPS-only model does not fit the observed gravity changes well with a maximum difference of ~2.50 μGal in the near field (Figure 5.8), while the GRACE-only model can fit the observed gravity changes with a RMS misfit of ~1.69 μGal (Figure 5.8). In contrast, the joint model shows good agreement with a RMS misfit of ~1.63 μGal for GRACE gravity changes. The seismic moment of 3.5×10^{22} N.m determined from the Joint slip model, equivalent to a M_W 9.0 earthquake, is consistent with the GCMT solution, 3.5×10^{22} N.m.

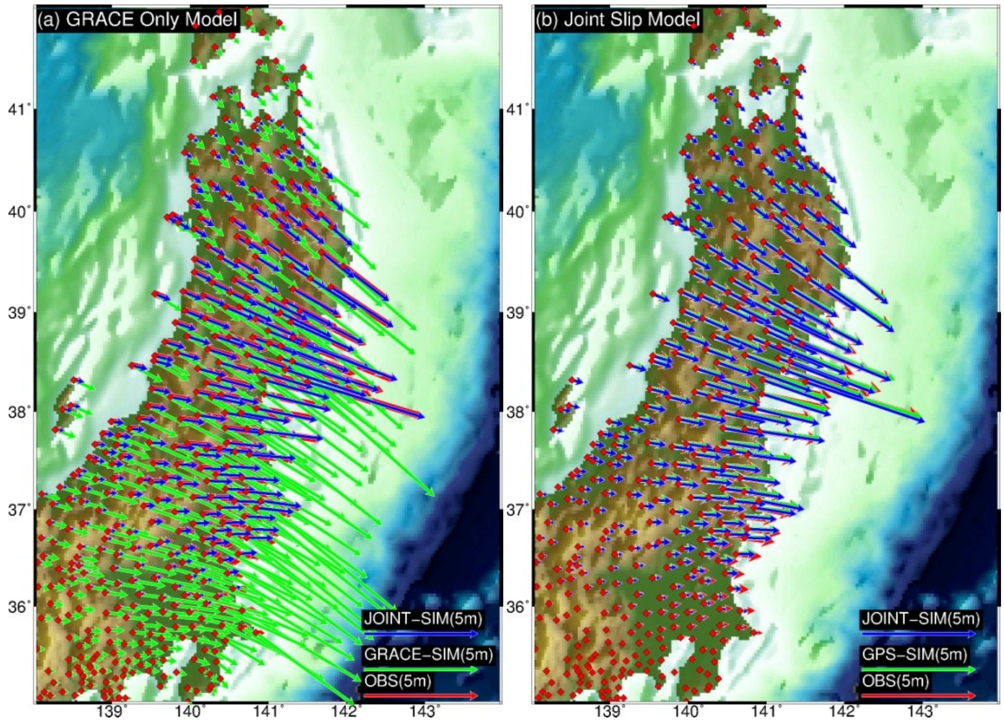

Figure 5.7 Comparison of observed, modelled horizontal GPS coseismic displacements and residuals using GPS measurements provided by Ozawa *et al*. (2011). (a) Comparison of horizontal GPS coseismic displacements simulated from GRACE gravity only slip model and the Joint slip model. (b) as (a), but the green arrows represent the simulation from the GPS data slip model.

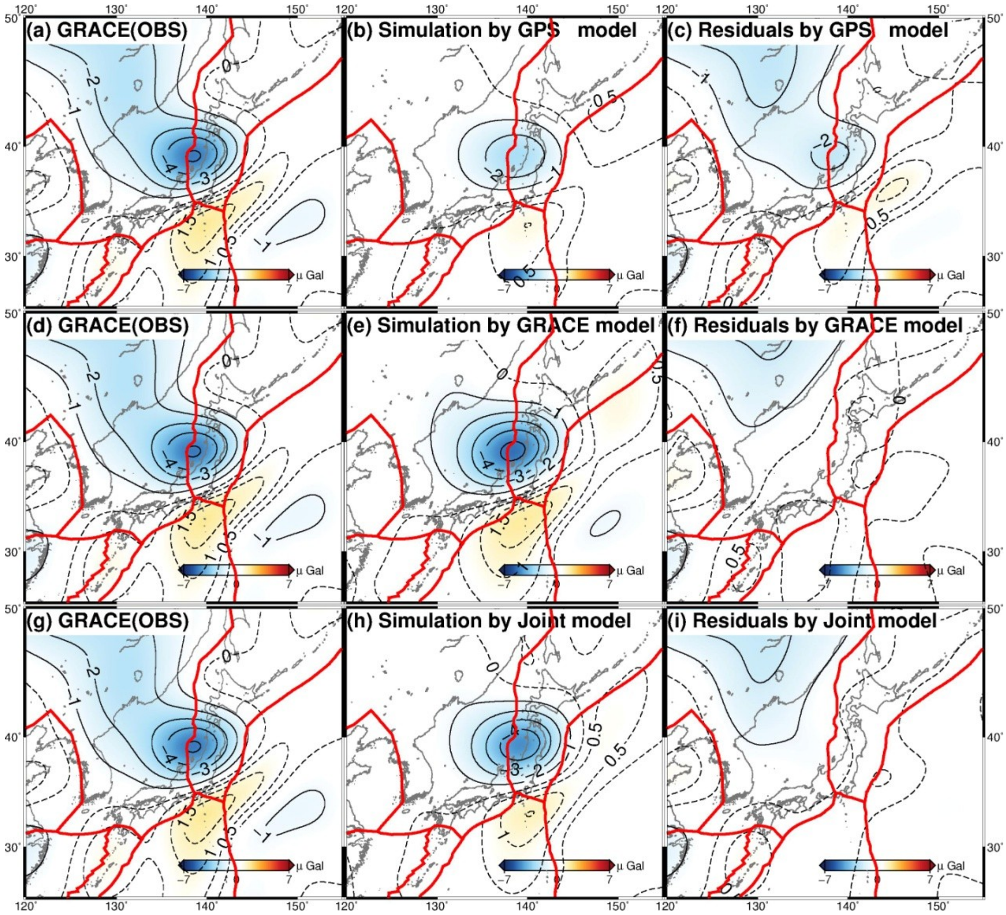

Figure 5.8 GRACE gravity changes based on three coseismic slip models. (a,b,c) GPS-only; (d,e,f) GRACE data only; (g,h,i) joint model using GPS and GRACE data. Column show: (a,d,g) observed; (b,e,h) modelled; (c,f,i) residuals.

5.4.4 Checkerboard test for slip model resolution

A checkerboard test was carried out to examine the slip model resolution inferred from the data used in this thesis. A theoretical model with a magnitude of 9.1 (Figure 5.9(a)) was used to simulate 3D surface displacements at the 1231 GPS sites and GRACE gravity changes. The finite fault geometry model of the 2011 Japan earthquake was employed for constructing theoretical slip model. 20 separated slip asperities were assumed on the fault (Figure 5.9 (a)), which is much more complicated than the real slip model (Figure 5.6) to examine the resolution of GPS and GRACE inferred slip models. Using the same inversion strategy for the mainshock modelling, three slip models based on simulated GPS data, simulated GRACE gravity data and both of them combined were finally determined (Figure 5.9 (b, c and d)).

The resultant GPS-only slip model (Figure 5.9 (a)) shows that nine separate asperities close to the mainland of the islands are retrieved with accurate spatial extents and magnitudes. However, those slip patterns near the trench are not identified successfully. On the contrary, the model from the GRACE gravity changes is not sensitive to slip under the island, whilst two shallow slip patterns close to the seafloor surface are revealed. The joint slip model retrieves more information on the fault asperities, but the slip magnitudes looks larger than the input model, which may result from weak constraints on slip magnitudes during the slip inversion. The determined seismic moments are 5.28×10^{22}, 6.21×10^{22} and 7.2×10^{22} N.m for the GPS-only, GRACE-only and Joint slip models, respectively. The energy of the GPS-only slip model is closest to the input seismic energy of 5.4×10^{22} N.m. Thus, the joint inversion conducted in this thesis should be helpful to restore shallow slip asperities.

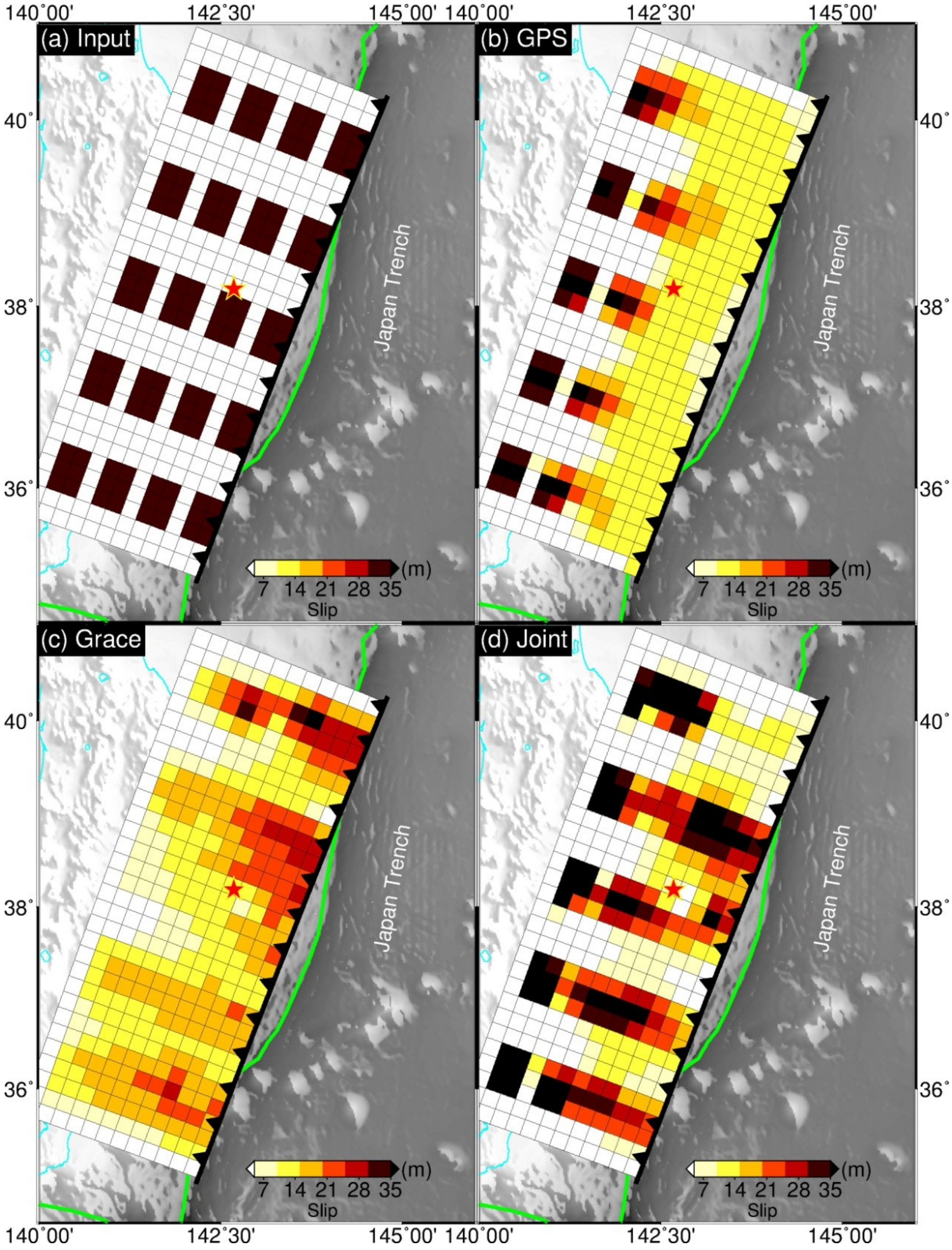

Figure 5.9 Checkerboard for testing slip model resolution with GRACE gravity and terrestrial GPS coseismic observations. (a) Input slip model with a magnitude of 9.1; (b) inferred slip model using only GPS displacements; (c) inferred slip model using GRACE gravity changes; and, (d) slip model determined from the joint inversion.

5.5 Discussion

5.5.1 Is the joint slip model reliable?

In Figure 5.2, the dashed contours represent the projection of the joint slip distribution onto the sea floor. The maximum slip of the joint slip model reaches the Japan trench, which is consistent with the slip model by Ide *et al.* (2011), in which they used seismic data. An independent validation was also carried out using the Seafloor GPS observations. Figure 5.10 shows that the joint model can explain seafloor GPS observations better than the GPS-only model, in particular at stations KAMN, KAM9 and MYGI. The residual RMS for the horizontal seafloor GPS observations determined from the Joint slip model is ~2.6 m, which is better than both the GPS-only and GRACE-only slip models with residual RMSs of 3.0 and 7.5 m, respectively. Therefore, it is believed that the joint inversion model should be more reliable than both GPS-only slip model and gravity-only slip model.

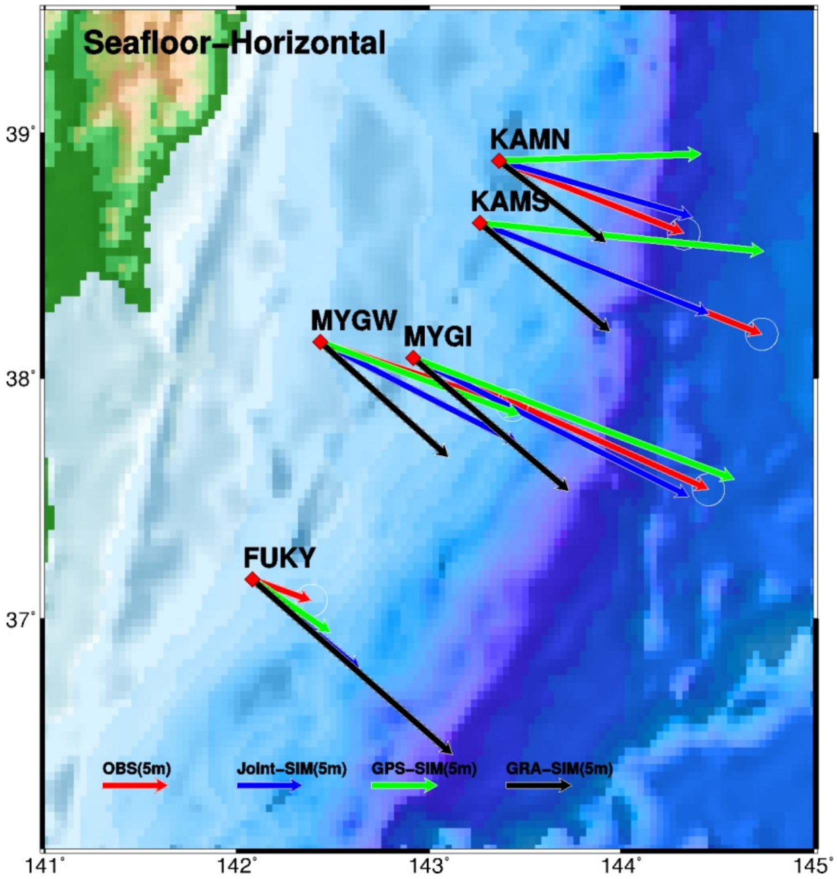

Figure 5.10 Independent validation of slip models using seafloor GPS observations.

5.5.2 Effects of the layered Earth model on the coseismic measurements

Only half-space elastic dislocation models were considered for the calculation of coseismic displacements and gravity changes in this chapter. As shown in previous studies (Wang et al., 2010; Feng et al., 2014), the complex crustal media could introduce significant effects to the surface changes relative to the simple half-space elastic Earth model. Figure 5.11 shows the comparison of slip models determined by Wang *et al.* (2013b) and the GPS only model in this thesis. Wang *et al*'s model was based on the layered Earth model and inland strong motion data were used. A complex fault curve was also considered in Wang *et al*'s modelling. To directly compare the spatial locations of slip and magnitudes between these two models, Wang *et al*'s model was projected onto the same simple straight fault plane used in this study. An inverse distance weighting method was applied to estimate the resampled model (Figure 5.11 (c)). As shown in Figure 5.10, Wang *et al*'s model produces similar spatial extent and magnitude of slip as the GPS-only model derived in this chapter. In both cases, the major slip is concentrated in the region from -100 to 100 km along strike. The maximum slip of Wang *et al*'s model appears at a depth of ~15 km, c.4 km deeper than that determined in this study (Figure 5.11 (a)).

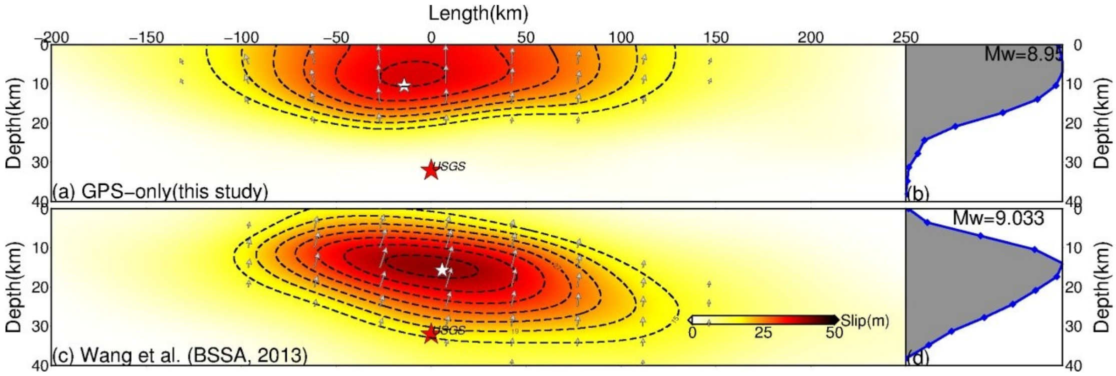

Figure 5.11 Comparison of GPS slip models from Wang *et al*. (2013b) and this chapter.

To further test the effects of the layered Earth model on the simulation of GRACE gravity changes, the GRACE gravity simulation from the Joint slip model based on the Crust2.0 crust model (Tenzer et al., 2009) was calculated using PSGRN/PSCMP software (Wang et al., 2006b). Seawater correction and a series of steps for GRACE data processing (shown in the early section) were all applied. Figure 5.12 shows the comparison of two results based on the layered Earth model (a) and the half-space one (b), respectively. Although slight differences can be identified on the foot wall side (Figure 5.12), the principal gravity patterns have been retrieved with the similar spatial distribution and magnitude as those used in this thesis. Therefore, it is inferred that although the layered Earth model may introduce some effects on the estimates of the optimal slip model, these differences should be less than the observation errors.

The assumption of a spherical curve may also affect the calculation of surface displacements. However, the principal GRACE gravity changes are centred around the epicentre with a radius of 1000 km. Based on the theoretical analysis, the effects of the spherical assumption at distances less than 20° (~2000 km) can be neglected in applications (Okada, 1985; Wang et al., 2006b). Therefore, the effects of using the plane coordinate approximation for Spherical Earth should be limited in the simulation.

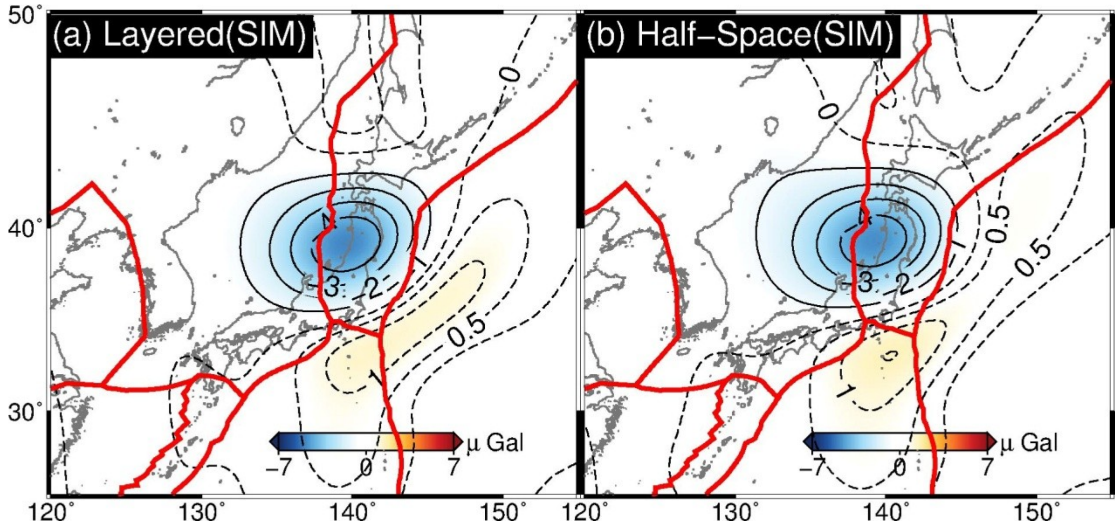

Figure 5.12 Comparison of simulated GRACE coseismic gravity changes from different Earth models. (a) Based on a layered Earth model used and (b) only elastic half-space Earth model used.

5.5.3 Coulomb stress changes on the fault surface from different coseismic slip models

Figures 5.13, 5.14 and 5.15 show the shear, normal and Coulomb stress changes, relatively, following the 2011 M_W 9.0 mainshock using an elastic dislocation method (Okada, 1992). Based on different slip models, stress changes vary significantly in space. For the GPS-only model, the maximum shear drop is about 20 MPa close to the epicentre, and the maximum stress increase is found beneath the main Japan island with a magnitude of 10 MPa. The Coulomb stress changes of the GRACE only model show a more complicated spatial distribution, and no concentrated positive shear stress is found. The joint model looks close to the GPS model, but significant differences can be observed in the northeast. In addition, the stress increase in the southwest tends to be significant.

The Coulomb stress calculation method has been described in Chapter 3. Positive Coulomb stress changes suggest that the coseismic rupture may exert positive effects on local seismic activity. Here, the afterslip model (green contours) is used (Ozawa et al., 2011). In comparison to the former two models, the Coulomb stress changes on the maximum afterslip centre in Figure 5.15 (c) are positive, but why significant afterslips in the blue region are still observed remains ambiguous.

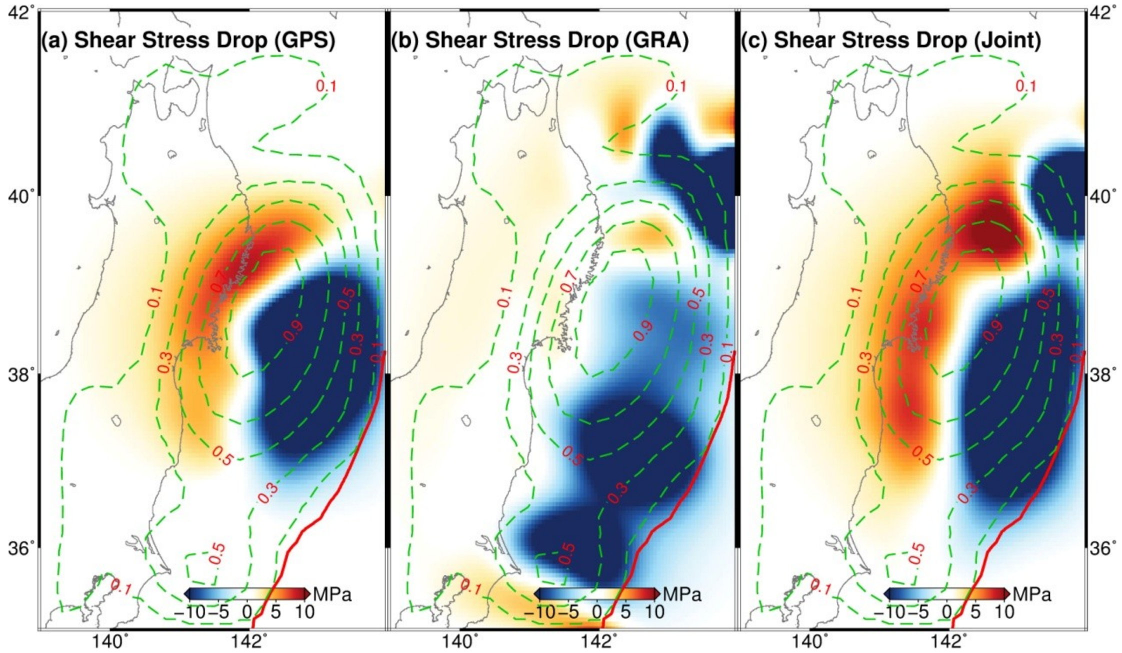

Figure 5.13 Shear stress changes caused by the slip models determined different datasets.

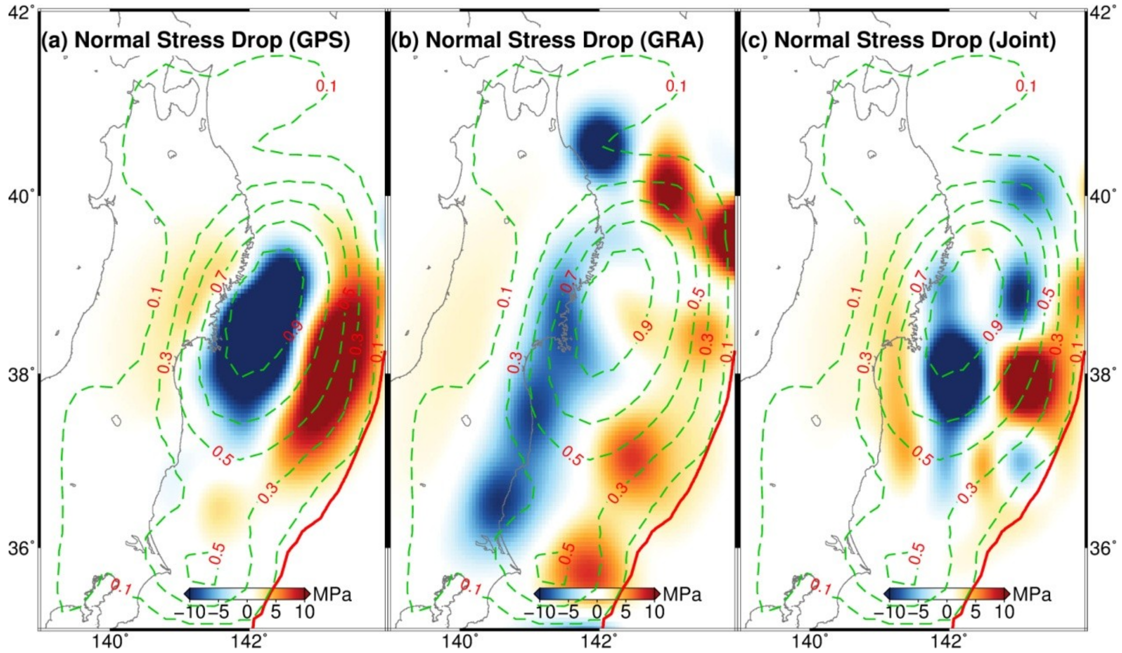

Figure 5.14 Normal stress changes altered by different slip models as defined in Figure 5.13.

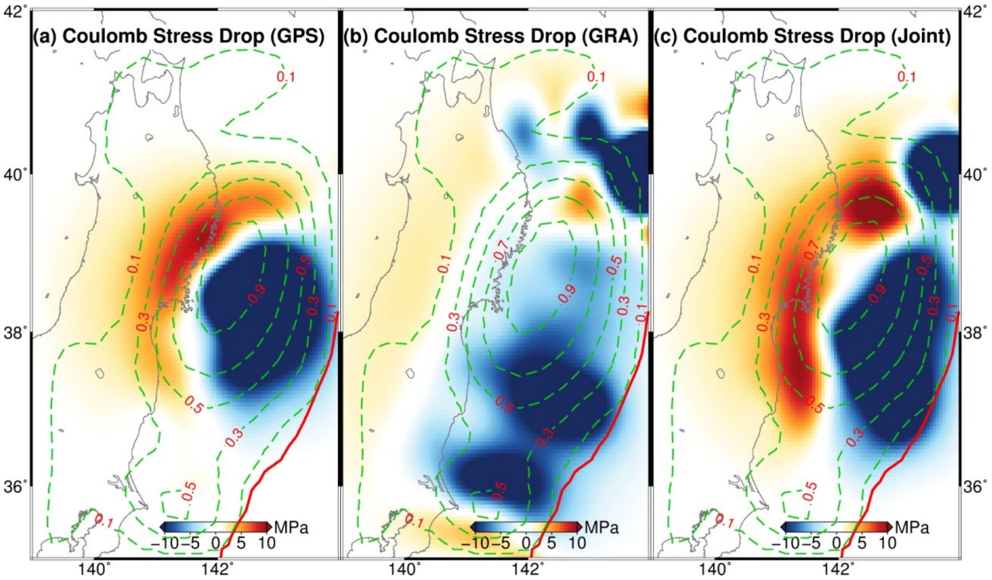

Figure 5.15 Coulomb stress changes from different slip models. The effective friction coefficient of 0.5 is used.

5.5.4 Comparison of co- and post-seismic slip models and its implications for the performance of the friction law

Since only postseismic GPS measurements have been used for postseismic modelling, then there may also be significant uncertainties in the afterslip models, as also discussed above for the coseismic modelling. In addition, other postseismic physical mechanisms after the mainshock, e.g. viscoelsatic relaxation, can also contribute to postseismic deformation as mentioned in previous studies (Ozawa et al., 2011; Diao et al., 2013). In this study, two previous afterslip models from previous studies (Ozawa et al., 2011; 2012) were collected for a simple comparison with the cosesimic Coulomb stress changes on the fault surface.

Once viscoelastic relaxation was fully taken into account in the postseismic relaxation, two separated afterslip patterns have been recognized in previous study (Sun et al., 2014), in which sea-floor postseismic time series were used to constrain the effect of viscoelastic relaxation. Figure 5.16 shows two afterslip models using GPS measurements in previous studies The maximum slips from these two postseismic slip models are both located around [39N,142E]. Meanwhile, significant afterslips greater than 1 m are observed in the coseismic rupture zone, which directly leads to a controversial phenomenon that following classic velocity-weakening asperity there should have no sustained slip on the velocity-weakening regions (coseismic rupture areas) (Johnson et al., 2012b; Fukuda et al., 2013). However, the cumulative afterslips determined by Sun *et al.* (Sun et al., 2014) show strong correlation with the patterns of the Coulomb stress changes caused by the Joint slip model. Based on the findings in Chapter 4 and this chapter, there may still exist large uncertainties in geodetic co- and post-seismic modelling, which can largely affect the estimates on the performance of the friction law in this case.

Note that no significant afterslip has been reported in the shallow layer of the crust from both postseismic slip models, which is consistent with the findings in this study that no positive Coulomb stress is produced by the coseismic rupture since the maximum coseismic slip revealed by the joint inversion has reached to the surface towards the Japan Trench.

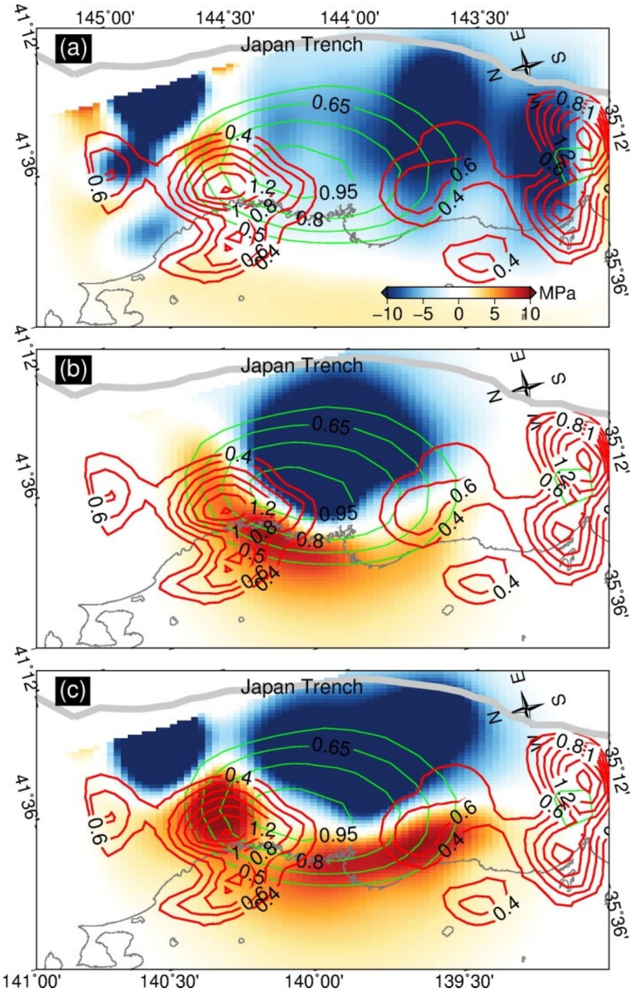

Figure 5.16 Relative spatial distribution between different postseismic slip models and coulomb stress changes. Green postseismic slip contours were determined by Ozawa et al. (2011) using the first 4 days postseismic GPS observations, whilst red ones were with full consideration of postseismic viscoelastic relaxation (Sun et al., 2014).

5.6 Conclusions

In this chapter, GPS coseismic surface displacements and GRACE gravity changes were combined to estimate the coseismic slip distribution of the 2011 M_W 9.0 Tohoku-Oki, Japan earthquake for the first time with their complementary features. The leave-one-out cross validation (LOOCV) method (Matthews and Segall, 1993) was employed to estimate their relative weights in the joint inversion. The optimal joint slip model suggests: (i) a maximum slip of ~40 m near the seafloor surface at the distance of 100 km east-south of the epicentre with a mean rake of 83.6° (inferred from |slip| > 0.5 m) near the bend of the Japan trench; and (ii) most of the energy was released in the shallow crustal zone, which provides further support for the view that this event could have ruptured to the surface (Kozdon and Dunham, 2013). It should be noted that neither of these features can be observed in the GPS-only model due to the lack of observations in the near field. Since the data errors of GRACE gravity data have not yet been estimated, the uncertainties of the joint slip model remain unsolved. However the GPS observations in the Japan islands can be explained well by the joint slip model with acceptable residuals (Figure 5.7), implying the GPS data used in the 2011 Tohoku-Oki earthquake are not sensitive to the seismic source, especially shallow zones close to the trench. Therefore, for future large earthquakes that have no near-filed observations, potential large variations in slip models determined from observations covering only one wall of faults, should be fully considered.

In this thesis, GRACE monthly geopotential fields from CSR at the University of Texas were used to detect coseismic gravity changes, with the March 2011 monthly gravity field excluded (see Section 2.2). It is believed that a better temporal resolution (e.g. 10 days) and a flexible starting date used in the GRACE gravity data processing can be helpful to improve coseismic gravity changes. However, further research is still needed.

Chapter 6

InSAR measurements for the 2010 M_W 6.8 Yushu earthquake

In contrast to previously described thrust faulting cases, this chapter focuses on a large strike-slip earthquake that occurred on the Yushu segment of the Garze-Yushu fault on 13 April 2010 with a magnitude of 6.8. Fault geometric parameters and slip models of the earthquake are investigated through inverting a number of co- and post-seismic interferograms in both Stripmap and ScanSAR modes. The relative spatial patterns of the co- and post-seismic slip models are compared in order to further test the performance of the rate-state friction law in this strike-slip event. Meanwhile, other postseismic physical mechanisms, poroelastic rebound and viscoelastic relaxation, are also discussed to assess whether they can significantly influence the estimate of shallow afterslip following the mainshock.

6.1 Introduction

A M_W 6.8 earthquake occurred on 13 April 2010 at 23:49:00 UTM in Qinghai Province, causing more than 2,500 deaths and 12,000 injuries. The mainshock was a purely left-lateral strike-slip event along the Yushu segment of the Garze-Yushu active fault (Chen et al., 2010). Field investigations suggested that the Garze-Yushu active fault had hosted at least four large historical earthquakes with magnitudes of 6.5-7.5 in the last 300 years (Chen et al., 2010; Lin et al., 2011), of which the 1738 M 6.5 earthquake is believed to be the most recent prior to the 2010 event. If the 2010 event is regarded as an earthquake recurrence of the 1738 event, a ~2 m slip deficit along the Yushu segment could have accumulated in the 272 years interval, based on an estimated strain accumulation of left-lateral interseismic slip at a rate of 7 to 14 mm yr^{-1} (Liu et al., 2011; Loveless and Meade, 2011; Wang et al., 2013d). This is roughly in agreement with the maximum surface offset of 1.8 m near Yushu City mapped in the field after the 2010 earthquake (Chen et al., 2010).

Inferring from recent large earthquakes on the different parts of the Bayan Har block, e.g. the 1997 M_W 7.5 Manyi, the 2001 M_W 7.9 Kokoxili, the 2008 M_W 7.9 Wenchuan and the 2008 M_W 7.2 Yutian events, block-like motion characters the present-day tectonic movements in northern Tibet (Chen et al., 2004; Diao et al., 2010). As a principal strike-slip fault on the south boundary of the block, major historic strike-slip earthquakes along the Yushu fault including the 2010 event may also result from continuing eastward extrusion of the northern Tibetan Plateau (Armijo et al., 1989; Lin et al., 2002; Elliott et al., 2010; Wen et al., 2011).

Table 6.1 Comparisons of InSAR coseismic modelling for the 2010 M_W 6.8 Yushu earthquake.

Previous Studies	Num of segments	Slip Model[a]	Data Sets	Total Length (km)	Geodetic Measurements		Maximum Slip(m)	Optimal Dips
					SAR[b]	GPS		
(Li et al., 2011)	3	REC	SAR and Seismic	93	T498A, T487A	N/A	1.4	[87.9,69,89.4]
(Chunyan et al., 2012)	3	REC	SAR	50	T004D, T487A	N/A	2.4	[75,80,85]
(Sun et al., 2013)	3	REC	SAR	67	T004D, T498A, T487A	N/A	1.4	[79.4,81.9, 89.7]
(Jiang et al., 2013)	1	TRI	SAR	80	T498A, T487A	N/A	1.8	[81,83,90]
(Wen et al., 2013)	4	REC	SAR	86.1	T487A, T139DWS	N/A	2.0	[90,67,100,85]
(Yokota et al., 2012)	2	REC	SAR and Seismic data	73	T487A	N/A	2.0 at 15 km	[84,84]
(Tobita et al., 2011)	1	REC	SAR	73	T487A, T139DWS	N/A	3.0 at 8 km	[90]
This study	2	VREC[c]	SAR	100	T004D, T498A, T276D, T233D, T083AWS, T487A	7	1.4 at 3 km depth	[86.5,79.5]

Notes: a) The slip model was determined by using uniform rectangular elements(**REC**) , Variable-REC (VREC) or triangles (**TRI**). **b)** SAR data azimuths are provided with track numbers: **A** for ascending, **D** for descending, **AWS** for ascending ScanSAR and **DWS** for descending ScanSAR. **c)** In previous studies, fixed patch sizes were used in data inversion, whilst the depth-dependent patches were adapted as proposed by Fialko *et al* (2004b) . A damping factor of 1.3 was used in this study.

The 2010 Yushu earthquake has been widely investigated using InSAR measurements (Table 6.1). With three coseismic interferograms, Li *et al.* (2011) suggested three separate slip sections in the coseismic rupture of the mainshock. A maximum slip of ~1.4 m near Yushu County was modelled near the surface. Combining seismic analysis, Li *et al.* (2011) inferred that the western slip concentration that was located ~20 km west of the epicentre (Figure 6.1(b)) on the west segment of the Yushu fault (also termed Jielong segment in other studies (e.g. Li *et al.*, 2012)), might be produced by the largest aftershock (M_W 6.1) one and a half hours after the mainshock. Several other studies based on InSAR measurements have reached the same conclusion regarding the west slip segment (Jiang et al., 2013; Qu et al., 2013; Sun et al., 2013; Wen et al., 2013). However, a joint inversion with InSAR and seismic data conducted by Yokota *et al* (2012) revealed that the Jielong segment may have ruptured within 8 seconds during the mainshock. Hence, the problem of whether the Jielong segment was the rupture resulting from the largest aftershock needs further investigation. Meanwhile, Wang *et al.* (2013c) reported an earthquake swarm with ~200 small events (M~1-5) following a M_W 5.8 aftershock on 29 May 2010 (hereafter termed M58). Since the seismogenic fault of M58 has not yet been fully confirmed, the tectonic background of the earthquake swarm remains unanswered.

To address these open questions, this chapter is organized as follows. In section 6.2, the SAR data are described covering coseismic and postseismic surface motions. Two approaches to InSAR processing are introduced to improve the interferometric coherence of three interferograms used in the coseismic modelling. In sections 6.3 and 6.4, InSAR co- and post-seismic observations are inverted for co- and post-seismic slip models. The source parameters of M58 are also investigated. In section 6.5, several issues are discussed in detail, such as the location of the M_W 6.1 largest aftershock, coseismic stress triggering on postseismic processes and the effects of other physical mechanisms on the estimate of shallow afterslip. In section 6.6, major contributions to understanding of the 2010 Yushu earthquake processes are summarized.

6.2 Geodetic data

Two different types of data were collected in this study: three-component coseismic offsets at seven campaign-mode GPS sites and InSAR observations in the satellite line of sight (LOS). The coseismic GPS displacements were provided by Meng *et al* (2013). The last occupation of the GPS observations was carried out from 20th April 2010. Thus the GPS coseismic offsets should also include postseismic motions in the first week after the main shock, which were not corrected for in the coseismic slip modelling.

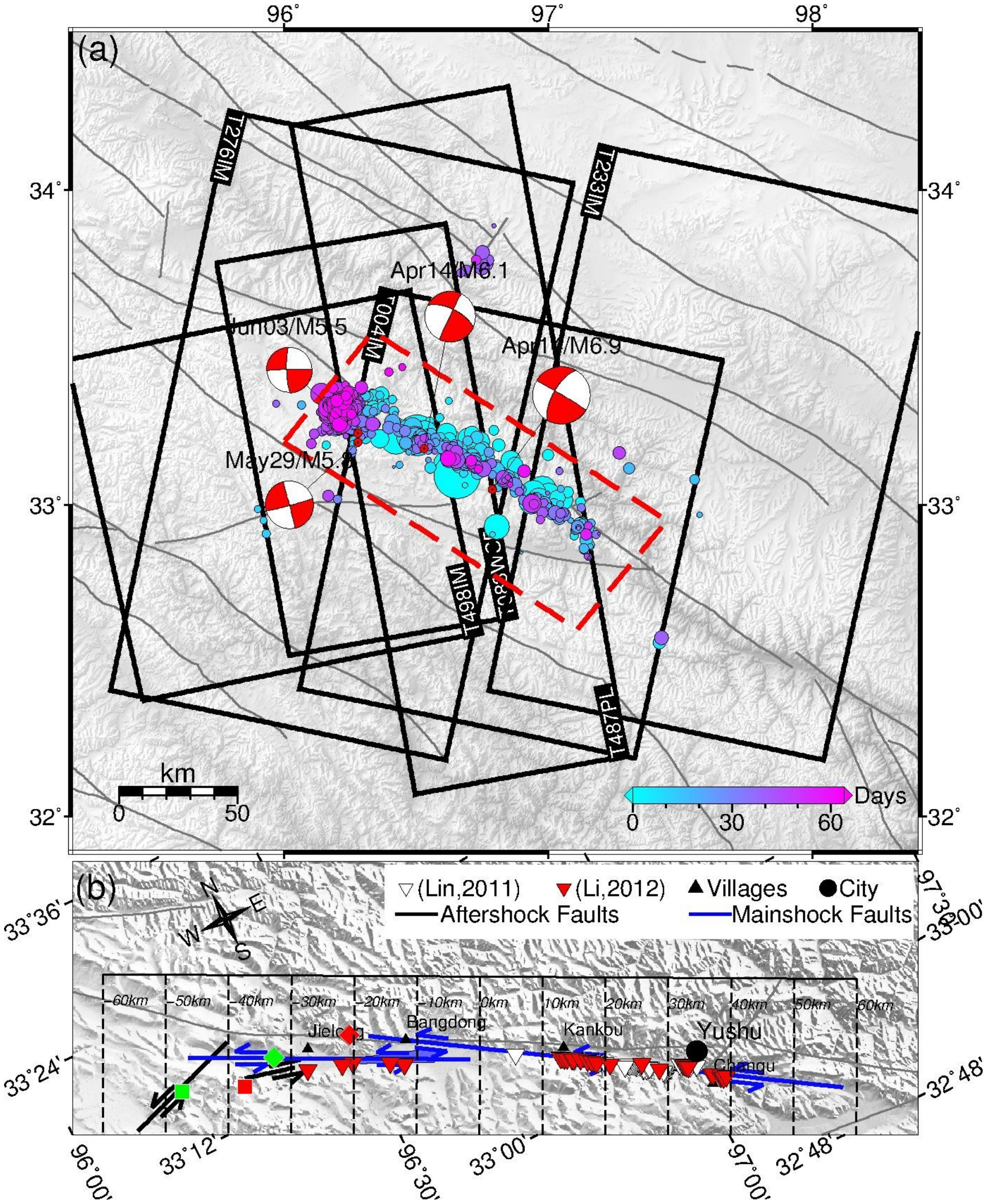

Figure 6.1 Spatial coverage of SAR data and tectonic setting. (a) Spatial coverage of SAR data with tectonic background. Grey lines show the active faults in Qinghai region (Deng et al., 2003), and colour dots represent the relocated aftershocks following the main shock (Wang et al., 2013c). The focal mechanisms of four large events in this sequence were collected from Harvard GCMT database (latest access in September 2013). (b) Fault geometric parameters used in this study. White triangles indicate the surface rupture markers obtained in the field (Li et al., 2012). Red diamond is the location of the M_W 6.1 earthquake determined by the China Seismic network, while the green one is determined by InSAR in this study. Squares are as for diamonds, but for the location of the M_W 5.8 event at the end of May 2010.

Data from five Envisat tracks and two ALOS tracks, spanning from April to October 2010 (Figure 6.2), were collected for co- and post-seismic deformation analysis. Due to ionospheric effects, ALOS track 488 was not used for modelling. Figure 6.2 shows all interferometric pairs processed in this thesis.

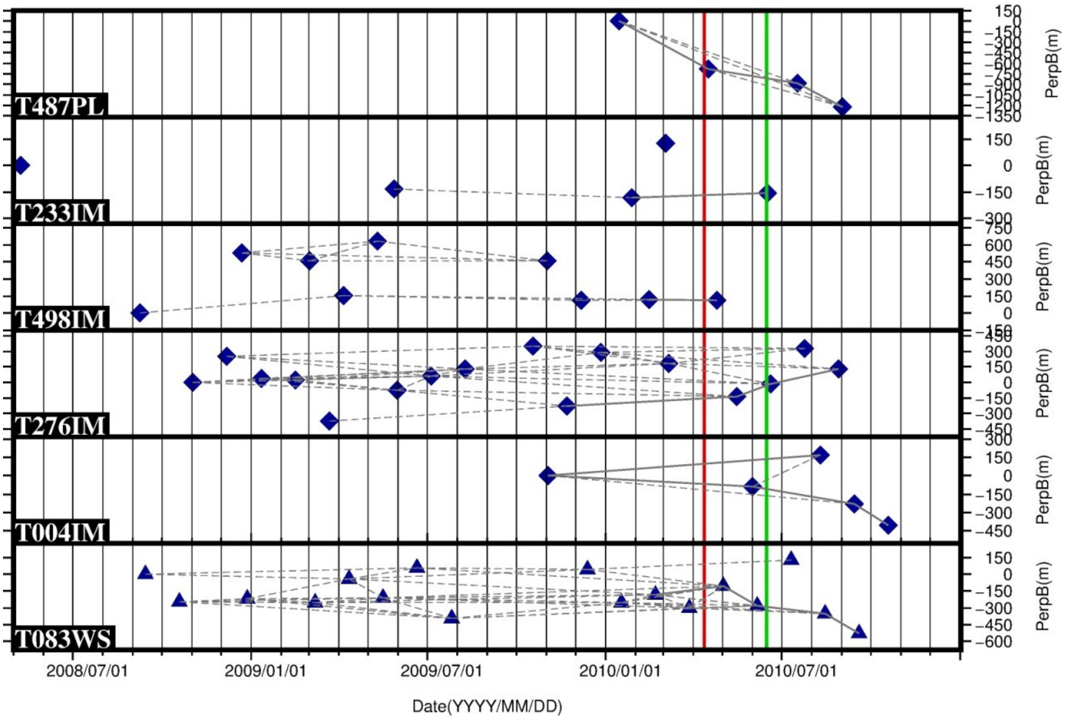

Figure 6.2 Baseline plot of the SAR data used in this study. Red line indicates the main shock of the 13 April 2010 M_W 6.8 Yushu earthquake and the green line represents the M_W 5.8 aftershock on 29 May 2010.

6.2.1 Coseismic interferograms

All interferograms (Figure 6.2) were processed using the JPL/Caltech ROI_PACv3.01 software (Rosen et al., 2004b). The 90-m-spacing DEM data from the Shuttle Radar Topography Mission (SRTM) were used for removing the topographic phase in differential interferograms (Farr et al., 2007). Goldstein filtering (Goldstein and Werner, 1998) and SNAPHU unwrapping algorithms (Chen and Zebker, 2000) were applied for retrieving continuous surface LOS changes. To save computational resources, only the 5th sub-swath of ScanSAR track 083 was processed using a ScanSAR interferometric processor (Liang et al., 2013) since the swath fully covered the epicentral area. An azimuth coseismic measurement was also obtained from ALOS track 487 using the spectra splitting method developed by Barbot *et al* (2008).

Misalignment between master and slave images is one of the major sources causing interferometric decorrelation, particularly in areas with rugged terrain when perpendicular baselines are large (e.g. > 400 m for C-band interferometric pairs). In this chapter, three interferograms from tracks 004, 276 and 233 (also listed in Table 6.2) show low coherence near the mainshock fault partly due to insufficiency of the polynomial warp function. No other interferometric pairs with short perpendicular baselines from these tracks are available (Figure 6.2). As introduced in Chapter 2, the DEM-assisted algorithm (Nitti et al., 2011) is capable of obtaining sub-pixel accuracy for InSAR pairs with relatively large baselines. Thus, based on this DEM-assisted algorithm (Nitti et al., 2011), the interferograms were reprocessed using the GAMMA software (Wegmüller and Werner, 1997).

A strong Goldstein filtering with an alpha value of 0.9 was applied to suppress high-frequency noise. As a result, the interferograms, particularly in regions near the fault were largely improved after considering the DEM data during the coregistration (Figure 6.10).

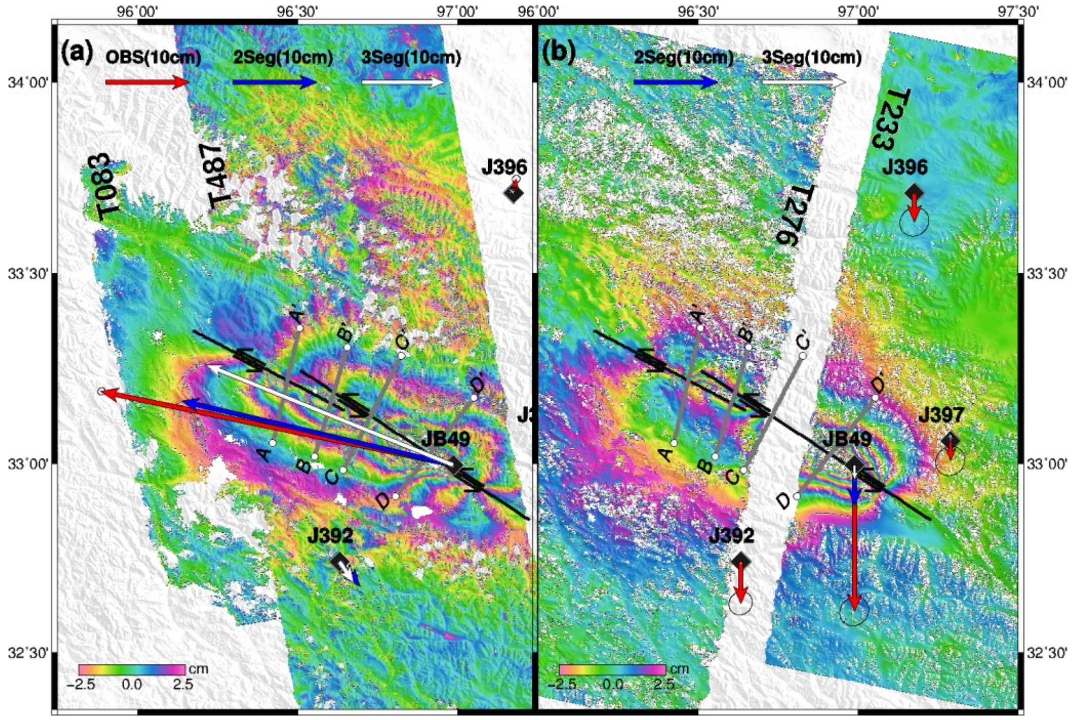

Figure 6.3 Coseismic interferograms overlaying the topographic relief generated from SRTM DEM data. (a) is the merged image from two ascending tracks 083 (ASAR ScanSAR) and 487 (ALOS), whilst (b) is a mosaiced image from both ASAR descending tracks of 276 and 233 in Stripmap mode. Profiles of A-A', B-B', C-C' and D-D' are used for model validation purposes (see Figure 6.7). Horizontal and vertical components of coseismic GPS measurements are shown in (a) and (b), respectively, of which red vectors imply original observations, blue ones indicate modelled displacements using the 2-segment slip model in this study and white ones are simulated from the previous 3-segment slip model (Li et al., 2011).

Six interferograms and one azimuth interferogram (seen in Table 6.2) were finally selected for coseismic slip modelling. Two mosaiced interferograms from ascending and descending tracks respectively are shown in Figure 6.3. Medium wave-length coseismic fringes from different tracks are comparable each other. Figure 6.10 shows all coseismic interferograms used in this chapter (the first column).

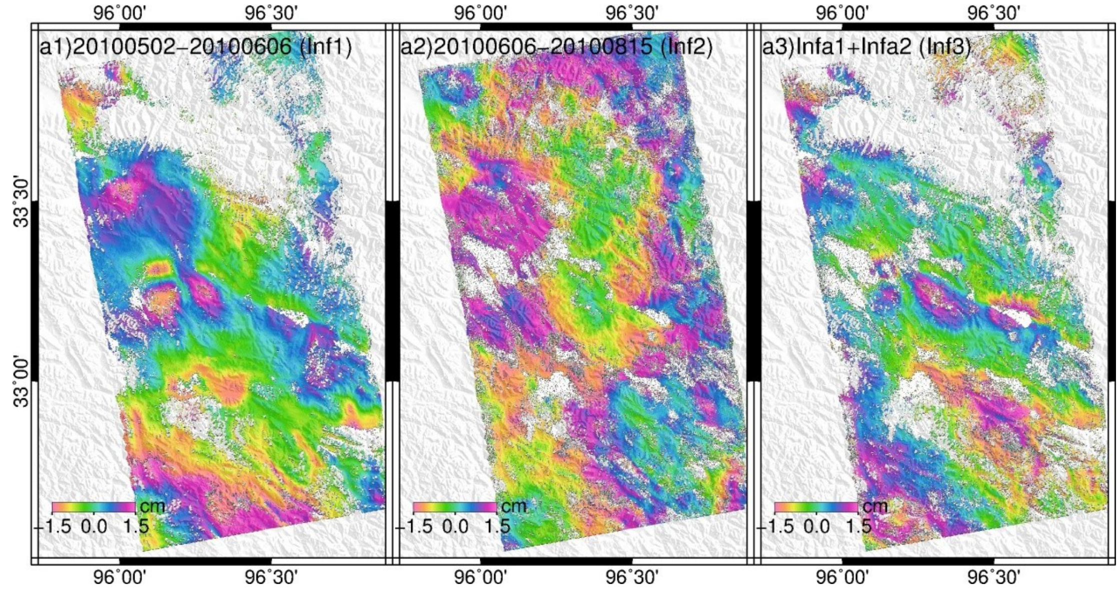

Figure 6.4 Postseismic interferogram based on the phase closure strategy. a) Rewrapped interferogram of 20100502-20100606 (Inf1). The first image in this interferogram was acquired 18 days after the mainshock. b) Rewrapped interferogram of 20100606-20100815 (Inf2) and c) Summation of (a) and (b) (Inf3).

6.2.2 Postseismic interferograms

Two ASAR ScanSAR interferograms of 20100502-20100606 (Inf1) and 20100606-20100815 (Inf2) from track 083 were generated spanning the postseismic period of the 2010 earthquake (Figure 6.4). Significant phase variations with long-wavelength signals can be found in the both interferograms, which can make earthquake interpretation very difficult. Since the acquisition of 20100606 was a common image in Inf1 and Inf2, the third interferogram (Inf3) of 20100502-20100815 was produced by directly calculating the summation of Inf1 and Inf2. Note that the perpendicular baseline of Inf3 is ~240 m that is larger than the critical baseline for ASAR ScanSAR mode, which is ~200 m (see Chapter 2). Thus it is unlikely that an interferogram can be generated with good interferometric coherence when calculating Inf3 directly using SAR images of 20100502 and 20100815. Meanwhile, the best-fit curved surface with a polynomial of degree 2 was also estimated from Inf3 to reduce its long-wavelength orbital errors.

By comparison with Inf1 and Inf2, far-field phase variation in Inf3 has been significantly attenuated. The long-wavelength signals in Inf1 and Inf2 were therefore likely caused by strong atmospheric effects in the common SAR image of 20100606. Four deformation lobes can be directly identified in Inf3 near the west tip of the main fault (Figure 6.4 (c)). Such quadrant deformation patterns may be caused by a strike-slip event. Significant near-field displacements near the epicentre can be seen in both Inf3 and another L-band ALOS postseismic interferogram (Figure 6.9 d), which is likely due to postseismic surface motions following the 2010 mainshock.

6.3 Coseismic fault modelling

6.3.1 Fault segmentation

In this chapter, a two-segment fault geometric model was employed based on geological surveys (Lin et al., 2011; Li et al., 2012). Figure 6.1 (b) has shown the spatial locations of the two fault segments. Li *et al.* (2011) and several other previous studies (Sun et al., 2013; Wen et al., 2013) employed a 3-segment fault model with an independent central segment extending from -10 km to 10 km to the epicentre in Figure 6.1(b). However, the central segment was completely blind and no direct geological evidence relative to its locations was reported. Sun *et al* (2013) has tested a two-segment fault model without this central segment. Their result implies that InSAR LOS displacements used in their study can be explained equally well using 2-segment and 3-segment slip models. It is then inferred that the InSAR data for this earthquake can only provide weak constraints on the central segment. Based on the principle of parsimony, i.e. that a simpler model is better in the case of equal performance. Therefore, the 2-segment model was selected in this study.

6.3.2 Downsampling and weighting

To reduce computational burden, a data resolution-based (Rbased) sampling algorithm (Lohman and Simons, 2005) was employed to downsample each coseismic interferogram into hundreds of points, based on the fault location a priori. The two-segment fault model determined from field surveys (Lin et al., 2011; Li et al., 2012) was used for data sampling (Table 6.2). Vertical dip angles of the two fault segments were fixed in data sampling. After the optimal dip angles of the faults were determined with resampled points, this step was repeated using the estimated dip angles. Since the dip angles of the mainshock faults are nearly vertical, the sampled points are almost identical with or without estimated dip angles.

To rank the contributions of different datasets in the inversion, the data were weighted using a leave-one-out cross-validation (LOOCV) strategy (Matthews and Segall, 1993). LOOCV was also applied in Chapter 5 for weighting each datapoint in the GRACE gravity data, but the statistical method in this case was different from Chapter 5. Unit weight was firstly assumed for datapoints in each dataset. An iterative method was designed to estimate the relative weights for all datasets. The weight of the *i*th dataset was calculated based on the residual RMS after removing the simulation from the best-fit slip model determined from all other datasets excluding the *i*th. The basic principle of the method is that any dataset that cannot be explained by other datasets may include considerable errors and should be weighted a relative low value. The relative weight (w_i) of each dataset was quantified by

$$\boldsymbol{w_i = \sqrt{\sum_{j=1}^{N_i}(d_j^i - \overline{d^i})^2} \Big/ \sqrt{\sum_{j=1}^{N_i}(s_j^i - \overline{s^i})^2}} \qquad \textbf{(6.1)}$$

where d_j^i is the observation of the *j*th point in the *i*th dataset, while $\overline{d_i}$ is the mean of the *i*th dataset. s_j^i is the residual after removing a simulated observation from the best-fit slip model determined from all other datasets and N_i is the total number in the *i*th dataset. Theoretically, w_i tends to be infinite when a slip model can fully explain observations, but no model will fit data 100% since any data will include observation errors. So Equation (6.1) can be applied freely. After nine iterations for all datasets, relative weights were determined as shown in Table 6.2.

6.3.3 Distributed slip model

The western and eastern fault planes were first extended by increasing their lengths to 35 and 76 km along strikes, and 20 km for both downdip widths in terms of the aftershock spatial extension and field surveys (Li et al., 2012; Wang et al., 2013c). A depth-dependent fault discretization strategy as used in previous studies (Simons et al., 2002; Fialko, 2004b; Tong et al., 2010) was employed to divide two fault planes into small patches. The smallest patch size of 0.8 km at the top of the faults was fixed and a damping factor of 1.2 was selected to increase sub-patch sizes with depth. The total sub-faults include 667 patches, only one-third of the fault models constructed in Li *et al.* (2011). Since no geological fault linking structure was found in the field survey (Li et al., 2012), it is noted that the two fault segments were treated as two independent faults without any additional constraint on slip between them.

Following the description on the slip inversion in Chapter 2, the elastic dislocation model in half space (Okada, 1985) was used to compute the Green's matrix that consists of two sub-matrices (G_{r_1}) and (G_{r_2}) corresponding to two bi-orthogonal slip vectors of r_1 and r_2 as suggested by Funning *et al* (2007). In this case, a pair of rakes [-45°, 45°] were employed for each sub fault. To determine an optimal smoothing factor, a tradeoff analysis between weighted residual standard deviation (WSTD) (Equation (6.2)) and the roughness of slip models (RSM) (Equation (6.3)) was then carried out as

$$\boldsymbol{WSTD} = \sqrt{\sum_{i=1}^{N}\left(\left(\boldsymbol{d}_{obs}^{i} - \boldsymbol{d}_{mod}^{i}\right)\boldsymbol{w}_{i}\right)^{2} \Big/ \boldsymbol{N}} \qquad \textbf{(6.2)}$$

and

$$\boldsymbol{RSM} = \|\boldsymbol{LS}\| \big/ \boldsymbol{N} \qquad \textbf{(6.3)}$$

where L is a finite-difference Laplacian matrix as defined by Harries *et al.* (1987) and W is a weight matrix whose diagonal elements were determined by the LOOCV method. Other notations in Equations (6.2 and 6.3) are as defined in Equation (6.1).

Table 6.2 Interferograms used in the coseismic (Cos) and postseismic (Pos) modelling.

Index	Track	Mode	Dir.	Mission	Time (YYYYMMDD)		Perp_B(m)	Method	Usage	Sample Number[a]	Weights	Res2	Res3
					Master	Slave							
1	T498	Stripmap	ASC	ASAR	20100215	20100426	10	ROI_PAC	Cos	262	3.341	0.0046	0.0063
2	T276	Stripmap	DES	ASAR	20091122	20100516	-94	GAMMA	Cos	598	1.455	0.017	0.014
3	T233	Stripmap	DEC	ASAR	20100128	20100617	-23	GAMMA	Cos	355	1.328	0.029	0.038
4	T004	Stripmap	DES	ASAR	20091103	20100601	90	GAMMA	Cos	453	1.576	0.030	0.029
5	T083	ScanSAR	ASC	ASAR	20100221	20100502	-73	ROI_PAC	Cos	699	4.119	0.0061	0.011
6	T487	Stripmap	ASC	PALSAR	20100115	20100417	681	ROI_PAC	Cos	908	2.484	0.014	0.022
7	T487	Stripmap	ASC	PALSAR	20100115	20100417	681	AZISAR	Cos	944	0.481	0.045	0.062
8	-	Horizontal	-	GPS	-	-	-	-	Cos	14	1.115	0.031	0.030
9	-	Vertical	-	GPS	-	-	-	-	Cos	7	1.983	0.062	0.068
10	T004	Stripmap	DES	ASAR	20100601	20100914	138	GAMMA	Pos	-	-	-	-
11	T083	ScanSAR	ASC	ASAR	20100502	20100606	175	ROI_PAC	*	-	-	-	-
12	T083	ScanSAR	ASC	ASAR	20100606	20100815	69	ROI_PAC	*	-	-	-	-
13	T487	Stripmap	ASC	PALSAR	20100417	20100718	202	ROI_PAC	*	-	-	-	-
14	T487	Stripmap	ASC	PALSAR	20100718	20100902	335	ROI_PAC	*	-	-	-	-
15[a]	T083	ScanSAR	ASC	ASAR	20100502	20100815	-	Inf7+Inf8	Pos	-	1	-	-
16[a]	T487	Stripmap	ASC	PALSAR	20100417	20100902	-	ROI_ROI	Pos	-	1	-	-

Notes: *, the interferograms denoted with an asterisk are used to generate new interferograms rather than directly used in the modelling. (a) Numbers of observation points are determined by the data Resolution based downsampling method (Lohman and Simons, 2005).

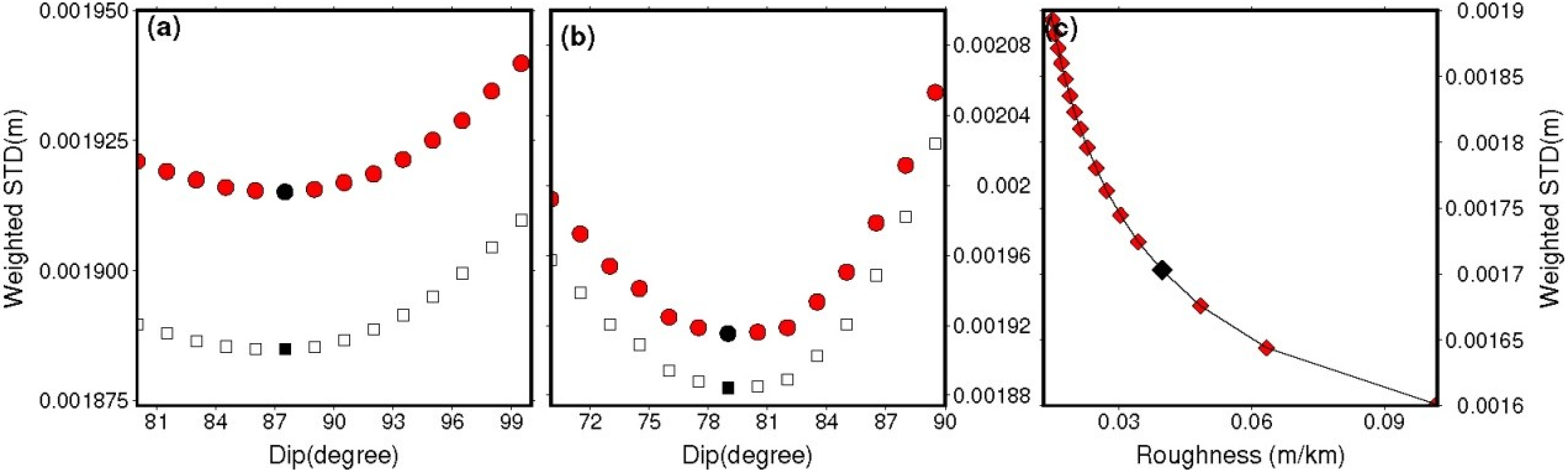

Figure 6.5 Tradeoffs between optimal smoothing factors, optimal dip angles and RMS. (a) Plot of weighted standard deviation (m) versus southward dipping angles for an optimal dip angle estimation of the west segment.(b) As for (a), but for the east segment. (c) Trade-off curve between roughness and weighted standard deviation of residuals. In (a) and (b) the circles represent models with a mean model roughness of 0.4 m/km, whist the squares for a model roughness of 0.5 m/km.

To further estimate the optimal dips of the two fault segments, a grid search method (Burgmann et al., 2002a) was applied, in which a set of dip angles were used in the slip inversion. Optimal dip angles of 86.5° and 79.5° dipping to the south were obtained robustly for the west and east segments, respectively, which are similar to GCMT solutions. Although the selected smoothing factors for the best-fit slip model can vary slightly with dip, the optimal estimates of the dip angles for two given different smoothing factors are identical (Figure 6.5 (a and b)).

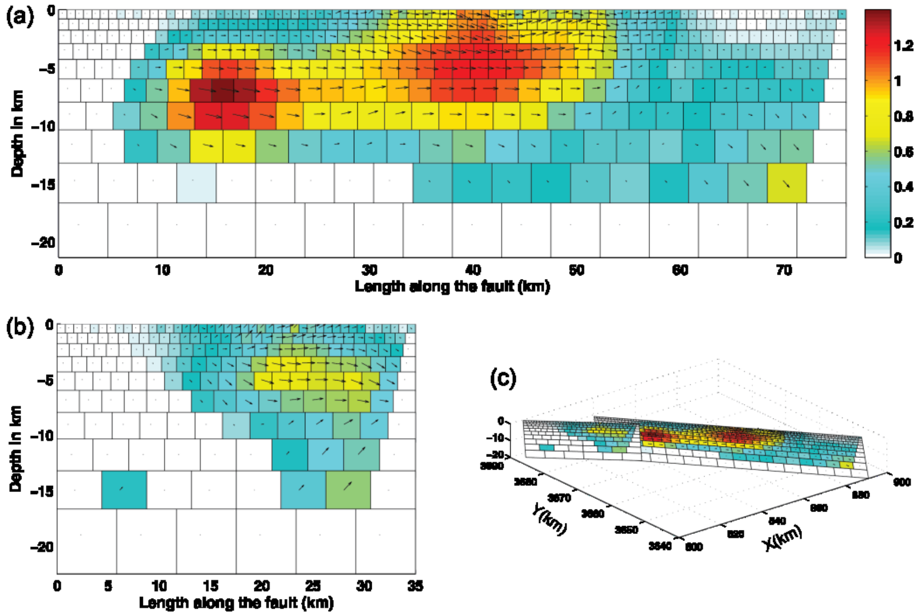

Figure 6.6 Coseismic slip models determined in this chapter. (a) Coseismic slip model for the east segment of the Yushu fault; (b) coseismic slip model for the west segment. (c) Slip model in 3D showing the relative positioning of the two fault segmentations in (a) and (b).

The best-fit slip model is presented in Figure 6.6. Three separate concentrated slip sections are consistent with previous three-segment solutions in location, magnitude and slip vectors (e.g. Li *et al*'s slip model (2011) in Figure 6.11). A maximum slip of 1.35 m appears at a depth of 7.5 km near the hypocenter. Since Li *et al*'s model (2011) has been thoroughly compared by others and no significant differences were found (e.g. Jiang et al., 2013; Wen et al., 2013), no further detailed comparison is made here with other published slip models. Figure 6.7 shows that LOS displacements modelled by the best-fit slip model have good agreement with range and azimuth observations of ALOS track 487 with correlations of 0.997, 0.997, 0.990 and 0.967 along Profiles A-A', B-B', C-C' and D-D', respectively. Good agreement between the spatial location of the fault planes and relocated aftershocks can also been found in Figure 6.7. Along Profile C-C', the fault position on the surface corresponds to a small valley, which may provide additional evidence for the reliability of the fixed fault segmentation in this chapter.

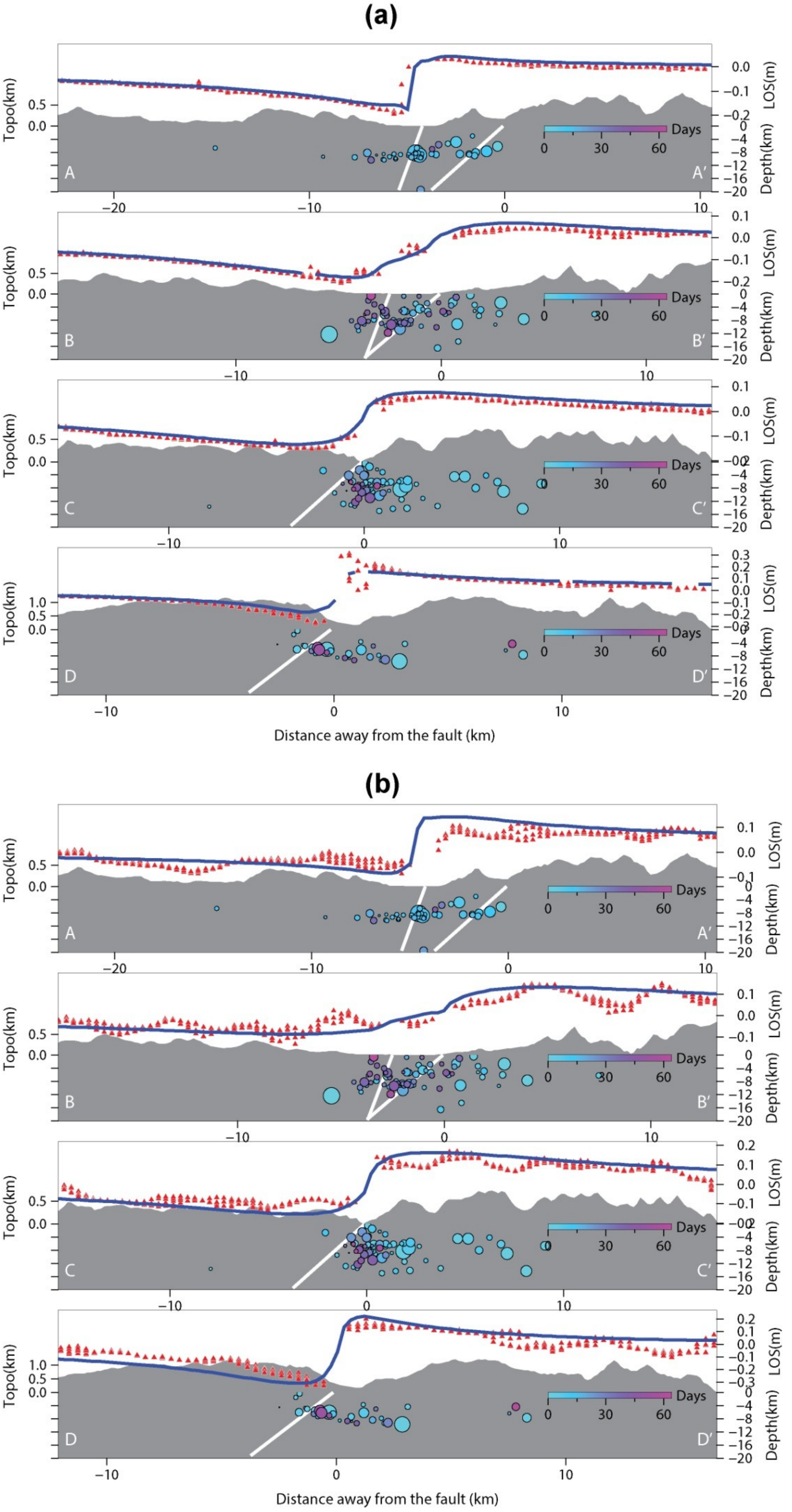

Figure 6.7 Comparison between determined and modelled InSAR (LOS) displacements. (a) Comparison of range changes from track 487 pair. Colour dots show the spatial distribution of aftershocks provided by Wang

et al. (2013c), and white thick lines suggest fault locations in the upper crust. (b) As (a), but for the azimuth measurements provided by the along-track interferometry from track 487. The profiles have been shown in Figure 6.3. Grey shading in (a) and (b) are topography profiles from the SRTM data. Red dots are the InSAR LOS displacements, whilst blue lines indicate the modelled ones.

6.4 Postseismic modelling

Three deformation lobes can be found in Inf3, which can be interpreted as being due to coseismic surface response of M58 and postseismic motion following the mainshock. By inverting the LOS changes of Inf3 using the improved particle swarm optimization (PSO) method, the fault parameters of M58 were determined (Feng et al., 2010b). To avoid large uncertainty of the fault parameters due to postseismic surface changes following the mainshock, an assumption that the moment magnitude of M58 should be identical with the GCMT solution was made in this study. So a magnitude range of [5.75,5.85] was fixed in the inversion. Dip and rake angles were also constrained with narrow ranges of [-85°, 95°] and [-10°, 10°], respectively. The optimal geometric parameters (Fault-I) of M58 suggest that it is located 48 km west of the epicentre of the mainshock with a strike of 70° on a nearly vertical fault plane. The solution is consistent with the seismic solution from GCMT (Figure 6.9). However, a 15-km southwest shift between the seismic location and the best-fit InSAR derived finite fault model has been observed (Figure 6.1(b) and Figure 6.9). As mentioned in Chapter 3, the conjugate fault plane of Fault-I may be able to generate similar surface displacements. The inversion for the conjugate fault plane striking at 160 (Fault-II) was also implemented. The best result shows that Fault-II does generate similar displacement patterns, but the residuals of the observations are significantly larger than Fault-I. Figure 6.9 also shows the relatively spatial locations of aftershocks (M>2) and two traces from Fault-I and Fault-II. A SW-NE trend can be identified, which is basically consistent with the orientation of Fault-I. Therefore, Fault-I is believed associated with M58.

To fully consider the contributions of M58 and postseismic slip of the mainshock to the postseismic interferograms, a joint inversion was conducted with postseismic interferograms from tracks 083 and 487. With the optimal fault parameters of the mainshock and M58, the mathematical expression for postseismic slip distributions on the mainshock fault and Fault-I can be written as

$$\begin{bmatrix} \boldsymbol{G_{M58}} & \boldsymbol{0} \\ \boldsymbol{0} & \boldsymbol{G_{afterslip}} \\ \boldsymbol{\alpha^2 L_{M58}} & \boldsymbol{0} \\ \boldsymbol{0} & \boldsymbol{\beta^2 L_{afterslip}} \end{bmatrix} \begin{bmatrix} \boldsymbol{S_{M58}} \\ \boldsymbol{S_{afterslip}} \end{bmatrix} = \boldsymbol{d} \tag{6.4}$$

where G_{M58} and $G_{afterslip}$ are the Green's matrices for M58 and the afterslip on the mainshock faults. The smoothing factors for M58 ($\boldsymbol{\alpha^2}$) and the afterslip (β^2) on the mainshock fault were tested with different inputs. No large effects from given smoothing factors were found. Therefore, identical smoothing factors α^2 and β^2 was employed in Equation (6.4). A unit weight was applied for both tracks of interferograms in inversion. The best-fit slip model of M58 is shown in

Figure 6.8. A pure left-lateral strike-slip rupture is concentrated on a nearly vertical SW-NE trending fault plane. A maximum slip of 0.38 m appears at a depth of ~7 km. The seismic moment release of M58 is ~7.15×10^{17} N.m, equivalent to a magnitude 5.87 earthquake. Considering contributions from subsequent aftershocks, the estimate of the seismic moment of M58 can be matched with the GCMT solution. The joint model reproduced the three distinct deformation lobes and near-field deformation along the mainshock faults (Figure 6.9(a-f)). Some significant residuals as seen in Figure 6.9(c) around N32.8°, have opposite signs with the near-field observations. Therefore they are most likely caused by atmosphere delays, rather than tectonic signals since this zone is far from the fault. Figure 6.9 shows that the modelled LOS displacements along Profile A-B are in good agreement with LOS range changes from both tracks 083 and 487 near the fault.

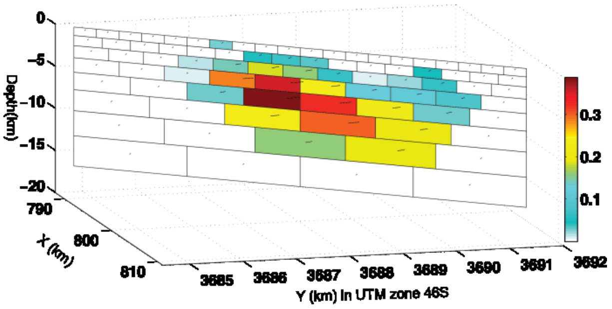

Figure 6.8 The best-fit slip model of the M_W 5.8 aftershock on 29 May 2010.

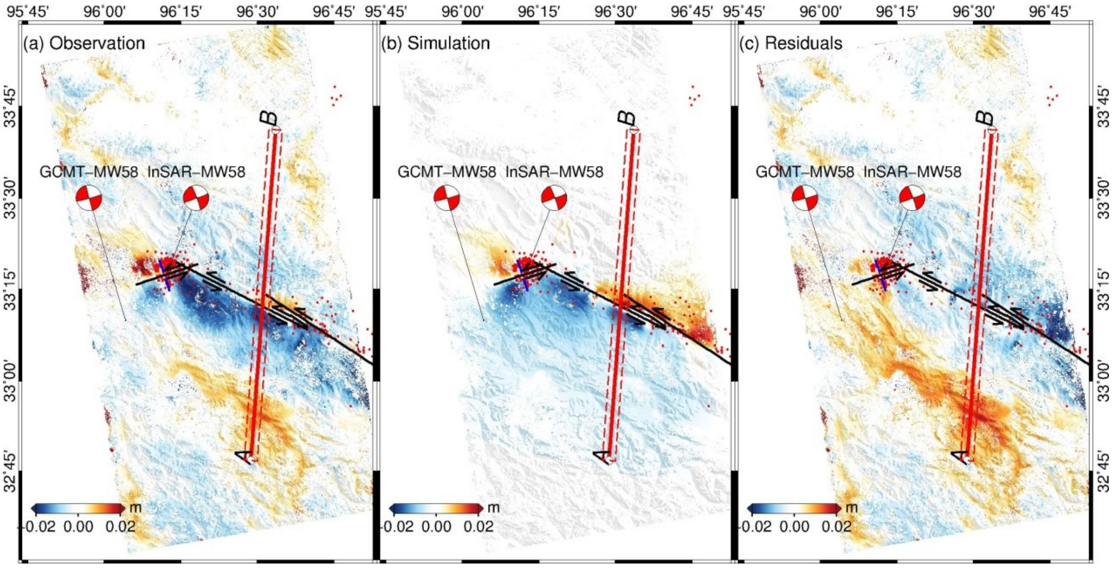

(Figure 6.9)

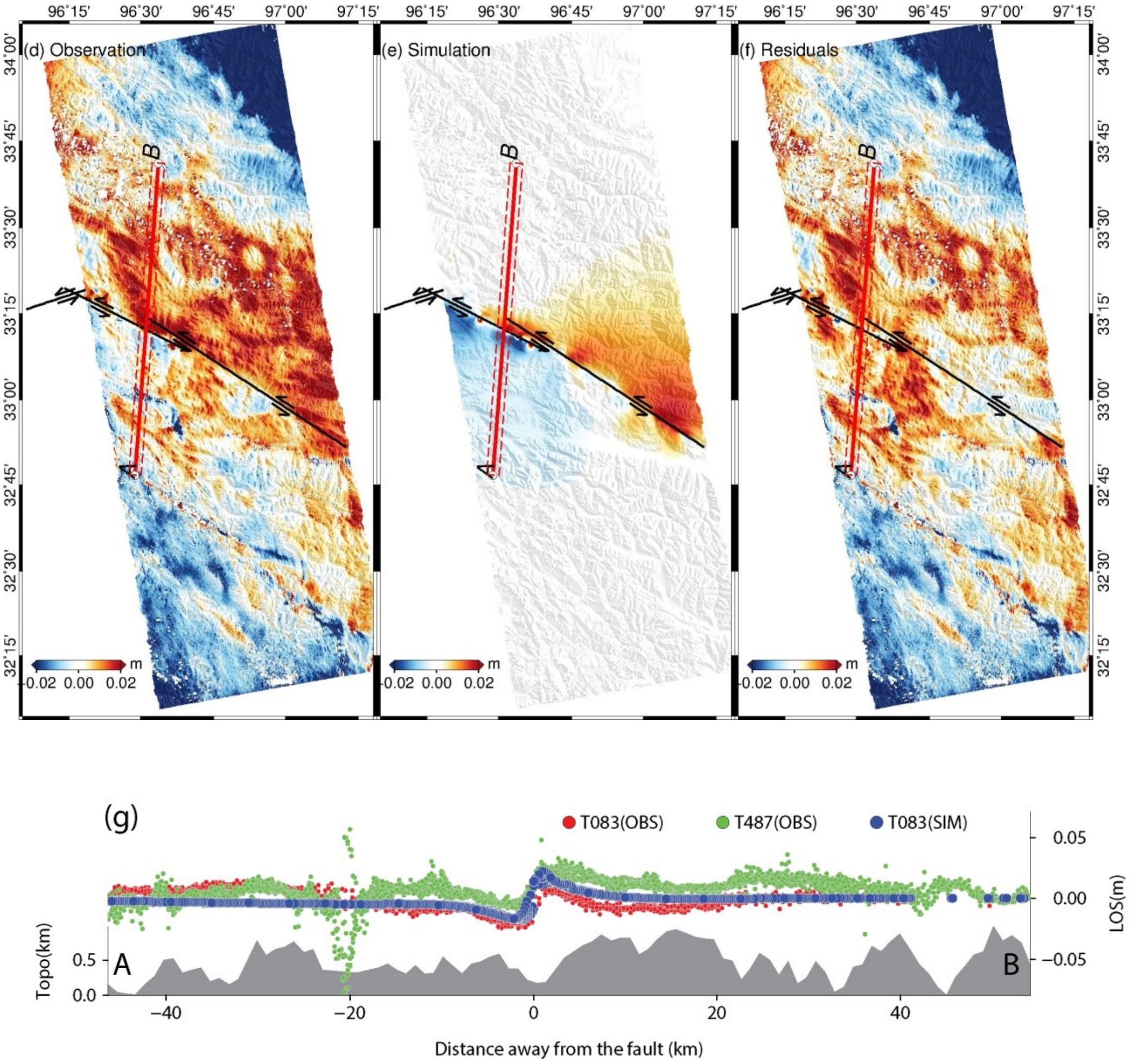

Figure 6.9 Observed, modelled LOS postseismic displacements and residuals. (a) Postseismic interferogram Inf3. Red line shows the location of the profile. (b) Modelled postseismic LOS displacements from the best-fit afterslip model and coseismic slip model of M58; (c) residuals between observations (a) and model (b). (d)-(f) are similar to (a)-(c), but for T487 L-band postseismic interferogram. LOS displacement along Profile A-B shows good agreement between modelled LOS displacements and the InSAR ones. Red dots are the aftershocks (M>2) provided by Wang et al. (2003).

6.5 Discussion

6.5.1 Where is the biggest M_W 6.1 aftershock located?

As shown in the fourth column of Figure 6.10, systematic residuals can be observed from tracks 004, 276, 083 and 498 after removing LOS displacements modelled by the best-fit slip model. Similar patterns can be seen in both residuals from ascending tracks 083 and 498. Since both tracks have similar SAR viewing geometry parameters, these characteristic residuals should be due to a tectonic source, as yet unexplained, rather than observation errors. At the corresponding locations in descending tracks 004 and 276 (Figure 6.10), some significant residuals can also be identified. To validate this speculation, the residual images from these four tracks were cropped into small regions focusing on characteristic residuals only and downsampled as shown in Figure 6.10 ((b-4), (c-4), (d-4) and (e-4)). A uniform finite-fault inversion for an additional source was performed using a global non-linear inversion method, MPSO that has been introduced in Chapter 2. Finally, a purely left-lateral strike-slip event with a magnitude of 6.1 was located ~32 km west of the epicentre (Figure 6.1 (b)). By including both the M_W 6.1 and the mainshock slip model, modelled LOS measurements in the fifth column of Figure 6.10 exhibit better agreement with the observations than those calculated from only the mainshock slip model (fourth column of Figure 6.10).

No other M~6.1 aftershock was recorded except for the M_W 6.1 aftershock one and half hours after the mainshock. Therefore, the additional M_W 6.1 source determined using the observed residuals should be the same event with the M_W 6.1 largest aftershock. Therefore, all three of the slip concentrations found in the coseismic slip model are likely due to rupture in the mainshock. Previously others (e.g. Li et al., 2011; Wen et al., 2013) attributed the western slip pattern to the biggest aftershock. However, the seismic moment release from the west part was equivalent to a M_W 6.3 event (Li et al., 2011; Wen et al., 2013), which is larger than the biggest aftershock. Based on geomorphologic evidence, Li *et al.* (2012) also argued that a 20-km wide step-over across the Longbao Lake should make a rupture jump between west and east two segments impossible. So they also supported the view that the west segment was ruptured by the biggest aftershock. Figure 6.7 presents that the west and east two segments along Profile A-A' intersect each other at a depth of ~15 km near the epicentre. Even at 5 km depth the distance between them should also be less than 3 km (Figure 6.7). Therefore, a rupture jump between these two segments may be likely based on previous numerical simulations (Harris and Day, 1993, 1999).

The slip pattern of the M_W 6.1 aftershock was not directly revealed in the slip inversion, even with six interferograms from different tracks in this chapter. Several reasons may lead to such a result, including: 1) the fault geometric parameters of the M_W 6.1 aftershock are not identical to those of the mainshock; 2) the fault length of the west segment of the mainshock is also not long enough to fully cover this event. A joint inversion using InSAR and seismic data has suggested that the western slip pattern was ruptured in the first 8 seconds during the mainshock (Yokota et al., 2012). This study provides additional new evidence to support their conclusion. Combing the locations of the M_W 6.1 and M_W 5.8 aftershocks between geodetic and seismic data (USGS), a 15-km systematic shift of the seismic locations could exist (Figure 6.1 (b)), which may be common features of seismic locations in Tibet as pointed out in previous studies (Elliott et al., 2010). Consequently, the epicentre of the seismic data should also be shifted westward about 15 km.

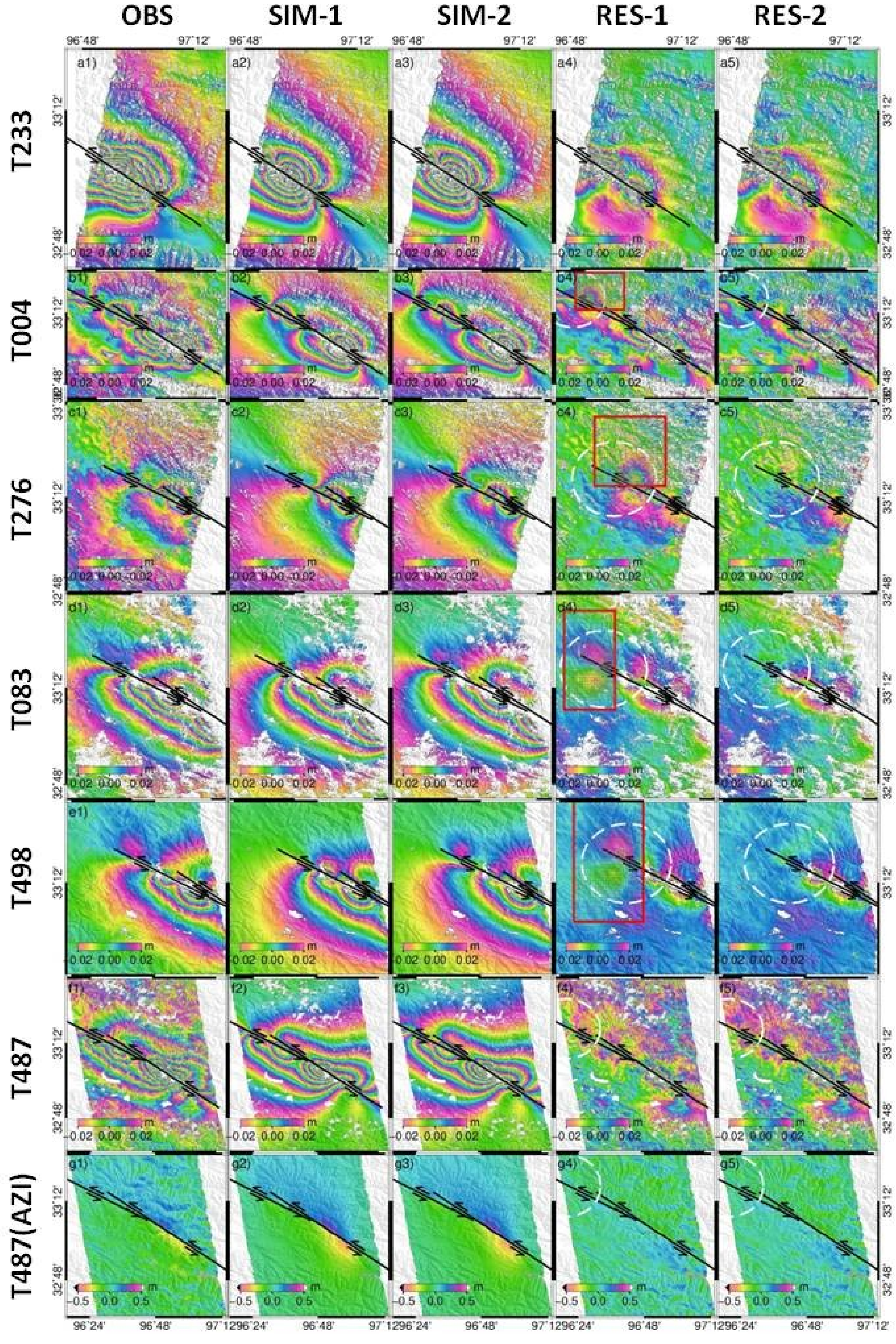

Figure 6.10 Comparison of observed, modelled LOS changes and residuals with/without the biggest aftershock. (a-1) Original interferogram of Track 233; (a-2) LOS changes modelled by the 2-segment slip model; (a-3) LOS changes modelled using the left-lateral source model of the biggest aftershock; (a-4) residuals between (a-1) and (a-2); (a-5) the final residuals when an additional MW 6.1 left-lateral event is taken into account. The rows of b(1-5), e(1-5), f(1-5) and g(1-5) are similar to a(1-5), but for tracks 004, 276, 083, 498, range change and azimuth changes of track 487, respectively. White dashed circle highlights the regions where differences can be seen before and after the MW 6.1 event is taken into account. Red rectangles show the regions masked for data downsampling which are then used for the determination of fault geometric parameters of the biggest aftershock.

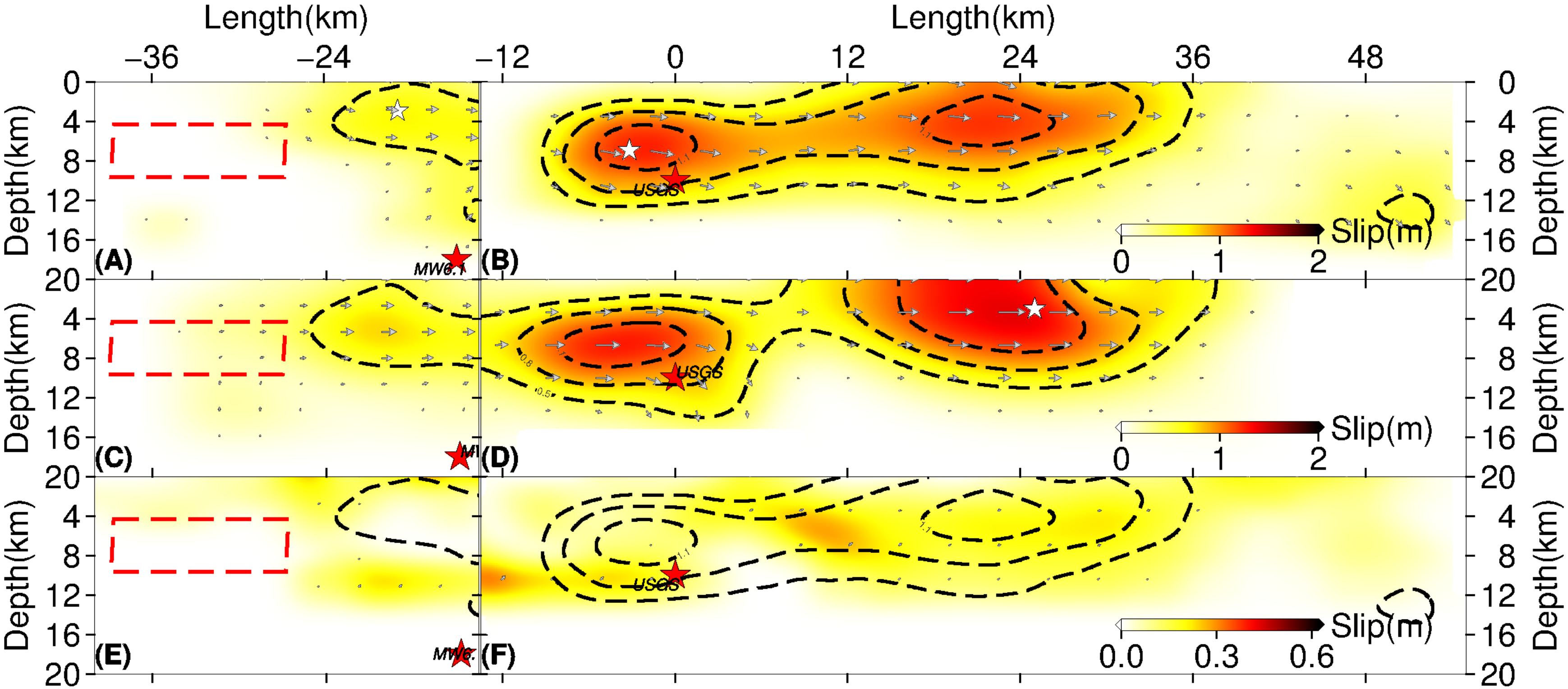

Figure 6.11 Comparison of coseismic slips and afterslip of the 2010 M_W 6.8 earthquake. Two-segment slip model including the west part (A) and the east part (B). (C) and (D) are similar to (A) and (B) but determined by Li et al. (2011), the three-segment model. (E) and (F) show the afterslip model inferred in this study. Red starts show the hypocenters for the mainshock and the largest aftershock released by USGS. Red rectangle indicates the spatial location of the largest aftershock one hour after the mainshock.

6.5.2 Coseismic stress triggering for postseismic processes

To examine the effects of coseismic stress changes on aftershocks and afterslip, Coulomb stress changes (σ_c) on an approximated fault plane parallel to the main faults with a strike of 116, dip of 90 and rake of 0 were calculated using a three-dimensional elastic dislocation model (Okada, 1992) as

$$\boldsymbol{\sigma_c = \tau + \mu\sigma_n} \tag{6.5}$$

where τ [MPa] is the shear stress caused by coseismic rupture, μ is a reduced effective friction coefficient when ignoring poroelastic pressure and σ_n [MPa] represents the normal stress changes (positive if the fault is unclamped). Typically, μ ranges from 0.47-1.0 (Parsons et al., 1999). A value of 0.5 was employed in this study.

Cumulative seismic moments of the afterslip and aftershocks from 14 April to 16 June 2010 were projected onto the same fault plane in Figure 6.12 (a). Figure 6.12 (b) shows the Coulomb stress change variation (indicated by red line) with depth. The seismic moments of the cumulative aftershocks (denoted by green line) and the afterslip (denoted by blue line) are also presented together with the Coulomb stress distribution. It is clear that the seismic moment from the afterslip is much larger than that the cumulative aftershocks. Most postseismic energy from the afterslip was released between 0 and 5 km depth. The maximum slip of the mainshock did not appear on the surface as seen in previous geodetic studies (Fialko et al., 2005; Kaneko and Fialko, 2011), thus the shallow afterslip determined in this chapter may be explained by a coseismic stress driven afterslip model (Barbot et al., 2009a). The coseismic Coulomb stress changes at greater than 15 km may still be significant to trigger earthquakes, but a limited number of aftershocks were observed there in the relocated aftershock dataset (Wang et al., 2013c). This could be explained by ductile deformation being predominant at depths of >15 km in this region (Wei et al., 2010b; Chen et al., 2014). Significant afterslip and aftershocks are also shown in the zone between the two east slip centres, 10 km east of the hypocentre. Based on the velocity-weakening asperity model, the place without seismic slip but hosting significant aseismic slip, should exhibit velocity strengthening behaviour. Therefore, theoretically the zone between the two east slip centres should have a relatively low seismic hazard risk.

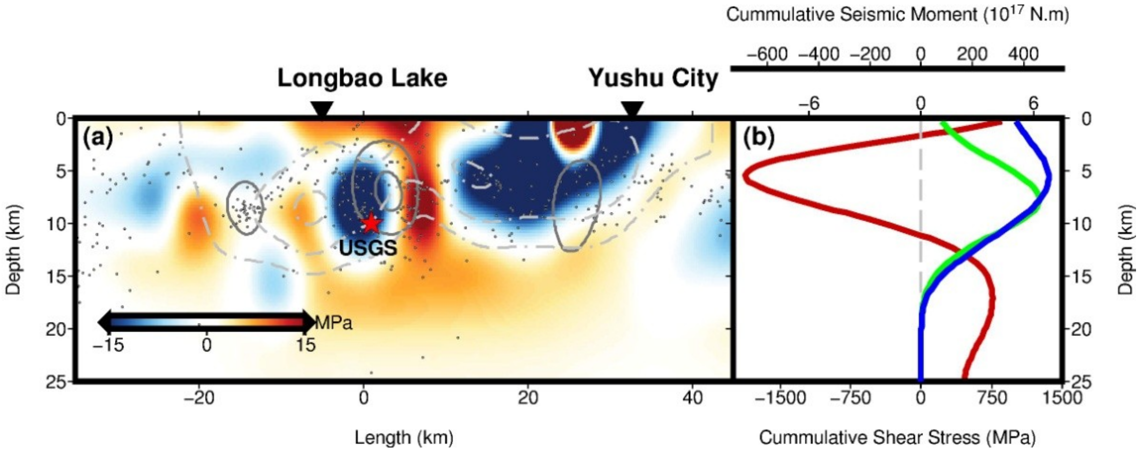

Figure 6.12 Comparison of slip patterns and seismic moment release over depth. (a) Spatial Coulomb stress distribution during the 2011 Yushu earthquake and spatial seismic moment release resulting from afterslip (white dashed contours) and aftershocks (solid grey contours), respectively. (b) Profile of accumulative Coulomb stress (red line with the bottom axis) along the depth and seismic moment release by the afterslip (blue with the shifted axis on the top) and aftershocks (green with the middle axis).

6.5.3 Possibility of other physical mechanisms contributing to postseismic observations

In the postseismic modelling, only afterslip was considered as a cause of the postseismic observations, but usually other physical postseismic mechanisms can contribute to postseismic surface motions, namely poroelastic rebound and viscoelastic relaxation. Elastic rebound in the upper porous elastic layer has been observed in several previous large earthquakes, e.g. the 1992 Landers Earthquake (Peltzer et al., 1998; Fialko, 2004a), and the two 2000 Iceland M~6.5 earthquakes (Jonsson et al., 2003). Potential poroelastic rebound after the 2010 mainshock was tested using an elastic layered dislocation method (Wang et al., 2006b). A series of forward simulations with finite thicknesses of an upper porous elastic layer ranging from 2 to 22 km at 5 km interval were carried out. Empirical Poisson's ratios of 0.31 and 0.25 for drained and undrained conditions in the upper elastic layer (Jonsson et al., 2003; Fialko, 2004a) were selected. As shown in Figure 6.11, four distinctive deformation polarities with a maximum deformation of ~0.15 m can be clearly identified in both simulated descending and ascending interferograms (Figure 6.13), but no similar deformation patterns can be observed in the postseismic interferograms (Figure 6.9). Hence, the possibility of elastic rebound can be directly ruled out in the postseismic processes following the 2010 Yushu mainshock.

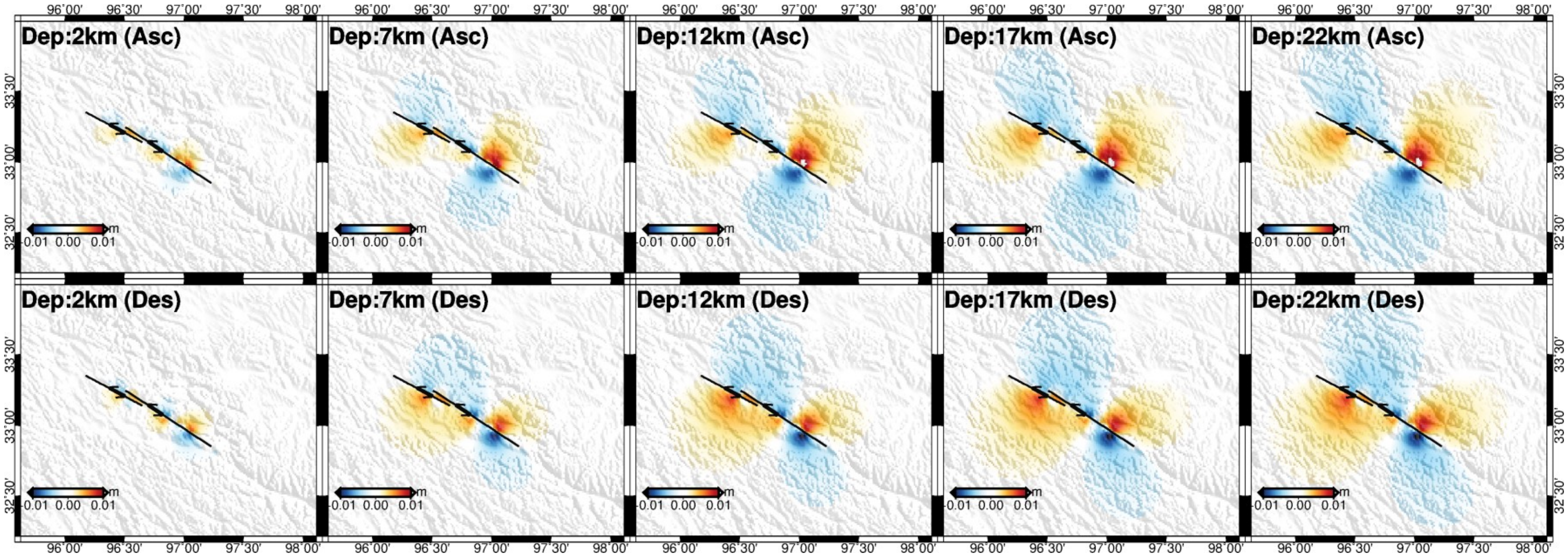

Figure 6.13 Numerical simulation for poroelastic rebound. Porous elastic layer thicknesses of 2, 7, 12, 17 and 22 km at the upper crust. The first row shows simulations with ascending SAR parameters, whilst the bottom one is for descending SAR viewing geometry.

Deformation caused by viscoelastic relaxation may be difficult to distinguish from the contribution of deep afterslip as mentioned in previous studies (Ryder et al., 2007b; Wen et al., 2012a). Even so, it may still be helpful to test the effects of potential viscoelastic relaxation on the shallow afterslip determined in the previous section. Some numerical tools, e.g. RELAX (Barbot et al., 2009b) and other finite element methods (Li and Liu, 2006; Li et al., 2009a), can simulate surface response due to viscoelastic relaxation with complicated crustal models, but limited observations in this thesis make them impractical. Instead, PSGRN/PSCMP (Wang et al., 2006b) was used to carry out a series of tests with a constant viscosity beneath a certain elastic layer thickness. Since the purpose of the simulation is to estimate maximum potential surface displacements from viscoelastic relaxation, possible data errors in the postseismic interferogram from ALOS track 487 cannot affect the conclusion in this section.

Through the analysis of postseismic observations in two large strike-slip earthquakes in northern Tibet, Ryder *et al.* (2007a; 2011) conclude that a consistent estimate of viscosity for the lower crust is 5×10^{17} Pa s that is smaller than the estimate of 1×10^{18} Pa s by Hilley *et al.* (2005). An upper bound of the viscosity is $\sim1\times10^{19}$ Pa s in western Himalaya estimated through postseismic observation modelling after the 2005 M_W 7.6 Kashmir earthquake (Wang and Fialko, 2014), which is similar to an estimate of 6-9 $\times10^{19}$ Pa s for the southern Tibet Plateau (Ryder et al., 2014). A lower bound of the viscosity in the lower crust is $\sim10^{16}$ Pa s inferred from topography analysis (Clark and Royden, 2000). Based on the L-band postseismic interferogram (Figure 6.9) spanning the period from 4 to 142 days after the mainshock, viscoelastic relaxation simulation was computed based on previous viscosity estimates. 2.1×10^{16} Pa s and 7.3×10^{17} Pa s were employed to see surface responses due to the viscoelastic response. A shear modulus of 30.0 GPa was used in all simulations.

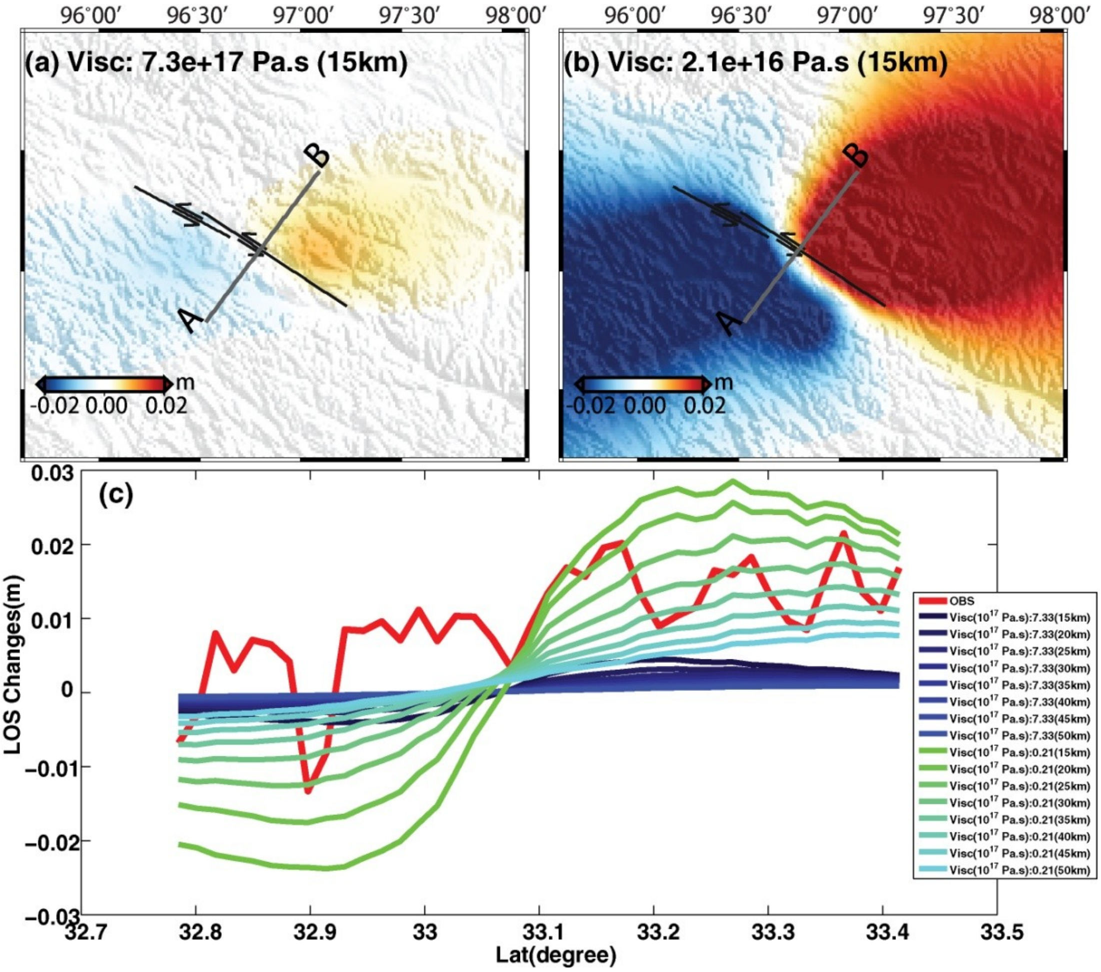

Figure 6.14 Simulated surface LOS range changes for ascending track 487 based on viscous relaxation in the lower crust and upper mantle. (a) Simulated surface changes with viscosity of 7.3×1017 Pa s and an upper elastic layer thickness of 15 km; (b) Simulation with viscosity of 2.1×1016 Pa s and an upper elastic layer thickness of 15 km; (c) profile analysis of A-B for a range of viscosity and elastic layer thickness values. Thick red line is the LOS range change from ALOS track 487 spanning the period between 4 and 141 days after the mainshock.

A series of elastic layers with different thicknesses from 15 to 50 km in the upper crust were calculated for two given viscosities (Figure 6.14). Obviously, for a given viscosity of 7.3×10^{17} Pa s, the maximum viscoelastic relaxation in ascending track 487 is ~0.002 m at ~10 km away from the fault (Figure 6.14 (c)). Even though a lower bound of viscosity of 2.1×10^{16} Pa s was used, the near-field postseismic changes from this viscoelastic relaxation should be $\leq$ 0.005 m which is much smaller than the observed near-field postseismic changes (Figure 6.9). Thus, the estimate of the shallow afterslip in this thesis cannot be affected by viscoelastic relaxation.

6.6 Conclusions

In this thesis, six tracks of SAR data and coseismic GPS measurements on seven GPS sites were used to determine the coseismic slip model, the source parameters of the M_W 5.8 aftershock and the shallow afterslip of the 2010 M_W 6.8 Yushu earthquake. A two-segment coseismic slip model with three separate slip centres is largely consistent with previous studies (Zhang et al., 2010c; Li et al., 2011; Yokota et al., 2012). A maximum slip of 1.4 m appears at a depth of 7 km near the epicentre. The presence of shallow slip deficit is significant. The M_W 6.1 biggest aftershock one and half hours after the mainshock was investigated though analysis of the residuals to the data after fitting the mainshock. The best fit result suggests that the biggest aftershock is located ~30 km west of epicentre at a depth of 10 km, which is not in the western slip area. Thus, the pattern of slip in the western area of coseismic slip ruptured during the mainshock, which further validates the conclusion derived from a joint inversion conducted by Yokota *et al* (2012).

The location of a M_W 5.8 aftershock on 29 May 2010 was refined by inverting an Envisat ScanSAR InSAR interferogram. The best-fit fault model suggests that the event is located ~15 km southwest of the seismic location estimated by USGS. A similar feature has also been found for the biggest M_W 6.1 aftershock. A systematic bias may exist in earthquake location using seismic data in Tibet as found in a previous study (Elliott et al., 2010). A limited number of seismic stations in Tibet and complex crustal velocity structures could cause such significant mis-estimation. The phenomenon should be taken into account in other seismic wave applications in this region.

Table 6.3 Fault parameters determined in this study.

Source	Segment.	Locations		Depth(km)	Focal Mechanisms			Fault Dimensions		Magnitude
		Lon(°)	Lat(°)		Strike(°)	Dip(°)	Rake(°)	Length(km)	Width(km)	
Foreshock on 13 April 21:40										
GCMT	-	96.712^{a}	33.160^{a}	10^{a}	116	81	-19	-	-	4.9
Main Shock on 13 April 23:50										
GCMT	-	96.666^{a}	32.224^{a}	17^{a}	300	88	23	-	-	6.9
ZH11	NW	96.5163	33.1962	4.5^{b}	116	88	2.7	20	20	6.3
	C	96.6908	33.1615	7^{b}	120	70	-2.6	13	20	6.37
	SE	96.8988	33.0281	3^{b}	124	89	0.2	29	20	6.63
This study	NW	96.5419	33.2536	4^{b}	295	86.5	0.1	60	20	6.5
	SE	96.7542	33.2023	3^{b}	121	79.5	-9.3	80	20	6.8
Biggest aftershock on 14 April 01:25										
GCMT	-	96.449^{a}	33.195^{a}	7.6^{a}	205	89	155	-	-	6.1
This study	-	96.3677^{c}	33.2699^{c}	7.0^{c}	286	80	9	12.2	5.4	6.1*
Aftershock on 29 May 02:29										
GCMT	-	96.070	33.165	7.0	75	88	1	-	-	5.8
This study	-	96.2008	33.284	3.8^{c}	70	89	6	7.7	5.2	5.8

Notes: a) the location information is checked through USGS online service by http://comcat.cr.usgs.gov/earthquakes/. b) The depths given here are estimated based on the location of maximum slip at each segment in our previous slip model (Li et al., 2011). c) The depths are for the centres of uniform rectangular solutions determined by geodetic inversion in this study. (*), the solutions denoted with an asterisk are determined in this study using fixed magnitude.

Chapter 7

Discussion and conclusions

In this thesis, several large earthquakes have been investigated using InSAR, GPS and GRACE gravity observations to examine the performance of the friction law. I started with a brief review of earthquake cycles (Chapter 1) followed by an introduction to several physical earthquake models for estimating faulting evolution on a pre-existing active fault. These models are all based on the rate-state friction law (Scholz, 1998; 2002) in which detailed physical parameters that could be estimated through geodetic modelling are needed. The major issues addressed in the later chapters were raised at the end of Chapter 1. InSAR observations and their modelling are the principal means for determination of co- and post-seismic slip models in this thesis. The principles of SAR and InSAR techniques were briefly summarised in Chapter 2. Four open-source InSAR packages were systematically compared for their abilities to generate interferograms. Detailed mathematic expressions for geodetic earthquake modelling were summarised followed by an introduction on a self-developed geodetic inversion package, PSOKINV.

The first case study is the 2003-2009 Qinghai earthquake sequence in Chapter 3. Three M_W 6.3 thrust-slip earthquakes in the sequence were probed using ASAR observations. Time-dependent postseismic displacements following the 2009 mainshock were retrieved using SBAS InSAR, and were applied to determine the afterslip history of the 2009 event using a new time-dependent inversion strategy. The afterslip model was validated using a traditional inversion method that can determine a slip model at each epoch with an individual measurement. Another large thrust-slip event, the 2011 M_W7.1 Van, Turkey earthquake was explored using multiple SAR sensor data including ASAR, CSK and Radarsat-2 (Chapter 4). Rapid afterslip was captured by a CSK postseismic interferogram. In comparison to these two intraplate thrust events, a megathrust earthquake, the 2011 M_W 9.1 Tohoku-Oki earthquake was investigated in Chapter 5. GRACE gravity changes and terrestrial GPS were combined to discover its coseismic slip model. A new joint inversion strategy with these two datasets has been developed and validated using a checkerboard test. In Chapter 6, a strike-slip event, the 2010 M_W 6.8 Yushu (Qinghai) strike-slip earthquake was revisited. Six SAR tracks covering the epicentral area were used together to investigate models for both co- and post-seismic slip distributions. Multiple postseismic physical mechanisms were also examined for their effects on the postseismic slip modelling in this case.

Our knowledge about fault frictional behaviour of natural earthquakes has been improved based on the outputs from these case studies. In this chapter, the questions raised in Chapter 1 are addressed based on the case studies in this thesis and some others that have been explored previously. Potential factors that can influence estimation of slip models are considered. I also summarise the new contributions from this study to the understanding of earthquakes investigated in this thesis. Finally, future work is suggested and a short summary is given at the end.

7.1 Discussion

Based on the frictional velocity weakening asperity earthquake model (Scholz, 2002; Johnson et al., 2012a), earthquakes result from unstable frictional sliding on faults followed by aseismic slips that can commonly be seen around coseismic asperities. Several physical earthquake models (Kaneko et al., 2010; Barbot et al., 2012) have been applied to assess faulting processes at a long time scale based on tectonic loading rates and laboratory experiments, in which the detailed frictional properties on faults are required. Modern geodetic modelling may offer an opportunity to identify the partitioning of frictional properties partitions using both co- and post-seismic observations. However, previous studies have shown overlaps between co- and post-seismic slip distributions determined through geodetic modelling, such as the 2008 Nima-Gaize, the 2008 Damxung earthquake and the 2011 Tohoku-Oki earthquakes (Ryder et al., 2010; Johnson et al., 2012a; Bie et al., 2013). Therefore, to assess whether the frictional law can be applied to natural events needs further efforts, which is the major goal of this thesis. The uncertainties in co- and post-seismic slip models due to the limitations of observations and/or inversion techniques have also been discussed across different events. The four issues raised in Chapter 1 are addressed based on the observations from all the case studies in Chapters 3,4,5 and 6:

1) ***Is the rate-state fault friction law suitable to describe faulting phenomena in natural events?***

The best-fit coseismic slip model of the 2009 M_{W} 6.3 Haixi earthquake determined using InSAR coseismic interferograms suggests two separate slip centres at a depth of 5 km: one with a maximum slip of 1.6 m near the fault bend, the other with a maximum slip of 0.8 m located ~12 km in the east. The spatial pattern of the cumulative afterslip between September 2009 and June 2010 generally corresponds to the coseismic slip zone, which challenges the rate-state frictional law. It is believed that the complex fault geometric structure may play a vital role in earthquake evolution in this case.

The best-fit coseismic slip of the 2011 M_{W} 7.1 Van thrust earthquake suggests that major slip is concentrated at the depths from 10-20 km with a maximum slip of ~6 m, whilst the afterslip in the first 4 days after the mainshock was located at about 5 km just above the coseismic rupture zone. The accumulative postseismic seismic moment reaches up to $1.5+10^{19}$ N.m, equivalent to a M_{W} 6.7 earthquake. Significant overlaps between co- and post-seismic slip models can be found at the depths between 10 and 25 km. A test without slip in the coseismic asperities was carried out to check the uncertainties in the afterslip models, showing that the new slip model can explain observations equally well as the model without additional constraints at depth. A complementary spatial extent between co- and post-seismic slip models is observed.

Large variations of published coseismic slip models of the 2011 M_{W} 9.1 Tohoku-Oki earthquake were observed (MacInnes et al., 2013). A joint inversion with GRACE coseismic gravity changes and GPS displacements was conducted for coseismic slip modelling. The best slip model suggests that the maximum slip of ~42 m appears near the surface towards the Japan trench. A comparison was made between afterslip models and Coulomb stress changes calculated based on different slip models. The patterns of afterslip >2 m show correlation with the coseismic Coulomb stress changes computed with the joint slip model in space. Large uncertainties in the coseismic slip models of this earthquake has been found because GPS displacements data used in modelling are all far from the source (e.g. Tajima et al., 2013). Thus, uncertainties in postseismic afterslip models inferred from postseismic GPS displacements at the same locations cannot be avoided. However, it is difficult to quantify the uncertainties in the afterslip collected in this thesis because no near-field postseismic data is available for postseismic modelling.

The 2010 M_W 6.8 Yushu earthquake is the only strike-slip event considered in this thesis. Interferograms in both Stripmap and ScanSAR modes were used to estimate co- and post-seismic slip models for the event. The determined coseismic slip model has three large slip centres, which is similar to published models (e.g. Li et al., 2011; Jiang et al., 2013), whilst the afterslip model for the 2010 event was determined for the first time in this thesis. The best-fit afterslip model suggests that the major afterslip is located along the shallow part of the fault and the zone between the two large eastern coseismic slip centres, which is consistent with the rate and state velocity weakening asperities model.

Table 7.1 Earthquake models studied using geodetic observations and the performance of the friction law.

#	Event	Mw	Fault Type	Post-seismic Deformation Model	Complementary patterns	References
1	1966 Parkfield	6.0	strike-slip	logarithm	Don't know	(Smith and Wyss, 1968)
2	1976 Guatemala	7.5	strike-slip	logarithm	Don't know	(Bucknam et al., 1978)
3	1989 Loma Pieta	7.1	thrust slip	-	YES*	(Pollitz et al., 1998)
4	1992 Landers	7.5	strike-slip	logarithm	YES***	(Pollitz et al., 2000; Fialko, 2004a; Perfettini and Avouac, 2007)
5	1994 Northridge	6.7	thrust	logarithm	YES*	(Unruh et al., 1997; Wald and Graves, 2001)
6	1999 Izimit	7.5	strike-slip	logarithm	YES***	(Burgmann et al., 2002b)
7	1999 Chi-chi	7.6	thrust	logarithm	YES***	(Hsu et al., 2007)
8	2001 Kokoxili	7.9	strike-slip	logarithm	YES***	(Lasserre et al., 2005; Wen et al., 2012a)
9	2002 Denali	7.9	strike-slip	logarithm	YES***	(Freed et al., 2006)
10	2003 Tokachi-oki	8.0	thrust	logarithm	YES***	(Miyazaki et al., 2004)
11	2003 Zemmouri	6.8	thrust	linear**	YES***	(Cetin et al., 2012)
12	2003 Bam	6.5	strike-slip	logarithm	YES***	(Fielding et al., 2009; Li et al., 2009b)
13	2004 Sumatra-Andama	9.1	thrust	logarithm	YES***	(Chlieh et al., 2007)
14	2004 Parkfield	6.0	strike-slip	logarithm	YES***	(Barbot et al., 2013; Chang et al., 2013)
15	2005 Kashimir	7.6	thrust	-	YES***	(Pathier et al., 2006; Yan et al., 2013; Wang and Fialko, 2014)

16	2005 Nias-Simeulue	8.7	thrust	logarithm	YES***	(Hsu et al., 2006)
17	2007 Sumatra	8.5	thrust	logarithm	YES***	(Lubis et al., 2013)
18	2008 Nima-Gaize	6.3	normal	logarithm	NO	(Ryder et al., 2010)
19	2008 Damxung	6.3	normal	logarithm	NO	(Bie et al., 2013)
20	2009 Haixi	6.3	thrust	logarithm	NO	This thesis
21	2010 Baja	7.2	strike-slip	logarithm	YES***	(Gonzalez-Ortega et al., 2014)
22	2010 Maule	8.8	thrust	logarithm	YES***	(Agurto et al., 2012)
23	2010 Yushu	6.8	strike-slip	-	YES***	This thesis
24	2011 Van	7.1	thrust	-	YES***	(Feng et al., 2014; This thesis)
25	2011 Tohoku-Oki	9.1	thrust	logarithm	YES***	(Johnson et al., 2012a; This thesis; Diao et al., 2013)

Notes: *, no detailed co- and post-seismic slip models were given in the literature, but from the descriptions of postseismic deformation, the complementary slip patterns may be able to be inferred. **, the postseismic displacement history was retrieved using InSAR time-series analysis. A linear model was estimated in the data processing. ***, Small overlaps between co- and postseismic slip models can be found, but most afterslips were distributed in the zones without significant coseismic slips.

Table 7.1 lists 26 earthquakes that have been investigated using co- and post-seismic geodetic observations in this thesis and previous studies. Due to the lack of high spatial resolution geodetic data, early studies, such as those of the 1966 Parkfield earthquake and the 1976 Guatemala earthquake (Smith and Wyss, 1968; Bucknam et al., 1978), did not provide the detailed afterslip distributions on faults. So it is difficult to know if complementary patterns between co- and post-seismic slip models existed in these earthquakes. Postseismic displacement time series following these two earthquakes have been reported with log(time) relationships. Some others, e.g. the 1997 M_W 7.5 Manyi earthquake (Ryder et al., 2007a), the 1992 M_W 7.5 Landers earthquake (Fialko, 2004b) and the 1999 Hector-mine earthquake (Hearn, 2003), have been investigated using GPS or InSAR in the case of afterslip. However, only deep creep was reported. It has also been pointed out that the contributions from viscoelastic relaxation in the upper mantle have not been clearly distinguished from those due to deep creep.

In some normal faulting events (Ryder et al., 2010; Bie et al., 2013) significant afterslip has been reported in the coseismic slip zones, which challenges the frictional law. Although the discrepancy between early afterslip and the friction law in the 2011 Japan earthquake was also exposed (Johnson et al., 2012a), the large variations of its coseismic slip may significantly affect this conclusion. In this thesis, a new coseismic slip model has been determined as discussed above, in which a significant spatial correlation between coseismic Coulomb stress and afterslip (>2 m) has been found. Following the 2005 Nias-Simeulue earthquake (Hsu et al., 2006), complementary slip patterns were imaged using several GPS stations just above the rupture zone of the mainshock. A similar phenomenon has also been reported in the 2003 Tokachi-Oki earthquake (Miyazaki et al., 2004). Robust afterslip under the coseismic slip zone following the 2005 Kashmir earthquake (Wang and Fialko, 2014) has also been recorded using InSAR and GPS data. In this study, no significant effects from viscoelastic relaxation on the afterslip model have been found. From early postseismic deformation using GPS and InSAR, significant shallow afterslip following the 2010 Baja earthquake has been suggested (Gonzalez-Ortega et al., 2014), where no significant coseismic slip was revealed. Although poroelastic rebound and fault zone contraction could also have contributed to the postseismic observations, the shallow afterslip cannot be influenced by other physical postseismic mechanisms (Gonzalez-Ortega et al., 2014). Therefore, it is suggested that the laboratory based friction theory can be appropriate for many natural events. To those events with significant overlaps between seismic and aseismic slip, slip uncertainties from geodetic modelling may limit our understanding of the distribution of frictional properties on faults.

The 2009 M_W 6.3 Haixi earthquake investigated in Chapter 3 is an exceptional case, in which postseismic afterslip has been revealed on the coseismic slip zone. From recent numerical studies (Dolan and Haravitch, 2014; Lindsey et al., 2014), structure maturity of a fault is found in correlation with slip spatial distribution. It may be then inferred that the frictional properties of faults are not constant during faulting evolution, which should vary during the rupture history of faults. The observations in this thesis may suggest that the 2009 mainshock fault is still at the early stage of its faulting history and that the fault structure plays the main role in the development of faulting at this site.

2) *Can rapid aftershock influence the estimates from coseismic modelling?*

Using SBAS InSAR, line-of-sight (LOS) postseismic displacements after the 2009 Haixi earthquake were recovered with seven Envisat ASAR images. The first SAR image after the mainshock was acquired on 16 September 2009. No observations were available for the period of rapid deformation within the first month after the mainshock. However, applying a log deformation model in the SBAS InSAR inversion, the accumulative postseismic displacements in the first month were assessed up to 50 % of the total moment release in the first year after the mainshock. Postseismic displacements in the first 4 days after the 2011 Van earthquake obtained by a CSK interferogram have been used to determine significant shallow afterslip that released a total seismic moment of about $1.5+10^{19}$ N.m, equivalent to a M_W 6.7 earthquake. When an ASAR coseismic pair covering the first 7 days after the mainshock was used in coseismic modelling, the maximum modelled coseismic slip is ~1 m smaller than without this pair. The difference between these results is suggested to be due to the postseismic displacements recorded in the ASAR pair.

Similar results have been found for the 2014 M_W 6.1 Napa, California earthquake, where coseismic slip models from only GPS data and only one Sentinel-1A coseismic interferogram are unable to be reconciled (Feng et al, 2014, in preparation). The seismic moment of the InSAR inferred slip model is at least 1.5 times greater than the GPS only slip model, suggesting that the InSAR measurements covering one week after the mainshock include significant postseismic displacements. Regional cGPS measurements at GPS sites tens of km away from the fault do record at least ~5 mm postseismic displacements in the first 7 days after the mainshock (Feng et al. 2014, in preparation). Therefore, the estimate of the magnitude of coseismic slip can significantly be influenced by early afterslip, but the spatial extent of major coseismic slip should be able to be determined reliably using near-field observations, including InSAR.

3) ***Do the uncertainties in the geodetic modelling bias our understanding of fault frictional properties?***

As discussed earlier, uncertainties in afterslip were found for the 2011 Van earthquake. An afterslip model without slip constraints in the coseismic asperities shows a significant overlap with the coseismic slip model at depth. When slip in the coseismic asperities was fixed at zero, new afterslip can still explain the postseismic observations as well as the afterslip model determined without such constraints. Afterslip at depth should mainly account for signals in the far fields. Since the magnitude of the deep slip is small, it has been impossible to use a single interferogram to isolate postseismic signals from observation errors. For the 2011 Japan earthquake, the nearest inland GPS station is about 120 km away from the epicentre, which may explain why large variations of coseismic slip models have been found in previous published results although data from thousands of GPS stations were available for this case. In the checkerboard test carried out in Chapter 5, asperities close to the Japan trench even cannot be recovered successfully with these GPS observations only. Thus, it can be inferred that the lack of near-field observations may also be an issue when retrieving a reliable afterslip model. With effective constraints in the afterslip inversion in Chapter 4, the expected afterslip patterns have been determined, but assessing whether these expected slips are more realistic than those without additional constraints is beyond the ability of the limited observations used in this thesis.

4) ***Do other postseismic mechanisms in the lower crust and upper mantle after a large earthquake affect the estimation of shallow afterslip?***

Poroelastic rebound and viscoelastic relaxation have been widely observed after large earthquakes in the previous studies (e.g. Peltzer et al., 1998; Johnson and Segall, 2004). Although no clear postseismic deformation pattern caused by these two physical mechanisms has been found in the earthquakes investigated in this thesis, theoretical simulation may also be helpful to identify their effects on shallow afterslip modelling. Deep creep has been believed to be undistinguishable from viscoelastic relaxation in previous studies (Ryder et al., 2007a; Wen et al., 2012a). Whether the contribution from deep slip is completely mixed with viscoelastic relaxation has been beyond the scope of this thesis. A series of forward simulations of viscoelastic relaxation were implemented in the 2010 Yushu earthquake. Due to significant noise in the interferogram that recorded postseismic measurements, it is difficult to provide strong constraints on the estimates of local viscosity in the lower crust and upper mantle. So, the lower bound of the viscosity of the upper mantle in Tibet determined in other studies was employed (Clark and Royden, 2000). Theoretical simulation shows that viscoelastic relaxation could mainly affect long wavelength postseismic displacements, which cannot significantly influence estimates of shallow afterslip that mainly generates significant surface changes close to faults. Clearly different deformation polarities can be generated due to poroelastic rebound, which can be directly employed to estimate this mechanism in postseismic analysis. Note that effects of locally inhomogeneous materials have not yet been considered in the inversion tool used in this thesis.

7.2 Contributions of this research

In this thesis, four events have been investigated in detail and contributions to the understanding of their fault parameters and other aspects have been achieved as follows:

1) Three large M_W 6.3 earthquakes were investigated in terms of their geometric fault parameters and slip models in the 2003-2009 Qinghai earthquake sequence. A coseismic LOS interferogram associated with the 2003 M_W 6.3 Delingha earthquake was generated for the first time. Although the dip directions of the seismic faults associated with the 2003 and 2008 earthquakes cannot be conclusively determined, the locations of the major slip of these two earthquakes have been robustly obtained. Maximum slips of the 2003, 2008 and 2009 mainshocks are located at depths of ~10, 15 and 5 km respectively, suggesting that the shear strength of the upper crust in this region shows stratification.
2) The 2011 M_W 7.1 Van, Turkey earthquake is another thrust event, which did not break the surface. A north-dipping fault was found to be associated with the mainshock. A correlation between the coseismic slip pattern and surface topography was discovered, suggesting that the surface topography could play an important role in the earthquake nucleation during the earthquake cycle as do sea mounts in locating subduction zone earthquakes.
3) Locations of the maximum slips in several previous slip models of the 2011 M_W 9.1 Tohoku-Oki earthquake have been outlined in this thesis. Significant variations have been revealed. The largest distance of the maximum slips between two of the collected slip models is ~100 km. A joint slip inversion strategy using both GRACE gravity changes and terrestrial GPS observations was proposed to re-estimate the coseismic slip model of this event. The best-fit slip model suggests that the maximum slip of ~42 m appears at the seafloor close to the Japan Trench, of which the maximum slip is located 100 km south east of the slip centre determined using the inland GPS data only.
4) The 2010 Yushu earthquake is one of the best-investigated events in the Tibet Plateau. A number of coseismic slip models have been reported after the earthquake using InSAR interferograms. With more SAR images than previous studies, the biggest aftershock occurring one hour after the mainshock has been analyzed. It is believed that the biggest aftershock is not located within the western segment of the three slip concentrations. The results are consistent with a joint inversion using seismic data and coseismic InSAR observations (Yokota et al., 2012). Another M_W 5.8 aftershock on 29 May 2010 has also been observed using an ASAR ScanSAR interferogram. The best slip model for this aftershock suggests that the main fault for this large aftershock strikes at 70° with a nearly vertical dip angle, which is on a secondary fault, rather than on the extension of the main fault. An earthquake swarm spanning the period from 29 May to 20 June 2010 may have been mainly triggered by this event.

7.3 Limitations and future work

7.3.1 Limitations

This research has improved our understanding of several events based on the existing data. However, the results and the interpretations drawn from them may not be ideal at present due to the following reasons:

1) ***Limited Data***. Although many data have been collected for the 2003 Qinghai earthquake sequence, data used in the 2003 and 2008 Qinghai mainshocks cannot determine unique solutions for the seismic faults. Conjugate finite slip models at depth can generate certain differences in surface deformation patterns, but to distinguish the differences between them is beyond the ability of current datasets. More observations from different means should be helpful to identify an optimal model from these slip models. In the 2011 Van earthquake, the afterslip vectors were determined using only one InSAR pair. Significant variations of rake angles relative to the coseismic rupture have been found in the current afterslip model for this earthquake. Whether such slip variations are significantly influenced by data uncertainties remains unanswered
2) ***Limited Knowledge on Data Errors***. It is a challenge to estimate data errors in a single interferogram. Empirical structure functions can work for estimating effects from long-wavelength atmospheric signals, but are not sufficient to allow selection of an optimal slip model from the two afterslip models of the 2011 Van earthquake determined in Chapter 4. A LOOCC method was introduced to estimate relative weights for GRACE gravity changes in the 2011 M_W 9.1 Tohoku-Oki earthquake in Chapter 5. Although the determined weights can result in a better data fit to near-field gravity changes, no independent quantitative way has been implemented to validate the feasibility of this method.
3) ***Complex Earth Model***. Simple elastic half-space dislocation has been widely used for co- and post-seismic modelling. Although a better data fit with a layered Earth model has been pointed out in Chapter 4, the simple elastic half-space model was still used in geodetic modelling in other cases. Slight differences of GRACE gravity changes from layered and half-space elastic Earth models respectively have also been found in Chapter 5. Since the calculation of GRACE based gravity changes based on the theoretical model is very time-consuming, only elastic half-space Earth model was considered in the final data analysis.

7.3.2 Future work

Earthquakes are always complicated. The four large earthquakes investigated in this thesis are only a very small sample of large events in the satellite era. Although another 22 events from previous studies, they still represent a limited sample for which to draw conclusions regarding the performance of the friction law in natural events. Together with other findings in this thesis, a list of future work is suggested to improve our knowledge of the physics of earthquakes.

1) ***To Build a Geodetic Database with Co- and Post-seismic Slip Models***. The seismic inversion validation (SIV) project has suggested a good proxy approach to collect and validate slip models. Following the principles of SIV, in addition to the coseismic slip models, original observations and afterslip models should also be compiled from already published results. An InSAR-derived earthquake parameter database has been released in previous studies (Ferreira et al., 2011; Weston et al., 2011; Wright et al., 2013), which can tell which earthquakes can be further considered using InSAR observations. An easy-to-access data format and useful processing codes need be designed. Hopefully, useful data and slip models can gradually be collected from the community, which can provide many more opportunities to improve our understanding of earthquake physics, including various faulting behaviours.
2) ***To Fulfil Automated or Semi-automated Geodetic Inversion***. Geodetic inversion is a complicated process. The availability of geodetic observations will increase rapidly with new deployments of SAR satellites and new generations of geodetic techniques. PSOKINV has been developed as a mature inversion package that can handle multiple geodetic observations. This package can be used to build an automated or semi-automated inversion platform to provide rapid response to future large earthquakes. To meet the need for automated inversion and rapid response, several elements should be included: a robust and efficient inversion package, a flexible structure that can allow users to customize own inversion flow anytime, an effective validation package with advanced mathematic models, and an automated output package including resultant images and inversion information.
3) ***To Approach 4D Physical Faulting Evolution Assessment***. Global strain maps have been gradually built up along some large strike-slip faults using modern geodetic measurements (e.g. Wang and Wright, 2012; Walters et al., 2014). It is possible to implement inversions to identify future asperities based on these data. With knowledge of co- and post-seismic slip models, fault frictional properties can be partly retrieved with numerical analysis. Combining with results from laboratory experiments, a full physical faulting model can be developed to explain observations covering different phases of an earthquake cycle.

References

Agram, P.S., Jolivet, R., Riel, B., Lin, Y.N., Simons, M., Hetland, E., Doin, M.P., and Lasserre, C., 2013, New Radar Interferometric Time Series Analysis Toolbox Released: EOS, Transactions American Geophysical Union, v. 94, p. 69-70.

Agurto, H., Rietbrock, A., Ryder, I., and Miller, M., 2012, Seismic-afterslip characterization of the 2010 Mw 8.8 Maule, Chile, earthquake based on moment tensor inversion: Geophys. Res. Lett., v. 39.

Aksoy, E., Türkmen, İ., and Turan, M., 2005, Tectonics and sedimentation in convergent margin basins: an example from the Tertiary Elazığ basin, Eastern Turkey: Journal of Asian Earth Sciences, v. 25, p. 459-472.

Altiner, Y., Söhne, W., Güney, C., Perlt, J., Wang, R., and Muzli, M., 2013, A geodetic study of the 23 October 2011 Van, Turkey earthquake: Tectonophysics, v. 588, p. 118-134.

Amelung, F., Baker, S., Biggs, J., and Gourmelen, N., 2011, GeodMod - Matlab-based Geodetic Modeling Software: Miami.

Ammon, C.J., Lay, T., Kanamori, H., and Cleveland, M., 2011, A rupture model of the 2011 off the Pacific coast of Tohoku Earthquake: Earth Planets Space, v. 63, p. 693-696.

Antonia, R., and Smalley, R., 2001, Scaling range exponents from X-wire measurements in the atmospheric surface layer: Boundary-layer meteorology, v. 100, p. 439-457.

Aoki, Y., Segall, P., Kato, T., Cervelli, P., and Shimada, S., 1999, Imaging Magma Transport During the 1997 Seismic Swarm off the Izu Peninsula, Japan: Science, v. 286, p. 927-930.

Armijo, R., Tapponnier, P., and Han, T., 1989, Late Cenozoic right-lateral strike-slip faulting in southern Tibet: Journal of Geophysical Research: Solid Earth, v. 94, p. 2787-2838.

Aster, R.C., Borchers, B., and Thurber, C.H., 2013, Parameter estimation and inverse problems, Academic Press.

Atzori, S., and Antonioli, A., 2011, Optimal fault resolution in geodetic inversion of coseismic data: Geophys. J. Int., v. 185, p. 529-538.

Avouac, J.-P., 2011, The lessons of Tohoku-Oki: Nature, v. 475, p. 300.

Bahr, H., and Hanssen, R.F., 2012, Reliable estimation of orbit errors in spaceborne SAR interferometry - the network approach: J Geod.

Bamler, R., and Hartl, P., 1998, Synthetic aperture radar interferometry: Inverse Problems, v. 14, p. R1-R54.

Baran, I., Stewart, M., and Claessens, S., 2005, A new functional model for determining minimum and maximum detectable deformation gradient resolved by satellite radar interferometry: Geoscience and Remote Sensing, IEEE Transactions on, v. 43, p. 675-682.

Barbot, S., Agram, P., and De Michele, M., 2013, Change of apparent segmentation of the San Andreas fault around Parkfield from space geodetic observations across multiple periods: Journal of Geophysical Research: Solid Earth, v. 118, p. 6311-6327.

Barbot, S., Fialko, Y., and Bock, Y., 2009a, Postseismic deformation due to the Mw6.0 2004 Parkfield earthquake: Stress-driven creep on a fault with spatially variable rate-and-state friction parameters: J. Geophys. Res., v. 114.

Barbot, S., Fialko, Y., and Sandwell, D., 2009b, Three-dimensional models of elastostatic deformation in heterogeneous media, with applications to the Eastern California Shear Zone: Geophys. J. Int., v. 179, p. 500-520.

Barbot, S., Hamiel, Y., and Fialko, Y., 2008, Space geodetic investigation of the coseismic and postseismic deformation due to the 2003 MW7.2 Altai earthquake: Implications for the local lithospheric rhecology: J. geophys. Res, v. 113.

Barbot, S., Lapusta, N., and Avouac, J.-P., 2012, Under the Hood of the Earthquake Machine: Toward Predictive Modeling of the Seismic Cycle: Science, v. 336, p. 707-710.

Barka, A.A., and Kadinsky-Cade, K., 1988, Strike-slip fault geometry in Turkey and its influence on earthquake activity: Tectonics, v. 7, p. 663-684.

Bechor, N.B.D., and Zebker, H.A., 2006, Measuring two-dimensional movements using a single InSAR pair: Geophys. Res. Lett., v. 33, p. L16311.

Bekaert, D., Wright, T.J., Hooper, A.J., and Walters, R.J., 2013, A Tropospheric Correction Method for Short and Long-Swath InSAR Processing, Living Planet Symposium 2013 Edinburgh, ESA.

Ben-Dov, N.B., and Herring, T.A., 2011, Multiple Aperture InSAR (MAI) with C-Band and L-Band: Noise and Precision, Proceedings of the ESA Fringe Workshop 2011: Frascati, Italy.

Berardino, P., Fornaro, G., Lanari, R., and Sansosti, E., 2002, A New Algorithm for Surface Deformation Monitoring Based on Small Baseline Differential SAR Interferograms: IEEE Transactions on Geoscience and Remote Sensing, v. 40, p. 2375-2383.

Bie, L., Ryder, I., Nippress, S.E.J., and Bürgmann, R., 2013, Coseismic and post-seismic activity associated with the 2008 Mw 6.3 Damxung earthquake, Tibet, constrained by InSAR: Geophysical Journal International.

Biggs, J., Bergman, E., Emmerson, B., Funning, G.J., Jackson, J., Parsons, B., and Wright, T.J., 2006, Fault identification for buried strike-slip earthquakes using InSAR: The 1994 and 2004 Al Hoceima, Morocco earthquakes: Geophys. J. Int., v. 166, p. 1347-1362.

Biggs, J., Wright, T., Lu, Z., and Parsons, B., 2007, Multi-interferomgram method for measuring interseismic deformation: Denali Fault, Alaska: Geophys. J. Int., v. 170, p. 1165-1179.

Bilek, S.L., DeShon, H.R., and Engdahl, E.R., 2012, Spatial variations in earthquake source characteristics within the 2011 Mw = 9.0 Tohoku, Japan rupture zone: Geophysical Research Letters, v. 39, p. L09304.

Bilek, S.L., Schwartz, S.Y., and DeShon, H.R., 2003, Control of seafloor roughness on earthquake rupture behavior: Geology, v. 31, p. 455-458.

Bilich, A., Cassidy, J.F., and Larson, K.M., 2008, GPS Seismology: Application to the 2002 Mw 7.9 Denali Fault Earthquake: Bull. Seism. Soc. Am., v. 98, p. 593-606.

Bird, P., 2003, An updated digital model of plate boundaries: Geochem. Geophys. Geosyst., v. 4.

Boatwright, J., and Cocco, M., 1996, Frictional constraints on crustal faulting: Journal of Geophysical Research: Solid Earth, v. 101, p. 13895-13909.

Bouchon, M., Durand, V., Marsan, D., Karabulut, H., and Schmittbuhl, J., 2013, The long precursory phase of most large interplate earthquakes: Nature Geosci, v. 6, p. 299-302.

Brace, W.F., and Byerlee, J.D., 1966, Stick-slip as a Mechanism for Earthquakes: Science, v. 153, p. 990-92.

Braitenberg, C., Wang, Y., Fang, J., and Hsu, H.T., 2003, Spatial variations of flexure parameters over the Tibet–Quinghai plateau: Earth and Planetary Science Letters, v. 205, p. 211-224.

Brodsky, E.E., and Lay, T., 2014, Recognizing Foreshocks from the 1 April 2014 Chile Earthquake: Science, v. 344, p. 700-702.

Bruhat, L., Barbot, S., and Avouac, J.-P., 2011, Evidence for postseismic deformation of the lower crust following the 2004 Mw6.0 Parkfield earthquake: J. Geophys. Res., v. 116.

Buckley, S.M., and Gudipati, K., 2011, Evaluating ScanSAR Interferometry Deformation Time Series Using Bursted Stripmap Data: Geoscience and Remote Sensing, IEEE Transactions on, v. 49, p. 2335-2342.

Bucknam, R.C., Plafker, G., and Sharp, R.V., 1978, Fault movement (afterslip) following the Guatemala earthquake of February 4, 1976: Geology, v. 6, p. 170-173.

Burgmann, R., Ayhan, M.E., Fielding, E.J., Wright, T.J., McClusky, S., Aktug, B., Demir, C., Lenk, O., and Turkezer, A., 2002a, Deformation during the 12 November 1999 Duzce, Turkey, earthquake, from GPS and InSAR data: Bulletin of the Seismological Society of America, v. 92, p. 161-171.

Burgmann, R., Ergintav, S., Segall, P., Hearn, E.H., McClusky, S., Reilinger, R.E., Woith, H., and Zschau, J., 2002b, Time-Dependent Distributed Afterslip on and Deep below the Izmit Earthquake Rupture: Bull. Seism. Soc. Am., v. 92, p. 126-137.

Burgmann, R., Rosen, P.A., and Fielding, E.J., 2000, Synthetic aperture radar interferometry to measure Earth's surface topography and its deformation: Annual Review of Earth and Planetary Sciences, v. 28, p. 169-209.

Cambiotti, G., and Sabadini, R., 2012, A source model for the great 2011 Tohoku earthquake (Mw=9.1) from inversion of GRACE gravity data: Earth and Planetary Science Letters, v. 335-336, p. 72-79.

Casu, F., Lanari, R., Sansosti, E., Poland, M., Miklius, A., Solaro, G., and Tizzani, P., 2009, SBAS-InSAR analysis of surface deformation at Mauna Loa and Kilauea volcanoes in Hawaii, Geoscience and Remote Sensing Symposium,2009 IEEE International,IGARSS 2009, Volume 4, p. IV-41-IV-44.

Cetin, E., Meghraoui, M., Cakir, Z., Akoglu, A.M., Mimouni, O., and Chebbah, M., 2012, Seven years of postseismic deformation following the 2003 Mw = 6.8 Zemmouri earthquake (Algeria) from InSAR time series: Geophys. Res. Lett., v. 39, p. L10307.

Chang, S.-H., Avouac, J.-P., Barbot, S., and Lee, J.-C., 2013, Spatially variable fault friction derived from dynamic modeling of aseismic afterslip due to the 2004 Parkfield earthquake: Journal of Geophysical Research: Solid Earth, v. 118, p. 3431-3447.

Chaussard, E., Wdowinski, S., Cabral-Cano, E., and Amelung, F., 2014, Land subsidence in central Mexico detected by ALOS InSAR time-series: Remote Sensing of Environment, v. 140, p. 94-106.

Chen, C.W., and Zebker, H.A., 2000, Network approaches to two-dimensional phase unwrapping: intractability and two new algorithms: Journal of the Optical Society of America A, v. 17, p. 401-414

Chen, G., U., X.X., U., A.Z.H., Zhang, X., Yuan, R., Yann, K., and Jean-Mathieu, N., 2013, Seismotectonics of the 2008 and 2009 Qaidam Earthquakes and its Implication for Regional Tectonics: Acta Geologica Sinica - English Edition, v. 87, p. 618-628.

Chen, L., Berntsson, F., Zhang, Z., Wang, P., Wu, J., and Xu, T., 2014, Seismically constrained thermo-rheological structure of the eastern Tibetan margin: Implication for lithospheric delamination: Tectonophysics, v. 627, p. 122-134.

Chen, L., Wang, H., Ran, Y., Sun, X., Su, G., Wang, J., Tan, X., Li, Z., and Zhang, X., 2010, The MS7.1 Yushu earthquake surface rupture and large historical earthquakes on the Garzê-Yushu Fault: Chinese Science Bulletin, v. 55, p. 3504-3509.

Chen, Q., Freymueller, J.T., Wang, Q., Yang, Z., Xu, C., and Liu, J., 2004, A deforming block model for the present-day tectonics of Tibet: Journal of Geophysical Research: Solid Earth, v. 109, p. B01403.

Chen, W.-P., Chen, C.-Y., and Nabelek, J.L., 1999, Present-day deformation of the Qaidam basin with implications for intra-continental tectonics: Tectonics, v. 305, p. 165-181.

Cheng, M., and Tapley, B.D., 2004, Variations in Earth's oblateness during the past 28 years: J. Geophys. Res., v. 109.

Chlieh, M., Avouac, J.-P., Hjorleifsdottir, V., Song, T.-R.A., Ji, C., Sieh, K., Sladen, A., Hebert, H., Prawirodirdjo, L., Bock, Y., and Galetzka, J., 2007, Coseismic Slip and Afterslip of the Great Mw 9.15 Sumatra-Andaman Earthquake of 2004: Bull. Seism. Soc. Am., v. 97, p. S152-S173.

Chorowicz, J., Luxey, P., Lyberis, N., Carvalho, J., Parrot, J.-F., Yürür, T., and Gündogdu, N., 1994, The Maras Triple Junction (southern Turkey) based on digital elevation model and satellite imagery interpretation: Journal of Geophysical Research: Solid Earth, v. 99, p. 20225-20242.

Chunyan, Q.U., Xinjian, S., Yunhua, L.I.U., Guohong, Z., Xiaogang, S., Guifang, Z., Liming, G.U.O., and Yufei, H.A.N., 2012, Ground Surface Ruptures and Near-Fault, Large-Scale Displacements Caused by the Wenchuan Ms8.0 Earthquake Derived from Pixel Offset Tracking on Synthetic Aperture Radar Images: Acta Geologica Sinica - English Edition, v. 86, p. 510-519.

Clark, M.K., and Royden, L.H., 2000, Topographic ooze: Building the eastern margin of Tibet by lower crustal flow: Geology, v. 28, p. 703-706.

Comninou, M., and Dundurs, J., 1975, The angular dislocation in a half space: Journal of Elasticity, v. 5, p. 203-216.

Cowgill, E., Gold, R.D., Xuanhua, C., Xiao-Feng, W., Arrowsmith, J.R., and Southon, J., 2009, Low Quaternary slip rate reconciles geodetic and geologic rates along the Altyn Tagh fault, northwestern Tibet: Geology, v. 37, p. 647-650.

Curlander, J.C., and McDonough, R.N., 1991, Synthetic Aperture Radar: Systems and Signal Processing, Wiley.

Cutrona, L., 1990, Synthetic aperture radar: Radar Handbook, second edition, ed. M. Skolnik, McGraw-Hill, New York.

Daneill, J.E., Khazai, B., Wenzel, F., and Vervaeck, A., 2011, The CATDAT damaming earthquakes database: Nat. Hazards Earth Syst. Sci., v. 11, p. 2235-2251.

Das, S., and Watts, A.B., 2009, Effect of Subducting Seafloor Topography on the Rupture Characteristics of Great Subduction Zone Earthquakes, *in* Lallemand, S., and Funiciello, F., eds., Subduction Zone Geodynamics: Frontiers in Earth Sciences, Springer Berlin Heidelberg, p. 103-118.

Dehghani, M., Valadan Zoej, M.J., Entezam, I., Mansourian, A., and Saatchi, S., 2009, InSAR monitoring of progressive land subsidence in Neyshabour, northeast Iran: Geophysical Journal International, v. 178, p. 47-56.

Delouis, B., Giardini, D., Lundgren, P., and Salichon, J., 2002, Joint Invertion of InSAR, GPS, teleseismic, and strong-motion data for the spatial and temporal distribution of earthquake slip: Application to the 1999 Izmit mainshock: Bull. Seism. Soc. Am., v. 92, p. 278-299.

DeMets, C., 1997, Afterslip no longer an afterthought: Nature, v. 386, p. 549-549.

DeMets, C., Gordon, R.G., and Argus, D.F., 2010, Geologically current plate motions: Geophysical Journal International, v. 181, p. 1-80.

Deng, Q., Zhang, P., Ran, Y., Yang, X., Min, W., and Chu, Q., 2003, Basic characteristics of active tectonics of China: Science in China Series D: Earth Sciences, v. 46, p. 356-372.

Dewey, J.F., and Pindell, J.L., 1985, Neogene block tectonics of eastern Turkey and northern South America: Continental applications of the finite difference method: Tectonics, v. 4, p. 71-83.

Diao, F., Xiong, X., Wang, R., Zheng, Y., Walter, T.R., Weng, H., and Li, J., 2013, Overlapping post-seismic deformation processes: afterslip and viscoelastic relaxation following the 2011 Mw 9.0 Tohoku (Japan) earthquake: Geophysical Journal International.

Diao, G.-L., Wang, X.-S., Gao, G.-Y., Nie, X.-H., and Feng, X.-D., 2010, Tectonic Block Attribution of the Wenchuan and Yushu Earthquakes Distinguished by Focal Mechanism Types: Chinese Journal of Geophysics, v. 53, p. 849-854.

Dieterich, J., 1978, Time-dependent friction and the mechanics of stick-slip: Pure and Applied Geophysics, v. 116, p. 790-806.

Dieterich, J., 1994, A constitutive law for rate of earthquake production and its application to earthquake clustering: Journal of Geophysical Research: Solid Earth, v. 99, p. 2601-2618.

Dieterich, J.H., 1979a, Modeling of rock friction: 1. Experimental results and constitutive equations: Journal of Geophysical Research: Solid Earth, v. 84, p. 2161-2168.

Dieterich, J.H., 1979b, Modeling of rock friction: 2. Simulation of preseismic slip: Journal of Geophysical

Research: Solid Earth, v. 84, p. 2169-2175.

Dixon, T.H., and Moore, J.C., 2007, The Seismogenic Zone of Subduction Thrust Faults, Columbia University Press.

Dobretsov, N.L., Buslov, M.M., Delvaux, D., Berzin, N.A., and Ermikov, V.D., 1996, Meso-and Cenozoic tectonics of the Central Asian mountain belt: effects of lithospheric plate interaction and mantle plumes: International Geology Review, v. 38, p. 430-466.

Doğan, B., and Karakaş, A., 2013, Geometry of co-seismic surface ruptures and tectonic meaning of the 23 October 2011 Mw 7.1 Van earthquake (East Anatolian Region, Turkey): Journal of Structural Geology, v. 46, p. 99-114.

Dolan, J.F., and Haravitch, B.D., 2014, How well do surface slip measurements track slip at depth in large strike-slip earthquakes? The importance of fault structural maturity in controlling on-fault slip versus off-fault surface deformation: Earth and Planetary Science Letters, v. 388, p. 38-47.

Donnellan, A., and Lyzenga, G.A., 1998, GPS observations of fault afterslip and upper crustal deformation following the Northridge earthquake: Journal of Geophysical Research: Solid Earth, v. 103, p. 21285-21297.

Donnellan, A., Parker, J.W., and Peltzer, G., 2002, Combined GPS and InSAR Models of Postseismic Deformation from the Northridge Earthquake: Pure and Applied Geophysics, v. 159, p. 2261-2270.

Ducret, G., Doin, M.P., Grandin, R., Lasserre, C., and Guillaso, S., 2011, Dem corrections before unwrapping in a Small Baseline strategy for InSar time series analysis, Geoscience and Remote Sensing Symposium (IGARSS), 2011 IEEE International, p. 1353-1356.

Ducret, G., Doin, M.P., Grandin, R., Lasserre, C., and Guillaso, S., 2014, DEM Corrections Before Unwrapping in a Small Baseline Strategy for InSAR Time Series Analysis: Geoscience and Remote Sensing Letters, IEEE, v. 11, p. 696-700.

Dunham, E.M., Belanger, D., Cong, L., and Kozdon, J.E., 2011, Earthquake Ruptures with Strongly Rate-Weakening Friction and Off-Fault Plasticity, Part 2: Nonplanar Faults: Bulletin of the Seismological Society of America, v. 101, p. 2308-2322.

Ebmeier, S.K., Biggs, J., Mather, T.A., Elliott, J.R., Wadge, G., and Amelung, F., 2012, Measuring large topographic change with InSAR: Lava thicknesses, extrusion rate and subsidence rate at Santiaguito volcano, Guatemala: Earth and Planetary Science Letters, v. 335–336, p. 216-225.

Elliott, J.R., Biggs, J., Parsons, B., and Wright, T.J., 2008, InSAR slip rate determination on the Altyn Tagh Fault, northern Tibet, in the presence of topographically correlated atmospheric delays: Geophysical Research Letters, v. 35.

Elliott, J.R., Copley, A.C., Holley, R., Scharer, K., and Parsons, B., 2013, The 2011 Mw 7.1 Van (Eastern Turkey) earthquake: Journal of Geophysical Research: Solid Earth, v. 118, p. 1-19.

Elliott, J.R., Nissen, E.K., England, P.C., Jackson, J.A., Lamb, S., Li, Z., Oehlers, M., and Parsons, B., 2012, Slip in the 2010-2011 Canterbury earthquakes, New Zealand: J. Geophys. Res., v. 117.

Elliott, J.R., Parsons, B., Jackson, J.A., Shan, X., Sloan, R.A., and Walker, R.T., 2011, Depth segmentation of the seismogenic continental crust: The 2008 and 2009 Qaidam earthquakes: Geophys. Res. Lett, v. 38.

Elliott, J.R., Walters, R.J., England, P.C., Jackson, J.A., Li, Z., and Parsons, B., 2010, Extension on the Tibetan plateau: recent normal faulting measured by InSAR and body wave seismology: Geophys. J. Int., v. 183, p. 503-535.

Emardson, T.R., Simons, M., and Webb, F.H., 2003, Neutral atmospheric delay in interferometric synthetic aperture radar applications: Statistical description and mitigation: Journal of Geophysical Research: Solid Earth, v. 108, p. 2231.

Fagereng, Å., and Toy, V.G., 2011, Geology of the earthquake source: an introduction: Geological Society, London, Special Publications, v. 359, p. 1-16.

Farr, T.G., Caro, E., Crippen, R., Duren, R., Hensley, S., Kobrick, M., Paller, M., Rodriguez, E., P. Rosen, L.R., Seal, D., Shaffer, S., Shimada, J., Umland, J., Werner, M., Oskin, M., Burbank, D., and Alsdorf, D., 2007, The Shuttle Radar Topography Mission: Reviews of Geophysics, v. 45.

Fattahi, H., and Amelung, F., 2013, DEM Error Correction in InSAR Time Series: Geoscience and Remote Sensing, IEEE Transactions on, v. 51, p. 4249-4259.

Fattahi, H., and Amelung, F., 2014, InSAR uncertainty due to orbital errors: Geophysical Journal International, v. 199, p. 549-560.

Feng, G., and Jonsson, S., 2012, Shortcomings of InSAR for studying megathrust earthquakes: The case of the Mw9.0 Tohoku-Oki earthquake: Geophys. Res. Lett., v. 39.

Feng, W.-P., Xu, L.-S., and Li, Z.-H., 2010a, Fault parameters of the October 2008 Damxung M(w)6.3 earthquake from InSAR inversion and its tectonic implication: CHINESE JOURNAL OF GEOPHYSICS-CHINESE EDITION, v. 53, p. 1134-1142.

Feng, W.-P., Xu, L.-S., Xu, Z.-H., Li, Z.-H., Li, C.-L., and Zhao, H., 2009, Source parameters of the 2008 Gerze M(w)6.4 and M(w)5.9 earthquakes from InSAR measurements: CHINESE JOURNAL OF GEOPHYSICS-CHINESE EDITION, v. 52, p. 983-993.

Feng, W., Li, Z., Elliott, J.R., Fukushima, Y., Hoey, T., Singleton, A., Cook, R., and Xu, Z., 2013a, The 2011 MW 6.8 Burma earthquake: fault constraints provided by multiple SAR techniques: Geophysical Journal International, v. 195, p. 650-660.

Feng, W., Li, Z., Hoey, T., Zhang, Y., Wang, R., Samsonov, S., Li, Y., and Xu, Z., 2014, Patterns and mechanisms of coseismic and postseismic slips of the 2011 MW 7.1 Van (Turkey) earthquake revealed by multi-platform synthetic aperture radar interferometry: Tectonophysics, v. 632, p. 188-198.

Feng, W., Li, Z., John, E., Yo, F., Hoey, T., Singleton, A., Cook, R., Xu, Z., and Parsons, B., 2013b, The 2011 Mw 6.8 Burma earthquake: fault constraints provided by multiple SAR techniques: Geophysical Journal International.

Feng, W.P., and Li, Z.H., 2010, A novel hybrid PSO/simplex algorithm for determining earthquake source paramers using InSAR data: Progress in Geophs.(In Chinese), v. 25, p. 1189-1196.

Feng, W.P., Li, Z.H., and Li, C.L., 2010b, Optimal source parameters of the 6 April 2009 Mw6.3 L'Aquila, Italy earthquake from InSAR observations: Progress in Geophs.(In Chinese), v. 25, p. 1550-1559.

Fernandez, J., Tizzani, P., Manzo, M., Borgia, A., Gonzalez, P.J., Marti, J., Pepe, A., Camacho, A.G., Casu, F., Berardino, P., Prieto, J.F., and Lanari, R., 2009, Gravity-driven deformation of Tenerife measured by InSAR time series analysis: Geophysical Research Letters, v. 36.

Ferreira, A.M.G., Weston, J., and Funning, G.J., 2011, Global Compilation of interferometric synthetic aperture radar earthqake source models: 2. Effects of 3-D Earth structure: J. Geophys. Res., v. 116.

Ferretti, A., Fumagalli, A., Novali, F., Prati, C., Rocca, F., and Rucci, A., 2011, A New Algorithm for Processing Interferometric Data-Stacks: SqueeSAR: IEEE Transactions on Geoscience and Remote Sensing, v. 49, p. 3460-3470.

Ferretti, A., Monti-Guarnieri, A., Prati, C., and Rocca, F., 2007, Guidelines for SAR Interferometry Processing and Interpretation: Didier Massonnet, ESA Publications.

Ferretti, A., Prati, C., and Rocca, F., 2001, Permanent scatterers in SAR interferometry: IEEE Transactions on Geoscience and Remote Sensing, v. 39, p. 8-20.

Fialko, Y., 2004a, Evidence of fluid-filled upper crust from observations of post-seismic deformation due to the 1992 M_W7.3 Landers earthquake: J. Geophys. Res., v. 109.

Fialko, Y., 2004b, Probing the mechanical properties of seismically active crust with space geodesy: Study of the co-seismic deformation due to the 1992 Mw7.3 Landers (southern California) earthquake: J. Geophys. Res., v. 109.

Fialko, Y., 2006, Interseismic strain accumulation and the earthquake potential on the southern San Andreas fault system: Nature, v. 441, p. 968~971.

Fialko, Y., Sandwell, D., Agnew, D., Simons, M., Shearer, P., and Minster, B., 2002, Deformation on Nearby Faults induced by the 1999 Hector Mine Earthquake: Science, v. 297, p. 1858-1862.

Fialko, Y., Sandwell, D., Simons, M., and Rosen, P., 2005, Three-dimensional deformation caused by the Bam, Iran, earthquake and the origin of shallow slip deficit: Nature, v. 435, p. 295-299.

Fialko, Y., Simons, M., and Agnew, D., 2001, The complete (3-D) surface displacement field in the epicentral area of the 1999 Mw7.1 Hector Mine earthquake, California, from space geodetic observations: Geophysical Research Letters, v. 28, p. 3063-3066.

Fielding, E.J., Blom, R.G., and Goldstein, R.M., 1998, Rapid subsidence over oil fields measured by SAR interferometry: Geophysical Research Letters, v. 25, p. 3215-3218.

Fielding, E.J., Lundgren, P.R., Burgmann, R., and Funning, G.J., 2009, Shallow fault-zone dilatancy recovery after the 2003 Bam earthquake in Iran: Nature, v. 458, p. 64-68.

Fielding, E.J., Lundgren, P.R., Taymaz, T., Yolsal-Cevikbilen, S., and Owen, S.E., 2013, Fault-slip Source Models for the 2011 M 7.1 Van Earthquake in Turkey from SAR interferometry, Pixel Offset Tracking, GPS and Seismic Waveform Analysis: Seismological Research Letters, v. 84.

Freed, A.M., 2007, Afterslip (and only afterslip)following the 2004 Parkfield, California, earthquake: Geophys. Res. Lett., v. 34.

Freed, A.M., Bürgmann, R., Calais, E., Freymueller, J., and Hreinsdóttir, S., 2006, Implications of deformation following the 2002 Denali, Alaska, earthquake for postseismic relaxation processes and lithospheric rheology: Journal of Geophysical Research: Solid Earth, v. 111, p. B01401.

Fuchs, M.J., Bouman, J., Broerse, T., Visser, P., and Vermeersen, B., 2013, Observing coseismic gravity change from the Japan Tohoku-Oki 2011 earthquake with GOCE gravity gradiometry: Journal of Geophysical Research: Solid Earth, v. 118, p. 2013JB010033.

Fujiwara, T., Kodaira, S., No, T., Kaiho, K., Takahashi, N., and Kaneda, Y., 2011, The 2011 Tohoku-Oki Earthquake: Displacement Reaching the Trench Axis: Science, v. 334, p. 1240.

Fukahata, Y., and Wright, T.J., 2008, A non-linear geodetic data inversion using ABIC for slip distribution on a fault with an unknown dip angle: Geophys. J. Int., v. 173, p. 353-364.

Fukuda, J.i., Higuchi, T., Miyazaki, S.i., and Kato, T., 2004, A new approach to time-dependent inversion of geodetic data using a Monte Carlo mixture Kalman filter: Geophysical Journal International, v. 159, p. 17-39.

Fukuda, J.i., and Johnson, K.M., 2008, A Fully bayesian Inversion for Spatial Distribution of Fault Slip with Objective Smoothing: Bull. Seism. Soc. Am., v. 98, p. 1128~1146.

Fukuda, J.i., Kato, A., Kato, N., and Aoki, Y., 2013, Are the frictional properties of creeping faults persistent? Evidence from rapid afterslip following the 2011 Tohoku-oki earthquake: Geophysical Research Letters, v. 40, p. 3613-3617.

Funning, G.J., Barke, R.M.D., Lamb, S.H., Minaya, E., Parsons, B., and Wright, T.J., 2005a, The 1998 Aiquile, Bolivia earthquake: A seismically active fault revealed with InSAR: Earth and Planetary Science Letters, v. 232, p. 39-49.

Funning, G.J., Parsons, B., and Wright, T.J., 2007, Fault slip in the 1997 Manyi, Tibet earthquake from linear elastic modelling of InSAR displacements: Geophys. J. Int., v. 169, p. 988-1008.

Funning, G.J., Parsons, B., Wrigth, T.J., Jackson, J.A., and Fielding, E., 2005b, Surface displacements and source paramenters of the 2003 Bam (Iran) earthquake from Envisat advanced synthetic aperture radar imagery: J. Geophys. Res., v. 110.

Gan, W., Zhang, P., Shen, Z.-K., Niu, Z., Wang, M., Wan, Y., Zhou, D., and Cheng, J., 2007, Present-day crustal motion within the Tibetan Plateau inferred from GPS measurements: Journal of Geophysical Research, v. 112, p. B08416.

Gatelli, F., Guamieri, A.M., Parizzi, F., Pasquali, P., Prati, C., and Rocca, F., 1994, The wavenumber shift in SAR interferometry: Geoscience and Remote Sensing, IEEE Transactions on, v. 32, p. 855-865.

Geller, R.J., 1991, Shake-up for earthquake prediction: Nature, v. 352, p. 275-276.

Geller, R.J., Jackson, D.D., Kagan, Y.Y., and Mulargia, F., 1997, Earthquakes Cannot Be Predicted: Science, v. 275, p. 1616.

Goldstein, R.M., and Werner, C.L., 1998, Radar interferogram filtering for geophysical applications: Geophysical Research Letters, v. 25, p. 4035-4038.

Gonzalez-Ortega, A., Fialko, Y., Sandwell, D., Alejandro Nava-Pichardo, F., Fletcher, J., Gonzalez-Garcia, J., Lipovsky, B., Floyd, M., and Funning, G., 2014, El Mayor-Cucapah (Mw 7.2) earthquake: Early near-field postseismic deformation from InSAR and GPS observations: Journal of Geophysical Research: Solid Earth, v. 119, p. 2013JB010193.

Görgün, E., 2013, The 2011 October 23 Mw 7.2 Van-Erciş, Turkey, earthquake and its aftershocks: Geophysical Journal International.

Gusman, A.R., Tanioka, Y., Sakai, S., and Tsushima, H., 2012, Source model of the great 2011 Tohoku earthquake estimated from tsunami waveforms and crustal deformation data: Earth and Planetary Science Letters, v. 341–344, p. 234-242.

Haeussler, P.J., Schwartz, D.P., Dawson, T.E., Stenner, H.D., Lienkaemper, J.J., Sherrod, B., Cinti, F.R., Montone, R., Craw, P.A., Crone, A.J., and Personius, S.F., 2004, Surface Rupture and Slip Distribution of the Denali and Totschunda Faults in the 3 November 2002 M 7.9 Earthquake, Alaska: Bull. Seism. Soc. Am., v. 94, p. S23-S52.

Han, S.-C., Riva, R., Sauber, J., and Okal, E., 2013, Source parameter inversion for recent great earthquakes from a decade-long observation of global gravity fields: Journal of Geophysical Research: Solid Earth, v. 118, p. 1240-1267.

Han, S.-C., Sauber, J., and Luthcke, S., 2010, Regional gravity decrease after the 2010 Maule (Chile) earthquake indicates large-scale mass redistribution: Geophysical Research Letters, v. 37, p. L23307.

Han, S.-C., Sauber, J., and Pollitz, F., 2014, Broadscale postseismic gravity change following the 2011 Tohoku-Oki earthquake and implication for deformation by viscoelastic relaxation and afterslip: Geophysical Research Letters, p. 2014GL060905.

Han, S.-C., Sauber, J., and Riva, R., 2011, Contribution of satellite gravimetry to understanding seismic source processes of the 2011 Tohoku-Oki earthquake: Geophys. Res. Lett., v. 38.

Han, S.-C., Shum, C.K., Bevis, M., Ji, C., and Kuo, C.-Y., 2006, Crustal Dilatation Observed by GRACE After the 2004 Sumatra-Andaman Earthquake: Science, v. 313, p. 658-662.

Han, S.-C., and Simons, F.J., 2008, Spatiospectral localization of global geopotential fields from the Gravity Recovery and Climate Experiment (GRACE) reveals the coseismic gravity change owing to the 2004 Sumatra-Andaman earthquake: J. Geophys. Res., v. 113.

Hanssen, R.F., 2001, Radar Interferometry: Data interpretation and error analysis: Kluwer Acad., Netherlands, Springer Netherlands.

Hanssen, R.F., Weckwerth, T.M., Zebker, H.A., and Klees, R., 1999, High-Resolution Water Vapor Mapping from Interferometric Radar Measurements: Science, v. 283, p. 1297-1299.

Harris, R.A., and Day, S.M., 1993, Dynamics of fault interaction: parallel strike-slip faults: Journal of Geophysical Research: Solid Earth, v. 98, p. 4461-4472.

Harris, R.A., and Day, S.M., 1999, Dynamic 3D simulations of earthquakes on en echelon faults: Geophys. Res. Lett., v. 26, p. 2089-2092.

Harris, R.A., and Segall, P., 1987, Detection of a Locked Zone at Depth on the Parkfield, California, Segment of the San Andreas Fault: J. geophys. Res, v. 92, p. 7945-7962.

Hashimoto, C., Noda, A., Sagiya, T., and matsu'ura, M., 2009, Interplate seismogenic zones along the Kuri-Japan trench inferrred from GPS data inversion: Nature Geoscience, v. 2, p. 141-144.

He, Y.M., Wang, W.M., and Yao, Z.X., 2003, Static deformation due to shear and tensile faults in a layered half-space: Bull. Seism. Soc. Am., v. 93, p. 2253-2263.

Hearn, E.H., 2003, What can GPS data tell us about the dynamics of post-seismic deformation?: Geophysical Journal International, v. 155, p. 753-777.

Heki, K., 2011, Ionospheric electron enhancement preceding the 2011 Tohoku-Oki earthquake: Geophysical Research Letters, v. 38, p. L17312.

Heki, K., and Matsuo, K., 2010, Coseismic gravity changes of the 2010 earthquake in central Chile from satellite gravimetry: Geophys. Res. Lett., v. 37.

Hetland, E.A., and Simons, M., 2010, Post-seismic and interseismic fault creep II: transient creep and interseismic stress shadows on megathrusts: Geophys. J. Int., v. 181, p. 99-112.

Hetzel, R., 2013, Active faulting, mountain growth, and erosion at the margins of the Tibetan Plateau constrained by in situ-produced cosmogenic nuclides: Tectonophysics, v. 582, p. 1-24.

Hicks, S.P., Rietbrock, A., Haberland, C.A., Ryder, I.M.A., Simons, M., and Tassara, A., 2012, The 2010 Mw 8.8 Maule, Chile earthquake: Nucleation and rupture propagation controlled by a subducted topographic high: Geophys. Res. Lett., v. 39, p. L19308.

Hilley, G.E., Bürgmann, R., Zhang, P.Z., and Molnar, P., 2005, Bayesian inference of plastosphere viscosities near the Kunlun Fault, northern Tibet: Geophysical Research Letters, v. 32, p. L01302.

Hooper, A., 2008, A multi-temporal InSAR method incorporating both persistent scatterer and small baseline approaches: Geophys. Res. Lett., v. 35.

Hooper, A., Pietrzak, J., Simons, W., Cui, H., Riva, R., Naeije, M., Terwisscha van Scheltinga, A., Schrama, E., Stelling, G., and Socquet, A., 2013, Importance of horizontal seafloor motion on tsunami height for the 2011 Mw=9.0 Tohoku-Oki earthquake: Earth and Planetary Science Letters, v. 361, p. 469-479.

Hooper, A., Segall, P., and Zebker, H., 2007, Persistent scatterer interferometric synthetic aperture radar for crustal deformation analysis, with application to volcan Alcedo, Galapagos: J. Geophys. Res., v. 112.

Hsu, Y.-J., Segall, P., Yu, S.-B., Kuo, L.-C., and Willams, C.A., 2007, Temporal and spatial variations of post-seismic deformation following the 1999 Chi-Chi, Taiwan earthquake: Geophys. J. Int., v. 169, p. 367-379.

Hsu, Y.-J., Simons, M., Avouac, J.-P., Galetzka, J., Sieh, K., Chieh, M., Natawidjaja, D., Prawirodirdjo, L., and Bock, Y., 2006, Frictional Afterslip Following the 2005 Nias-Simeulue Earthquake, Sumatra: Science, v. 312, p. 1921-1925.

Hu, J., Li, Z., Zhang, L., Ding, X., Zhu, J., Sun, Q., and Ding, W., 2012, Correcting ionospheric effects and monitoring two-dimensional displacement fields with multiple-aperture InSAR technology with application to the Yushu earthquake: Science China Earth Sciences, v. 55, p. 1961-1971.

Hu, J., Li, Z.W., Ding, X.L., Zhu, J.J., Zhang, L., and Sun, Q., 2014, Resolving three-dimensional surface displacements from InSAR measurements: A review: Earth-Science Reviews, v. 133, p. 1-17.

Huang, Q., and Ding, X., 2012, Spatiotemporal Variations of Seismic Quiescence prior to the 2011 M 9.0 Tohoku Earthquake Revealed by an Improved Region–Time–Length Algorithm: Bulletin of the Seismological Society of America, v. 102, p. 1878-1883.

Ide, S., Baltary, A., and Beroza, G.C., 2011, Shallow Dynamic Overshoot and Energetic Deep Rupture in the 2011 Mw 9.0 Tohoku-Oki Earthquake: Science, v. 332, p. 1426-1429.

Iinuma, T., Hino, R., Kido, M., Inazu, D., Osada, Y., Ito, Y., Ohzono, M., Tsushima, H., Suzuki, S., Fujimoto, H., and Miura, S., 2012, Coseismic slip distribution of the 2011 off the Pacific Coast of Tohoku Earthquake (M9.0) refined by means of seafloor geodetic data: J. Geophys. Res., v. 117.

Irmak, T.S., Dogan, D., and Karakas, A., 2012, Source mechanism of the 23 October, 2011, Van(Turkey) earthquake (Mw=7.1) and aftershocks with its tectonic implications: Earth Planets Space, v. 64, p. 991-1003.

Isacks, B., Oliver, J., and Sykes, L.R., 1968, Seismology and the new global tectonics: Journal of Geophysical Research, v. 73, p. 5855-5899.

Jackson, C.R., Apel, J.R., and Commerce, U.S.D.o., 2004, Synthetic Aperture Radar: Marine User's Manual, U.S. Department of Commerce, National Oceanic and Atmospheric Administration.

Jackson, J., and McKenzie, D., 1984, Active tectonics of the Alpine–Himalayan Belt between western Turkey and Pakistan: Geophysical Journal of the Royal Astronomical Society, v. 77, p. 185-264.

Jarvis, A., Reuter, H.I., Nelson, A., and Guevara, E., 2008, Hole-filled seamless SRTM data V4: http://srtm.csi.cgiar.org.

Ji, C., 2011, Slip model of the 2011 Mw9.1 Japan earthquake, p. http://www.geol.ucsb.edu/faculty/ji/big_earthquakes/earthquakes.html.

Jiang, G., Xu, C., Wen, Y., Liu, Y., Yin, Z., and Wang, J., 2013, Inversion for coseismic slip distribution of the 2010 Mw 6.9 Yushu Earthquake from InSAR data using angular dislocations: Geophysical Journal

International.

Jiang, M., Li, Z.W., Ding, X.L., Zhu, J.J., and Feng, G.C., 2011, Modeling minimum and maximum detectable deformation gradients of interferometric SAR measurements: International Journal of Applied Earth Observation and Geoinformation, v. 13, p. 766-777.

Johnson, K.M., and Fukuda, J.i., 2010, New method for estimation the spatial distribution of locked asperities and stress-driven interseismic creep on faults with application to the San Francisco Bay Area, California: J. Geophys. Res., v. 115.

Johnson, K.M., Fukuda, J.i., and Segall, P., 2012a, Challenging the rate-state asperity model: Afterslip following the 2011 M9 Tohoku-oki, Japan, earthquake: Geophysical Research Letters, v. 39, p. L20302.

Johnson, K.M., Fukuda, J.i., and Segall, P., 2012b, Challenging the rate-state asperity model: Afterslip following the 2011 M9 Tohoku-oki, Japan, earthquake: Geophysical Research Letters, v. 39, p. n/a-n/a.

Johnson, K.M., and Segall, P., 2004, Viscoelastic earthquake cycle models with deep stress-driven creep along the San Andreas fault system: J. Geophys. Res, v. 109.

Jolivet, R., Agram, P.S., Lin, N.Y., Simons, M., Doin, M.-P., Peltzer, G., and Li, Z., 2014, Improving InSAR geodesy using Global Atmospheric Models: Journal of Geophysical Research: Solid Earth, p. n/a-n/a.

Jolivet, R., Cattin, R., Chamotrooke, N., Lasserre, C., and Peltzer, G., 2008, Thin-plate modeling of interseismic deformation and asymmetry across the Altyn Tagh fault zone: Geophysical Research Letters, v. 35.

Jolivet, R., Lasserre, C., Doin, M.-P., Guillaso, S., Peltzer, G., Dailu, R., Sun, J., Shen, Z.-K., and Xu, X., 2012, Shallow creep on the Haiyuan Fault (Gansu, China) revealed by SAR Interferometry: J. Geophys. Res., v. 117.

Jolivet, R., Lasserre, C., Doin, M.P., Peltzer, G., Avouac, J.P., Sun, J., and Dailu, R., 2013, Spatio-temporal evolution of aseismic slip along the Haiyuan fault, China: Implications for fault frictional properties: Earth and Planetary Science Letters, v. 377–378, p. 23-33.

Jonsson, S., 2002, Modeling Volcano and earthquake deformation from satellite radar interferometric observations, Stanford University.

Jonsson, S., Segall, P., Pedersen, R., and Bjornsson, G., 2003, Post-earthquake ground movements correlated to pore-pressure transients: Nature, v. 424, p. 179-183.

Jónsson, S., Zebker, H., Segall, P., and Amelung, F., 2002, Fault Slip Distribution of the 1999 Mw7.1 Hector Mine, California Earthquake, Estimated from Satellite Radar and GPS Measurements: Bull. Seism. Soc. Am., v. 92, p. 1377~1389.

Jung, H.-S., Won, J.-S., and Kim, S.-W., 2009, An Improvement of the Performance of Multiple-Aperture SAR Interferometry (MAI): IEEE Transactions on Geoscience and Remote Sensing, v. 47, p. 2859-2869.

Jungkyo, J., Duk-jin, K., and Sang-Eun, P., 2014, Correction of Atmospheric Phase Screen in Time Series InSAR Using WRF Model for Monitoring Volcanic Activities: Geoscience and Remote Sensing, IEEE Transactions on, v. 52, p. 2678-2689.

Kagan, Y.Y., and Jackson, D.D., 2011, Global earthquake forecasts: Geophysical Journal International, v. 184, p. 759-776.

Kagan, Y.Y., and Jackson, D.D., 2014, Statistical earthquake focal mechanism forecasts: Geophysical Journal International.

Kampes, B.M., Hanssen, R.F., and Perski, Z., 2003, RADAR INTERFEROMETRY WITH PUBLIC DOMAIN TOOLS, Third international Workshop on ERS SAR Interferometry(Fringe03): Frascati, Italy.

Kanamori, H., 1977, The energy release in great earthquakes: Journal of Geophysical Research, v. 82, p. 2981-2987.

Kanamori, H., 1994, MECHANICS OF EARTHQUAKES: Annual Review of Earth and Planetary Sciences, v. 22, p. 207-237.

Kanamori, H., and Allen, C.R., 1986, Earthquake repeat time and average stress drop, Earthquake Source Mechanics, Volume 37: Geophys. Monogr. Ser.: Washington, DC, AGU, p. 227-235.

Kanamori, H., and Anderson, D.L., 1975, Theoretical basis of some empirical relations in seismology: Bulletin of the Seismological Society of America, v. 65, p. 1073-1095.

Kanamori, H., and Brodsky, E.E., 2004, The physics of earthquakes: Rep. Prog. Phys., v. 64, p. 1429-1496.

Kanda, R.V.S., Hetland, E.A., and Simons, M., 2012, An asperity model for fault creep and interseismic deformation in northeastern Japan: Geophysical Journal International.

Kaneko, Y., Avouac, J.-P., and Lapusta, N., 2010, Towards inferring earthquake patterns from geodetic observations of interseismic coupling: Nature Geosci, v. 3, p. 363-369.

Kaneko, Y., and Fialko, Y., 2011, Shallow slip deficit due to larege strike-slip earthquakes in dynamic rupture simulations with elasto-plastic off-fault response: Geophys. J. Int., v. 186, p. 1389-1403.

Kaneko, Y., Fialko, Y., Sandwell, D.T., Tong, X., and Furuya, M., 2013, Interseismic deformation and creep along the central section of the North Anatolian Fault (Turkey): InSAR observations and implications for rate-and-state friction properties: Journal of Geophysical Research: Solid Earth, v. 118, p. 316-331.

Kennedy, J., and Eberhart, R., 1995, Particle swarm optimization, Neural Networks, 1995. Proceedings., IEEE International Conference on, Volume 4, p. 1942-1948 vol.4.

Kenny, C., 2009, Why do people die in earthquakes? The costs, benefits and institutions of disaster risk reduction in developing countries.

King, G., and Nabelek, J., 1985, Role of fault bends in the initiation and terminiation of earthquake rupture: Science, v. 228, p. 984-987.

King, G.C.P., Stein, R.S., and Lin, J., 1994, Static Stress Changes and the Triggering of Earthquakes: Bull. Seism. Soc. Am., v. 84, p. 935-953.

Klinger, Y., Michel, R., and King, G.C.P., 2006, Evidence for an earthquake barrier model from Mw ~7.8 Kokoxili (Tibet) earthquake slip-distribution: Earth and Planetary Science Letters, v. 242, p. 354-364.

Knipe, R.J., 1989, Deformation mechanisms — recognition from natural tectonites: Journal of Structural Geology, v. 11, p. 127-146.

Knospe, S.H.G., and Jonsson, S., 2010, Covariance Estimation for DInSAR Surface-Deformation Measurements in Presence of Anisotropic Atmospheric Noise: Transactions on Geoscience and Remote Sensing, v. 48, p. 2057-2065.

Kobayashi, T., Takada, Y., Furuya, M., and Murakami, M., 2009, Locations and types of ruptures invoved in the 2008 Sichuan earthquake inferred SAR image matching: Geophys. Res. Lett., v. 36.

Kodaira, S., No, T., Nakamura, Y., Fujiwara, T., Kaiho, Y., Miura, S., Takahashi, N., Kaneda, Y., and Taira, A., 2012, Coseismic fault rupture at the trench axis during the 2011 Tohoku-oki earthquake: Nature Geoscience, v. 5, p. 646-650.

Kositsky, A.P., and Avouac, J.-P., 2010, Inverting geodetic time series with a principal component analysis-based inversion method: J. Geophys. Res., v. 115.

Kozdon, J.E., and Dunham, E.M., 2013, Rupture to the Trench: Dynamic Rupture Simulations of the 11 March 2011 Tohoku Earthquake: Bulletin of the Seismological Society of America, v. 103, p. 1275-1289.

Kruger, F., and Ohrnberger, M., 2005, Tracking the rupture of the Mw = 9.3 Sumatra earthquake over 1,150[thinsp]km at teleseismic distance: Nature, v. 435, p. 937-939.

Lanari, R., Casu, F., Manzo, M., Zeni, G., Berardino, P., Manunta, M., and Pepe, A., 2007, An Overview of the Small BAseline Subset Algorithm: A DInSAR Technique for Surface Deformation Analysis: Pure and Applied Geophysics, v. 164, p. 637-661.

Lanari, R., Mora, O., Manunta, M., Mallorqui, J.J., Berardino, P., and Sansosti, E., 2004, A Small-Baseline Approach for Investigation Deformations on Full-Resolution Differential SAR Interferograms: IEEE Transactions on Geoscience and Remote Sensing, v. 42, p. 1377-1386.

Lapusta, N., and Barbot, S., 2012, Models of earthquakes and aseismic slip based on laboratory-derived rate-and-state friction laws, *in* Bizzarri, A., and Bhat, H.S., eds., The Mechanics of Faulting: From Laboratory to Real Earthquakes.

Larson, K.M., 2009, GPS seismology: J Geod, v. 83, p. 227-233.

Lasserre, C., Peltzer, G., Crampre, F., Klinger, Y., Woerd, J.V.d., and Tapponnier, P., 2005, Coseismic deformation of the 2001 Mw=7.8 Kokoxili earthquake in Tibet, measured by synthetic aperture radar interferometry: J. Geophys. Res., v. 110, p. B12408.

Lauknes, T.R., 2011, InSAR Tropospheric Stratification Delays: Correction Using a Small Baseline Approach: Geoscience and Remote Sensing Letters, IEEE, v. 8, p. 1070-1074.

Lay, T., Ammon, C.J., Kanamori, H., Xue, L., and Kim, M.J., 2011, Possible large near-trench slip during the 2011 Mw9.0 off the Pacific coast of Tohoku Earthquake: Earth Planets Space, v. 63, p. 687-692.

Li, C., Pang, J., and Zhang, Z., 2012, Characteristics, Geometry, and Segmentation of the Surface Rupture Associated with the 14 April 2010 Yushu Earthquake, Eastern Tibet, China: Bulletin of the Seismological Society of America, v. 102, p. 1618-1638.

Li, P., Li, Z., Shi, C., and Feng, W., 2013, Impacts of geoid height on large-scale crustal deformation mapping with InSAR observations: Chinese J. Geophys. (in Chinese), v. 56, p. 1857-1867.

Li, Q., and Liu, M., 2006, Geometrical impact of the San Andreas Fault on stress and seismicity in California: Geophys. Res. Lett, v. 33.

Li, Q., Liu, M., and Zhang, H., 2009a, A 3-D viscoelastoplastic model for simulating long-term slip on non-planar faults: Geophys. J. Int., v. 176, p. 293-306.

Li, Z., 2004, Production of Regional 1km ×1 km Water Vapor Fields through the Integration of GPS and MODIS Data: ION GNSS 2004, Long Beach, California, p. 21-24.

Li, Z., Elliott, J.R., Feng, W., Jackson, J.A., and Parsons, B.E., 2011, The 2010 Mw 6.8 Yushu (Qinghai, China) earthquake: constraints provided by InSAR and body wave seismology: J. Geophys. Res., v.

116.

Li, Z., Feng, W., Xu, Z., Cross, P., and Zhang, J., 2008, The 1998 Mw5.7 Zhangbei-Shangyi (China) earthquake revisited: A buried thrust fault revealed with interferomertic synthetic aperture radar: Geochem. geophys. Geosyst., v. 9, p. Q04026.

Li, Z., Fielding, E., and Cross, P., 2009b, Integration of InSAR Time-Series Analysis and Water-Vapor Correction for Mapping Postseismic Motion After the 2003 Bam (Iran) Earthquake: IEEE Transactions on Geoscience and Remote Sensing.

Li, Z., Fielding, E.J., Cross, P., and Muller, J.-P., 2006, Interferometric synthetic aperture radar atmospheric correction: GPS topography-dependent turbulence model: J. Geophys. Res., v. 111.

Li, Z., Fielding, E.J., Cross, P., and Preusker, R., 2009c, Advanced InSAR atmospheric correction: MERIS/MODIS combination and stacked water vapour models: International Journal of Remote Sensing, v. 30, p. 3343-3363.

Li, Z., Liu, Y., Zhou, X., Cross, P., and Feng, W., 2009d, Using small baseline Interferometric SAR to map nonlinear ground motion: a case study in Northern Tibet: Journal of Applied Geodesy, v. 3, p. 163-170.

Liang, C., Zeng, Q., Jia, J., Jiao, J., and Cui, X.a., 2013, ScanSAR interferometric processing using existing standard InSAR software for measuring large scale land deformation: Computers & Geosciences, v. 51, p. 439-448.

Lin, A., Fu, B., Guo, J., Zeng, Q., Dang, G., He, W., and Zhao, Y., 2002, Co-Seismic Strike-Slip and Rupture Length Produced by the 2001 Ms 8.1 Central Kunlun Earthquake: Science, v. 296, p. 2015-2017.

Lin, A., Rao, G., Jia, D., Wu, X., Yan, B., and Ren, Z., 2011, Co-seismic strike-slip surface rupture and displacement produced by the 2010 Mw6.9 Yushu earthquake, China, and implications for Tibetan tectonics: Journal of Geodynamics, v. 52, p. 249-259.

Lin, J., and Stein, R.S., 2004, Stress triggering in thrust and subduction earthquakes and stress interaction between the southern San Andreas and nearby thrust and strike-slip faults: J. Geophys. Res., v. 109, p. B02303.

Lin, Y.-n.N., Kositsky, A.P., and Avouac, J.-P., 2010, PCAIM joint inversion of InSAR and ground-based geodetic time series: Application to monitoring magmatic inflation beneath the Long Valley Caldera: Geophys. Res. Lett., v. 37, p. L23301.

Lindsey, E.O., Fialko, Y., Bock, Y., Sandwell, D.T., and Bilham, R., 2014, Localized and distributed creep along the southern San Andreas Fault: Journal of Geophysical Research: Solid Earth, p. 2014JB011275.

Liu-Zeng, J., Tapponnier, P., Gaudemer, Y., and Ding, L., 2008, Quantifying landscape differences across the Tibetan plateau: Implications for topographic relief evolution: J. Geophys. Res., v. 113, p. F04018.

Liu, Y., Xu, C., Li, Z., Wen, Y., and Forrest, D., 2011, Interseismic slip rate of the Garze-Yushu fault belt in the Tibetan Plateau from C-band InSAR observations between 2003 and 2010: Advances in Space Research, v. 48, p. 2005-2015.

Liu, Y., Xu, C., Wen, Y., He, P., and Jiang, G., 2012, Fault rupture model of the 2008 Dangxiong (Tibet, China) Mw 6.3 earthquake from Envisat and ALOS data: Advances in Space Research, v. 50, p. 952-962.

Lohman, R.B., 2004, The inversion of geodetic data for earthquake parameters: Pasadena, California, California Institute of Technology.

Lohman, R.B., and Simons, M., 2005, Some thoughts on the use of InSAR data to constrain models of surface deformation: Noise structure and data downsampling: Geochemistry, Geophysics, Geosystems, v. 6, p. Q01007.

Loveless, J.P., and Meade, B.J., 2011, Partitioning of localized and diffuse deformation in the Tibetan Plateau from joint inversions of geologic and geodetic observations: Earth and Planetary Science Letters, v. 303, p. 11-24.

Lu, Z., Kwoun, O., and Rykhus, R., 2007, Interferometric synthetic aperture radar (InSAR): its past, present and future: Photogrammetric engineering and remote sensing, v. 73, p. 217.

Lubis, A.M., Hashima, A., and Sato, T., 2013, Analysis of afterslip distribution following the 2007 September 12 southern Sumatra earthquake using poroelastic and viscoelastic media: Geophysical Journal International, v. 192, p. 18-37.

Luttrell, K.M., Tong, X., Sandwell, D.T., Brooks, B.A., and Bevis, M.G., 2011, Estimates of stress drop and crustal tectonics stress from the 27 February 2010 Maule, Chile, earthquake: Implications for fault strength: J. Geophys. Res., v. 116.

MacInnes, B.T., Gusman, A.R., LeVeque, R.J., and Tanioka, Y., 2013, Comparison of Earthquake Source Models for the 2011 Tohoku Event Using Tsunami Simulations and Near-Field Observations: Bulletin of the Seismological Society of America, v. 103, p. 1256-1274.

Marcotte, D., 1996, Fast Variogram Computation With FFT: Computers & Geosciences, v. 22, p. 1175-1186.

Marinkovic, P., and Larsen, Y., 2013, Consequences of Long-Term ASAR Local Oscillator Frequency Decay - an Empirical Study of 10 Years of Data Living Planet Symposium 2013 Edinburgh, ESA.

Marone, C., 1998a, The effect of loading rate on static friction and the rate of fault healing during the earthquake cycle: Nature, v. 391, p. 69-72.

Marone, C., 1998b, LABORATORY-DERIVED FRICTION LAWS AND THEIR APPLICATION TO SEISMIC FAULTING: Annual Review of Earth and Planetary Sciences, v. 26, p. 643-696.

Marone, C.J., Scholz, C.H., and Bilham, R., 1991, On the Mechanics of Earthquake Afterslip: J. Geophys. Res., v. 96, p. 8441-8542.

Maruyama, T., 1964, Statical elastic dislocations in an infinite and semi-infinite medium: Bull Earth Res Inst Univ Tokyo, v. 42, p. 286-368.

Massonnet, D., and Feigl, K.L., 1998, Radar Interferometry and its aplication to changes in the earth's surface: Reviews of Geophysics, v. 36, p. 441-500.

Massonnet, D., Rossi, M., Carmona, C., Adragna, F., Pelter, G., Feigl, K., and Rabaute, T., 1993, The displacement field of the Landers earthquake mapped by radar interferometry: Nature, v. 364, p. 138-142.

Masterlark, T., and Wang, H.F., 2002, Transient Stress-Coupling Between the 1992 Landers and 1999 Hector Mine, California, Earthquakes: Bull. Seism. Soc. Am., v. 92, p. 1470-1486.

Matsuo, K., and Heki, K., 2011, Coseismic gravity changes of the 2011 Tohoku-Oki earthquake from satellite gravimetry: Geophys. Res. Lett., v. 38.

Matthews, M.V., and Segall, P., 1993, Estimation of depth-dependent fault slip from measured surface deformation with application to the 1906 San Francisco Earthquake: Journal of Geophysical Research: Solid Earth, v. 98, p. 12153-12163.

McKenzie, D.P., 1969, The relation between fault plane solutions for earthquakes and the directions of the principal stresses: Bulletin of the Seismological Society of America, v. 59, p. 591-601.

Meade, B.J., 2007, Algorithms for the calculation of exact displacements, strains and stresses for triangular dislocation elements in a uniform elastic half space: Computers & Geosciences, v. 33, p. 1064-1075.

Meng, G., Ren, J., Su, X., Yang, Y., Zhu, Z., Ge, L., and Li, X., 2013, Coseismic Deformation of the 2010 Mw 6.9 Yushu Earthquake Derived from GPS Data: Seismological Research Letters, v. 84, p. 57-64.

Menke, W., 1989, Geophysical Data Analysis: Discrete Inverse Theroy: New York, Elsevier.

Métivier, F., Gaudemer, Y., Tapponnier, P., and Meyer, B., 1998, Northeastward growth of the Tibet plateau deduced from balanced reconstruction of two depositional areas: The Qaidam and Hexi Corridor basins, China: Tectonics, v. 17, p. 823-842.

Meyer, F., 2010, A review of ionospheric effects in low-frequency SAR Signals, correction methods, and performance requirements, Geoscience and Remote Sensing Symposium (IGARSS), 2010 IEEE International, p. 29-32.

Meyer, F., Bamler, R., Jakowski, N., and Fritz, T., 2006, The Potential of Low-Frequency SAR Systems for Mapping Ionospheric TEC Distributions: Geoscience and Remote Sensing Letters, IEEE, v. 3, p. 560-564.

Michel, R., Avonac, J.-P., and Taboury, J., 1999a, Measuring ground displacements from SAR amplitude images: application to the Landers earthquake: Geophys. Res. Lett., v. 26, p. 875~878.

Michel, R., Avouac, J.-P., and Taboury, J., 1999b, Measuring near field coseismic displacements from SAR images: application to the Landers earthquake: Geophys. Res. Lett., v. 26, p. 3017~3020.

Minson, S.E., Simons, M., Beck, J.L., Ortega, F., Jiang, J., Owen, S.E., Moore, A.W., Inbal, A., and Sladen, A., 2014, Bayesian inversion for finite fault earthquake source models – II: the 2011 great Tohoku-oki, Japan earthquake: Geophysical Journal International, v. 198, p. 922-940.

Miyazaki, S., Segall, P., Fukuda, J., and Kato, T., 2004, Space time distribution of afterslip following the 2003 Tokachi-oki earthquake: Implications for variations in fault zone frictional properties: Geophysical Research Letters, v. 31, p. L06623.

Molnar, P., and Tapponnier, P., 1975, Cenozoic Tectonics of Asia: Effects of a Continental Collision: Science, v. 189, p. 419-426.

Molnar, P., and Tapponnier, P., 1977, Relation of the tectonics of eastern China to the India-Eurasia collision: Application of slip-line field theory to large-scale continental tectonics: Geology, v. 5, p. 212-216.

Moro, M., Cannelli, V., Chini, M., Bignami, C., Melini, D., Stramondo, S., Saroli, M., Picchiani, M., Kyriakopoulos, C., and Brunori, C.A., 2014, The October 23, 2011, Van (Turkey) earthquake and its relationship with neighbouring structures: Sci. Rep., v. 4.

Nelder, J.A., and Mead, R., 1965, A Simplex Method for Function Minimization: The Computer Journal, v. 7, p. 308-313.

Nettles, m., Ekstrom, G., and Koss, H.C., 2011, Centroid-moment-tensor analysis of the 2011 off he Pacific coast of Tohoku Earthquake and its larger foreshocks and aftershocks: Earth Planets Space, v. 63, p. 519-523.

Nitti, D.O., Hanssen, R.F., Refice, A., Bovenga, F., and Nutricato, R., 2011, Impact of DEM-Assisted Coregistration on High-Resolution SAR Interferometry: IEEE Transactions on Geoscience and Remote Sensing, v. 49, p. 1127-1143.

Noda, H., Lapusta, N., and Kanamori, H., 2013, Comparison of average stress drop measures for ruptures with heterogeneous stress change and implications for earthquake physics: Geophysical Journal International.

Ogawa, R., Chao, B.F., and Heki, K., 2011, Acceleration signal in GRACE time-variable gravity in relation to interannual hydrological changes: Geophys. J. Int., v. 184, p. 673-679.

Okada, Y., 1985, Surface Deformation Due to Shear and tensile faults in a half-space: Bull. Seism. Soc. Am., v. 75, p. 1135-1154.

Okada, Y., 1992, Internal deformation due to shear and tensile faults in a half-space: Bull. Seism. Soc. Am., v. 85, p. 1018-1040.

Okubo, S., 1992, Gravity and Potential Changes due to Shear and Tensile Faults in a Half-Space: J. Geophys. Res., v. 97, p. 7137-7144.

Okubo, S., 1993, Reciprocity theorem to compute the static deformation due to a point dislocation buried in a spherically symmetric earth: Geophysical Journal International, v. 115, p. 921-928.

Ozawa, S., Nishimura, T., Munekane, H., Suito, H., Kobayashi, T., Tobita, M., and Imakiire, T., 2012, Preceding, coseismic, and postseismic slips of the 2011 Tohoku earthquake, Japan: J. Geophys. Res., v. 117.

Ozawa, S., Nishimura, T., Suito, H., Kobayashi, T., Tobita, M., and Imakiire, T., 2011, Coseismic and postseismic slip of the 2011 magnitude- 9 Tohoku - Oki earthquake: Nature, v. 475, p. 373-377.

Pacheco, J.F., Sykes, L.R., and Scholz, C.H., 1993, Nature of seismic coupling along simple plate boundaries of the subduction type: Journal of Geophysical Research: Solid Earth, v. 98, p. 14133-14159.

Parsons, B.E., Wright, T.J., Powe, P., Andrews, J., Jackson, J.A., Walker, R., Khatib, M.M., Talebian, M., Bergman, E., and Engdadl, E.R., 2006, The 1994 Sefidabeh (eastern Iran) earthquakes revisited: new evidence from satellite radar interferometry and carbonate dating about the growth of an active fold above a blind thrust fault: Geophys. J. Int., v. 164, p. 202~217.

Parsons, T., Stein, R.S., Simpson, R.W., and Reasenberg, P.A., 1999, Stress sensitivity of fault seismicity: A comparison between limited-offset oblique and major strike-slip faults: Journal of Geophysical Research: Solid Earth, v. 104, p. 20183-20202.

Pathier, E., Fielding, E.J., Wright, T.J., Walker, R., Parsons, B.E., and Hensley, S., 2006, Displacement field and slip distribution of the 2005 Kashmir earthquake from SAR imagery: Geophys. Res. Lett., v. 33.

Peltzer, G., Rosen, P., and Rogez, F., 1998, Poroelastic rebound along the Landers 1992 earthquake surface rupture: J. Geophys. Res., v. 103, p. 30131-30145.

Perfettini, H., and Avouac, J.-P., 2007, Modeling afterslip and aftershocks following the 1992 Landers earthquake: J. geophys. Res, v. 112.

Plattner, C., Wdowinski, S., Dixon, T.H., and Biggs, J., 2010, Surface subsidence induced by the Crandall Canyon Mine (Utah) collapse: InSAR observations and elasto-plastic modelling: Geophysical Journal International, v. 183, p. 1089-1096.

Pollitz, F.F., Bürgmann, R., and Segall, P., 1998, Joint estimation of afterslip rate and postseismic relaxation following the 1989 Loma Prieta earthquake: Journal of Geophysical Research: Solid Earth, v. 103, p. 26975-26992.

Pollitz, F.F., Peltzer, G., and Burgmann, R., 2000, Mobility of continental mantle: Evidence from postseismic geodetic observations following the 1992 Landers earthquake: Journal of Geophysical Research-Solid Earth, v. 105, p. 8035-8054.

Pritchard, M.E., Simons, M., Rosen, P.A., Hensley, S., and Webb, F.H., 2002, Co-seismic slip from the 1995 July 30 M_W=8.1 Antofagasta, Chile, earthquake as constrained by InSAR and GPS observations: Geophys. J. Int., v. 150, p. 362-376.

Qu, C., Zhang, G., Shan, X., Zhang, G., Song, X., and Liu, Y., 2013, Coseismic deformation derived from analyses of C and L band SAR data and fault slip inversion of the Yushu Ms7.1 earthquake, China in 2010: Tectonophysics, v. 584, p. 119-128.

Reeves, J.A., Knight, R., Zebker, H.A., Schreüder, W.A., Shanker Agram, P., and Lauknes, T.R., 2011, High quality InSAR data linked to seasonal change in hydraulic head for an agricultural area in the San Luis Valley, Colorado: Water Resour. Res., v. 47, p. W12510.

Reid, H., 1910, The mechanism of the earthquake, the State Earthquake Investigation Commission: Washington, DC, Carnegie Institution, p. 192.

Relinger, R., McClusky, S., Vernant, P., Lawrence, S., Ergintav, S., Cakmak, R., Ozener, H., Hahubia, F., Mahmoud, S., Sakr, K., ArRajehi, A., Paradissis, D., Al-Aydrus, A., Prilepin, M., Guseva, T., Evren, E., Dmitrotsa, A., Filikov, S.V., Gomez, F., Al-Ghazzi, R., and Karam, G., 2006, GPS constraints on continental deformation in the Africa-Arabia-Eurasia continental collision zone and implications for the dynamics of plate interactions: J. Geophys. Res., v. 111.

Riva, R.E.M., and Govers, R., 2009, Relating viscosities from postseismic relaxation to a realistic viscosity structure for the lithosphere: Geophysical Journal International, v. 176, p. 614-624.

Rocca, F., Prati, C., and Ferretti, A., 1997, An overview of ERS-SAR interferometry, ERS Symposium on Space at the Service of Our Environment, 3 rd, Florence, Italy.

Rodell, M., Houser, P.R., Jambor, U., Gottschalck, J., Mitchell, K., Meng, C.J., Arsenault, K., Cosgrove, B., Radakovich, J., Bosilovich, M., Entin*, J.K., Walker, J.P., Lohmann, D., and Toll, D., 2004, The Global Land Data Assimilation System: Bulletin of the American Meteorological Society, v. 85, p. 381-394.

Romano, F., Piatanesi, A., Lorito, S., D'Agostino, N., Hirata, K., Atzori, S., Yamazaki, Y., and Cocco, M., 2012, Clues from joint inversion of tsunami and geodetic data of the 2011 Tohoku-oki earthquake: Scientific Reports, v. 2.

Romano, F., Trasatti, E., Lorito, S., Piromallo, C., Piatanesi, A., Ito, Y., Zhao, D., Hirata, K., Lanucara, P., and Cocco, M., 2014, Structural control on the Tohoku earthquake rupture process investigated by 3D FEM, tsunami and geodetic data: Sci. Rep., v. 4.

Rosen, P., Gurrola, E.M., Sacco, G., and Zerbker, H.A., 2011a, InSAR Scientific Computing Environment - The Home Stretch, AGU 2011: San Francisco, CA.

Rosen, P., Lavalle, M., Pi, X., Buckley, S., Szeliga, W., Zebker, H., and Gurrola, E., 2011b, Techniques and tools for estimating ionospheric effects in interferometric and polarimetric SAR data, Geoscience and Remote Sensing Symposium (IGARSS), 2011 IEEE International, p. 1501-1504.

Rosen, P.A., Henley, S., Peltzer, G., and Simons, M., 2004a, Updated Repeat Orbit Interferometry Package Released: EOS, Transactions American Geophyical Union, v. 85.

Rosen, P.A., Hensley, S., and chen, c., 2010, Measurement and mitigation of the ionosphere in L-band Interferometric SAR data, Radar Conference, 2010 IEEE, p. 1459-1463.

Rosen, P.A., hensley, S., Joughin, I.R., Li, F.K., Madsen, S.n., Rodriguez, S., and .Goldstein, R.M., 2000, Synthetic Aperture Radar Interferometry: Proceedings of the IEEE, v. 88.

Rosen, P.A., Hensley, S., Peltzer, G., and Simons, M., 2004b, Updated repeat orbit interferometry package released: EOS, Transactions American Geophysical Union, v. 85, p. 47-47.

Rosen, P.A., Hensley, S., Zebker, H.A., Webb, F.H., and Fielding, E.J., 1996, Surface deformation and coherence measurements of Kilauea Volcano, Hawaii, from SIR-C radar interferometry: Journal of Geophysical Research: Planets, v. 101, p. 23109-23125.

Rubinstein, J.L., Ellsworth, W.L., Beeler, N.M., Kilgore, B.D., Lockner, D.A., and Savage, H.M., 2012, Fixed recurrence and slip models better predict earthquake behavior than the time- and slip-predictable models: 2. Laboratory earthquakes: Journal of Geophysical Research: Solid Earth, v. 117, p. B02307.

Ruina, A., 1983, Slip instability and state variable friction laws: Journal of Geophysical Research: Solid Earth, v. 88, p. 10359-10370.

Ruina, A.L., 1980, Friction laws and instabilities: A quasistatic analysis of some dry frictional behavior, Cornell University.

Ryder, I., and Burgmann, R., 2008, Spatial variations in slip deficit on the central San Andreas Fault from InSAR: Geophys. J. Int., v. 175, p. 837-852.

Ryder, I., Burgmann, R., and Pollitz, F., 2011, Lower crustal relaxation beneath the Tibetan Plateau and Qaidam Basin following the 2001 Kokoxili earthquake: Geophys. J. Int., v. 187, p. 613-630.

Ryder, I., Burgmann, R., and Sun, J., 2010, Tandem afterslip on connected fault planes following the 2008 Nima-Gaize (Tibet) earthquake: J. Geophys. Res., v. 115.

Ryder, I., Parsons, B., Wright, T.J., and Funning, G.J., 2007a, Post-seismic motion following the 1997 Manyi (Tibet) earthquake: InSAR observations and modelling: Geophysical Journal International, v. 169, p. 1009-1027.

Ryder, I., Parsons, B., Wright, T.J., and Funning, G.J., 2007b, Post-seismic motion following the 1997 Manyi (Tibet) earthquake: InSAR observations and modelling: Geophys. J. Int., v. 169, p. 1009-1027.

Ryder, I., Wang, H., Bie, L., and Rietbrock, A., 2014, Geodetic imaging of late postseismic lower crustal flow in Tibet: Earth and Planetary Science Letters, v. 404, p. 136-143.

Sagiya, T., Kanamori, H., Yagi, Y., Yamada, M., and Mori, J., 2011, Rebuilding seismology: Nature, v. 473, p. 146-148.

Salvi, S., Stramondo, S., Funning, G.J., Ferretti, A., Sarti, F., and Mouratidis, A., 2012, The Sentinel-1 mission for the improvement of the scientific understanding and the operational monitoring of the seismic cycle: Remote Sensing of Environment, v. 120, p. 164-174.

Samieie-Esfahany, S., Hanssen, R., van Thienen-Visser, K., and Muntendam-Bos, A., 2009, On the effect of horizontal deformation on InSAR subsidence estimates, Proceedings of the Fringe 2009 Workshop, ESA SP, Volume 677.

Samsonov, S., 2010, Topographic Correction for ALOS PALSAR Interferometry: Geoscience and Remote Sensing, IEEE Transactions on, v. 48, p. 3020-3027.

Sandwell, D., Mellors, R., Tong, X., Wei, M., and Wessel, P., 2011, Open Radar Interferometry Software for Mapping Surface Deformation: EOS, Transactions American Geophysical Union, v. 92, p. 234.

Sato, M., Ishikawa, T., Ujihara, N., Yoshida, S., Fujita, M., Mochizuki, M., and Asada, A., 2011a, Displacement Above the Hypocenter of the 2011 Tohoku-Oki Earthquake: Science, v. 332, p. 1395-1395.

Sato, M., Ishikawa, t., Ujihara, N., Yoshida, S., Fujita, M., and ochizuki, M., 2011b, Displacement Above the

Hypocenter of the 2011 Tohoku-Oki Earthquake: Science, v. 332, p. 1395.

Savage, J.C., 1998, Displacement field for an edge dislocation in a layered half-space: J. Geophys. Res., v. 103, p. 2439-2446.

Savage, J.C., and Burford, R.O., 1973, Geodetic determination of relative plate motion in central California: Journal of Geophysical Research, v. 78, p. 832-845.

Savage, J.C., and Svarc, J.L., 2009, Postseismic relaxation following the 1992 M7.3 Landers and 1999 M7.1 Hector Mine earthquakes, southern California: Journal of Geophysical Research: Solid Earth, v. 114, p. B01401.

Schättler, B., 2002, ASAR Level 0 Product Analysis for Image, Wide-Swath and Wave Mode, *in* Sawaya-Lacoste, H., ed., Proceedings of the Envisat Calibration Review: Postbus, Netherlands, ESA Publications Division.

Schmidt, D.A., and Bürgmann, R., 2003, Time-dependent land uplift and subsidence in the Santa Clara valley, California, from a large interferometric synthetic aperture radar data set: Journal of Geophysical Research: Solid Earth, v. 108, p. 2416.

Scholz, C., Molnar, P., and Johnson, T., 1972, Detailed studies of frictional sliding of granite and implications for the earthquake mechanism: Journal of Geophysical Research, v. 77, p. 6392-6406.

Scholz, C.H., 1998, Earthquakes and friction laws: Nature, v. 391, p. 37-42.

Scholz, C.H., 2002, The Mechanics of Earthquakes and Faulting: Cambridge, U. K., Cambridge Univ. Press.

Scholz, C.H., and Aviles, C.A., 1986, The fractal geometry of faults and faulting, Earthquake Source Mechanics, Volume 37: Geophys. Monogr. Ser.: Washington, DC, AGU, p. 147-155.

Scholz, C.H., Aviles, C.A., and Wesnousky, S.G., 1986, Scaling Differences Between Large Interplate and Intraplate Earthquakes: Bull. Seism. Soc. Am., v. 76, p. 65-70.

Scholz, C.H., Wyss, M., and Smith, S.W., 1969, Seismic and aseismic slip on the San Andreas Fault: Journal of Geophysical Research, v. 74, p. 2049-2069.

Schurr, B., Asch, G., Rosenau, M., Wang, R., Oncken, O., Barrientos, S., Salazar, P., and Vilotte, J.P., 2012, The 2007 M7.7 Tocopilla northern Chile earthquake sequence: Implications for along-strike and downdip rupture segmentation and megathrust frictional behavior: Journal of Geophysical Research: Solid Earth, v. 117, p. B05305.

Segall, P., 2000, Four-dimensional geodesy: time dependent inversion for earthquake and volcanic sources, *in* Schwarz, K.-P., ed., Geodesy Beyond 2000, Volume 121: International Association of Geodesy Symposia, Springer Berlin Heidelberg, p. 278-278.

Segall, P., and Matthews, M., 1997, Time dependent inversion of geodetic data: Journal of Geophysical Research: Solid Earth, v. 102, p. 22391-22409.

Shao, G.F., Li, X., Ji, C., and Maeda, T., 2011, Focal mechanism and slip history of the 2011 Mw 9.1 off the Pacific coast of Tohoku Earthquake, constrained with teleseismic body and surface waves: Earth Planets Space, v. 63, p. 559-564.

Shaw, B.E., 2009, Constant Stress Drop from Small to Great Earthquakes in Magnitude-Area Scaling: Bulletin of the Seismological Society of America, v. 99, p. 871-875.

Shearer, P., and Bürgmann, R., 2010, Lessons Learned from the 2004 Sumatra-Andaman Megathrust Rupture: Annual Review of Earth and Planetary Sciences, v. 38, p. 103-131.

Shen, Z.-K., Sun, J., Zhang, P., Wan, Y., Wang, M., Burgmann, R., Zeng, Y., Gan, W., Liao, H., and Wang, Q., 2009, Slip maxima at fault junctions and rupturing of barriers during the 2008 Wenchuan earthquake: Nature Geosci, v. 2, p. 718-724.

Shen, Z.-K., Wang, M., Li, Y., Jackson, D.D., Yin, A., Dong, D., and Fang, P., 2001, Crustal deformation along the Altyn Tagh fault system, western China, from GPS: Journal of Geophysical Research: Solid Earth, v. 106, p. 30607-30621.

Shirzaei, M., and Walter, T.R., 2011, Estimating the Effect of Satellite Orbital Error Using Wavelet-Based Robust Regression Applied to InSAR Deformation Data: IEEE Transactions on Geoscience and Remote Sensing, v. 49, p. 4600-4605.

Sibson, R.H., 1977, Fault rocks and fault mechanisms: Journal of the Geological Society, v. 133, p. 191-213.

Sibson, R.H., 1980, Transient discontinuities in ductile shear zones: Journal of Structural Geology, v. 2, p. 165-171.

Simons, M., Fialko, Y., and Rivera, L., 2002, Coseismic Deformation from the 1999 Mw 7.1 Hector Mine, California, Earthquake as Inferred from InSAR and GPS Observations: Bull. Seism. Soc. Am., v. 92, p. 1390-1402.

Simons, M., Minson, S.E., Sladen, A., Ortega, F., Jiang, J., Owen, S.E., Meng, L., Ampuero, J.P., Wei, S., Chu, R., Helmberger, D.V., Kannamori, H., Hetland, E., Moore, A.W., and Webb, F.H., 2011, The 2011 Magnitude 9.0 Tohoku-Oki Earthquake: Mosaicking the Megathrust from Seconds to Centuries: Science, v. 332, p. 1421-1425.

Simons, M., and Rosen, P., 2007, Interferometric Synthetic Aperture Radar Geodeys, *in* Schubert, G., ed., Treatise on Geophysics, Vol 3: Geodesy, Volume 3, Elsevier, p. 391-446.

Singh, S.J., 1971, Deformation of a multilayered half-space by stress dislocations and concentrated forces:

Bull. Seism. Soc. Am., v. 61, p. 1625-1637.

Singleton, A., Li, Z., Hoey, T., and Muller, J.P., 2014, Evaluating sub-pixel offset techniques as an alternative to D-InSAR for monitoring episodic landslide movements in vegetated terrain: Remote Sensing of Environment, v. 147, p. 133-144.

Smith-Konter, B.R., Sandwell, D.T., and Shearer, P., 2011, Locking depths estimated from geodesy and seismology along the San Andreas Fault System: Implications for seismic moment release: J. Geophys. Res., v. 116.

Smith, S.W., and Wyss, M., 1968, Displacement on the San Andreas fault subsequent to the 1966 Parkfield earthquake: Bulletin of the Seismological Society of America, v. 58, p. 1955-1973.

Solomon, S.C., Huang, P.Y., and Meinke, L., 1988, The seismic moment budget of slowly spreading ridges: Nature, v. 334, p. 58-60.

Stark, P.B., and Parker, R.L., 1992, Bounded-Variable Least-Squares: an Algorithm and Applicatins: Comp. Stat., v. 10, p. 129-141.

Steketee, J.A., 1958, Volterra's dislocation in a semi-infinite elastic medium: Can. J. Phys., v. 36, p. 192-205.

Stewart, G.S., and Kanamori, H., 1982, Complexity of rupture in large strike-slip earthquakes in Turkey: Physics of the Earth and Planetary Interiors, v. 28, p. 70-84.

Stramondo, S., Del Frate, F., Picchiani, M., and Schiavon, G., 2011, Seismic Source Quantitative Parameters Retrieval From InSAR Data and Neural Networks: Geoscience and Remote Sensing, IEEE Transactions on, v. 49, p. 96-104.

Strang, G., and Borre, K., 1997, Linear Algebra, Geodesy, and GPS, Wellesley-Cambridge Press.

Sudhaus, H., and Jonsson, S., 2009, Improved source modelling through combined use of InSAR and GPS under consideration of correlated data errors: application to the June 2000 Kleifar vatn earthquake, Iceland: Geophys. J. Int., v. 176, p. 389~404.

Sun, C.-H., Xu, F., Yang, Y.-B., Qian, R.-Y., and Meng, X.-H., 2012, Focal Mechanism Solutions of the 2003 Delingha, Qinghai M6.7 Earthquake Sequence and Their Tectonic Implications: Chinese Journal of Geophysics, v. 55, p. 680-688.

Sun, J., Shen, Z.-K., Bürgmann, R., Wang, M., Chen, L., and Xu, X., 2013, A three-step maximum a posteriori probability method for InSAR data inversion of coseismic rupture with application to the 14 April 2010 Mw 6.9 Yushu, China, earthquake: Journal of Geophysical Research: Solid Earth, v. 118, p. 4599-4627.

Sun, T., Wang, K., Iinuma, T., Hino, R., He, J., Fujimoto, H., Kido, M., Osada, Y., Miura, S., Ohta, Y., and Hu, Y., 2014, Prevalence of viscoelastic relaxation after the 2011 Tohoku-oki earthquake: Nature, v. 514, p. 84-87.

Sun, W., Okubo, S., Fu, G., and Araya, A., 2009, General formulations of global co-seismic deformations caused by an arbitrary dislocation in a spherically symmetric earth model - applicable to deformed earth surface and space-fixed point: Geophys. J. Int., v. 177, p. 817-833.

Swenson, S., and Wahr, J., 2006, Post-processing removal of correlated errors in GRACE data: Geophys. Res. Lett., v. 33, p. L08402.

Tajima, F., Mori, J., and Kennett, B.L.N., 2013, A review of the 2011 Tohoku-Oki earthquake (Mw 9.0): Large-scale rupture across heterogeneous plate coupling: Tectonophysics, v. 586, p. 15-34.

Talebian, M., Feilding, E.J., Funning, G.J., Ghorashi, M., Jackson, J., Nazari, H., Parsons, B., Priestley, K., Rosen, P.A., Walker, R., and Wright, T.J., 2004, The 2003 Bam (Iran) earhtquake: Rupture of a blind strike-slip fault: Geophys. Res. Lett., v. 31.

Tao, Q.-x., and Liu, G.-l., 2014, Properties of L-band differential InSAR for monitoring mining-induced subsidence in coalfield of Jining, Northern China: Journal of Central South University, v. 21, p. 1508-1517.

Tapley, B.D., Bettadpur, S., Ries, J.C., Thompson, P.F., and Watkins, M.M., 2004, GRACE Measurements of Mass Variability in the Earth System: Science, v. 305, p. 503-505.

Tarantola, A., 2005, Inverse problem theory and methods for model parameter estimation, siam.

Teng, W., Jonsson, S., and Hanssen, R.F., 2014, Improved SAR Image Coregistration Using Pixel-Offset Series: Geoscience and Remote Sensing Letters, IEEE, v. 11, p. 1465-1469.

Tenzer, R., Hamayun, Novak, P., Gladkikh, V., and Vajda, P., 2011, Global Crust-Mantle Density Contrast Estimation from EGM2008, DTM2008, Crust2.0, and ICE-5G: Pure and Applied Geophysics.

Tenzer, R., Hamayun, K., and Vajda, P., 2009, Global maps of the CRUST 2.0 crustal components stripped gravity disturbances: J. Geophys. Res., v. 114.

Thatcher, W., 1975, Strain accumulation and release mechanism of the 1906 San Francisco Earthquake: Journal of Geophysical Research, v. 80, p. 4862-4872.

Titus, S.J., DeMets, C., and Tikoff, B., 2005, New slip rate estimates for the creeping segment of the San Andreas fault, California: Geology, v. 33, p. 205-208.

Tobita, M., Nishimura, T., Kobayashi, T., Hao, K.X., and Shindo, Y., 2011, Estimation of coseismic deformation and a fault model of the 2010 Yushu earthquake using PALSAR interferometry data: Earth and Planetary Science Letters, v. 307, p. 430-438.

Tong, X., Sandwell, D.T., and Fialko, Y., 2010, Coseismic slip model of the 2008 Wenchuan earthquake derived from joint inversion of interferometric synthetic aperture radar, GPS, and field data: J. Geophys. Res., v. 115.

Tong, X., Sandwell, D.T., and Smith-Konter, B., 2013, High-resolution interseismic velocity data along the San Andreas Fault from GPS and InSAR: Journal of Geophysical Research: Solid Earth, v. 118, p. 369-389.

Tong, X., Smith-Konter, B., and Sandwell, D.T., 2014, Is there a discrepancy between geological and geodetic slip rates along the San Andreas Fault System?: Journal of Geophysical Research: Solid Earth, v. 119, p. 2013JB010765.

Trelea, I.C., 2003, The particle swarm optimization algorithm: convergence analysis and parameter selection: Information Processing Letters, v. 85, p. 317-325.

Tse, S.T., and Rice, J.R., 1986, Crustal earthquake Instability in Relation to the Depth Variation of Frictional Slip Properties: J. Geophys. Res., v. 91, p. 9452-9472.

Unruh, J.R., Twiss, R.J., and Hauksson, E., 1997, Kinematics of postseismic relaxation from aftershock focal mechanisms of the 1994 Northridge, California, earthquake: Journal of Geophysical Research: Solid Earth, v. 102, p. 24589-24603.

USGS, 2011, Magnitude 7.1 - EASTERN TURKEY, *in* http://earthquake.usgs.gov/earthquakes/eqinthenews/2011/usb0006bqc/, ed., Volume 2013.

Utkucu, M., 2013, 23 October 2011 Van, Eastern Anatolia, earthquake (Mw 7.1) and seismotectonics of Lake Van area: Journal of Seismology, p. 1-23.

Utkucu, M., and Durmus, H., 2012, A teleseismic finite-fault rupture model for the August 17, 1999, Izmit earthquake (Mw=7.6): implications for the seismic nucleation phase: Annals of Geophysics, v. 55.

Velez, M.L., Euillades, P., Caselli, A., Blanco, M., and Díaz, J.M., 2011, Deformation of Copahue volcano: Inversion of InSAR data using a genetic algorithm: Journal of Volcanology and Geothermal Research, v. 202, p. 117-126.

Wald, D.J., and Graves, R.W., 2001, Resolution analysis of finite fault source inversion using one- and three-dimensional Green's functions: 2. Combining seismic and geodetic data: Journal of Geophysical Research: Solid Earth, v. 106, p. 8767-8788.

Waldhauser, F., and Ellsworth, W.L., 2000, A Double-Difference Earthquake Location Algorithm: Method and Application to the Northern Hayward Fault, California: Bulletin of the Seismological Society of America, v. 90, p. 1353-1368.

Walters, R.J., Elliott, J.R., D'Agostino, N., England, P.C., Hunstad, I., Jackson, J.A., Parsons, B., Phillips, R.J., and Roberts, G., 2009, The 2009 L'Aquila earthquake (central Italy): A source mechanism and implications for seismic hazard: Geophys. Res. Lett., v. 36.

Walters, R.J., Elliott, J.R., Li, Z., and Parsons, B., 2013, Rapid strain accumulation on the Ashkabad fault (Turkmenistan) from atmosphere-corrected InSAR: Journal of Geophysical Research: Solid Earth, v. 118, p. 3674-3690.

Walters, R.J., Parsons, B., and Wright, T.J., 2014, Constraining crustal velocity fields with InSAR for Eastern Turkey: Limits to the block-like behavior of Eastern Anatolia: Journal of Geophysical Research: Solid Earth, v. 119, p. 5215-5234.

Wang, E., Xu, F.-Y., Zhou, J.-X., Wan, J., and Burchfiel, B.C., 2006a, Eastward migration of the Qaidam basin and its implications for Cenozoic evolution of the Altyn Tagh fault and associated river systems: Geological Society of America Bulletin, v. 118, p. 349-365.

Wang, H., and Wright, T.J., 2012, Satellite geodetic imaging reveals internal deformation of western Tibet: Geophys. Res. Lett., v. 39.

Wang, H., Wright, T.J., Yu, Y., Lin, H., Jiang, L., Li, C., and Qiu, G., 2012a, InSAR reveals coastal subsidence in the Pearl River Delta, China: Geophysical Journal International, v. 191, p. 1119-1128.

Wang, K., and Fialko, Y., 2014, Space geodetic observations and models of postseismic deformation due to the 2005 M7.6 Kashmir (Pakistan) earthquake: Journal of Geophysical Research: Solid Earth, p. 2014JB011122.

Wang, K., Hu, Y., and He, J., 2012b, Deformation cycles of subduction earthquakes in a viscoelastic Earth: Nature, v. 484, p. 327-332.

Wang, L., Hainzl, S., Zöller, G., and Holschneider, M., 2012c, Stress- and aftershock-constrained joint inversions for coseismic and postseismic slip applied to the 2004 M6.0 Parkfield earthquake: Journal of Geophysical Research: Solid Earth, v. 117, p. B07406.

Wang, L., Shum, C.K., Simons, F.J., Tapley, B., and Dai, C., 2012d, Coseismic and postseismic deformation of the 2011 Tohoku-Oki earthquake constrained by GRACE gravimetry: Geophys. Res. Lett., v. 39.

Wang, L., Shum, C.K., Simons, F.J., Tassara, A., Erkan, K., Jekeli, C., Braun, A., Kuo, C., Lee, H., and Yuan, D.-N., 2012e, Coseismic slip of the 2010 Mw8.8 Great Maule, Chile, earthquake quantified by the inversion of GRACE observations: Earth and Planetary Science Letters, v. 335-336, p. 167-179.

Wang, Q., Zhang, P.-z., Freymueller, J.T., Bilham, R., Larson, K.M., Lai, X.a., You, X., Niu, Z., Wu, J., Li, Y., Liu, J., Yang, Z., and Chen, Q., 2001, Present-Day Crustal Deformation in China Constrained by

Global Positioning System Measurements: Science, v. 294, p. 574-577.

Wang, R., 1999, A Simple Orthonormalization Method for Stable and Efficient Computation of Green's Functions: Bull. Seism. Soc. Am., v. 89, p. 733-741.

Wang, R., Diao, F., and Hoechner, A., 2013a, SDM-A geodetic inversion code incorporating with layered crust structure and curved fault geometry, EGU General Assembly Conference Abstracts, Volume 15, p. 2411.

Wang, R., Lorenzo-Martin, F., and Roth, F., 2006b, PSGRN/PSCMP-a new code for calculating co- and post-seismic deformation, geoidf and gravity changes based on the viscoelastic-gravitational dislocation theory: Computers & Geosciences, v. 32, p. 527-541.

Wang, R., Parolai, S., Ge, M., Jin, M., Walter, T.R., and Zschau, J., 2013b, The 2011 Mw 9.0 Tohoku-Oki Earthquake: Comparison of GPS and Strong-Motion Data Bull. Seism. Soc. Am., v. 103.

Wang, T., and Jonsson, S., 2014, Phase-Ramp Reduction in Interseismic Interferograms From Pixel-Offsets: Selected Topics in Applied Earth Observations and Remote Sensing, IEEE Journal of, v. PP, p. 1-1.

Wang, W., Sun, W., and Jiang, Z., 2010, Comparison of fault models of the 2008 Wenchuan earthquake (Ms8.0) and spatial distributions of co-seismic deformations: Tectonophysics, v. 491, p. 85-95.

Wang, W., Wu, J., Fang, L., and Wang, C., 2013c, Relocation of the Yushu M_S7.1 earthquake and its aftershocks in 2010 from HypoDD: Science China Earth Sciences, v. 56, p. 182-191.

Wang, Y., Wang, M., Shen, Z.-K., Ge, W., Wang, K., Wang, F., and Sun, J., 2013d, Inter-seismic deformation field of the Ganzi-Yushu fault before the 2010 Mw 6.9 Yushu earthquake: Tectonophysics, v. 584, p. 138-143.

Wang, Y., Zheng, J., Zhang, W., Li, S., Liu, X., Yang, X., and Liu, Y., 2012f, Cenozoic uplift of the Tibetan Plateau: Evidence from the tectonic–sedimentary evolution of the western Qaidam Basin: GEOSCIENCE FRONTIERS, v. 3, p. 175-187.

Ward, S., and Barrientos, S., 1986, An inversion for slip distribution and fault shape from geodetic observations of the 1983, Borah Peak, Idaho, earthquake: J. geophys. Res, v. 91, p. 4909-4919.

Weertman, J., and Weertman, J.R., 1964, Elementary dislocation theory, Macmillan.

Wegmüller, U., and Werner, C., 1997, Gamma SAR processor and interferometry software: ESA SP, p. 1687-1692.

Wei, M., Kaneko, Y., Liu, Y., and McGuire, J.J., 2013, Episodic fault creep events in California controlled by shallow frictional heterogeneity: Nature Geosci, v. 6, p. 566-570.

Wei, M., Sandwell, D., and Smith-Konter, B., 2010a, Optimal combination of InSAR and GPS for measuring interseismic crustal deformation: Advances in Space Research, v. 46, p. 236-249.

Wei, S., Chen, Y.J., Sandvol, E., Zhou, S., Yue, H., Jin, G., Hearn, T.M., Jiang, M., Wang, H., Fan, W., Liu, Z., Ge, Z., Wang, Y., Feng, Y., and Ni, J., 2010b, Regional eartqhuakes in northern Tibetan Plateau: Implications for lithospheric strength in Tibet: Geophys. Res. Lett., v. 37.

Wen, X., Du, F., and Zhang, P., 2011, Correlation of major earthquake sequences on the northern and eastern boundaries of the Bayan Har Block, and its relation to the 2008 Wenchuan Earthquake: Chinese J. Geophys. (in Chinese), v. 54, p. 706-716.

Wen, Y., Li, Z., Xu, C., Ryder, I., and Burgmann, R., 2012a, Postseismic motion after the 2001 Mw 7.8 Kokoxili earthquake in Tibet Observed by InSAR time series: J. Geophys. Res., v. 117.

Wen, Y., Xu, C., Liu, Y., and He, P., 2012b, Source parameters of 2008 Qinghai Dachaidan Mw 6. 3 earthquake from InSAR inversion and automated fault discretization method: Geomatics and Information Science of Wuhan University, v. 37, p. 458-462.

Wen, Y., Xu, C., Liu, Y., Jiang, G., and He, P., 2013, Coseismic slip in the 2010 Yushu earthquake (China), constrained by wide-swath and strip-map InSAR: Nat. Hazards Earth Syst. Sci., v. 13, p. 35-44.

Wessel, P., and Smith, W.H.F., 1998, New, improved version of generic mapping tools released: EOS, Transactions American Geophysical Union, v. 79, p. 579-579.

Weston, J., Ferreira, A.M.G., and Funning, G.J., 2011, Global compilation of interferometric synthetic aperture radar earthquake source models: 1. Comparisons with seismic catalogs: J. Geophys. Res., v. 116.

Wright, T., Fielding, E., and Parsons, B., 2001a, Triggered slip: observations of the 17 August 1999 Izmit (Turkey) earthquake using radar interferometry: Geophys. Res. Lett., v. 28, p. 1079-1082.

Wright, T., Parsons, B., and Fielding, E., 2001b, Measurement of interseismic strain accumulation across the North Anatolian Fault by Satellite radar interferometry: Geophys. Res. Lett., v. 28, p. 2117-2120.

Wright, T.J., Elliott, J.R., Wang, H., and Ryder, I., 2013, Earthquake cycle deformation and the Moho: Implications for the rheology of continental lithosphere: Tectonophysics, v. 609, p. 504-523.

Wright, T.J., Lu, Z., and Wicks, C., 2003, Source model for the Mw6.7, 23 October 2002, Nenana Mountain Earthquake (Alaska) from InSAR: Geophys. Res. Lett., v. 30.

Wright, T.J., Lu, Z., and Wicks, C., 2004a, Constraining the Slip Distribution and Fault Geometry of the M_W7.9, November 2002, Denali Fault earthquake with Interferometric Synthetic Aperture Radar and Global Positioning System Data: Bull. Seism. Soc. Am., v. 94, p. S175-S189.

Wright, T.J., Parsons, B.E., Jackson, J.A., Haynes, M., Fielding, E.J., and England, P.C., 1999, Source parameters of the 1 Octorber 1995 Dinar (Turkey) earthquake from SAR interferometry and seismic bodywave modelling: Earth and Planetary Science Letters, v. 172, p. 23-37.

Wright, T.J., Parsons, B.E., and Lu, Z., 2004b, Toward mapping surface deformation in three dimensions using InSAR: Geophysical Reserch Letters, v. 31, p. L01607.

Xia, W., Zhang, N., Yuan, X., Fan, L., and Zhang, B., 2001, Cenozoic Qaidam Basin, China: A Stronger Tectonic Inversed, Extensional Rifted Basin: AAPG Bulletin, v. 85, p. 715-736.

Xu, C., Ding, K., Cai, J., and Grafarend, E.W., 2009, Methods of determining weight scaling factors for geodetic–geophysical joint inversion: Journal of Geodynamics, v. 47, p. 39-46.

Yagi, Y., and Fukahata, Y., 2011, Rupture process of the 2011 Tohoku-oki earthquake and absolute elastic strain release: Geophys. Res. Lett., v. 38.

Yamazaki, Y., Cheung, K.F., and Lay, T., 2013, Modeling of the 2011 Tohoku Near-Field Tsunami from Finite-Fault Inversion of Seismic Waves: Bulletin of the Seismological Society of America, v. 103, p. 1444-1455.

Yamazaki, Y., Lay, T., Cheung, K.F., Yue, H., and Kanamori, H., 2011, Modeling near-field tsunami observations to improve finite-fault slip models for the 11 March 2011 Tohoku earthquake: Geophys. Res. Lett., v. 38.

Yan, Y., Pinel, V., Trouvé, E., Pathier, E., Perrin, J., Bascou, P., and Jouanne, F., 2013, Coseismic displacement field and slip distribution of the 2005 Kashmir earthquake from SAR amplitude image correlation and differential interferometry: Geophysical Journal International.

Yang, H., Liu, Y., and Lin, J., 2013a, Geometrical effects of a subducted seamount on stopping megathrust ruptures: Geophysical Research Letters, p. n/a-n/a.

Yang, Y.-R., Johnson, K.M., and Chuang, R.Y., 2013b, Inversion for absolute deviatoric crustal stress using focal mechanisms and coseismic stress changes: The 2011 M9 Tohoku-oki, Japan, earthquake: Journal of Geophysical Research: Solid Earth, v. 118, p. 2013JB010224.

Yanovskaya, T., 2003, Inverse problems of geophysics, Trieste Univ. Abdus Salam Int.

Yin, A., Dang, Y.-Q., Wang, L.-C., Jiang, W.-M., Zhou, S.-P., Chen, X.-H., Gehrels, G.E., and McRivette, M.W., 2008a, Cenozoic tectonic evolution of Qaidam basin and its surrounding regions(Part 1): The southern Qilian Shan-Nan Shan thrust belt and northern Qaidam basin: GSA Bulletin, v. 120, p. 813-846.

Yin, A., Dang, Y.-Q., Zhang, M., Chen, X.-H., and McRivette, M.W., 2008b, Cenozoic tectonic evolution of the Qaidam basin and its surrounding regions (Part 3): Structural geology, sedimentation, and regional tectonic reconstruction: Geological Society of America Bulletin, v. 120, p. 847-876.

Yin, A., Rumelhart, P.E., Butler, R., Cowgill, E., Harrison, T.M., Foster, D.A., Ingersoll, R.V., Qing, Z., Xian-Qiang, Z., Xiao-Feng, W., Hanson, A., and Raza, A., 2002, Tectonic history of the Altyn Tagh fault system in northern Tibet inferred from Cenozoic sedimentation: Geological Society of America Bulletin, v. 114, p. 1257-1295.

Yokota, Y., Kawazoe, Y., Yun, S., Oki, S., Aoki, Y., and Koketsu, K., 2012, Joint inversion of teleseismic and InSAR datasets for the rupture process of the 2010 Yushu, China, earthquake: Earth Planets Space, v. 64.

Yue, H., and Lay, T., 2011, Inversion of high-rate (1 sps) GPS data for rutpure process of the 11 March 2011 Tohoku earthquake (Mw 9.1): Geophys. Res. Lett., v. 38.

Yue, H., and Lay, T., 2013, Source Rupture Models for the Mw 9.0 2011 Tohoku Earthquake from Joint Inversions of High-Rate Geodetic and Seismic Data: Bulletin of the Seismological Society of America, v. 103, p. 1242-1255.

Yun, S.-H., Zebker, H., Segall, P., hooper, A., and Poland, M., 2007, Interferogram formation in the presence of complex and large deformation: Geophys. Res. Lett., v. 34.

Zahradník, J., and Sokos, E., 2014, The Mw 7.1 Van, Eastern Turkey, earthquake 2011: two-point source modelling by iterative deconvolution and non-negative least squares: Geophysical Journal International, v. 196, p. 522-538.

Zebker, H., and Goldstein, R.M., 1986, Topographic mapping from interferometric synthetic aperture radar observations: J. Geophys. Res., v. 91, p. 4993-4999.

Zebker, H.A., and Chen, K., 2005, Accurate Estimation of Correlation in InSAR Observations: IEEE Geoscience and Remote Sensing Letters, v. 2, p. 124-127.

Zebker, H.A., Hensley, S., and Wortham, C., 2010, Geodetically Accurate InSAR Data Processor: IEEE Transactions on Geoscience and Remote Sensing, v. 48, p. 4309-4321.

Zebker, H.A., Rosen, P.A., and Goldstein, R.M., 1994, On the derivation of coseismic displacement fields using differential radar interferometry: The Landers earthquake: J. Geophys. Res., v. 99, p. 19617~19634.

Zebker, H.A., Rosen, P.A., and Hensley, S., 1997, Atmospheric effects in interferometric synthetic aperture radar surface deformation and topographic maps: J. Geophys. Res., v. 102, p. 7547-7563.

Zebker, H.A., and Villasenor, J., 1992, Decorrelation in Interferometric Radar Echoes: IEEE Transactions on Geoscience and Remote Sensing, v. 30, p. 950~959.

Zha, X., and Dai, Z., 2013, Constraints on the seismogenic faults of the 2003–2004 Delingha earthquakes by InSAR and modeling: Journal of Asian Earth Sciences, v. 75, p. 19-25.

Zhang, P.-Z., Wen, X.-z., Shen, Z.-K., and Chen, J.-h., 2010a, Oblique, High-Angle, Listric-Reverse Faulting and Associated Development of Strain: The Wenchuan Earthquake of May 12, 2008, Sichuan, China: Annu. Rev. Earth Planet. Sci., v. 38, p. 353-382.

Zhang, Y., Feng, W., Xu, L., Zhou, C., and Chen, Y., 2009a, Spatio-temporal rupture process of the 2008 great Wenchuan earthquake: SCIENCE IN CHINA SERIES D-EARTH SCIENCES, v. 52, p. 145-154.

Zhang, Y., Xu, L., and Chen, Y.-t., 2010b, Fast inversion of rutpure process of the 14 April 2010 Yushu, Qinghai, earthquake: Earth Sci, v. 23, p. 201-204.

Zhang, Y., Xu, L., and Chen, Y.-T., 2010c, Source process of the 2010 Yushu, Qinghai, earthquake: Science China (Earth Science), v. 53, p. 1249-1251.

Zhang, Z.-Z., Chao, B.F., Lu, Y., and Hsu, H.-T., 2009b, An effective for GRACE time-variable gravity: Fan filter: Geophys. Res. Lett., v. 36.

Zhou, J., Xu, F., Wang, T., Cao, A., and Yin, C., 2006, Cenozoic deformation history of the Qaidam Basin, NW China: Results from cross-section restoration and implications for Qinghai–Tibet Plateau tectonics: Earth and Planetary Science Letters, v. 243, p. 195-210.

Zhou, X., Sun, W., Zhou, B., Fu, G., Dong, J., and Nie, Z., 2012, Geodetic observation detecting coseismic displacements and gravity changes caused by the Mw=9.0 Tohoku-Oki earthquake: J. Geophys. Res., v. 117.

Zhu, L., and Rivera, L.A., 2002, A note on the dynamic and static displacements from a point source in multilayered media: Geophys. J. Int., v. 148, p. 619-627.

Ziv, A., 2012, Inference of coseismic slip via joint inversion of GPS and aftershock data: The 2004 Parkfield example: J. Geophys. Res., v. 117.

Zoback, M.L., Zoback, M.D., Adams, J., Assumpcao, M., Bell, S., Bergman, E.A., Blumling, P., Brereton, N.R., Denham, D., Ding, J., Fuchs, K., Gay, N., Gregersen, S., Gupta, H.K., Gvishiani, A., Jacob, K., Klein, R., Knoll, P., Magee, M., Mercier, J.L., Muller, B.C., Paquin, C., Rajendran, K., Stephansson, O., Suarez, G., Suter, M., Udias, A., Xu, Z.H., and Zhizhin, M., 1989, Global patterns of tectonic stress: Nature, v. 341, p. 291-298.

Appendix

A.1 Principles of the Small Baseline InSAR Method

The Small BAseline Subset (SBAS) approach was proposed by Berardino *et al.* (2002) for detecting Earth surface deformation and, above all, analyzing their temporal evolution. With many years of developments, this method has achieved great success in a number of applications for detecting small tectonic movements, subsidence, glacier motion and DEM error (e.g. Hooper, 2008; Casu et al., 2009; Li et al., 2009b; Cetin et al., 2012; Wang and Wright, 2012; Fattahi and Amelung, 2013; Ducret et al., 2014). If N+1 SAR images from one SAR orbit track relative to the same area are acquired at the ordered time $(\boldsymbol{t_0}, \ldots, \boldsymbol{t_N})$, the number of possible interferograms (M), satisfies $\frac{\boldsymbol{N+1}}{\boldsymbol{2}} \leq \boldsymbol{M} \leq \boldsymbol{N}\frac{\boldsymbol{N+1}}{\boldsymbol{2}}$. At a given pixel in unwrapped interferograms, according to a linear deformation behaviour with time (Berardino et al., 2002; Schmidt and Bürgmann, 2003), the problem of solving observations errors and deformation rate can be written as

$$\boldsymbol{GS} = \boldsymbol{D} \qquad \textbf{(A.1)}$$

where $\boldsymbol{G}$ is the $\boldsymbol{M} \times \boldsymbol{k}$ design matrix including three components: $[\boldsymbol{G}_{\mathbf{a}}, \boldsymbol{G}_{\mathbf{de}}, \boldsymbol{G}_{\mathbf{v}}]$, representing the effects of atmosphere screen (APS), DEM error and deformation velocity between each epoch in light-of-sight (LOS). $\boldsymbol{S}$ is the unknown solution to including three components that can be re-written as $[\boldsymbol{S}_{\mathbf{a}}, \boldsymbol{S}_{\mathbf{de}}, \boldsymbol{S}_{\mathbf{v}}]^{\mathbf{T}}$. $\boldsymbol{S_a}$ and $\boldsymbol{S_{de}}$ are a $\boldsymbol{M} \times (\boldsymbol{N} + \mathbf{1})$ matrix and an $\boldsymbol{M}$-dimensional vector, respectively. $\boldsymbol{D}$ is the LOS displacement vector, $[\mathbf{d_0}, \ldots, \mathbf{d_M}]^{\mathbf{T}}$. $\mathbf{S_v}$ is an $\boldsymbol{M} \times \boldsymbol{p}$ matrix for the model parameters. $\boldsymbol{p}$ depends on the deformation model being assumed in the time series inversion. Thus $\boldsymbol{k}$ can be directly calculated by $\boldsymbol{k} = (\boldsymbol{N} + \mathbf{1}) + \mathbf{1} + \boldsymbol{p}$ that also relies on the used deformation model. For a cubic behaviour over time as used by Berardino *et al.* (2002), the LOS deformation rate at the given pixel at $\boldsymbol{i}^{\text{th}}$ acquisition can be expressed by

$$\boldsymbol{d_i} = \overline{\boldsymbol{\vartheta}}(\boldsymbol{t_i} - \boldsymbol{t_0}) + \boldsymbol{a}(\boldsymbol{t_i} - \boldsymbol{t_0})^2 + \boldsymbol{b}(\boldsymbol{t_i} - \boldsymbol{t_0})^3 \qquad \textbf{(A.2)}$$

where $[\bar{\vartheta}, a, b]$ are unknown parameters accounting for the mean velocity, the mean acceleration, and the mean acceleration variation (Berardino et al., 2002). $\boldsymbol{t_o}$ is the reference time. Then for each epoch between $\boldsymbol{t_i}$ and $\boldsymbol{t_j}$, the LOS changes can be written by

$$\Delta\boldsymbol{d_{ij}} = \boldsymbol{d_i} - \boldsymbol{d_j} \qquad \textbf{(A.3).}$$

The sub-design matrix $\boldsymbol{G}_{\mathbf{a}}$ is apparently rank deficient. Once the third part of independent

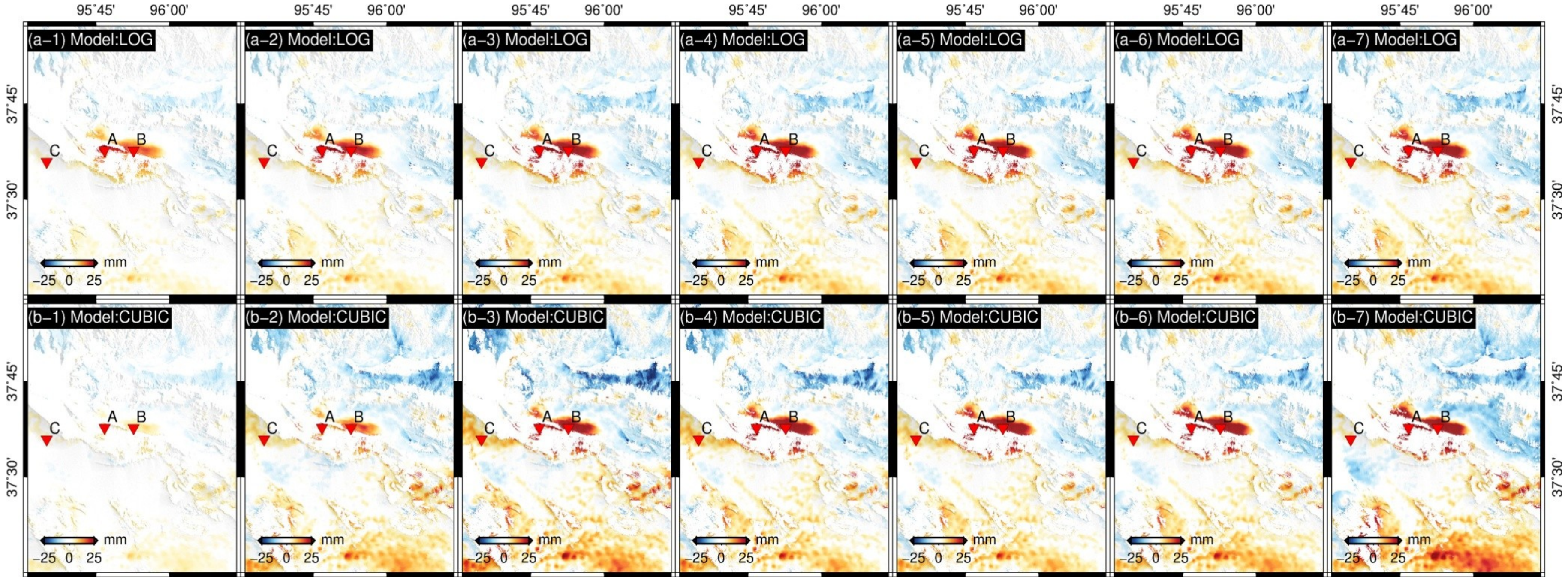

Figure A.1 Comparison of Time series results using different deformation models. (a-1~7) are derived using a log deformation model, in which the cumulative displacements represent for the periods until 20090916 (a-1), 20091021(a-2), 20091230 (a-3), 20100310 (a-4), 20100414 (a-5), 20100519 (a-6) and 20100623 (a-7), respectively. (b-1~7) are as for (a-1~7), but derived from a cubic deformation model.

observations for the contributions of APS can be considered in the phase inversion (Li et al., 2009b; Li et al., 2009c), $\boldsymbol{G}_{\mathbf{a}}$ can be ignored or become determined. In order to guarantee a physically sound solution for the deformation rate, rational assumptions can be considered for constructing $\boldsymbol{G}$. First of all, the APS component at $\boldsymbol{j}$th acquisition that has limited effects from APS, can be assumed to zero. A given deformation model can also be employed in the phase inversion. The cubic model proposed by Berardino et al. (2002) has been widely applied successfully for retrieving complex deformation history with a number of SAR images (Berardino et al., 2002; Lanari et al., 2004; Lanari et al., 2007)**,** which was also used in the postseismic deformation analysis of the 2009 M_{W} 6.3 Qinghai earthquake (Chapter 3). Postseismic deformation resulting from afterslip after large earthquakes have been frequently observed as accumulating logarithmically with time (e.g. Marone et al., 1991; Donnellan and Lyzenga, 1998). A logarithmic model can also be employed to depict postseismic relaxation as used in the 2003 M_{W} 6.5 Bam, Iran earthquake (Li et al., 2009b) and some other cases (e.g. Gonzalez-Ortega et al., 2014). The phase inversion using a log-function for the postseismic deformation time series after the 2009 mainshock was also implemented in Chapter 3. The orbital errors have been reduced by using an improved network method prior to time series inversion. 17 postseismic interferograms were clipped into the same geo-reference region as shown in Figure (A.1). In the resultant postseismic times series derived by using the cubic deformation model, significant long wavelength errors can be observed in the far field (Figure (A.1)). A significant difference between the log and cubic models for the postseismic deformation at the first acquisition (20090916) (Figure A.1 (a-1 and b-1)), showing that the cumulative postseismic displacements in the first month from the cubic model is much smaller than derived from the log model.

A.2 Gravity simulation for GRACE observations

GRACE-based gravity observations were successfully applied to detect the coseismic gravity changes following the 2011 M_{W} 9.1 Tohoku-Oki earthquake. Based on the elastic dislocation models (Okubo, 1992, 1993), the coseismic gravity changes on the Earth's surface caused by the mainshock were calculated using the given slip models. Based on the general expression given by Sun *et al.* (2009), the coseismic gravity change can be defined by

$$\boldsymbol{\delta g(r,\theta,\varphi)} = \Delta \boldsymbol{g(r,\theta,\varphi)} - \boldsymbol{\beta u(r,\theta,\varphi)} \qquad \textbf{(A.4)}$$

where $[r,\theta,\varphi]$ represent the radial distance, the co-latitude and the longitude under the spherical coordinate system. The first term $\Delta g(r,\theta,\varphi)$ on the right hand of Equation (A.4) side is the gravity change at a fixed-space point and the second term $-\beta u(r,\theta,\varphi)$ gives the free air effects on the Earth's surface. But the gravity change observations from the satellite do not include the term $-\beta u(r,\theta,\varphi)$ since the Satellite gravity mission cannot observe this part. Meanwhile, as a megathrust subduction zone event, major coseismic displacements take place on the ocean floor. The rapid compensation from sea water after the coseismic rupture of the mainshock should be fully taken into account in the simulation (e.g. Han and Simons, 2008; Cambiotti and Sabadini, 2012; Wang et al., 2012d; Wang et al., 2012e). The final step for simulating the gravity observations from the satellite is to truncate the high-frequency components of the coseismic gravity changes by converting the theoretical gravity results into the spherical harmonic coefficients. Operations used in GRACE data processing, e.g. 300-km Fan filtering (Zhang et al., 2009b), were also applied in the gravity change simulation. Based on different slip models inferred in previous studies (Ji, 2011; Wang et al., 2013b) and this thesis, the theoretical gravity changes were calculated (Figure A.2). The simulations are all based on the elastic half-space Earth model. The simulation derived from the Joint slip model determined in this thesis shows better agreement with the observations that other published slip models (Figure A.2 (a)). The simulation from Wang *et al*'s slip model has similar amplitude, but different deformation patterns can be observed. The maximum gravity change (Figure A.2 (d)) from the simulation based on Ji *et al*'s model seems too large in contrast to the observations (Figure A.2 (a)).

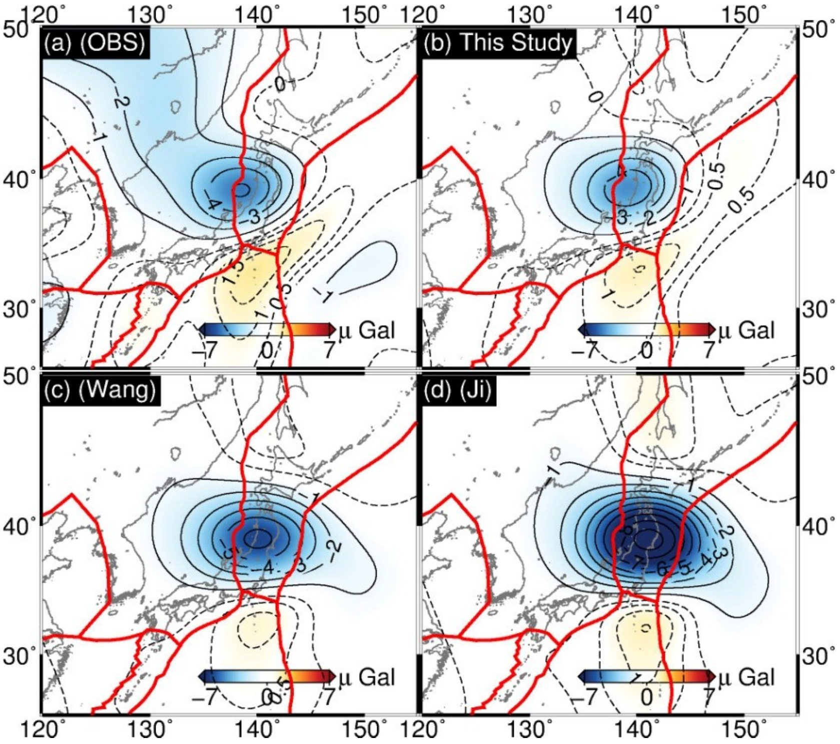

Figure A.2 Comparison between GRACE-based coseismic gravity changes and predicted ones using different slip models. (a) The GRACE-based coseismic gravity changes; (b) the modelled gravity changes by the joint slip model determined in this thesis; (c) the modelled gravity changes by Wang *et al*'s slip model (Wang et al., 2013b), and (d) the prediction by Ji *et al*'s slip model (Ji, 2011).

Complicated operations have been considered in the predicted gravity simulation, which may make theoretical gravity change to slip nonlinear. To test this potential issue, a series of simulations were performed based on slips on a 100-km-long and 100-km-wide fault plane. Only upward slip was considered. Figure A.3 shows that modelled GRACE-based gravity changes vary linearly with slip. But the variation of gravity changes between different filtering is significant. At the same given location, the predicted gravity change corresponding to a 50-m slip using the smoothing strategy (Figure A.3), including decorrelation P3M15 and 300 km Fan, is ~43% smaller than that filtered by

300-km Gaussian method only. Thus, the filtering method used in modelling should be strictly consistent with data processing.

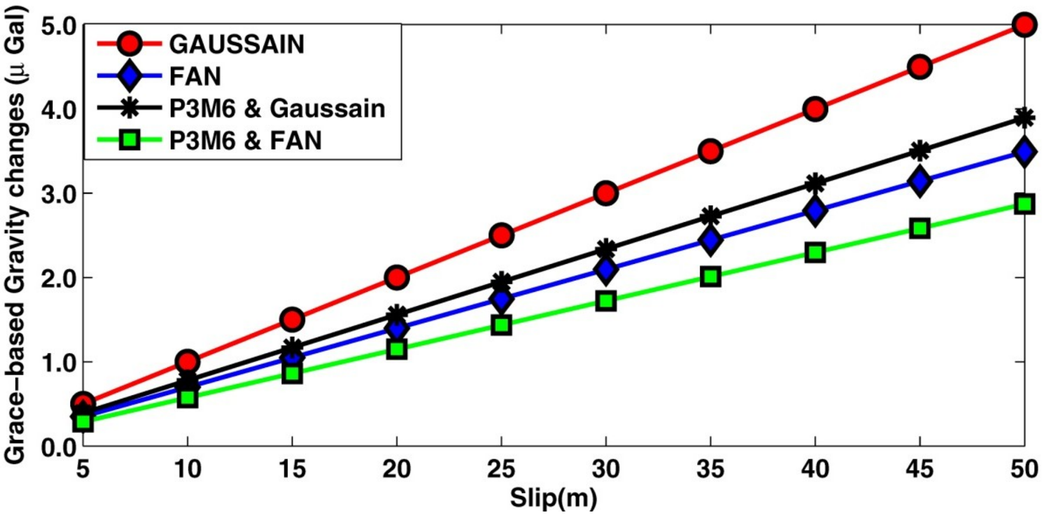

Figure A.3 Comparison of the theoretical gravity calculations using different filtering methods.

A.3 Selected publications during the PhD study

1. ***Feng, W.***, Li, Z., Li, Q. *et al.*, 2014. Coseismic slip distribution of the 2011 Mw 9.0 Tohoku (Japan) earthquake from a joint inversion with GRACE Gravity changes and inland GPS measurements, ***Geophysical Journal International***, (in revision)
2. ***Feng, W.,*** Li, Z., Hoey, T., et al., 2014. Patterns and mechanisms of co- and post-seismic slips of the 2011 M_W 7.1 Van (Turkey) earthquake revealed by multi-platform synthetic aperture radar interferometry. ***Tectonophysics*** 632, 188-198. doi: 10.1016/j.tecto.2014.06.011.
3. ***Feng, W.***, Li, Z., Elliott, J. R., et al., 2013. The 2011 M_W 6.8 Burma earthquake: fault constraints provided by multiple SAR techniques. ***Geophysical Journal International*** 195, 650-660. doi:10.1093/gji/ggt254.